ELECTROHYDRODYNAMICS IN POLYELECTROLYTE LAYER GRAFTED NARROW-FLUIDIC CHANNELS

A Thesis Submitted in Partial Fulfillment of the Requirements for the Degree of

DOCTOR OF PHILOSOPHY

by

Gaikwad Harshad Sanjay

(Roll No. 166103004)

Department of Mechanical Engineering

Indian Institute of Technology Guwahati

Guwahati-781039, India.

December 2020

Department of Mechanical Engineering,
Indian Institute of Technology Guwahati,
Guwahati-781039, India.

Declaration

I hereby certify that the information reported in the dissertation "**Electrohydrodynamics in Polyelectrolyte Layer Grafted Narrow-Fluidic Channels**" is entirely my own research, performed under the guidance of Dr. Pranab Kumar Mondal. Any part of this work has not earlier been submitted for the award of any degree, diploma, associate-ship, fellowship or it's equivalent to any University or Institution. I have not violated any copyright and plagiarism law. All text and figures are my own.

19 December 2020

Gaikwad Harshad Sanjay
Roll No. 166103004
Department of Mechanical Engineering,
Indian Institute of Technology Guwahati,
Guwahati – 781039, Assam,
India.

Department of Mechanical Engineering,
Indian Institute of Technology Guwahati,
Guwahati-781039, India.

Certificate

It is certified that the work contained in this thesis entitled "**Electrohydrodynamics in Polyelectrolyte Layer Grafted Narrow-Fluidic Channels**" submitted by **Gaikwad Harshad Sanjay** to the Indian Institute of Technology Guwahati for the award of the degree of Doctor of Philosophy has been carried out under my supervision in the Department of Mechanical Engineering, Indian Institute of Technology Guwahati. This work has not been submitted elsewhere for the award of any other degree or diploma.

19 December 2020

Dr. Pranab Kumar Mondal

Assistant Professor

Department of Mechanical Engineering,

Indian Institute of Technology Guwahati,

Guwahati – 781039, Assam,

India.

To my family

For their limitless love, support and patience.

ACKNOWLEDGEMENT

I would like to take this opportunity to express my sincere gratitude towards many people who helped me during my PhD tenure at IIT Guwahati. I appreciate their support and help rendered during various phases of my research work.

Important of all, I would like to show my deepest and sincerest gratitude to my supervisor, Dr. Pranab Kumar Mondal, for his valuable guidance, inspiration, and time-to-time advice. It was a privilege to work with him on various problems and methods, and have fruitful discussions on multifarious academic and non-academic subjects. Diverse ideas put forward, and the concepts suggested by him, were the real catalysts those expedited my research work and helped me to introduce this altogether unique dissertation. I firmly believe that the various concepts, the incorporated solution methodologies and the non-intuitive insights penned down in this dissertation, which were intermittently and meticulously proofread by him, will sound scientific and be rewarded by many professionals. Further, I would extend my sincerest gratitude towards my doctoral committee members, Prof. Vinayak Kulkarni, Dr. Pankaj Mishra, and Dr. Bhaskar Kumar for their valuable suggestions and shading light on several deficits which were unintentionally left in my work. Research in my PhD tenure led me through a significant learning process and in that respect, I am grateful to Prof. Gautam Biswas (Department of Mechanical Engineering, IIT Kanpur), Dr. Sweta Tiwari (Department of Mathematics, IIT Guwahati) and Dr. P. Kaushik (Department of Mechanical Engineering, NIT Surat), for clarifying most of the doubts, questions and several ambiguities. Apart from that, I shall acknowledge here ‘Param Ishan’, High-Performance Computing (HPC) facility, Computer and Communication Center, IIT Guwahati.

I am thankful to my seniors Dr. Srinivas Gorthi, Abhijit Gogoi, Rajkumar Sarma, Sudip Shyam, Aritra Mukharjee for supporting and motivating to overcome any problems either in work and otherwise. Over these years, I have cherished my memories of hostel life with my best friends Sagar Pawar, Pranav Satpute, Dr. Shailesh Varade, Dr. Soham Singh, Dr. Siddhesh Desai, Dr. Sumit Agarwal, Ashish Yadav, to name a few. Those were the unforgettable days as I had wonderful companions like Ankush Sontakke, Shweta Kumbhar, Sandesh Phalke, Dr. Vinod Pandey, Dr. Hiranya Deka and Dr. Shruti Rapur at IIT Guwahati. Apart from that, I would also thank Gaurav Kumar (Department of Mechanical Engineering, Cochin University of Science and Technology, Kerala, India), for his contribution in the analysis conducted for Chapter 3 of this dissertation.

Most importantly, I am very much thankful to my family for understanding my preoccupation with this work and foregoing their demands in my time. None of this would have been possible without the love and patience of them. I shall always be grateful for being a constant source of love, concern, support and strength for all these years.

Gaikwad Harshad Sanjay

ABSTRACT

Polyelectrolytes are the polymeric macromolecules whose repeating units bear an ionic group. A layer of such polyelectrolytes or a polyelectrolyte layer, grafted on the walls of the narrow-fluidic channels, often termed as the soft narrow-fluidic channels, has immense practical implications in the on-chip microscale transport. A critical review of the existing literature, however, suggests that there exist quite a few applications in which the polyelectrolyte layer can demonstrate its profound efficacy. These include the transport of biofluids, mixing in narrow-fluidic assays, rotational force induced micromixing, and the energy conversion mechanism in the microfluidic batteries. Through the present dissertation, we frame the objectives and discuss the analysis pertinent to each aforesaid application in the respective chapters. A summary of these analyses is given as follows.

The first problem deals with the transport of biofluids through the soft narrow-fluidic channels. These biofluids typically show the non-Newtonian rheology which can be mimicked using the Ostwald's de'Waele power-law model. The complex interplay between the soft layer modulated rich electrochemistry, and the non-Newtonian rheology of the biofluids induce the non-trivial variations in underlying flow dynamics; and for a window of parameters defined for the analysis, provide a significant enhancement in the flow rate. Notably, the rise in the net throughput was found to be appreciable for both the regimes of the power-law rheology viz., the shear-thinning and the shear-thickening regimes.

Encouraged by such noteworthy outcomes in the first problem, for the second and third problems as well, we deployed the soft layer modulated electroosmotic flow to regulate the mixing in the respectively defined domains of analyses. The second problem considers a slit narrow-fluidic channel having the walls grafted with the soft layer patches, whereas, the third problem considers a rotating rectangular narrow-fluidic channel having the walls grafted with the homogenous soft layer. In the second problem, the grafting of the soft layer patches follows two different patterns: symmetric and asymmetric pattern, based on the symmetry defined by the channel centerline. It is also worth to mention here that through the analysis conducted in the third problem, we propose for the first time the use of variation calculus method to elucidate the electrohydrodynamics in the rotating soft narrow-fluidic channel. The results of both these analyses (second and third) reveal that the enriched electrostatics and the frictional resistance, tunable through a grafted soft layer properties, delineate its substantial capacity in inducing the intriguing vortex configurations and thus, achieving the giant mixing performance. The parameters of the soft layer those

provide such distinguishable flow controllability include its thickness, the ionic density of the grafted layers, and the drag coefficient associated with the frictional resistance offered by grafted layer to the flow. However, for a particular range of these parameters, the adverse consequences of the Coriolis force in case of the third problem lead to a reduction in the mixing.

In the fourth problem, we consider the soft layer grafted on the walls of the narrow-fluidic channel to improve the electrochemomechanical energy conversion associated with the transport of viscoelastic fluid. The rheology of the viscoelastic fluid is depicted by a simplified Phan-Thien-Tanner model. In this problem, other than the soft layer modulated electrostatics and the frictional resistance; we also investigate the influence of a few factors on the conversion efficiency. These are the hydrodynamics slip at the solid (or wall)-liquid interface, pertinent analysis beyond the Debye-Hückel approximation, the electrical conductance of the Stern layer and that of the walls of the channel on the underlying conversion efficiency. Also, we highlight in this study, the adverse influence of the electroviscous effect that stems through the resistance of the conduction current to the primary pressure-driven flow on the conversion efficiency.

LIST OF ABBREVIATIONS AND SYMBOL

Abbreviations

ATRP	Atom-Transfer-Radical-Polymerization
DH	Debye-Hückel
EL	Electrolyte Layer
EDL	Electric Double Layer
EOF	Electroosmotic Flow
FDM	Finite Difference Method
FEM	Finite Element Method
LOC	Lab-On-A-Chip
MEMS	Micro-Electro-Mechanical-Systems
NP	Nernst-Planck
PB	Poisson-Boltzmann
PDMS	Polydimethylsiloxane
PL	Polymeric Layer
PEL	Polyelectrolyte Layer
PNP	Poisson-Nernst-Planck
PTT	Phan-Thein-Tanner
sPTT	Simplified Phan-Thien-Tanner
μ TAS	Micro-Total-Analysis-Systems

Latin symbols

$c \in c_{1,2}$	Concentration of the uncharged species (1 or 2)
c_0	Concentration of the uncharged species in unmixed state
c_∞	Concentration of the uncharged species in the mixed state
$D_e \in D_{e,\pm}$	Ionic diffusion coefficient of the electrolyte ions (positive/negative)
$\mathbf{D}$	Deformation rate tensor or strain-rate tensor
Du	Dukhin number
D_S	Diffusion coefficient of the uncharged species
d	Thickness of polyelectrolyte layer or polyelectrolyte layer thickness

E_0	Reference electric field
E_x	Strength of the electric field in the x direction
E_S	Streaming potential
e_0	Charge of electron
$F_E \in F_{E,x/y}$	Electroosmotic force (in x or y direction)
F_d	Darcy's frictional drag force
F_V	Volumetric body force
$f_{e,\pm}$	Ionic friction coefficients of the positive/negative electrolyte ions
G	Pressure
H_0^2	Hilbert space with zero magnitude of vector at and outside of the boundary, and differentiable up to 2nd order
I_m	Mixing index
k_B	Boltzmann constant
ls	Slip length
m_0	Flow consistency coefficient
$\left(N_x, N_y, N_z\right)$	Number of grid points in the x, y and z direction, respectively
N_p	Number density of the polyelectrolyte ions
$n_e \in n_{e,\pm}$	Number density of the electrolyte ions (positive/negative)
n_∞	Number density of the electrolyte ions in the electroneutral region
n_0	Power-law index or flow behavior index
$\mathbf{p}_g$	Gyroscopic pressure
Pe_I	Ionic Peclet number
Q_x	Flow rate through the channel in the x direction
Q_{in}	Inlet flow rate
Re	Reynold number
Ro	Rossby number
Re_ω	Rotational Reynolds number
S	Entropy of mixing

$S_{\max}$	Maximum entropy of mixing
Sc	Schmidt number
T	Absolute temperature
$\mathbf{u} = (u, v, w)$	Velocity field in the entire channel domain
u_{HS}	Helmholtz-Smoluchowaski velocity
U_{in}	Velocity at the inlet of the channel
$u_{\pm}$	Ionic velocity
Wi_k	Weissenberg number

Subscripts

e	Electrolyte layer
p	Polyelectrolyte layer

Greek symbols

α	Drag parameter of polyelectrolyte layer
Γ	Dimensionless pressure gradient
γ_w	Electrical conductance of the channel walls
$\dot{\gamma}$	Magnitude of strain-rate tensor
ε	Extensibility parameter of the viscoelastic fluid
ε_e	Electrical permittivity of the electrolyte
ε_r	Relative permittivity of the electrolyte
ε_0	Electrical permittivity of the free space
ζ	Zeta potential
η	Dynamic viscosity of the fluid or electrolyte
η_{eff}	Effective viscosity of the fluid in case of electroviscous effect
η_{app}	Apparent viscosity of the fluid in case of power-law model
κ	Debye-Hückel parameter of electrolyte layer
κ_p	Debye-Hückel parameter of polyelectrolyte layer

κ_r	Ratio of Debye-Hückel parameter of electrolyte layer to the polyelectrolyte layer
λ	Relaxation time of the viscoelastic fluid
μ_c	Darcy's friction coefficient for polyelectrolyte matrix
ξ_C	Energy conversion efficiency
ξ_m	Mixing efficiency
Π	Total functional
ρ	Density of the fluid or electrolyte
$\rho_{e/p}$	Volumetric charge density of the electrolyte and polyelectrolyte
σ_{stern}	Electrical conductance of the Stern layer
$\boldsymbol{\tau}$	Stress tensor
τ_w	Wall shear stress
Φ	Total electric potential
ϕ_A	Applied electric potential
ψ	Induced electrostatic potential
ψ_s	Stream function
$\boldsymbol{\Omega}$	Total rotational speed of the channel
Ω^*	Rotational speed in the z direction
Ω_b	Domain of Hilbert space
ω_v	Vorticity

CONTENTS

LIST OF FIGURES

(= 0.5 and 1.5). (b) Influence of wall conductance: Plots show the variation of energy conversion efficiency ξ_C with DH parameter of EL κ for different values of γ_w(= 0, -2 and -4) and viscoelastic parameter εWi_k^2 (= 0.5 and 1.5). The other parameters considered for this analysis are: $d = 0.3$, $\Gamma = 1.0$, $\alpha = 2.0$, $\kappa_p = 10$. The shaded portions with different colours help to identify the set of plots obtained for the particular value of a parameter, Dukhin number in the case of (a) and viscoelastic parameter in the case of (b).

LIST OF TABLES

CHAPTER 1

Introduction

The narrow-fluidic channels having the inner surfaces grafted with the soft polyelectrolyte layer find a huge importance in the applications which deal with the electrokinetic phenomena, namely, the electroosmotic flow and the streaming potential (S. Das et al., 2015). In view of the present thesis too, the applications designed on the basis of these phenomena wherein the polyelectrolyte layers can prove their magnificent efficacy are of immediate interest to us. Recognizing this demand, in this very first chapter of the thesis, we start by setting quick familiarity with the aforesaid topics of electrokinetics and the polyelectrolyte layer modulated electrostatics. The applications considered in the present study with their significance, working principles, and the major deficits and drawbacks, which can be suppressed by the polyelectrolyte layers are elaborated in the same chapter. The ongoing discussion also contains the literature review which highlights the lately set benchmarks in the recent developments of these applications. Towards the closure of this chapter, finally, a brief idea will be given about the theorized objectives and the organization of the thesis.

1.1 A Brief Review of the Electric Double Layer Formation

Charged surfaces upon interacting with the electrolytes lead to the formation of an *electric double layer* (EDL) (J H Masliyah & Bhattacharjee, 2006). Under the influence of such EDLs, the electrolytes redistribute their ions in two sorts of categories usually called as *coions* and *counterions*. Coions carry the same charge as that of beared by the charged surface while the counterions carry the opposite. The term '*electric double layer*' emerges from the fact that an EDL encompasses two sublayers: the Stern layer which envelops the immobile counterions and the Gouy-Chapman layer (or diffuse layer) which envelops the mobile counterions (J H Masliyah & Bhattacharjee, 2006; R. J. Hunter, 1981). A typical EDL that would form on the charged surface is shown in Fig. 1.1(a).

In the electric double layer, the dense cluster of the counterions formed inside the Stern layer, as shown in Fig. 1.1(a), develops an electrostatic potential ψ according to the Gauss's law. Up to an imaginary plane, also termed as a *shear plane*, this electrostatic potential remains constant and begins to reduce onwards in the perpendicular direction to the charged surface on which the EDL forms. The potential at the shear plane is also termed as *Zeta potential* (ζ) (J H Masliyah & Bhattacharjee, 2006). Very far away from the Stern layer, the magnitude of ψ or zeta potential declines to zero since the counterions' density diminishes to zero. In this electroneutrality condition, these counterions exist with the coions. The region where such electroneutrality condition persists is called as the *electroneutral region*. EDL begins from the charged surface and vanishes near the electroneutral region. If the convection of ions is neglected, the distribution of the counterions, as well as the coions within the aforesaid bounds of the EDL, can be obtained by the Boltzmann analogy[1].

To solve the potential distribution inside the EDL, we use the Gauss's law which in the form of Poisson equation can be written as (J H Masliyah & Bhattacharjee, 2006; R. J. Hunter, 1981):

$$\nabla^2\psi = -\frac{\rho_e}{\varepsilon_e} \tag{1.1}$$

where ρ_e is the volumetric charge density and ε_e is the electrical permittivity of the electrolyte. The charge density ρ_e is a function of the coions' and counterions' number

[1] For Boltzmann analogy, refer to Chapter 2: Section 2.1.1.

densities. Any change in the charge density leads to a variation in the electrostatic potential ψ and effectively modulates the EDL thickness or Debye length. Such type of variation in ψ and the corresponding EDL characteristics (i.e., Debye length) is of immense importance in the electrokinetic phenomena.

1.2 Electrokinetic Phenomena: A Foundation for Building Applications

Electrokinetic phenomena occur when one attempts to mobilize the counterions from the electric double layer, particularly from the diffuse layer (J H Masliyah & Bhattacharjee, 2006). The most employed means to actuate the motion of counterions are the externally applied electric field and the pressure gradient applied across the channel. These flow actuation mechanisms, although allowing the counterions to move through the channel, lead to altogether the different consequence. It is worth mentioning here that the external electric field develops the electroosmotic flow inside the channel. On the other hand, the pressure-driven flow produces electric power by generating the streaming potential. The working principles of both the electroosmotic flow and the streaming potential generation, are schematically shown in Figs. 1.1(a)-(b).

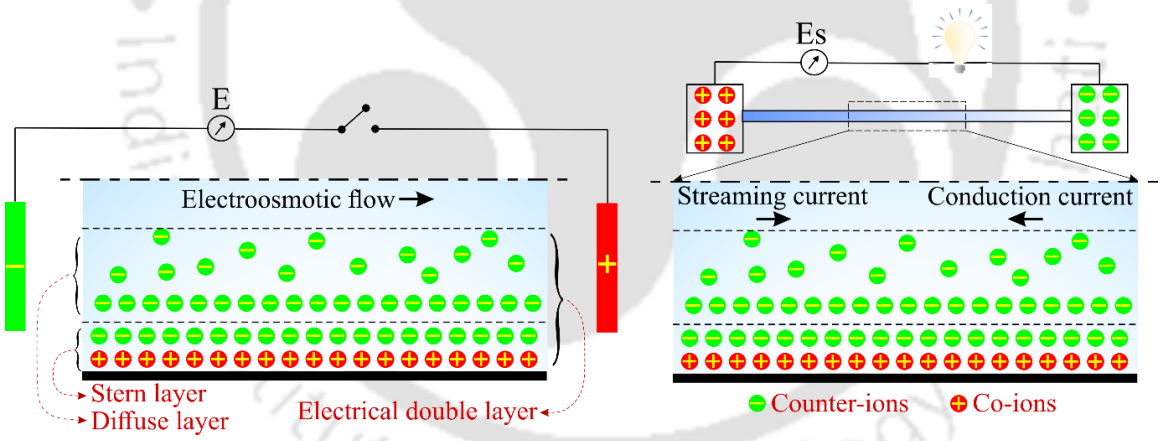

Figure 1.1: Schematics in (a) and (b) show the working principle of both the electroosmotic flow and the streaming potential generation phenomenon, respectively.

Electroosmotic flow. An external electric field applied across the channel, by imposing the proportional Lorentz force, sets the counterions from the EDL (particularly from the diffuse layer) into the motion. The hydrodynamic resistance imposed by the viscosity of the fluid diffuses such motion of the ions towards the bulk of the fluid, thus causing the net flow of the fluid through the channel. The movement of counterions and the flow direction can be tuned by modulating the applied field. This flow is often termed as *electroosmotic flow* or EOF in short (J H Masliyah & Bhattacharjee, 2006).

Streaming potential. On the other hand, when an external source apart from the electric or magnetic field, say a pressure gradient, for instance, is applied across the channel, it establishes the convection of ions, called as *streaming current* (refer to Fig. 1.1(b)). The streaming current over the period of time leads to the accumulation of counterions towards the outlet of the channel, and a deficiency of them towards the inlet. This particular situation can be picturized as the electric battery made up of the narrow-fluidic channel, with two electrodes those set a potential drop across the channel ends, known as the *streaming potential* (J H Masliyah & Bhattacharjee, 2006). If a system reaches a steady-state, the streaming potential develops a *conduction current* opposite to that of the streaming current. Such state or condition is acknowledged as the *current-neutrality condition*. At this condition, the summation of the streaming current and the conduction current is zero. By and large, it can be conceived that the mechanical energy as the input given in terms of the pressure-driven flow, and the chemical energy provided by the electric double layer; is converted into the electrical energy, that is in the form of streaming potential. Such conversion of energy is defined as *electrochemomechanical energy conversion* (Chanda et al., 2014; J H Masliyah & Bhattacharjee, 2006), and it is schematically shown in Fig. 1.1(b).

1.3 A Few Limitations of the Electrokinetic Phenomena Based Conventional Working Principles

The electrokinetic phenomena discussed, namely, the electroosmotic flow and the streaming potential, show tremendous applicability due to their minimalistic requirement of the fluid volume and the other advantages like a noise-free operation, a requirement of no mechanical moving components, to name a few (Hessel et al., 2005; N.-T. Nguyen et al., 2002; N.-T. Nguyen & Wu, 2005). The researchers have even molded the conventional working principles of various applications with the mentioned electrokinetic phenomena. However, on account of the rising demands of such state-of-the-art applications and the micro-scale systems, these working principles need some significant modifications in the intrinsic aspects. By saying '*intrinsic aspect*', we point to the 'electric double layer' or the method of its formation. The accustomed or standard approach of EDL formation[2], which is usually employed in the concerned electrokinetic phenomena, encounters with a few limitations. These limitations are elaborated as follows.

[2] The 'accustomed or standard approach of EDL formation' refers to the approach in which the EDL formation takes place on the commonly used charged surfaces.

***Provision of limited flow controllability*.** In the applications wherein the 'standard approach of EDL formation' is mostly employed, one has the only couple of variables other than the thermodynamic quantities (e.g. absolute temperature) to modulate the EDL characteristics. These variables are the charge density over the charged surface and the ionic concentration of the electrolyte. Even with these features, the up-to-date applications still fail to achieve a considerable enhancement in the respective performances. For example, it is the enhanced net pumping in case of electroosmotic flow and higher conversion efficiency in case of streaming potential generation. Therefore, the applicability of these electrokinetic phenomena, i.e., the electroosmotic flow and the streaming potential, that depends on the 'standard EDL formation approach', in recent years is found to be somewhat restricted (Chanda et al., 2014; Chen & Das, 2015a, 2017; S. Das et al., 2015; Kaushik et al., 2019; A. Sadeghi et al., 2019; M. Sadeghi et al., 2020).

***Lack of bio-lubrication effect*.** In the context of this ongoing discussion, it is also important to mention that the rigid surfaces of the channel walls, on which the EDL formations take place, fail to provide a lubrication effect to the biofluids or bio-samples in a separate manner. The standard approach of the EDL formation mostly considers the rigid surfaces or surfaces with no-protective cushioning provided for the candidate fluids. As a result, once the important test samples say the biofluids are directly exposed to such rigid surfaces, the quality of these samples may degrade. In view of that, while architecting the new devices for biofluids, it becomes an imperative condition that the walls of the channel must be grafted with the soft or protective cushioning that would refrain the contact of bio-samples with the rigid surfaces (Raviv et al., 2003).

The aspects related to each limitation, penned in the purview of achieving the effective functionality in the up-to-date applications, need effortless approaches if implemented separately. However, if not considered the *grafted polyelectrolyte layers* as an option, the combination of the two aspects mentioned above, in a single domain of analysis remains a challenge. In other words, we would like to suggest here, the soft polyelectrolyte layer as a solution to the aforementioned limitations. The questions 'What? Why? and How?' one would ask about the polyelectrolyte layers are addressed in the upcoming section.

1.4 Solution: A Polyelectrolyte Layer

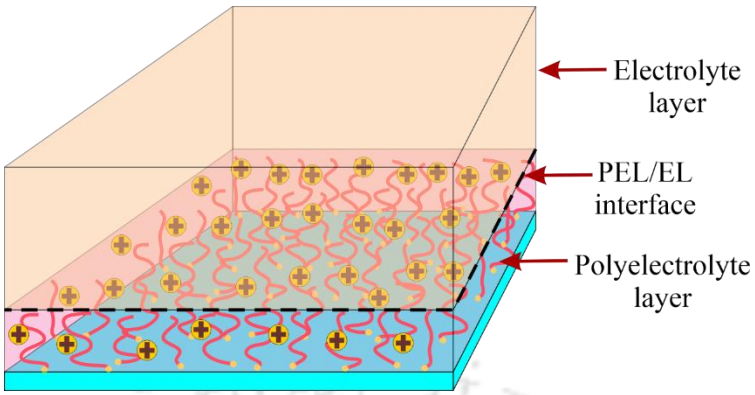

Figure 1.2: Schematic shows the typical polyelectrolyte layer grafted on a rigid surface in the presence of the electrolyte layer.

Rigid narrow-fluidic channels, the narrow-fluidic channels having the bare walls, usually adopt the 'standard approach of EDL formation'. Therefore, the drawbacks discussed in the previous section, many times, appear in case of rigid narrow-fluidic channels. To overcome these drawbacks, most recently, the research community has endorsed the implementation of the grafted polyelectrolyte layer (PEL) or a soft layer on the inner surfaces of the channel walls (a typical soft layer is shown in Fig. 1.2). The channels with such soft layers can be fabricated on the Polydimethylsubstrate (PDMS) substrates (Hu et al., 2002). A potential reason to call PELs as the '*soft layers*' or '*smart layers*' is; these layers can induce very strong electrokinetics and offer a new volumetric body force to tune the hydrodynamics inside the soft narrow-fluidic channels (S. Das et al., 2015). The key features which furnish these advantages are the PEL thickness, the charge density of PEL's repeating ionic groups, and the frictional resistance offered by the PEL matrix to the flow of fluid (Chanda et al., 2014; Chen & Das, 2016, 2017). The last feature, i.e., the frictional resistance of the PEL which is defined on the basis of Darcy's analogy of the '*flow through porous media*' is also termed as *Darcy's frictional drag* (Donald A. Nield & Bejan, 2006). The magnitude of this drag depends on the PEL's grafting density and a few other intrinsic elements. For example, one element is the Kuhn's length of the polyelectrolytes (Chen & Das, 2016). The grafting density of PEL relies on the type of grafting techniques. Of the huge list of these, the '*grafting-from*' technique - 'Atom-Transfer-Radical-Polymerization' (ATRP) is the most suitable one as the highest attainable grafting density of the PEL is within reach of this method (S. Das et al., 2015).

Another benefit of the grafted PEL is the simplistic modifications in the governing equations of electrostatics and hydrodynamics. If we graft the PEL on the surface of interest

in the presence of an electrolyte, as shown in Fig. 1.2, we get the following set of equations for both the electrostatics and the hydrodynamics (Chanda et al., 2014).

Poisson equation

Electrolyte layer

$$\nabla^2 \psi_e = -\frac{\rho_e}{\varepsilon_e} \tag{1.2a}$$

Polyelectrolyte layer

$$\nabla^2 \psi_p = -\frac{\rho_e + \rho_p}{\varepsilon_e} \tag{1.2a}$$

Momentum equations

Electrolyte layer

$$\frac{\partial \mathbf{u}_e}{\partial t} + \left(\mathbf{u}_e.\nabla\right)\mathbf{u}_e = -\nabla G + \nabla.\boldsymbol{\tau}_e + F_E \tag{1.3a}$$

Polyelectrolyte layer

$$\frac{\partial \mathbf{u}_p}{\partial t} + \left(\mathbf{u}_p.\nabla\right)\mathbf{u}_p = -\nabla G + \nabla.\boldsymbol{\tau}_p + F_E + F_d \tag{1.3b}$$

In Eqs. (1.2) and (1.3), we notice that apart from the polyelectrolyte layer, we also need the respective governing equations of both the electrostatics and hydrodynamics for the electrolyte layer when it coexists with the polyelectrolyte layer. It is important to mention in the context of these equations that the major contribution of the polyelectrolyte layer is always manifested in tandem with the contribution of the electrolyte layer. Otherwise, it is unwise to argue that the polyelectrolyte layer gains its prominence due to its own charge distribution and matrix structure. Therefore, what we can conceive from Eqs. (1.2) and (1.3) is, the PEL modulated electrostatics and hydrodynamics in the presence of the electrolyte also depends on the electrolyte properties and its flow domain.

In Eqs. (1.2) and (1.3), subscripts 'e' and 'p' help to identify the equations according to the electrolyte layer and polyelectrolyte layer, respectively. Therefore, the electrostatic potential ψ, stress tensor $\boldsymbol{\tau}$, and the velocity field $\mathbf{u} = (u, v, w)$, can be denoted in both the EL and PEL sophistically.[3] For example, $\psi = \psi_e$ in EL, and $\psi = \psi_p$ in PEL. The volumetric charge densities of the electrolyte ions ρ_e and the polyelectrolyte ions ρ_p are given by the following expressions (Chanda et al., 2014).

For electrolyte

$$\rho_e = z_e e_0 \left(n_{e,+} - n_{e,-} \right) \tag{1.4a}$$

For polyelectrolyte

$$\rho_p = Z_p e_0 N_p \tag{1.4b}$$

where z_e is the valence on a single electrolyte ion and e_0 is the electronic charge. In Eqs. (1.4a)-(1.4b), the terms $n_{e,+}$ and $n_{e,-}$ are the number densities of the positive and negative electrolyte ions, respectively. Note that while deriving Eq. (1.4), we consider the Gouy-Chapman model of a symmetric $z_e : z_e$ electrolyte. For such electrolytes, we assume $z_e = +z_{e,+} = -z_{e,-}$ (J H Masliyah & Bhattacharjee, 2006; R. J. Hunter, 1981). Here, the terms $z_{e,+}$ and $z_{e,-}$ are the valences on a single - positive and negative ions of the electrolyte, respectively. In Eq. (1.4b), Z_p is the valence on a single polyelectrolyte ion and N_p is the number density of these ions (S. Das et al., 2015).

In Eqs. (1.3a)-(1.3b), the term ∇G represents the gradient of the pressure field. The electroosmotic force F_E in case of EL, is a function of potential ψ_e, whereas, for the PEL, it is a function of potential ψ_p. The last term F_d in the momentum equation [Eq. (1.3b)] derived for the PEL accounts for Darcy's frictional drag imposed by the macromolecules of the PEL on the motion of the fluid (S. Das et al., 2015). It is important to mention here that the potential and the velocity distribution obtained inside the entire domain shown in Fig. 1.2 is also the function of PEL thickness d. The influence of the PEL thickness can be taken into account while deriving the boundary conditions defined at the interface

[3] The terms ρ_e and ρ_p in Eq. (1.2) do not represent volumetric charge densities in *EL* and *PEL*. Rather, they are defined for *electrolyte* and *polyelectrolyte* independently. Therefore, ρ_e is charge density of the electrolyte ions, in both the EL and PEL, and ρ_p is the charge density of the polyelectrolyte ions in PEL only. In EL, ρ_e depends on ψ_e, and in PEL, it depends on ψ_p. This method of terminology of charge density is an exception which is defined in the main text for other quantities.

formed between the polyelectrolyte layer and electrolyte layer (PEL/EL (polyelectrolyte layer and electrolyte layer) interface is shown in Fig. 1.2) (Chanda et al., 2014; S. Das et al., 2015).

On the closer look at these equations [Eqs. (1.2) and (1.3)], it appears that the polyelectrolyte layers grafted on the walls of the narrow-fluidic channels offer multiple variables to achieve enhanced functionalities in the applications of the electrokinetic phenomena. These variables are the PEL thickness d, the charge density of the electrolyte ions ρ_e and polyelectrolyte ions ρ_p, Darcy's frictional drag in PEL F_d, and the charge density over the walls of the channel. Many times, the last variable, the charge density over the walls is neglected as the PEL itself provides the appreciable modifications in the electrohydrodynamics without any provision of the charge on the walls. It is also worth to mention here that, being made up of the protein-like structure, the polyelectrolyte layer offers a protective cushioning to the important samples such as DNA or proteins[4], thus preventing their degradation which is observed in case of the rigid narrow-fluidic channels. On account of this reason, it is found that the PEL constituted a noteworthy role in several biological or chemical but non-electrokinetic applications until recently (S. Das et al., 2015). Therefore, as an opportunity, the problems related to the contribution of such smart layers in the electrokinetically assisted clinical and pathological applications are worth pursuing at present.

Recognizing this importance, in the present thesis, we focus on a few applications which find enough significance in the clinical, pathological or alike areas wherein the PEL can manifest a prominent role. The applications of our interest are:

transport of biofluids through the rectangular narrow-fluidic channels

mixing of the co-injected streams of biological/chemical species

electrohydrodynamics and mixing in the rotating narrow-fluidic channels

giant enhancement in the energy conversion efficiency

The working principles of the first three applications are based on the electroosmotic pumping, and that of the last one is derived using the streaming potential generation phenomenon. The prime objective of the present thesis will be to improve the electrostatic

[4] The aspect of protective cushioning provided by the soft layer is covered in the forthcoming subsection 1.5.1

and flow dynamic characteristics to achieve the improved functionalities in the said applications. Besides, through the present thesis, we shall also focus on reliving these applications from the drawbacks they mostly encounter with such as the degradation of the bio-samples in case of the electroosmotic pumping (as previously discussed), approximately rigid body motion of the fluid through the rotating narrow-fluidic channel, the electroviscous effect in the energy conversion and much more to count in.

What follows after this section is the brief introduction of the applications considered for the analyses, working principles of them, and the drawbacks they mostly encounter with. The succeeding sections will be of great help to define and elaborate the key concepts related to each problem distinctively. To constitute a seamless discussion, the following introductions of each application will be supported with the detailed review of the archived literature, covering all the recent developments made for each application. We shall also highlight here the reported studies (if any) which have used the polyelectrolyte layer to achieve the designated objectives.

1.5 A Quick Review of the Archived Literature

Having discussed the topics of dissertation in the previous sections, we will now introduce the applications of our interest wherein the PEL modulated electrostatics and hydrodynamics can render their effectiveness. The literature review performed to know the recently set benchmarks in the development of each application is described here. Note that, since we have considered different applications for this study, the drawbacks, as well as deficits observed pertinent to each application, are also different. Therefore, for the sake of brevity in the presentation, we have mentioned these drawbacks and deficits while discussing the literature review pertinent to each application.

1.5.1 Transport of Biofluids

Electroosmotic pumping in a soft narrow-fluidic channel finds many practical applications such as an ion rectification, chemical sensing, flow control, characterization of elastomers and switching of the ion transports, to name a few (Chen & Das, 2015b). It is worth to mention here that, the literature on electroosmotic pumping is also rich in seminal contributions from numerous researchers which dealt with the PEL electrostatics. The very first studies date back to late eighties, wherein the PEL was incorporated to enhance the electroosmotic pumping. It was Donath and Voigt (Donath & Voigt, 1986), who first envisaged the use of polyelectrolyte layer for the enhancement of electroosmotic

pumping in the narrow-fluidic channels. The extensive use of the PEL in the electroosmotic pumping, however, can be found in the literature cited later in this chapter. The recent studies have shown that the sandwiched PEL between the channel walls and an electrolyte solution, alters the underlying flow dynamics non-intuitively (Andrews & Das, 2015; M. H. Matin & Ohshima, 2016). These PELs grafted on the walls of the microchannels can also be treated as the flow suppressors, since the friction drag offered by the PEL attenuates the flow rate in the channel (Chen & Das, 2017). The regulation of the flow rate through the soft narrow-fluidic channel can also be achieved by several avenues discovered by the researchers from different backgrounds. To tune or to increase the flow rate in the soft narrow-fluidic channel, the magnitude of the potential or the charge density at the walls is the key factor to take into consideration. Benson et al. (Benson et al., 2013) shown that the use of Field Effect Transistor is a considerable option to influence the charge density at the walls and therefore, the electroosmotic flow. However, in the endeavour of achieving a higher net throughput in the soft narrow-fluidic channel, one should take note of an important aspect. It is, the pH of the electrolytic solution, which can modulate the charge density or the potential at the walls, and for a particular range of it, as shown by Chen and Das (Chen & Das, 2015b), can reduce the potential, and hence, the electroosmotic flow.

Another way to achieve enormous increment in the net throughput through the soft narrow-fluidic channel is the collaboration of the electroosmotic flow with the pressure-driven flow (Meisam Habibi Matin & Ohshima, 2015). Apart from that, a recent study conducted by Chen and Das (Chen & Das, 2017) also shown that the end-charged polyelectrolyte brushes offer an astonishing increment in the electroosmotic transport as compared to the normal polyelectrolyte brushes. The prime factor which led to this observation was the charge distribution of the mobile ions concentrated far away from the walls, thus experiencing less shear resistance offered by the no-slip condition at the walls. More recently, Kaushik et al. (Kaushik et al., 2019) shown that the PEL modulated electroosmotic pumping can be of great assistance in the devices operating in the rotational framework as well. Also, a group of researchers led by Sadeghi (A. Sadeghi, 2018a, 2018b; A. Sadeghi et al., 2019; M. Sadeghi et al., 2020) has reported in their studies that, the rectangular soft narrow-fluidic channel through electroosmotic pumping indeed provides the best avenues to facilitate the multiple fluidic functionalities such as the mixing dynamics and a solute dispersion. Owing to this benefit of the PEL modulated electroosmotic flow, the soft narrow-fluidic channels are majorly employed in different

biological and chemical applications such as electrokinetics of biological cells, the effect of EDL in bacterial adhesion to surfaces, and charging and swelling of cellulose films (de Kerchove & Elimelech, 2005; Freudenberg et al., 2007; Makino & Ohshima, 2011; Poortinga et al., 2002).

In the applications mentioned, the PEL grafted on the walls of the channel renders one more benefit. It is the bio-lubrication effect. In the paradigm of transport of biofluids, one of the significant challenges is the prevention of the biological samples' degradation during their transportation in the lab-on-a-chip (LOC) platform (Raviv et al., 2003). The degradation of such samples occurs due to their direct contact with the mechanical components or the channel walls. This is the major disadvantage of such assays, where a covering the inner surfaces of the channel walls by a polyelectrolyte layer seems to be a remedial solution. The PEL, in this case, provides a smart cushioning to the biofluids. This benefit of the soft layers was first shown by Raviv et al. (Raviv et al., 2003). The study reported that, through the implementation of a PEL on the channel walls, the lubrication coefficient considerably increases (Raviv et al., 2003). Such lubricated surfaces having the grafted PELs are essential in artificial implants and a few biological systems.

Notably, many biofluids used in the said systems depict non-Newtonian rheology. For example, in the drug delivery applications, the emulsions comprising of the ionized oil and aqueous solution of anticancer drug, follow a rheological behaviour. These emulsions delineate both types of rheological behaviours: shear-thinning and shear-thickening one. The oil-water (O-W) and water-oil (W-O) emulsions show a shear-thinning nature (Demachi et al., 2000). It is also found from the literature that, an increment in the aggregate concentration leads to an increase in the dilatancy or shear-thickening nature of the pharmaceutical formulations (J Mastropietro, 2013). A typical example of the biofluids, which is also the most common sample used for in-vitro detection of the different diseases is the 'blood'. The non-Newtonian rheology, particularly the pseudo-plastic nature of the blood, is rendered by the separate layer of the plasma, which runs parallel to the channel or artery walls (Fahraeus & Lindqvist, 1930). All in all, this ongoing discussion reveals that the emulsions contained by the biofluids such as blood which are mostly tested in the devices designed with the PEL grafted narrow-fluidic channels, offer them either the pseudo-plastic or dilatancy behaviour. However, considering the above all pertinent issues, a thorough understanding of the underlying transport of non-Newtonian fluids through a

soft narrow-fluidic channel that appears to be an important aspect, is remained untouched in the literature till date. Moreover, these studies can have immense practical implications.

Another application of microscale paradigm where the biological fluids like 'blood', or chemical fluids can work in tandem with the polyelectrolyte layers is the narrow-fluidic mixing assay. In particular, the EOF assisted one which is highlighted in the next subsection.

1.5.2 Narrow-Fluidic Mixing Assays

The requirement of a minimal volume of the bio-samples and biofluids on a LOC platform for micro total analysis has motivated the researchers to investigate several aspects of the micromixing in recent years (Chew et al., 2007). As reviewed in the brief report of Hessel et al. (Hessel et al., 2005) and Nguyen et al. (N.-T. Nguyen & Wu, 2005), to achieve the efficient functionality in the mixing dynamics, various techniques consistent with either active methods or passive contrivances have been engineered by the researchers following the state-of-the-art technologies. The passive methods are much time consuming as they entirely depend on molecular diffusion (N.-T. Nguyen & Wu, 2005). On the contrary, the active mechanisms by impeding the fluid flow in the channel and using the external sources such as the electroosmotic flow, show a rapid and efficient mixing in the targeted applications. The 'targeted applications' cover the micro-arrays, DNA sequencing, sample preparation and analysis, cell separation and detection, and environmental monitoring (N.-T. Nguyen & Wu, 2005). The additional means (e.g. local impedance and electroosmotic flow) employed in the active techniques expedite the development of the vortices in the flow passage. Such quick onset of the vortical flow[5] observed in case of the active methods, on the other hand, takes a huge amount of time stretch in the passive methods (N.-T. Nguyen & Wu, 2005). Owing to this fact, the active methods outperform passive methods in a number of applications. In the preceding two decades, among the several active methods, the EOF assisted mixing mechanism, which is also one of the main problems addressed in the present thesis, has got a remarkable attraction of the researchers.

In EOF assisted mixing techniques, the use of patterned zeta potential patches at channel walls appears as the most overwhelmingly employed method to induce a qualitatively enhanced vortical flow (Basati et al., 2019; Ebrahimi et al., 2014; Hadigol et al., 2011; Loucaides et al., 2012; Nayak, 2014; Qian & Bau, 2002). This method of

[5] The term '*vortical flow*' refers to the flow having vortices formed in its passage.

patterned patch modulated fluidic functionalities can be effectively advanced further by considering a few additional aspects. For example, as reported by Hadigol et al. (Hadigol et al., 2011), the pseudo-plastic behaviour of the non-Newtonian fluid, which provides comparatively higher flow velocity is one of the countable aspects. The higher velocity of the fluid in most of the cases leads to a notable vortex configuration in the flow passage. However, the non-Newtonian rheology can influence the mixing, even without any consideration of the potential patterns at the walls (Bag & Bhattacharyya, 2018). Also, the application for the AC electrokinetics, and use of symmetry and asymmetry of the zeta potential patterns, albeit these are quite the debatable alternatives to enhance the mixing in the channels, can be considered in the paradigm of enhanced mixing having the patterned zeta potential patches (Loucaides et al., 2012; Nayak, 2014).

In a similar line of research, the modern studies have also shown that the conducting or non-conducting links (or ribs) (Alipanah & Ramiar, 2017; Ebrahimi et al., 2014) or conducting blocks (Nayak et al., 2018) placed at the intermittent positions of the channel can induce the local vortices and tune the mixing dynamics therein. The efficiency in such narrow-fluidic assemblies is the function of the length and the conductivity of the link, their location in the channel (Ebrahimi et al., 2014) and the strength of the AC electroosmosis (Alipanah & Ramiar, 2017). Here, the influence of non-Newtonian rheology (Alipanah & Ramiar, 2017) is one of the important factors. It can also be highlighted that the conducting link used in AC electroosmosis imitates a micro-stirrer, provided that the flexibility of the link which depends on Young's modulus is taken into account (Azimi et al., 2017). In the narrow-fluidic assays, the intermittently applied transverse electric field also alters the mixing dynamics by developing the local vortices (Krishnaveni et al., 2017; Pacheco, 2008). Apart from these methods, the unusual geometrical shapes of the microchannel, configured deliberately to monitor the vortical flow structures, are indeed capable of increasing the mixing efficiency. For instance, the wavy channel (Banerjee et al., 2019), converging-diverging or diverging-converging sections (Basati et al., 2019) and the patterned grooves (H. Wang et al., 2003), provide a significant rise in the mixing efficiency.

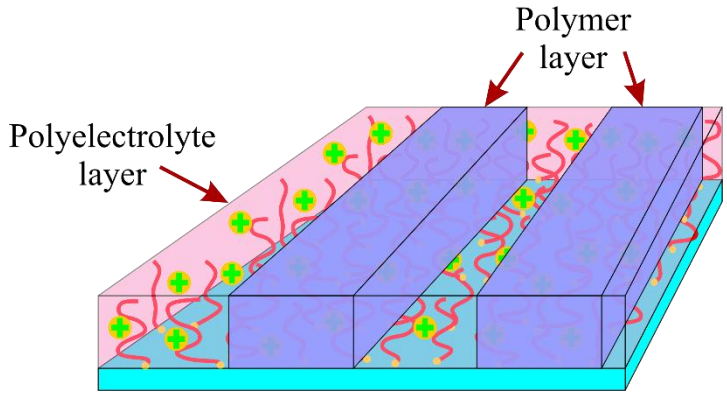

Figure 1.3: Schematic depicts the patterned polyelectrolyte layer – polymer layer structure.

It appears from these studies that the different vortical flow configurations developed using either the patterned zeta potential patches or the impendence causing solid structures such as a conducting link, certainly provide a dynamic avenue to attain the highest possible mixing efficiency. In view of that, the underlying flow dynamics under the influence of periodic patterning of the polyelectrolyte layer – polymer layer is expected to exhibit some unique aspects like the formation of vortices, increment in the retention time of the species,[6] and efficient mixing. A typical schematic of the patterned PEL-PL structure is shown in Fig. 1.3.

The discussion about the latest grafting techniques of the patterned PEL structure such as the micro-contact printing on the surface of miniaturized platforms, as reported in the refereed literature (Alom Ruiz & Chen, 2007; S. Das et al., 2015; Husemann et al., 1999; Prucker et al., 1999; von Werne et al., 2003; B. Zhao et al., 2000), is suggestive of the practicality of this unique architecture as shown in Fig. 1.3, obtained by using the PEL and PL. These deposited polyelectrolyte layers additionally allow the augmentation in several demanding functionalities through the controllable physical and chemical properties (Brilliantov et al., 2016; S. Das et al., 2015). These unique aspects are primarily attributed to the local and confined effect of the EDL on the underlying hydrodynamics. As such, the utilization of patterned PEL modulated electrokinetic effect for the enhancement in micromixing, could be a novel proposition in the paradigm of small scale transport processes, which is remaining unexplored in the literature to date.

We now move to discuss another application relying on the working principle of electroosmotic effect, i.e., the EOF assisted mixing in the rotating narrow-fluidic channels.

[6] The term '*retention time*' of species is often referred to the time taken by the candidate species to significantly mix with each other in the pre-defined confinements.

1.5.3 Electroosmotically Assisted Rotational Microfluidics

Rotational microfluidics deals with the micro-scale transport phenomena, which take the rotation led centrifugal and Coriolis forces into account. The translational motion of the fluid along the length of the channel in such phenomena is termed as the *primary flow* (Ng & Qi, 2015). In most of the cases, the centrifugal force or electroosmotic force, or the externally applied pressure gradient across the channel, actuates the primary flow. On the other hand, the Coriolis force that too stems from the rotational motion of the channel sets in a different kind of flow of the fluid, known as *secondary flow*. The direction of this flow is perpendicular to both the direction to the axis of rotation and the direction of the primary flow. The cooperation between these primary and secondary flows established by the unique Coriolis force also develops the non-intuitive vortex structures in the flow passage. These vortex structures are considered to be a countable factor while studying the targeted mixing phenomenon.

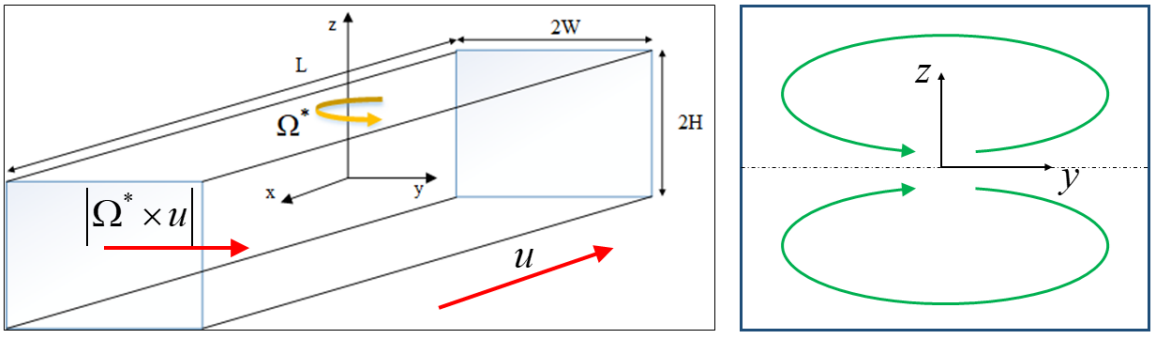

(a) **(b)**

Figure 1.4: (a) Schematic shows a rotating narrow-fluidic channel with Coriolis force $\Omega^* \times u$. The term Ω^* is the rotational speed of the channel, u is the flow velocity in the x direction, and the height and width of the channel is $2H$ and $2W$, respectively. (b) Schematic shows the geometry of the standard-double vortex that forms corresponding to the flow configuration shown in (a).

On account of this atypical flow dynamics, the rotational microfluidics in micro-electro-mechanical-systems (MEMS) and CD-based LOC platforms offers several advantageous features and have made significant advances in the field over the past few decades (Ducrée *et al.* 2006; Duffy *et al.* 1999; Stone *et al.* 2004). Of these features, the periodic-helical motion of the secondary flow vortices set by the Coriolis force and the lateral wall confinement renders an intriguing nature to the mixing in the rotational microfluidics (Ng & Qi 2015). The presence of such secondary flow vortices that appear with different configurations such as, standard double vortex and four vortex configuration was reported in the earliest studies (Kheshgi & Scriven, 1985; Nandakumar et al., 1991;

Speziale, 1982).

Research in the paradigm of rotational fluidics has also advanced extensively to explore the effect of electric field on the underlying transport phenomena in recent years. It appears from the literature that Kaushik and his co-workers have majorly contributed in the EOF assisted rotational microfluidics (Abhimanyu et al., 2016; Kaushik et al., 2016; Kaushik, Abhimanyu, et al., 2017; Kaushik, Mondal, et al., 2017; Kaushik & Chakraborty, 2017). The prime aspects, which were investigated by this research group are the influence of the power-law rheology and the viscoelasticity, consideration of the transverse and vertical pressure gradients, transience in the rotational electrohydrodynamics, and symmetric and asymmetric zeta potential on the walls of the channel. These studies have also addressed, the effects of the lateral wall confinement, and the appearance of sister vortices in the double vortex configuration (Abhimanyu et al., 2016; Kaushik et al., 2016; Kaushik, Abhimanyu, et al., 2017; Kaushik, Mondal, et al., 2017; Kaushik & Chakraborty, 2017). In such endeavours of achieving enhanced flow rate through the rotating narrow-fluidic channels, the higher zeta potential at the walls and fluid with the third-grade rheology are some of the countable factors to produce the distinguishable outcomes (Li et al., 2015; Xie & Jian, 2014).

The application of an electric field on the microflows in the rotating platform offers a few distinctive transport features. Among the several, the notable feature is, the electroosmotic pumping and the inevitable Joule heating effect dries out the dissolved air/gas bubbles from the fluid being transported (Chang & Wang 2011; Ng & Qi 2015; Wang *et al*. 2004). It may be mentioned in this context here that the electroosmotic pumping not only enhances the net throughput but also, upon interacting with the rotation induced forcing, promotes the onset of double vortex structures in the fluidic pathways (Ng & Qi 2015). Even with these benefits, the underlying flow dynamics in the miniaturized assays integrated on the rotating platforms is, however, encountered a few serious challenges. First, for example, the increasing magnitude of the Coriolis force adversely affects the axial momentum and triggers a rigid body type motion with increasing the magnitude of the rotational speed beyond no-flow limits (Stewartson 1957). Second, ensuring a considerable amount of the mixing efficiency in rotating devices/systems leads to the intervention of the geometrical and physical features of the centrifuges. Alongside above all issues, the direct exposure of fluid samples, typically bio-samples, to the binding surfaces of rotating micro-

total-analysis-systems (μTAS), leads to a significant deterioration of samples' quality as well.

One of the promising solutions to overcome these challenges could be the application of a grafted PEL on the walls of rotating narrow-fluidic channels. The benefit of using grafted PEL in the narrow pathways is its contributing effect towards the flow controllability. Physico-chemical structure of the layered polyelectrolyte together with the interaction between the polymeric macromolecules and electrolyte ions impacts on the flow dynamics non-intuitively at the microfluidic scale, leading to a greater degree of flow control in the narrow confinements (Das *et al.* 2015; Reshadi & Saidi 2019; Sadeghi *et al.* 2020). It is worth adding here that the flow dynamics in a soft narrow-fluidic channel, embedded in the rotating platform, upon interacting with the Coriolis force that stems from the rotational effect, would establish a necessary fluidic functionality of the enhanced quality of vortices in the course of flow. Moreover, these soft PELs, as discussed before, additionally provide a bio-lubrication effect to the bio-samples (S. Das et al., 2015; Raviv et al., 2003).[7] The grafted polyelectrolyte layer modulated electrostatics under the application of the electric field brings about a rich flow dynamics in the rotating fluidic environment, attributed primarily to the complex coupling of different forces that are in use. It is anticipated that the stronger electroosmotic effect, together with the frictional drag offered by the PEL, can modulate the rotational flow dynamics non-trivially, leading to an enhancement in the mixing performance following the formation of dumbbell-shaped vortices in the field. Nevertheless, no analysis has been reported to date considering the aforementioned effects in tandem in the rotational narrow-fluidic platform.

It can be noticed that in the sections 1.5.1-1.5.3, we have listed down, by reviewing the open literature; the applications of microscale paradigm wherein the PEL led electroosmotic pumping can provide the distinguishable outcomes. Nonetheless, this is only a single phenomenon (i.e., electroosmotic pumping), on which we have debated till now. The remaining one that also can be conspicuously tuned by the PEL is the streaming potential generation. The application, a pertinent literature review and effective influence of the shear-thinning rheology of the viscoelastic fluids on this phenomenon are addressed in the following subsection.

[7] The discussion of the '*bio-lubrication effect*' is detailed in the subsection 1.5.1.

1.5.4 Electrochemomechanical Energy Conversion

Electrochemomechanical energy conversion has built an enormous appeal in many applications of microsystems (H Daiguji et al., 2004; Hirofumi Daiguji et al., 2006; Yang et al., 2003). In the past few decades, to enrich the energy conversion efficiency in the state-of-the-art applications, researchers have been in a continuous endeavour of exploiting new techniques integrated with the underlying microscale transport processes. Examples include the use of a charged porous plug, an array of microchannels, and use of the PEL grafted microchannels (Chanda et al., 2014; Chen & Das, 2015b; Patwary et al., 2016; Yang et al., 2003).

Among the methods as mentioned above, the transport of aqueous solution of electrolyte in the microchannel with built-in PEL has got a remarkable attraction of the researchers due to some advantageous features of this method (Chanda et al., 2014). Since the concerned domain for the generation of streaming potential in the micro-confinement is limited to the EDL of the channel, it quantitatively restricts the escalation in the magnitude of streaming potential for the up-to-date microfluidic applications. However, to generate high streaming potential in the process, a reduction in the channel cross-section is one of the ready solutions in hand, primarily at the cost of increased frictional pressure drop in the channel (J H Masliyah & Bhattacharjee, 2006). While exploring the solution to this problem, as shown in the recent study, the grafted PEL has tremendous potential in the giant enhancement of conversion efficiency in microchannels (Chanda et al., 2014). The researchers also focused on the several intrinsic aspects of PEL, particularly, the pH-dependent charge density, higher salt concentration, end-charged polyelectrolyte brushes and electrostatic potential obtained beyond the Debye-Hückel approximation (Chanda et al., 2014; Chen et al., 2018; Chen & Das, 2015a; S. Das et al., 2015; Patwary et al., 2016). The influence of such PEL modulated streaming potential on the autonomous capillary dynamics has been studied in a recent article (Gorthi et al., 2020). It may be mentioned in this context here that the energy conversion mechanism with the consideration of ionic size effect in soft nanochannels has also been reported very recently (Koranlou et al., 2019). With such a vast significance of PEL, it can be conjectured that the grafting of PELs on the walls of microchannels could be the best possible solution for designing the efficient micro electrochemomechanical energy converters without compromising their size.

The exploration of the rheological behaviour of the fluid in the underlying

phenomenon also seems to be an alternative for the enhancement of the energy conversion efficiency in microchannels. In the paradigm of electrokinetics, Berli and coworkers have shown the immense influence of the non-Newtonian fluids or polymer solutions on the several electrokinetic phenomena such as energy conversion, hydrodynamic slip in the electroosmotic flow of polymers and efficient electrokinetic pumping of non-Newtonian fluids (Berli, 2010a, 2010b, 2013). The same group also archived a sizable literature wherein the discussion about the influence of nonlinear rheology on a small scale electrokinetic phenomena have been detailed (Berli & Olivares, 2008; Olivares et al., 2009). In addition to that, one group of researchers has reported the intriguing inter-connection between the rheology of non-Newtonian fluids and streaming potential generation phenomenon (Bandopadhyay et al., 2014; Bandopadhyay & Chakraborty, 2011, 2015; T. Das et al., 2009; Dhar et al., 2014). The primary focus of the reported studies by the mentioned group has been on the exploration of several non-trivial aspects such as steric effects, helical flows, non-electrostatic ion-ion interactions, cross-stream migration effect and effect of ionic conductivity.

Pertinent to the present flow configuration, we believe that for the given physical conditions, the flow of elastic non-Newtonian fluids attains a higher velocity in the microchannel with built-in soft layers on account of the effect of the shear-thinning nature of the fluid. Further, the higher flow velocity that increases with the relaxation time of the viscoelastic fluid leads to a higher magnitude of streaming potential and hence, results in the enhanced energy conversion efficiency. Extensive research investigations of the analysis of underlying flow dynamics of nonlinear viscoelastic fluid, such as the simplified Phan-Thien-Tanner (sPTT) fluid, in the narrow confinements are noteworthy in recent years. The attributable factor behind this motivation is the high applicability of viscoelastic fluids in diverse research and industrial areas (A. M. Afonso et al., 2013; A. M. M. Afonso et al., 2009; Bird et al., 2006; Ferrás et al., 2016). It is worth adding here that the phenomenon of electrochemomechanical energy conversion in soft microchannels becomes complex in the processes involved with the transport of elastic non-Newtonian fluid. The rheology-modulated enhancement in the flow velocity and its coupling with softness[8] induced increase in the electrostatic potential brings about the added complexity. Also, it may be mentioned here that the higher wall potential obtained in the case of analysis without Debye-Hückel approximation further gives rise to more efficient

[8] The term '*softness*' refers to the effectiveness of the soft polyelectrolyte layer.

electrochemomechanical conversion in the soft microchannel (Chen & Das, 2015a).

In addition to these methods, lately, the intrinsic parameters of the small scale electrokinetics such as slip at the walls and spatial variation of the electrical conductance inside the microchannels have established a renewed interest to the researchers (Davidson & Xuan, 2008b; Garai & Chakraborty, 2010; Ren & Stein, 2008). It is worth adding here that hydrodynamic slip leads to significant modulation of the polymer flows (Berli, 2013), while this effect has a marked influence on the conversion efficiency inside the soft nanochannels as well (Liu & Jian, 2019; Xing & Jian, 2018). Therefore, the conglomeration of the slip driven flow dynamics and viscoelasticity of the polymer fluids may constitute a new avenue for effectively modulating the conversion efficiency in soft nanochannels. Moreover, in the available literature of this paradigm (S. Das & Chakraborty, 2010; Davidson & Xuan, 2008a; Goswami & Chakraborty, 2010; Hughes et al., 2013), it is claimed that the consideration of the wall and Stern layer conductance mitigates the discrepancies in the experimental and theoretical observations. Nevertheless, such effects of hydrodynamic slip and the spatial variation of electrical conductance, on the rheology-modulated energy conversion inside the soft microchannels have never been reported in the literature.

Based on this literature review and the potential gaps identified from the discussion made in the preceding sections, we now frame the objectives for the present thesis pertinent to each application considered as follows.

1.6 Objectives of the Thesis and Problem Definitions

The prime objectives of the problems addressed in the present thesis are to establish the PEL's efficacy in the selected applications, as discussed next. Based on the working principle, we divide these applications into two categories: the first category deals with the electroosmotic pumping applications (i.e., first three applications discussed in section 1.5), whereas the second category involves the applications that work on the basis of streaming potential generation phenomenon (i.e., last application discussed in section 1.5). Several objectives defined after reviewing the recent developments pertaining to each application wherein the polyelectrolyte layers can prove their effectiveness are elaborated as follows.

Influence of the polyelectrolyte layer in EOF assisted transport of non-Newtonian biofluids. In this first objective, we aim to study the transport of non-Newtonian biofluids under the influence of PEL modulated electrostatics and the frictional drag. Due to shear-

thinning nature, we expect a considerable rise in the flow velocity under electroosmotic actuation. Whereas, on the contrary, it may show a reduction for the higher frictional drag. We also examine in this study an important aspect. That is, for a selected range of the system parameters, the shear-thinning nature might lead to a reduction in the net throughput as compared to the rigid narrow-fluidic channel. On the contrary, these effects can be very mild for the shear-thickening regimes.

Influence of patterned-soft layer in the microfluidic mixing applications. The second objective deals with the influence of patterned PEL structure on the vortical flow and the associated mixing phenomenon. Through this study, we investigate the dependency of the recirculation zones on the physical and geometrical parameters of the PEL. We perform distinct analyses with different types of patterning for the same window of parameters and discuss the implication of each configuration in the purview of their practical applications. In this problem, we also study the influence of PEL on the mixing length[9] and the onset of recirculation zones.

Influence of polyelectrolyte layer in EOF assisted rotational microfluidics. We study, in the third objective, the effect of PEL on the primary and the secondary flow structures, usually seen inside the rotating narrow-fluidic channel. The variation in the size and the strength of the recirculation zones that lead to alteration in the mixing performance is the focus of this study. Since the Coriolis force due to rotation as well as the frictional drag imposed by the PEL adversely affects the net transport of the fluid through the rotating soft narrow-fluidic channel, we investigate the influence of such complex underlying dynamics on the net throughput of the candidate fluids. We will also introduce here, for the first time, the variational calculus method for the rotational electrohydrodynamics.

Influence of polyelectrolyte layer and the viscoelastic fluid, in tandem, on the electrochemomechanical energy conversion phenomenon. In this problem, the fundamental issues concerning with the PEL modulated energy conversion phenomenon of viscoelastic fluid are discussed in a narrow fluidic channel. We aim to show here that the electroosmotic effect and lower frictional drag of PEL for the viscoelastic fluid always depict an enhancement in the energy conversion efficiency. It is also established that even for the higher shear-thinning nature of the viscoelastic fluids and the higher electroosmotic

[9] The term '*mixing length*' refers to the distance from the inlet of the channel where the candidate species significantly mix with each other.

effect, the conversion efficiency decreases. This is primarily attributed to the adverse influence of the electroviscous effect. In this study, the influence of three more important aspects, i.e., the electrical conductance of the Stern layer, the electrical conductance of the walls of the channel and the slip condition at the solid (or wall) – liquid interface are discussed in a pinpointed manner.

Having discussed the objectives of the thesis, now we elaborate in the next section, a manner in which we have arranged these objectives into a separate problem and carried out the respective work.

1.7 Organization of the Thesis

Contents of the present dissertation are divided into six main chapters. In the first (or present) chapter, after introducing the topic of interest and discussing the literature review, we have set our objectives pertinent to each application considered. Thereafter, we have discussed the problems addressed in this thesis in chapters two to five. Our findings and the inferences obtained from each chapter are summarized in the epilogue which also contains the scope of the future work. A detailed solution procedure of the variational calculus method deployed for performing the analysis in Chapter 4 is outlined in appendix A.

The key points addressed in each chapter are summarized as follows.

Chapter 2: Softness Induced Enhancement in a Net Throughput of Non-Linear Biofluids in Narrow-Fluidic Channels under the Electric Double Layer Phenomenon. In this chapter, we study the electrohydrodynamics of a non-Newtonian fluid in the soft narrow-fluidic channels. The non-Newtonian rheology is described by the Ostwald's de'Waele power-law model, and the governing equations specific to the defined computational domain are solved using the in-house developed finite difference method. We address several aspects of the problem in this study by considering both regimes of the power-law model, i.e., the shear-thinning and the shear-thickening rheological behaviour.

Chapter 3: Efficient Electroosmotic Mixing in a Soft Narrow-Fluidic Channel: The Role of a Patterned-Soft Layer. We propose in this chapter the novel and efficient - EOF assisted mixing technique in a patterned-soft narrow-fluidic channel. In this study, we have investigated the effectiveness of two different patterns of the PEL graftings on the mixing dynamics viz., the symmetric and the asymmetric pattern. This problem also highlights the

impact of the physical and geometrical parameters of the system on the underlying mixing dynamics. The velocity distribution in the present chapter is obtained using the stream function/vorticity approach.

***Chapter 4: Tutorial Review of Mixing in a Rotating Soft Narrow-Fluidic Channel under the Electric Double Layer Effect: A Variational Calculus Approach*.** We study in this analysis the mixing dynamics in the rotating rectangular soft narrow-fluidic channel. The results are obtained in the asymptotic limit of the geostrophic plug flow using the variational calculus method. We have analyzed the mixing dynamics from the perspectives of both the qualitative assessment (Poincaré map analysis) and the quantitative evaluation (entropy of mixing). The morphological variation in the different types of vortices, their basis of formation and finally, the consequential influence of the formed vortices on the underlying mixing dynamics is highlighted in this study.

Chapter 5: Rheology-modulated High Electrochemomechanical Energy Conversion in Soft Narrow-Fluidic Channel. In this chapter, we study the influence of the polyelectrolyte layer and the viscoelastic fluid on the energy conversion mechanism. The velocity distribution is obtained using the simplified Phan-Thien-Tanner model, and the analysis is performed in the purview of both the '*with and without Debye-Hückel approximation*'. In this study, we have also considered a few important aspects, i.e., the interfacial slip at the solid (or wall)-liquid interface, the electrical conductance of the Stern layer and that of the walls of the channel.

CHAPTER 2

Softness Induced Enhancement in a Net Throughput of Non-Linear Biofluids in Narrow-Fluidic Channels under the Electric Double Layer Phenomenon

A theoretical analysis of the transport of biofluids those depict a typical non-Newtonian 'power-law' behaviour, through the soft narrow-fluidic channel is a novel proposition to uncover the several fundamental issues. These issues are important for the understanding of different fluidic functionalities, including the enhancement of net throughput of biofluids for their in-vitro analysis. In this chapter, we study the transport of such biofluids in a soft narrow-fluidic channel. We show through this analysis that, the complex interplay between the non-Newtonian rheology, and the soft layer modulated interfacial electrochemistry, offers a non-intuitive flow dynamic for the present flow configuration. This study demonstrates that the rheological effect of the fluid and its coupling with the soft layer modulated electrostatics brings about effective flow controllability. Also, we show in this study that the stronger electrical body forces stemming from the ionic interactions between the polyelectrolyte and electrolyte lead to a relative enhancement in the net throughput for both the regimes of the power-law fluid viz., shear-thinning and shear-thickening.

2.1 Problem Description and Mathematical Modelling

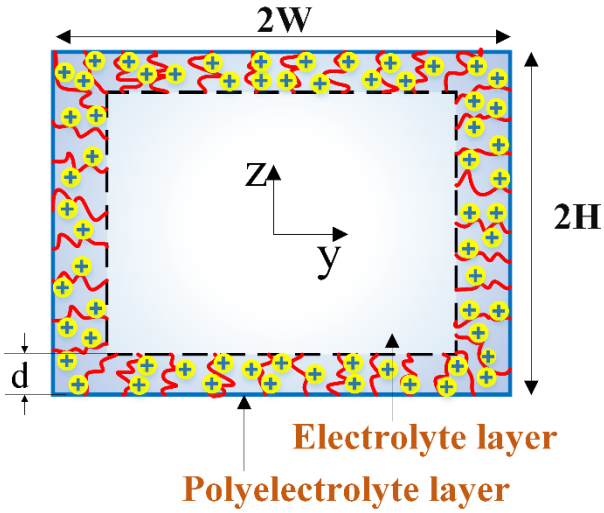

Figure 2.1: Schematic shows a soft narrow-fluidic channel having a square cross-section with height $2H$ and width $2W$. The thickness of PEL is d.

In this analysis, we consider a soft narrow-fluidic channel having a square cross-section with the dimensions, as shown in Fig. 2.1. Since we have assumed here that the channel length is much larger than its height and width, the thermo-physical properties remain invariant along the length of the channel. On account of this, the flow through the channel is considered to be in the x direction, and the axial gradient of the electrostatic potential $\partial\psi/\partial x$ is taken as zero. The distribution of the induced electrostatic potential ψ and the velocity field $\mathbf{u}$ can be obtained by the respective governing equations which are derived as follows.

In this context, we would like to discuss an important point here: The key objective of the present dissertation is to uncover the noteworthy capacity of the polyelectrolyte layer in the various applications considered. Therefore, the governing equations of the electrostatics and the assumptions based on which they are derived, remain entirely the same throughout the thesis. Taking note of this point, we, in the following section, make an effort to derive the generalized governing equations of the PEL modulated electrostatics those can be considered as pertinent for all the applications or problems studied in this thesis. On the other hand, the governing equations of the hydrodynamics vary with the chapters and hence, derived in the respective chapter only.

We now derive the generalized governing equation of the PEL modulated electrostatics for the present thesis.

2.1.1 Electrostatics

In a soft narrow-fluidic channel, the polyelectrolyte layer grafted on the channel walls acts as a charged entity that establishes EDL in the presence of electrolytic solution. The distribution of electrostatic potential induced inside such EDLs can be obtained using the Poisson-Nernst-Planck (PNP) model (Bird et al., 2006). This model primarily comprises two equations: the Nernst-Planck (NP) equation that deals with the distribution of the electrolyte ions, later derived as the Boltzmann analogy, and the Poisson equation that describes the actual potential distribution. In PEL modulated electrostatics, as mentioned in the preceding chapter (Chapter 1), the Poisson equation is used for two separate sections, leading to the solution to two different equations [Eqs. (1.2a)-(1.2b)] according to the distinct domains formed by the electrolyte layer and the polyelectrolyte layer (Chanda et al., 2014). On using these equations, which apply to the PNP model, the distribution of the potential for the present problem can be elucidated. For the sake of clarity in the presentation, along with the Nernst-Planck equation, we rewrite these Poisson equations [Eqs. (1.2a)-(1.2b)] derived for both the electrolyte layer and polyelectrolyte layer as follows. For the description of these equations, the expressions of the volumetric charge densities of the electrolyte and polyelectrolyte ions [Eqs. (1.4a)-(1.4b)] are also taken into account.

Nernst-Planck equation:

$$\frac{\partial n_{e,\pm}}{\partial t} + \nabla.\left(n_{e,\pm}\mathbf{u}\right) = D_{e,\pm}\nabla^2 n_{e,\pm} + \frac{D_{e,\pm}e_0 z_{e,\pm}}{k_B T}\nabla.\left[n_{e,\pm}\nabla\Phi\right] \tag{2.1}$$

Poisson equation:

Electrolyte layer

$$\nabla^2\psi_e = -\frac{z_e e_0\left(n_{e,+} - n_{e,-}\right)}{\varepsilon_e} \tag{2.2a}$$

Polyelectrolyte layer

$$\nabla^2\psi_p = -\frac{z_e e_0\left(n_{e,+} - n_{e,-}\right) + Z_p e_0 N_p}{\varepsilon_e} \tag{2.2b}$$

In Eqs. (2.1)-(2.2), $D_{e,\pm}$ is the ionic diffusivity of the positive/negative electrolyte ions, Φ is the total electric potential, t is time, k_B is the Boltzmann constant, and T is the absolute temperature. Note that the remaining terms are already defined in Chapter 1. The left-hand side (LHS) of Eq. (2.1) represents the convection of ions with the transient term $\partial n_{e,\pm}/\partial t$,

whereas the terms in the right-hand side (RHS) represent the diffusion-based distribution of ions. In Eq. (2.1), the total electric field $\nabla\Phi$ is given by $\nabla\Phi = \nabla\phi_A + \nabla\psi$ where ϕ_A is the externally applied electric potential. In the purview of the weak-field limits, we approximate this total electric field $\nabla\Phi$ as the induced electric field $\nabla\psi$ only, i.e., $\nabla\Phi \sim \nabla\psi$ (Bandopadhyay et al., 2016; J H Masliyah & Bhattacharjee, 2006; Saville, 1977). The weak-field approximation states that to obtain significant perturbations $\delta\psi$ in the electrostatic potential ψ, the ratio of the applied electric field $\nabla\phi_A$ to the induced electric field $\nabla\psi$ should be very high (Saville, 1977). For instance, it should be of the order of $O\left(10^0\right)$. The magnitude of this ratio $\nabla\phi_A / \nabla\psi$ for the present study can be estimated using the following order of magnitude analysis:

The order of the induced electric field $\nabla\psi$ is obtained from the ratio of; the order of the reference electrostatic potential $\psi_{ref}\left[=\zeta=\left(k_BT/\left(z_e e_0\right)\right)\right]$ to that of the Debye length of the EDL. The order of ψ_{ref} can be estimated as 10^1mV, and that of the Debye length can be considered as 10^{-7} to 10^{-8} m (J H Masliyah & Bhattacharjee, 2006). The order of external electric field $\nabla\phi_A$, from the literature, is found to be $O\left(10^3 - 10^4\right)$ V/m (Mondal, Ghosh, et al., 2014; Mukherjee et al., 2017; Peng & Li, 2016; Saville, 1977). Therefore, if compared, we observe that the ratio $\nabla\phi_A / \nabla\psi$ becomes $O\left(10^{-2} - 10^{-3}\right)$ for the aforementioned considerations, which is much less than the weak-field limit, i.e., $O\left(10^0\right)$. This implies the external electric field $\nabla\phi_A$ has an insignificant contribution to the spatial distribution of the electrolyte ions. On account of this, we assume that $\nabla\phi_A \to 0$ and $\nabla\Phi \sim \nabla\psi$. Using this approximation, we simplify Eq. (2.1) as:

$$\frac{\partial n_{e,\pm}}{\partial t} + \nabla.\left(n_{e,\pm}\mathbf{u}\right) = D_{e,\pm}\nabla^2 n_{e,\pm} + \frac{D_{e,\pm}e_0 z_{e,\pm}}{k_B T}\nabla.\left[n_{e,\pm}\nabla\psi\right] \qquad (2.3)$$

For further simplification of Eq. (2.3), we extend the order of magnitude analysis in the following manner. For Eq. (2.3), the scales of LHS and RHS can be obtained as:

$$\left[\frac{\partial n_{e,\pm}}{\partial t} + \nabla.\left(n_{e,\pm}\mathbf{u}\right)\right] \sim \frac{n_\infty u_{HS}}{H} \quad \text{and} \quad \left[D_{e,\pm}\nabla^2 n_{e,\pm} + \frac{D_{e,\pm}e_0 z_{e,\pm}}{k_B T}\nabla.\left[n_{e,\pm}\nabla\psi\right]\right] \sim \frac{D_{e,\pm}n_\infty}{H^2}$$

To estimate these scales, we consider $l_{ref} = H$, $u_{ref} = \left[u_{HS} = \left(-\varepsilon_e\zeta E_0\right)/\eta\right]$ and

$t_{ref} = H/u_{ref}$, where η is the dynamic viscosity, H is the half-height of the channel, E_0 is the reference electric field strength, n_∞ is the number densities of the electrolyte ions in the electroneutral region, and u_{HS} is the Helmholtz-Smoluchowski velocity. On dividing the scale of LHS by RHS, i.e., the scale of convection of ions by the diffusion's, we get the ionic Peclet number Pe_I as $\mathrm{Pe}_I = u_{HS}H/D_{e,\pm}$. For the present study, the magnitude of ionic Peclet number Pe_I is of the order of $O\left(10^{-2}-10^{-3}\right)$, since the order of u_{HS}, H and $D_{e,\pm}$, following their typical value/range considered in small scale analysis, are taken as $O\left(10^{-5}\right)$ m/s (Mukherjee et al., 2017), $O\left(10^{0}-10^{2}\right)\mu$m (Duffy et al., 1999) and $O\left(10^{-8}-10^{-9}\right)$ m^2/s (R. J. Hunter, 1981), respectively. Such minuscule order of Pe_I suggests that the convection of electrolyte ions is negligible in the present study, and therefore, Eq. (2.3) can be simplified as:

$$0 = \nabla^2 n_{e,\pm} + \frac{e_0 z_{e,\pm}}{k_B T}\nabla.\left[n_{e,\pm}\nabla\psi\right] \tag{2.4}$$

Further, using the electroneutrality condition ($n_{e,\pm} = n_\infty$ at $\psi = 0$) and the no-flux condition ($\partial n_{e,\pm} = 0$ at $\partial\psi = 0$) (Bandopadhyay et al., 2016), we obtain the expression of the number densities of the electrolyte ions as:

$$n_{e,\pm} = n_\infty \exp\left[\mp\frac{z_e e_0 \psi}{k_B T}\right] \tag{2.5}$$

Note that Eq. (2.5) also proves the validity of the Boltzmann's analogy that offers the distribution of electrolyte ions inside the EDL.

2.1.1.1 Poisson-Boltzmann Equation

Using the expression of Boltzmann analogy given in Eq. (2.5), we further simplify the Poisson equations [Eqs. (2.2a)-(2.2b)] and derive the Poisson-Boltzmann (PB) equations for both the EL and PEL, respectively. In the rectangular coordinate system, the PB equations for both the EL and PEL can be written as:

Electrolyte layer

$$\frac{\partial^2\psi_e}{\partial x^2} + \frac{\partial^2\psi_e}{\partial y^2} + \frac{\partial^2\psi_e}{\partial z^2} = \frac{2 z_e e_0 n_\infty}{\varepsilon_e}\sinh\left(\frac{z_e e_0 \psi_e}{k_B T}\right) \tag{2.6a}$$

Polyelectrolyte layer

$$\frac{\partial^2\psi_p}{\partial x^2}+\frac{\partial^2\psi_p}{\partial y^2}+\frac{\partial^2\psi_p}{\partial z^2}=\frac{2z_e e_0 n_\infty}{\varepsilon_e}\sinh\left(\frac{z_e e_0\psi_p}{k_B T}\right)-\frac{Z_p e_0 N_p}{\varepsilon_e} \tag{2.6b}$$

Note that, in the PB equation derived for the PEL [Eq. (2.7b)], the Boltzmann distribution is dependent on the electrostatic potential induced inside the PEL, i.e., ψ_p. It is based on the fact that the electrolyte flowing through the PEL matrix obeys the potential distribution obtained inside the PEL.

2.1.1.2 Debye-Hückel Approximation

The Poisson-Boltzmann equations of EL and PEL as given, respectively, in Eqs. (2.6a) and (2.6b), can be simplified further using the Debye-Hückel (DH) approximation. According to this approximation,

$$\sinh\left(\frac{z_e e_0\psi}{k_B T}\right)\sim\frac{z_e e_0\psi}{k_B T} \tag{2.7}$$

if the reference potential or zeta potential becomes less than 25 mV. For any case, if ψ_{ref} (reference potential) or ζ (zeta potential) falls below 25mV, Eqs. (2.6a) and (2.6b) according to the DH approximation reduce to:

Electrolyte layer

$$\frac{\partial^2\psi_e}{\partial x^2}+\frac{\partial^2\psi_e}{\partial y^2}+\frac{\partial^2\psi_e}{\partial z^2}=\kappa^2\psi_e \tag{2.8a}$$

Polyelectrolyte layer

$$\frac{\partial^2\psi_p}{\partial x^2}+\frac{\partial^2\psi_p}{\partial y^2}+\frac{\partial^2\psi_p}{\partial z^2}=\kappa^2\psi_p-\frac{Z_p eN_p}{\varepsilon_e} \tag{2.8b}$$

In these equations, the term $\kappa=\sqrt{\left(2z_e^2e_0^2n_\infty\right)/\left(\varepsilon_e k_B T\right)}$ is the Debye-Hückel parameter of the electrolyte layer. The inverse of this parameter signifies the Debye length in the electrolyte layer. The DH parameter consists the information about the EDL such as the ionic concentration of the electrolyte and some fundamental properties of the electrolyte, like the relative permittivity of the electrolyte and the valence on a single electrolyte ion.

Dimensionless form of Poisson-Boltzmann equations. The dimensionless forms of Eqs. (2.8a) and (2.8b) can be obtained as:

Electrolyte layer

$$\frac{\partial^2\bar{\psi}_e}{\partial\bar{x}^2}+\frac{\partial^2\bar{\psi}_e}{\partial\bar{y}^2}+\frac{\partial^2\bar{\psi}_e}{\partial\bar{z}^2}=\bar{\kappa}^2\bar{\psi}_e \tag{2.9a}$$

Polyelectrolyte layer

$$\frac{\partial^2\bar{\psi}_p}{\partial\bar{x}^2}+\frac{\partial^2\bar{\psi}_p}{\partial\bar{y}^2}+\frac{\partial^2\bar{\psi}_p}{\partial\bar{z}^2}=\bar{\kappa}^2\bar{\psi}_p-\bar{\kappa}_p^2 \tag{2.9b}$$

Here, we introduce a new parameter for the potential distribution obtained inside the polyelectrolyte layer, i.e., the equivalent Debye-Hückel parameter of the PEL given by $\kappa_p=\sqrt{\left(z_eZ_pe_0^2N_p\right)/\left(\varepsilon_ek_BT\right)}$. It can be noticed from the expressions of both κ and κ_p that the electrical permittivity of the electrolyte remains the same in both the EL and PEL. This is particularly attributed to the negligence of the ion-partitioning effect, in which, if considered, one assumes that the electrical permittivity of the electrolyte in EL and PEL is different. In Eqs. (2.9a)-(2.9b), the dimensionless quantities are: $\bar{\kappa}=\kappa H$, $\bar{\kappa}_p=\kappa_pH$, $\left(\bar{\psi}_e,\bar{\psi}_p\right)=\left(\psi_e,\psi_p\right)/\psi_{ref}$ and $\left(\bar{x},\bar{y},\bar{z}\right)=\left(x,y,z\right)/H$.

Note that the Eqs. (2.9a)-(2.9b) are the generalized PB equations which are also used for the problems addressed in the forthcoming chapters (Chapters 3-5) to solve the distribution of the electrostatic potential in both the electrolyte layer and polyelectrolyte layer, respectively. For the present problem, these equations can be simplified as follows.

In the present problem, we consider the square cross-section of the channel in $y-z$ plane as a domain of analysis. Here, the electrostatic potential ψ in both the EL and PEL is assumed to remain invariant in the x direction, i.e., $\partial\left(\psi_e,\psi_p\right)/\partial x=0$. Using this condition, we get the final form of dimensionless PB equation for the present chapter as:

Electrolyte layer

$$\frac{\partial^2\bar{\psi}_e}{\partial\bar{y}^2}+\frac{\partial^2\bar{\psi}_e}{\partial\bar{z}^2}=\bar{\kappa}^2\bar{\psi}_e \tag{2.10a}$$

Polyelectrolyte layer

$$\frac{\partial^2\bar{\psi}_p}{\partial\bar{y}^2}+\frac{\partial^2\bar{\psi}_p}{\partial\bar{z}^2}=\bar{\kappa}^2\bar{\psi}_p-\bar{\kappa}_p^2 \tag{2.10b}$$

2.1.2 Electrohydrodynamics

To study the flow of non-Newtonian fluid through the PEL grafted narrow-fluidic channel, we invoke to the Cauchy momentum equation, which for the present analysis can be written as (Bird et al., 2006):

$$0 = -\nabla G + \nabla.\boldsymbol{\tau} + F_V \tag{2.11}$$

The volumetric force F_V for the present problem can be given as:

Electrolyte layer

$$F_V = F_E = e_0 z_e \left(n_{e,+} - n_{e,-}\right) E_x \tag{2.12a}$$

Polyelectrolyte layer

$$F_V = F_E + F_d = e_0 z_e \left(n_{e,+} - n_{e,-}\right) E_x - \mu_c \mathbf{u}^{n_0} \tag{2.12b}$$

In Eqs. (2.12a)-(2.12b), E_x is the applied electric field in the x direction, $\mu_c \mathbf{u}^{n_0}$ is Darcy's frictional drag derived for the power-law model, and n_0 is the power-law index. We write the constitutive equation for the power-law model as (Bird et al., 2006):

$$\boldsymbol{\tau} = m_0 \left(\dot{\gamma}\right)^{n_0} \tag{2.13}$$

Here m_0 is the fluid consistency coefficient, and $\dot{\gamma}$ is the magnitude of strain rate tensor as given by, $\dot{\gamma} = \left[\mathbf{D}:\mathbf{D}\right]^{1/2}/2$ where $\mathbf{D}$ is strain rate tensor: $\mathbf{D} = \left(\nabla\mathbf{u} + \nabla\mathbf{u}^T\right)/2$ (Bandopadhyay & Chakraborty, 2011; Chabra & Richardson, 2008; C. Zhao et al., 2008; C. Zhao & Yang, 2011). Employing this relation and using Eq. (2.13), the apparent viscosity $\eta_{app} = m_0 \left(\dot{\gamma}\right)^{n_0 - 1}$ for the present problem can be derived as:

$$\eta_{app} = m_0 \left[\left(\frac{\partial u}{\partial y}\right)^2 + \left(\frac{\partial u}{\partial z}\right)^2\right]^{(n_0-1)/2} \tag{2.14}$$

Using this expression [Eq. (2.14)], the shear stress in x direction for the planes perpendicular to both the y and z directions can be reduced to,

$$\tau_{xy} = m_0 \left[\left(\frac{\partial u}{\partial y}\right)^2 + \left(\frac{\partial u}{\partial z}\right)^2\right]^{(n_0-1)/2} \frac{\partial u}{\partial y} \quad \text{and} \quad \tau_{xz} = m_0 \left[\left(\frac{\partial u}{\partial y}\right)^2 + \left(\frac{\partial u}{\partial z}\right)^2\right]^{(n_0-1)/2} \frac{\partial u}{\partial z}$$

On the use of these expressions of shear stresses in x direction, and the volumetric force derived in [Eqs. (2.12a)-(2.12b)], the momentum equation [Eq. (2.11)] takes the following form for both the EL and PEL as:

Electrolyte layer

$$0 = -\frac{dG}{dx} + \frac{\partial}{\partial y}\left[m_0 \left(\left(\frac{\partial u_e}{\partial y} \right)^2 + \left(\frac{\partial u_e}{\partial z} \right)^2 \right)^{(n_0-1)/2} \right] \frac{\partial u_e}{\partial y} + \frac{\partial}{\partial z}\left[m_0 \left(\left(\frac{\partial u_e}{\partial y} \right)^2 + \left(\frac{\partial u_e}{\partial z} \right)^2 \right)^{(n_0-1)/2} \right] \frac{\partial u_e}{\partial z} - \varepsilon_e \kappa^2 \psi_e E_x \tag{2.15a}$$

Polyelectrolyte layer

$$0 = -\frac{dG}{dx} + \frac{\partial}{\partial y}\left[m_0 \left(\left(\frac{\partial u_p}{\partial y} \right)^2 + \left(\frac{\partial u_p}{\partial z} \right)^2 \right)^{(n_0-1)/2} \right] \frac{\partial u_p}{\partial y} + \frac{\partial}{\partial z}\left[m_0 \left(\left(\frac{\partial u_p}{\partial y} \right)^2 + \left(\frac{\partial u_p}{\partial z} \right)^2 \right)^{(n_0-1)/2} \right] \frac{\partial u_p}{\partial z} - \varepsilon_e \kappa^2 \psi_p E_x - \mu_c u_p^{n_0} \tag{2.15b}$$

In Eqs. (2.15a)-(2.15b), u_e and u_p are the fluid velocities in EL and PEL respectively.

Non-dimensionalisation of the transport equations. To make the transport equations [Eqs. (2.15a)-(2.15b)] dimensionless, we use the reference parameters defined in previously in the sub-section 2.1.1. Using these parameters, we obtain the transport equations in their dimensionless forms as:

Electrolyte layer

$$0 = 2\bar{\Gamma} + \frac{\partial}{\partial \bar{y}}\left[\left(\left(\frac{\partial \bar{u}_e}{\partial \bar{y}} \right)^2 + \left(\frac{\partial \bar{u}_e}{\partial \bar{z}} \right)^2 \right)^{(n_0-1)/2} \right] \frac{\partial \bar{u}_e}{\partial \bar{y}} + \frac{\partial}{\partial \bar{z}}\left[\left(\left(\frac{\partial \bar{u}_e}{\partial \bar{y}} \right)^2 + \left(\frac{\partial \bar{u}_e}{\partial \bar{z}} \right)^2 \right)^{(n_0-1)/2} \right] \frac{\partial \bar{u}_e}{\partial \bar{z}} + \frac{\bar{\kappa}^{n_0+1} \bar{\psi}_e}{{n_0}^{n_0}} \tag{2.16a}$$

Polyelectrolyte layer

$$0 = 2\bar{\Gamma} + \frac{\partial}{\partial \bar{y}}\left[\left(\left(\frac{\partial \bar{u}_p}{\partial \bar{y}} \right)^2 + \left(\frac{\partial \bar{u}_p}{\partial \bar{z}} \right)^2 \right)^{(n_0-1)/2} \right] \frac{\partial \bar{u}_p}{\partial \bar{y}} + \frac{\partial}{\partial \bar{z}}\left[\left(\left(\frac{\partial \bar{u}_p}{\partial \bar{y}} \right)^2 + \left(\frac{\partial \bar{u}_p}{\partial \bar{z}} \right)^2 \right)^{(n_0-1)/2} \right] \frac{\partial \bar{u}_p}{\partial \bar{z}} + \frac{\bar{\kappa}^{n_0+1} \bar{\psi}_p}{{n_0}^{n_0}} - \alpha^2 \bar{u}_p^{n_0} \tag{2.16b}$$

In these equations, $(\bar{u}_e, \bar{u}_p) = (u_e, u_p)/u_{HS}$ while $\bar{\Gamma}$ and α are the dimensionless pressure gradient and the frictional drag parameter, respectively. The expressions of these parameters, $\bar{\Gamma}$ and α, can be given as:

$$\bar{\Gamma}=\left(-\frac{1}{2}\frac{dG}{dx}\right)\Big/\left(\frac{m_0 u_{HS}^{n_0}}{H^{n_0+1}}\right) \text{ and } \alpha=\sqrt{\mu_c\Big/\left(\frac{m_0}{H^{n_0+1}}\right)}.$$

2.1.3 Boundary Conditions

To solve the Poisson-Boltzmann equations [Eqs. (2.10a)-(2.10b)] and the equations governing the hydrodynamics [Eqs. (2.16a)-(2.16b)], we use the following boundary conditions discussed as follows:

2.1.3.1 For Potential Distribution

$$\left.\begin{aligned}
&\left.\frac{\partial\bar{\psi}_p}{\partial(\bar{y},\bar{z})}\right|_{\bar{y},\bar{z}=\pm1}=0 && \text{: No-flux condition at walls}\\
&\bar{\psi}_p\big|_{\bar{y},\bar{z}=(\pm1)-\bar{d}}=\bar{\psi}_e\big|_{\bar{y},\bar{z}=(\pm1)-\bar{d}} && \text{: Potential continuity at PEL/EL interface}\\
&\left.\frac{\partial\bar{\psi}_p}{\partial(\bar{y},\bar{z})}\right|_{\bar{y},\bar{z}=(\pm1)-\bar{d}}=\left.\frac{\partial\bar{\psi}_e}{\partial(\bar{y},\bar{z})}\right|_{\bar{y},\bar{z}=(\pm1)-\bar{d}} && \text{: Induced electric field continuity at PEL/EL interface}\\
&\left.\frac{\partial\bar{\psi}_e}{\partial(\bar{y},\bar{z})}\right|_{\bar{y},\bar{z}=0}=0 && \text{: Symmetry condition at the center of the channel}
\end{aligned}\right\} \quad (2.17)$$

In this equation, the first boundary condition represents the uncharged wall condition or no-flux condition at the walls of the channel. The second and third boundary conditions represent the continuity in the potential $\bar{\psi}$ and potential gradient $d\bar{\psi}/d\bar{y}$ across the PEL/EL interface (Chanda et al., 2014). Note that while considering these boundary conditions (second and third), we have assumed that the relative permittivity of the electrolyte is almost the same in EL and PEL (Poddar et al., 2016). The fourth boundary condition represents the symmetry condition at the center of the channel.

2.1.3.2 For Velocity Distribution

$$\left.\begin{aligned}
&\bar{u}_p\big|_{\bar{y},\bar{z}=\pm1}=0 && \text{: No-slip boundary condition at walls}\\
&\bar{u}_p\big|_{\bar{y},\bar{z}=(\pm1)-\bar{d}}=\bar{u}_e\big|_{\bar{y},\bar{z}=(\pm1)-\bar{d}} && \text{: Velocity continuity at PEL/EL interface}\\
&\bar{\tau}_p\big|_{\bar{y},\bar{z}=(\pm1)-\bar{d}}=\bar{\tau}_e\big|_{\bar{y},\bar{z}=(\pm1)-\bar{d}} && \text{: Shear stress continuity at PEL/EL interface}\\
&\left.\frac{\partial\bar{u}_e}{\partial(\bar{y},\bar{z})}\right|_{\bar{y},\bar{z}=0}=0 && \text{: Symmetry condition at the center of the channel}
\end{aligned}\right\} \quad (2.18)$$

Of these boundary conditions, the first condition represents the no-slip boundary condition at the walls of the channel. The second and third conditions represent the continuity in the velocity and shear stress across the PEL/EL interface, respectively. The last boundary condition represents the symmetry condition at the center of the channel. The expression of shear stresses $\bar{\tau}_p\big|_{\bar{y},\bar{z}=(\pm1)-\bar{d}}$ and $\bar{\tau}_e\big|_{\bar{y},\bar{z}=(\pm1)-\bar{d}}$ in both the layers (PEL and EL respectively) appearing in Eq. (2.18) take the following forms.

Electrolyte layer

$$\bar{\tau}_e\big|_{\bar{y},\bar{z}=(\pm1)-\bar{d}} = \left[\left(\left(\frac{\partial \bar{u}_e}{\partial \bar{y}}\right)^2+\left(\frac{\partial \bar{u}_e}{\partial \bar{z}}\right)^2\right)^{\frac{n_0-1}{2}}\right]\frac{\partial \bar{u}_e}{\partial(\bar{y},\bar{z})}\bigg|_{\bar{y},\bar{z}=(\pm1)-\bar{d}} \tag{2.19a}$$

Polyelectrolyte layer

$$\bar{\tau}_p\big|_{\bar{y},\bar{z}=(\pm1)-\bar{d}} = \left[\left(\left(\frac{\partial \bar{u}_p}{\partial \bar{y}}\right)^2+\left(\frac{\partial \bar{u}_p}{\partial \bar{z}}\right)^2\right)^{\frac{n_0-1}{2}}\right]\frac{\partial \bar{u}_p}{\partial(\bar{y},\bar{z})}\bigg|_{\bar{y},\bar{z}=(\pm1)-\bar{d}} \tag{2.19b}$$

Note that from here onwards, we omit the overbars from the dimensionless quantities.

2.1.4 Numerical Methods

In this analysis, we use our in-house developed, finite difference method (FDM) based code, to solve the transport equations which govern the flow dynamics for the present problem. The details of this computational procedure are discussed as follows.

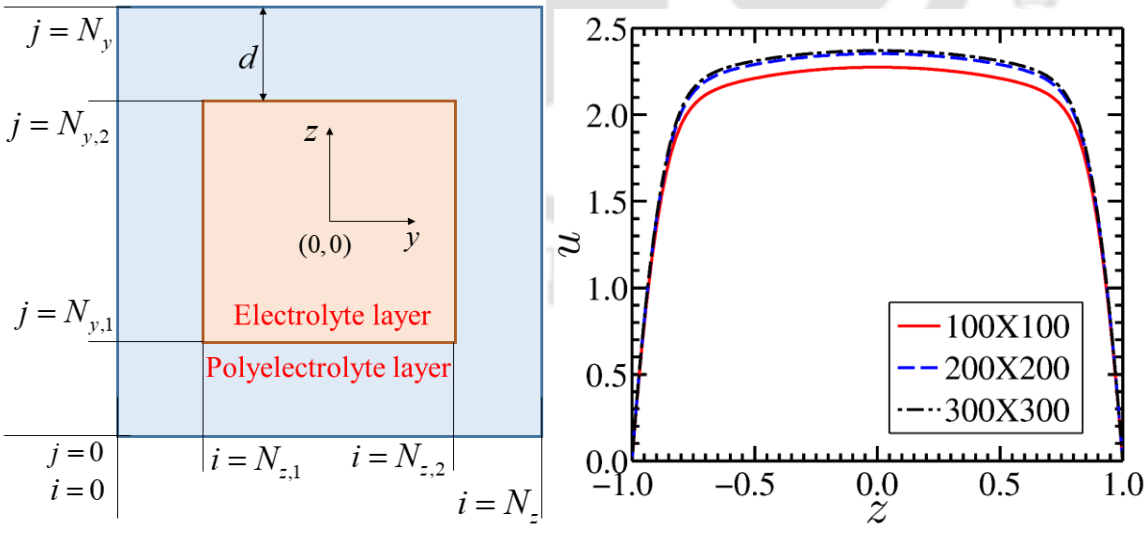

(a) **(b)**

Figure 2.2: (a) Schematic shows the computational domain of the present study. (b) Plots depict the velocity profiles for the different number of grid points viz., 100x100, 200x200 and 300x300, obtained for the grid dependence test.

2.1.4.1 Computational Domain

In Fig. 2.2(a), we show the computational domain of the present problem. The coordinate system is attached at the center of the channel, i.e., at (y, z) = (0,0). We have divided this domain in the uniform grid with the number of grid points $N_z \times N_y$. The interface between the electrolyte layer and polyelectrolyte layer is depicted by the grid lines $i = N_{z,1}, N_{z,2}$ and $j = N_{y,1}, N_{y,2}$, in z and y directions, respectively.

2.1.4.2 Solution Procedure

We first calculate the induced potential ψ in both the EL and PEL using central difference method. The discretized equations for the potential distribution [Eqs. (2.10a)-(2.10b)] read as:

Electrolyte layer

$$\psi_{i,j}^{k} = \frac{\dfrac{\psi_{i+1,j}^{k-1} + \psi_{i-1,j}^{k}}{(\Delta z)^2} + \dfrac{\psi_{i,j+1}^{k-1} + \psi_{i,j-1}^{k}}{(\Delta y)^2}}{\kappa^2 + 2\left(\dfrac{1}{(\Delta z)^2} + \dfrac{1}{(\Delta y)^2}\right)} \quad \text{where } \psi_{i,j} \in \psi_e \tag{2.20a}$$

Polyelectrolyte layer

$$\psi_{i,j}^{k} = \frac{\kappa_p^2 + \dfrac{\psi_{i+1,j}^{k-1} + \psi_{i-1,j}^{k}}{(\Delta z)^2} + \dfrac{\psi_{i,j+1}^{k-1} + \psi_{i,j-1}^{k}}{(\Delta y)^2}}{\kappa^2 + 2\left(\dfrac{1}{(\Delta z)^2} + \dfrac{1}{(\Delta y)^2}\right)} \quad \text{where } \psi_{i,j} \in \psi_p \tag{2.20b}$$

In these equations, Δy and Δz are the width and height of each grid element respectively. The superscript k of the $\psi_{i,j}$ represents the present iteration level in the numerical calculation. Using these equations, we calculate the potential distribution across the channel cross-section, which are then employed to calculate the velocity distribution of the fluid. As such, we use the following set of the discretized equations while calculating the velocity distribution in the channel.

Electrolyte layer

$$u_{i,j}^{k} = \frac{F_{1_{i,j}}^{k} + F_{2_{i,j}}^{k} + 2\Gamma + g_{i,j}^{k-1} F_{3_{i,j}}^{k}}{2g_{i,j}^{k-1} F_4 - \alpha^2} \quad \text{where } u_{i,j} \in u_e \tag{2.21a}$$

Polyelectrolyte layer

$$u_{i,j}^{k} = \frac{F_{1_{i,j}}^{k} + F_{2_{i,j}}^{k} + 2\Gamma + g_{i,j}^{k-1} F_{3_{i,j}}^{k}}{2g_{i,j}^{k-1} F_4 - \alpha^2} \quad \text{where } u_{i,j} \in u_p \tag{2.21b}$$

In Eqs. (2.21a)-(2.21b), the functions $F_{1_{i,j}}$ and $F_{2_{i,j}}$ are:

$$F_{1_{i,j}}^{k}=\left[\left(\frac{g_{i+1,j}^{k-1}-g_{i-1,j}^{k-1}}{2\Delta z}\right).\left(\frac{u_{i+1,j}^{k-1}-u_{i-1,j}^{k}}{2\Delta z}\right)\right]+\left[\left(\frac{g_{i,j+1}^{k-1}-g_{i,j-1}^{k-1}}{2\Delta y}\right).\left(\frac{u_{i,j+1}^{k-1}-u_{i,j-1}^{k}}{2\Delta y}\right)\right]$$

$$F_{2_{i,j}}^{k}=\frac{\kappa^{n_0+1}\psi_{i,j}^{k}}{n_0^{\,n_0}}\ ,\ F_{3_{i,j}}^{k}=\left(\frac{u_{i+1,j}^{k-1}+u_{i-1,j}^{k}}{(\Delta z)^2}\right)+\left(\frac{u_{i,j+1}^{k-1}+u_{i,j-1}^{k}}{(\Delta y)^2}\right),\ F_4=\frac{1}{(\Delta z)^2}+\frac{1}{(\Delta y)^2}$$

Note that the function $g_{i,j}$ takes care of the non-linearity of the system, stemming from the rheology of the power-law model used in describing the constitutive behaviour of the non-Newtonian fluid in this analysis. The function $g(y,z)$ is defined as:

$$g(y,z)=\left[\left(\frac{\partial u}{\partial z}\right)^2+\left(\frac{\partial u}{\partial y}\right)^2\right]^{\frac{n_0-1}{2}} \tag{2.22}$$

It is important to mention here that the term $g_{i,j}$ in these equations [Eqs. (2.21a)-(2.21b)] is calculated at the previous iteration level to relieve the non-linearity of the system. However, for the conciseness in the presentation, we have not included the discretization of the function $g_{i,j}$, since the calculation of $g_{i,j}$ in the system changes with respect to a boundary (forward difference or backward difference scheme) and the main domain (central difference scheme). It is important to mention here that, in this analysis, we have used Root Mean Square method to calculate the error in the calculation, while the least value of RMS error allowed in the calculation of potential and velocity distributions are 10^{-8} and 10^{-12} respectively.

2.1.4.3 Grid Dependence Test

In Fig. 2.2(b), we show the grid dependence study performed for the present analysis. It is observed from Fig. 2.2(b) that, a change in fluid velocity becomes negligible as the number of grid points $N_z \times N_y$ change from 200×200 to 300×300. Accordingly, we have considered $N_z \times N_y = 200\times200$ for the present numerical calculations. Also, we would like to add here that the results obtained from the present numerical framework using $N_z \times N_y = 200\times200$ grid points match well with the analytical as well as experimental results reported in the literature, depicted in Figs. 2.3(a)-(c). As such, this validation further supports that the results obtained from the present modelling framework are independent of the number of grid points.

2.2 Results and Discussions

Imposing the boundary conditions mentioned in Eqs. (2.17)-(2.18), we solve the governing equations of the potential and velocity distribution using our in-house developed FDM based code. We discuss several results obtained from this analysis in the forthcoming sections systematically. Before going to elaborate the results on hand, we first make an attempt to validate the numerical model.

2.2.1 Model Validation

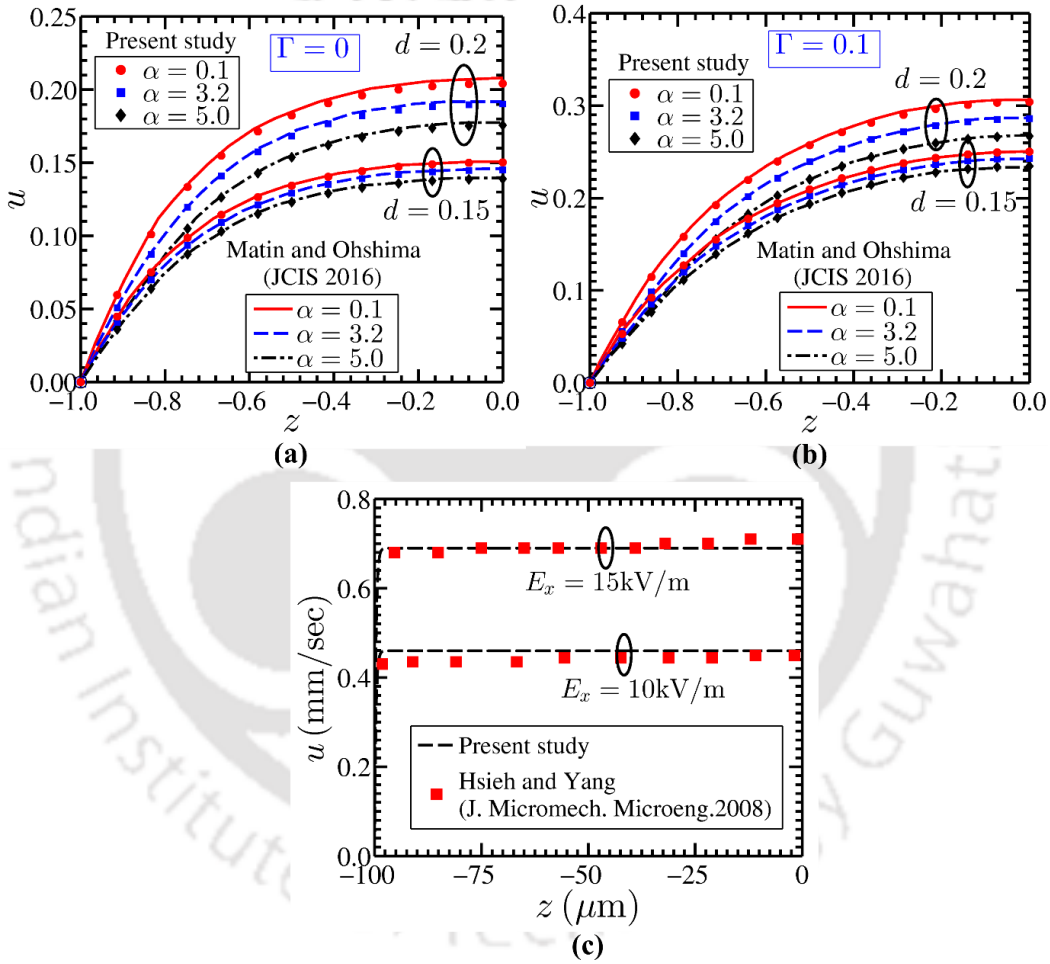

Figure 2.3: (a)-(b) Theoretical validation: Plots in (a) and (b) show the comparison of the velocity profiles obtained from the present analysis with the reported results of Matin and Ohshima (M. H. Matin & Ohshima, 2016) for $\Gamma = 0$ and $\Gamma = 0.1$, respectively. (c) Experimental validation: Plots in (c) shows the comparison of the velocity profiles obtained from the present analysis with those reported by Hsieh and Yang (Hsieh & Yang, 2008) in their experimental investigation. Note that these validation plots are obtained at $y = 0$.

In model validation, we have considered a dual benchmarking strategy. First, we validate the present numerical method with the results reported by Matin and Ohshima (M. H. Matin & Ohshima, 2016). We show in Figs. 2.3(a) and 2.3(b) the variation of flow

velocity with dimensionless pressure gradient $\Gamma = 0.0$ and $\Gamma = 0.1$ respectively. These plots are obtained for different values of α and d as mentioned in the figures. While validating our model with the results of the referred study (M. H. Matin & Ohshima, 2016), the width W of the channel is considered to be much higher than its height H. Note that the values of α and d considered in this study are in compliance with those as chosen by Matin and Ohshima (M. H. Matin & Ohshima, 2016). The dimensionless parameters considered for this validation are $n_0 = 1$, $\kappa_p = 2.0$, $\kappa = 4.0$. The results obtained from the present theoretical analysis show a good match with the reported results of Matin and Ohshima (M. H. Matin & Ohshima, 2016).

Secondly, we also make an effort in Fig. 2.3(c) to validate the present theoretical analysis with the experimental results reported by Hsieh and Yang (Hsieh & Yang, 2008). The validation plots are obtained for two different values of the axial electric field $E_x = 15\,\text{kV/m}$ and $E_x = 10\,\text{kV/m}$. While validating our analysis with experimental results reported in (Hsieh & Yang, 2008), we have shifted the PEL-EL interface to the walls of the channel by taking PEL thickness $d = 0.01$, keeping the values of other parameters same as that of considered in the referred study (Hsieh & Yang, 2008). These include: $\kappa = 1.06$ nm^{-1}, $\kappa_p = 0.883\ \text{nm}^{-1}$, $\varepsilon_e = 644.47\times10^{-2}\ \text{Fm}^{-1}$, $\eta = 803.4\times10^{-6}\,\text{Pa.sec}$, $H = 100\mu\text{m}$, $n_0 = 1$, $k_{PEL} = 2\times10^{-9}\,\text{m}^2$ (permeability of the PEL). We find from Fig. 2.3(c) a fairly accurate match between the present theoretical results and the experimental results reported by Hsieh and Yang (Hsieh & Yang, 2008).

2.2.2 Significance of Physical and Geometrical Parameters

The mathematical analysis used in addressing the problems considered in the present thesis involves a few physical as well as geometrical parameters of the systems. Some of these parameters, which mainly pertain to a polyelectrolyte layer modulated electrostatics and hydrodynamics, even remain the same in all the problems considered in the present thesis. Here we take an effort to briefly discuss the significance of a few important parameters as follows.

A typical height of the channel that can be considered for all the problems studied in the present thesis ranges from a few nanometers to hundreds of micrometers (Duffy et al., 1999; Hessel et al., 2005; N.-T. Nguyen et al., 2002; N.-T. Nguyen & Wu, 2005; Stone et al., 2004). For rotational hydrodynamics, the channel size (height or width) may extend

even up to a few millimeters (Duffy et al., 1999). On account of this aspect, we have considered that for the present thesis, the height or width of the channel varies within the limits of $O\left(10^0 - 10^2\right)\mu$m . Also, we obtain the scales of Debye length of the EDL and the thickness of PEL as follows. For an aqueous solution of KCl, the Debye length varies between 9.6 nm to 300 nm when the concentration of the electrolyte KCl is changed from 10^{-3} to 10^{-6} M (J H Masliyah & Bhattacharjee, 2006). Following this range, the thickness of the EDL for all the problems addressed in this thesis is considered to vary between 10 nm to 300 nm. The thickness of the PEL, on the other hand, depends on the method of manufacturing. If manufactured by using the layer-by-layer assembly method, the PEL thickness, as reported in the literature, can be extended up to a few microns in the range of $O\left(10^0\right)\mu$m only (S. Das et al., 2015).

From the scales of various quantities mentioned above, the dimensionless DH parameter of the EL κ falls in the range 1 to 100. Therefore, unless mentioned otherwise, in the present thesis, we have considered that the parameter κ to vary between the values 1 to 50 for all the problems considered. On the other hand, the magnitude of the DH parameter κ_p of PEL is kept as constant (=10) throughout the thesis.

We would also like to mention here the values of a few fundamental quantities which are important for the electrokinetically actuated transport phenomena. For all the problems investigated in the present thesis, the universal solvent 'water' is considered as the working fluid if not specifically mentioned. Based on this, the density ρ and the dynamic viscosity η of the fluid are considered as 1000 Kg/m^3 and 10^{-3}-10^{-4} Pa-sec, respectively. Apart from that, for an aqueous solution of the electrolyte KCL, the relative permittivity ε_r is 78.7 whilst the permittivity of the free space ε_0 is 8.996×10^{-12} F/m. The ionic diffusivity $D_{e,\pm}$ for such electrolytes ranges between 10^{-8}-10^{-9} m^2/sec (Bird et al., 2006; J H Masliyah & Bhattacharjee, 2006; R. J. Hunter, 1981). Note that for all the problems, the electrolytes are considered as the monovalent, i.e., $z_e = 1$ and if not mentioned explicitly, the reference strength of the applied electric field is considered as $O(10^3)$ V/m (Mondal, Ghosh, et al., 2014; Mukherjee et al., 2017; Peng & Li, 2016; Saville, 1977). The values of similar quantities pertaining to the polyelectrolytes are considered to be in the same range.

On using the considerations made above, the reference scale of the velocity, i.e., the Helmholtz-Smoluchowski velocity can be estimated in the range of 10^{-4} to 10^{-5} m/sec. In addition to that, we can also configure here a range of the dimensionless PEL thickness as d = 0.1 to 0.4 using the typical range of dimensional PEL thickness and height of the channel as mentioned before. The remaining parameter, which is pertinent to the present analyses is the dimensionless drag parameter of the PEL α. The magnitude of α depends on the dimensional drag coefficient of the PEL matrix, the dynamic viscosity of the fluid, and the height of the channel. The dimensional drag coefficient μ_c of the PEL is the ratio of the dynamic viscosity to the permeability of the PEL matrix. The porosity to the permeability of the PEL matrix varies in the range of $O(10^8 - 10^{10})$ Ns/m^4 (Gorthi et al., 2020; Donald A. Nield & Bejan, 2006). Therefore, for the properties of the universal solvent 'water' and a typical range of the channel height as mentioned before, we can estimate the range of dimensionless drag parameter α as $O(10^0 - 10^1)$.

Note that for the present study, the values/ranges of these parameters can be given parameter as DH parameter of EL $\kappa \in [12, 20]$, DH parameter of PEL κ_p = 10, and PEL thickness $d \in [0.0, 0.3]$. The important parameters for the present study, apart from the mentioned above, also include the dimensionless pressure gradient Γ and the power-law index n_0. For the present analysis, following the pertinent literature, the range or values of these parameters can be selected as Γ = 0.5 and $n_0 \in [0.7, 1.5]$ (Bird et al., 2006; Meisam Habibi Matin & Ohshima, 2015; Mondal, DasGupta, & Chakraborty, 2015).

2.2.3 Potential and Velocity Distribution

To understand the variant behaviour of the flow dynamics inside the soft narrow-fluidic channel, the relative strengths of the volumetric body forces is one of the important points to be looked at critically. In a soft narrow-fluidic channel, an inclusion of PEL on the walls of the channel and different volumetric body forces fetch a fascinating flow physics. In order to comprehend the variance in the electroosmotic body force in the soft narrow-fluidic channels for different system parameters viz., induced drag parameter α, PEL thickness d and DH parameter of EL κ, a variation in the potential distribution across the channel cross-section needs to be focused at once. Taking this aspect into consideration, first, we report in Fig. 2.4 the variation in the potential distribution in the channel. As such, the variation of potential distribution delineated in Fig. 2.4 will be required to support the

non-intuitive results described in the subsequent sections and in the forthcoming chapters.

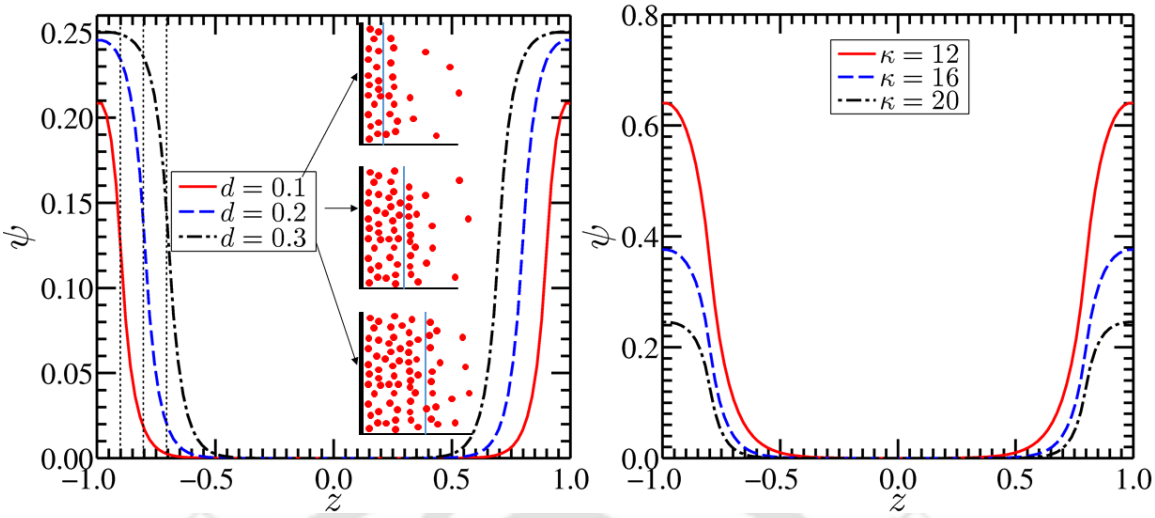

Figure 2.4: (a)-(b) Influence of PEL thickness and DH parameter of EL: Plots in (a)-(b) depict the potential distribution at $y = 0$, for three different values of PEL thickness d (= 0.1, 0.2 and 0.3), and DH parameter of EL κ (= 12, 16 and 20), respectively. The insets in (a) show a variation in the charge distribution with a PEL thickness. The other parameters considered for the present analysis are: (a) $\kappa = 20$, $\kappa_p = 10$; (b) $\kappa_p = 10$, $d = 0.2$.

In Figs. 2.4(a)-(b), we show the effect of PEL thickness d and DH parameter of EL κ respectively on the potential distribution. We consider different values of PEL thickness d as 0.1, 0.2 and 0.3 for Fig. 2.4(a), while for Fig. 2.4(b), we take three different values of DH parameter of EL κ as 12, 16 and 20. Having a closer look at Fig. 2.4, we observe that the potential in the channel gets enhanced with the increasing value of d from 0.1 to 0.3 as well as with the decreasing magnitude of κ from 20 to 12. In an effort to figure out the physical explanation behind this variation, we invoke to the variation of the charge distribution in the PEL. A variation in the softness of the narrow-fluidic channel is mainly attributable to the effect of charge distribution in the PEL. With an increment in the PEL thickness d from 0.1 to 0.3 and a decrement in DH parameter of EL κ from 20 to 12, the charge density in the PEL increases due to a relatively stronger interaction of the polyelectrolyte ions with the electrolyte ions. Such increment in the charge concentration in the PEL leads to an enhancement in the induced potential in the PEL and that too in the EL according to Poisson-Boltzmann potential distribution (Meisam Habibi Matin & Ohshima, 2015; R. J. Hunter, 1981). This phenomenon eventually gives rise to an enrichment in the potential as observed in Figs. 2.4(a) and 2.4(b) with a variation in the PEL thickness d from 0.1 to 0.3 and DH parameter of EL κ from 20 to 12, respectively. Taking this variation of the potential distribution (delineated in Fig. 2.4) into account, we

next move to discuss the variation of velocity distribution in the channel as depicted in Figs. 2.5(a)-(c).

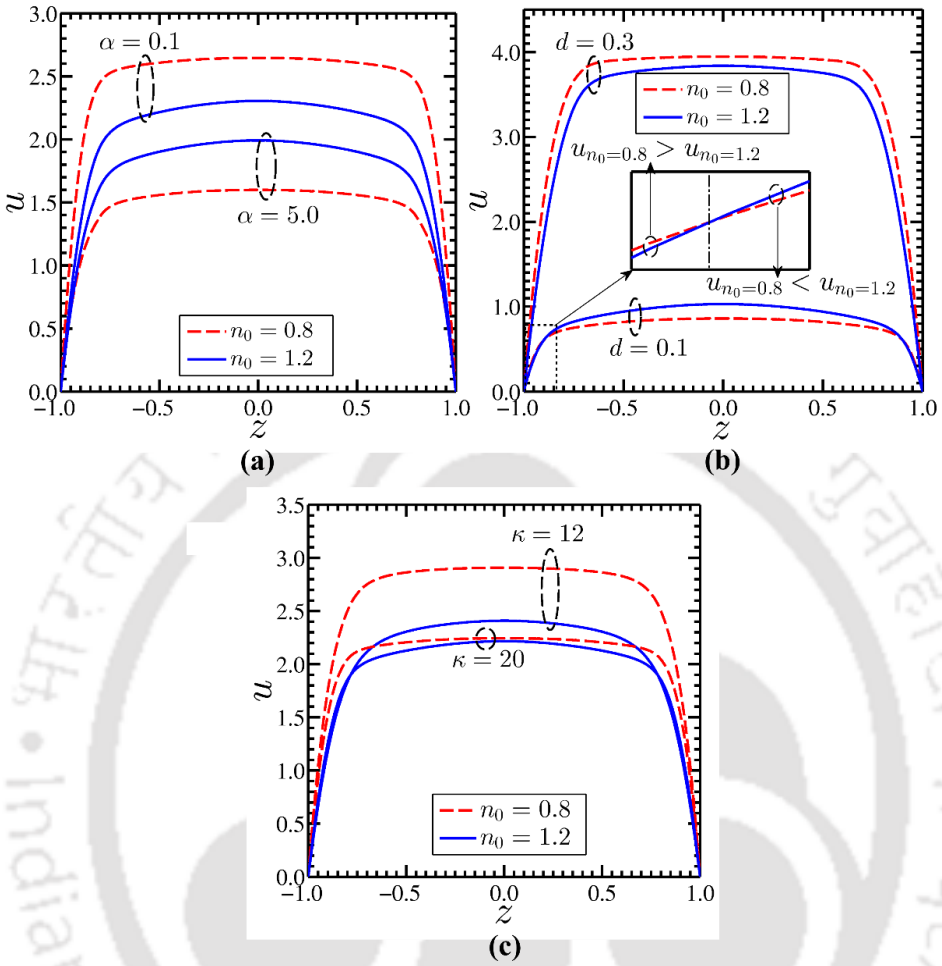

Figure 2.5: Plots depict the variation in the velocity distribution at $y = 0$ for shear-thinning ($n_0 = 0.8$) and shear-thickening fluids ($n_0 = 1.2$). We analyze the effect of, (a) induced drag parameter α, (b) PEL thickness d, and (c) DH parameter of EL κ. The inset of (b) shows that, $u_{n_0=0.8} > u_{n_0=1.2}$ near the walls of the channel, whereas towards the center of the channel, $u_{n_0=0.8} < u_{n_0=1.2}$, for a case of $d = 0.1$. The other parameters considered for the present analysis are: (a) $\kappa = 20$, $\kappa_p = 10$, $\Gamma = 0.5$, $d = 0.2$; (b) $\kappa = 20$, $\kappa_p = 10$, $\alpha = 2.5$, $\Gamma = 0.5$; and (c) $\kappa_p = 10$, $\alpha = 2.5$, $\Gamma = 0.5$, $d = 0.2$.

In Figs. 2.5(a)-(c), we show the variation in velocity distribution in the channel for three different parameters viz., induced drag parameter α, PEL thickness d and the DH parameter of EL κ, respectively. For all the variations depicted in Figs. 2.5(a)-(c), we have considered two different power-law indices $n_0 = 0.8$ and $n_0 = 1.2$ (Chabra & Richardson, 2008; Mondal, DasGupta, & Chakraborty, 2015). In Figs. 2.5(a)-(c), we observe the plug-like profile of the flow velocity for all values of α, d and κ considered. In fact, this observation holds true for both the shear-thinning ($n_0 = 0.8$) and shear-thickening ($n_0 = 1.2$)

fluids. The parameters governing the characteristics of PEL affect the velocity distribution and its magnitude by different aspects as clearly seen in Figs. 2.5(a)-(c). The frictional drag in the PEL impacts the underlying transport following the same nature as the Darcy friction drag does on the underlying transport through a porous media. An increment in the polymer grafting density resulting from an increasing value of drag parameter α enhances the Darcy drag which in effect reduces the velocities in the channel for both values of power-law index considered as witnessed in Fig. 2.5(a). The associated wall shear stress for a relatively higher value of drag parameter α (= 5) is also less for all the values of power-law index considered (n_0 = 0.7 to 1.5) as can be seen later in Fig. 2.6(a). As such, the lesser magnitude of wall shear stress for $\alpha = 5$ as seen in Fig. 2.6(a) conforms to the corresponding velocity magnitude in the channel in Fig. 2.5(a). Also, we observe from Fig. 2.5(a) that the velocity for the shear-thinning fluid (n_0 = 0.8) is higher than that of the shear-thickening fluid (n_0 = 1.2) for $\alpha = 0.1$, while for $\alpha = 5$, a reverse scenario of higher velocity attained by the shear-thickening fluid (n_0 = 1.2) is observed. We attribute this observation to the effect of viscous resistance of the non-Newtonian fluid on the underlying flow dynamics. Since the apparent viscosity of class of shear-thinning fluids ($n_0 < 1$) is less, the viscous resistance offered to the flow field of a shear-thinning fluid ($n_0 < 1$) becomes lesser as compared to that of the shear-thickening fluid ($n_0 > 1$) for a given strength of driving force being applied to make the flow occur. Consequently, a relatively lesser viscous resistance makes the flow velocity of the shear-thinning fluid (n_0 = 0.8) to be higher, as reflected in Fig. 2.5(a) for $\alpha = 0.1$. However, a closer look at Fig. 2.5(a) further reveals that the reduction in the flow velocity for a higher value of α (= 5) becomes relatively higher for the flow of a shear-thinning fluid (n_0 = 0.8). We attribute this observation to the effect of viscous resistance since viscous resistance experienced by the flow of a shear-thinning fluid (n_0 = 0.8) is lesser than that of the shear-thickening fluid (n_0 = 1.2). Note that, the higher the variation in the volumetric body forces, higher will be the change in the flow velocity of the shear-thinning fluid since the apparent viscosity, and hence the viscous resistance of this class fluid is lesser than that of its counterpart (shear-thickening fluid).

The effect of PEL on the underlying transport can be better understood by varying the PEL thickness as delineated in Fig. 2.5(b). As such, a change in the thickness of PEL

in the channel brings in a noticeable change on the underlying electrohydrodynamics as seen in Fig. 2.5(b). An increment in the PEL thickness augments the electrical forcing in the fluid domain on account of an enhanced ionic interaction between polyelectrolyte and electrolyte (Meisam Habibi Matin & Ohshima, 2015). Since the electrical body force due to EDL phenomenon in PEL grafted channel is higher than the rigid narrow-fluidic channel, the fluid in the soft narrow-fluidic channel experiences a relatively higher electrical force than that of the rigid narrow-fluidic channel (Meisam Habibi Matin & Ohshima, 2015). Therefore, the higher PEL thickness, as realized by a higher value of d (= 0.3) leads to a high velocity in the channel as depicted in Fig. 2.5(b). The higher velocity in the channel leads to an increment in the wall shear stress for higher PEL thickness as confirmed in Fig. 2.6(b).

Next, we describe, in Fig. 2.5(c), the variation of flow velocity influenced by the DH parameter of EL. It should be mentioned in this context here that we have kept, in this analysis, the value of κ_p fixed at 10, while the magnitude of κ has been varied from 12 to 20. With an increment in κ from 12 to 20, the maximum value of potential distribution in the channel decreases as depicted in Fig. 2.4(b). Therefore, the velocity magnitude for $\kappa = 12$ becomes higher than that of $\kappa = 20$ as witnessed in Fig. 2.5(c).

We would like to discuss other important points in the context of Fig. 2.5(b) as follows: One may find from Fig. 2.5(b) that the fluid velocity for shear-thinning fluid ($n_0 = 0.8$) is higher for particular cases of $d = 0.3$, whereas for the remaining case of $d = 0.1$, the velocity for shear-thickening fluid ($n_0 = 1.2$) is higher than that of the shear-thinning fluid ($n_0 = 0.8$). It may be mentioned here that the case of $d = 0.1$ nearly mimics a rigid narrow-fluidic channel due to the very small thickness of the PEL and hence, the electrical forcing is remaining effective only near the walls of the channel. Due to this, the electrical body force experienced by the shear-thinning fluid ($n_0 = 0.8$) is higher than the shear-thickening fluid ($n_0 = 1.2$) in the near-wall region, since the apparent viscosity and hence, the viscous resistance to the flow field becomes lesser for the flow of a shear-thinning fluid. As such, upon experiencing a relatively higher magnitude of electrical body force, the velocity of the shear-thinning fluid becomes higher than that of shear-thickening fluid near the walls as shown in the inset of Fig. 2.5(b). On the other hand, because of the higher viscosity of the shear-thickening fluid ($n_0 = 1.2$), the net momentum due to electrical

forcing gets transported to a relatively larger lateral extent of the channel, which in turn leads to a higher velocity of the shear-thickening fluid ($n_0 = 1.2$) in the center of the channel (for $d = 0.1$) as witnessed in Fig. 2.5(b).

We would like to discuss another important point in the context of Fig. 2.5(b) as follows: although the fluid velocity in the region closer to the walls of the channel is higher for the shear-thinning fluid ($n_0 = 0.8$) for both the values of d considered (see inset of Fig. 2.5(b)), the magnitude of velocity in the bulk region is seen to be higher for shear-thickening ($n_0 = 1.2$) fluid (almost comparable for $d = 0.3$). For the case of $d = 0.3$, since the electrical forcing acting on the fluid mass originating from the EDL becomes relatively stronger, the higher rate of momentum transport even by the shear-thinning fluid (although the viscosity is less) makes the fluid velocity to be almost equal with the velocity attained by the shear-thickening ($n_0 = 1.2$) fluid in the bulk region. Note that as observed in Fig. 2.4(a), the PEL thickness is also higher for $d = 0.3$ as compared to $d = 0.1$, thus offering a wide span of the electroosmotic force in the channel. For $d = 0.1$, the net electrical forcing applied on the fluid mass becomes relatively lesser (the ionic concentration between the PEL and EL is less for $d = 0.1$) and hence, the rate of momentum transport by the shear-thinning fluid is not comparable with that of the shear-thickening fluid (momentum transport by the shear-thickening fluid is always higher on account of a higher viscosity of this class of fluid), leading to a lesser velocity of the shear-thinning fluid in the bulk region as seen in Fig. 2.5(b).

2.2.4 Effect of Soft Layer on Wall Shear Stress

The grafting of PEL in the narrow-fluidic channel alters the underlying flow dynamics and the rate of volumetric transport through the channel following an alteration in the wall shear stress. We make an effort in Figs. 2.6(a)-(c), to see the variation of wall shear stress with power-law index obtained for different values of drag parameter α (= 0.1, 2.5 and 5), PEL thickness d (= 0.1, 0.2 and 0.3) and DH parameter of EL κ (= 12, 16 and 20), respectively.

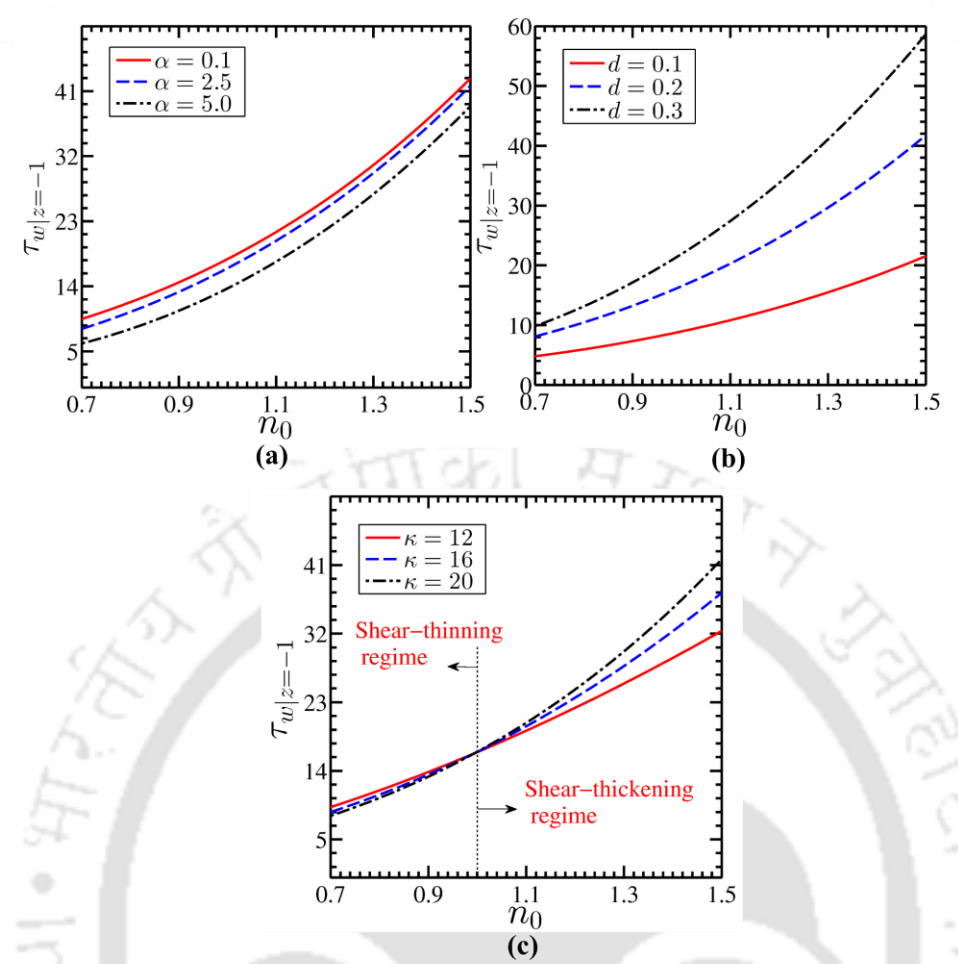

Figure 2.6: Variation in the wall shear stress at the location $z=-1$, $y=0$ with a power-law index for three different cases of (a) induced drag parameter α (= 0.1, 2.5 and 5), (b) PEL thickness d (= 0.1, 0.2 and 0.3), and (c) DH parameter of EL κ (= 12, 16 and 20). The other parameters considered for the present analysis are: (a) $\kappa=20$, $\kappa_p=10$, $\Gamma=0.5$, $d=0.2$; (b) $\kappa=20$, $\kappa_p=10$, $\alpha=2.5$, $\Gamma=0.5$; and (c) $\kappa_p=10$, $\alpha=2.5$, $\Gamma=0.5$, $d=0.2$.

We observe that the wall shear stress in the soft narrow-fluidic channel for all the parametric variations (viz., α, d and κ) considered in Figs. 2.6(a)-(c) gets enhanced with an increment in the power-law index, i.e., with a change in fluid rheology from shear-thinning ($n_0<1$) to the shear-thickening ($n_0>1$) behaviour. We attribute this variation to an increment in the apparent viscosity of the fluid, which increases with an increment in the non-Newtonian behaviour of the fluid. As the power-law index varies from 0.7 to 1.5, the apparent viscosity of the fluid increases, leading to an increment in the shear stress at the wall as depicted in Fig. 2.6. The plots depicted in Fig. 2.6(a) reflect the effect of change in the PEL drag parameter on the variation of wall shear stress. With an increment in the drag parameter α from 0.1 to 5, the wall shear stress reduces due to the reduction in fluid velocity near the walls of the channel. Note that a reduction in velocity with increasing α

is confirmed in Fig. 2.5(a). However, due to increasing viscosity of the non-Newtonian fluid with increasing value of the power-law index (n_0 = 0.7 to 1.5), the wall shear stress in the channel enhances more noticeably. Next, we look at Fig. 2.6(b), which shows the variation of wall shear stress obtained for different values of d (= 0.1, 0.2 and 0.3). It may be mentioned here that with the increasing value of PEL thickness d from 0.1 to 0.3, the softness of the channel increases, which in effect leads to a rise in the fluid velocity as confirmed in Fig. 2.5(b). Such enhancement in the fluid velocity with a higher value of d (= 0.3) as witnessed in Fig. 2.5(b) together with the stronger EDL effect leads to a higher velocity gradient in the channel and resulting in a higher wall shear stress as confirmed in Fig. 2.6(b). It is worth mentioning here that the wall shear stress for higher PEL thickness (d = 0.3) grows exponentially with the power-law index as clearly seen in Fig. 2.6(b). We further attribute this observation to a relatively higher apparent viscosity of the class of shear-thickening fluids ($n_0 > 1$) than the shear-thinning fluids ($n_0 < 1$).

Further, an inversion in the shear stress profiles is seen in the variation obtained for three different values of κ (= 12, 16 and 20), while varying the power-law index from 0.7 to 1.5 as delineated in Fig. 2.6(c). A closer look at Fig. 2.6(c) discloses that the inversion occurs at $n_0 = 1$ (Newtonian fluid). As mentioned before, for $\kappa = 12$, due to a comparatively higher surface potential (see Fig. 2.4(b)) the velocity of the shear-thinning fluid ($n_0 < 1$) becomes higher than the shear-thickening fluid ($n_0 > 1$), which results in a higher velocity gradient near the walls for the underlying transport of shear-thinning fluid. This higher velocity gradient gives rise to a higher wall shear stress for the flow of shear-thinning fluid for $\kappa = 12$ as one may verify from Fig. 2.6(c). On the contrary, for the case of $\kappa = 20$, a reverse scenario of increasing wall stress for shear-thickening fluid ($n_0 > 1$) is witnessed in Fig. 2.6(c) as well. In the region of $n_0 > 1$, due to comparatively low ionic concentration in PEL and low surface potential, the velocity of the shear-thickening fluid is higher than the shear-thinning fluid for the case of $\kappa = 20$, thus results in a higher wall shear stress for the shear-thinning fluid as confirmed in Fig. 2.6(c).

2.2.5 Volumetric Flow Rate

An intend of different types of annexations in the microfluidic devices/systems ultimately targets to achieve an enhancement in the flow rate as well as its control through these systems/devices, essentially to meet the demand of the μTAS and MEMS

applications. Accordingly, we here present the variation of flow rate in the soft narrow-fluidic channel for different values of parameters, which govern the hydrodynamics through PEL such as dimensionless PEL thickness d and drag parameter α. We write the explicit expression of the dimensionless volumetric flow rate as:

$$Q_x = \int_{-1}^{1}\int_{-1}^{1} u(z,y)dzdy \tag{2.23}$$

Here, we obtain the variation in the volumetric flow rate by varying the DH parameter of EL κ from 12 to 20 and power-law index n_0 from 0.7 to 1.5 (shear-thinning to shear-thickening nature). We discuss the variation of axial flow rate with PEL thickness d and drag parameter α systematically, as follows.

2.2.5.1 Effect of PEL Thickness

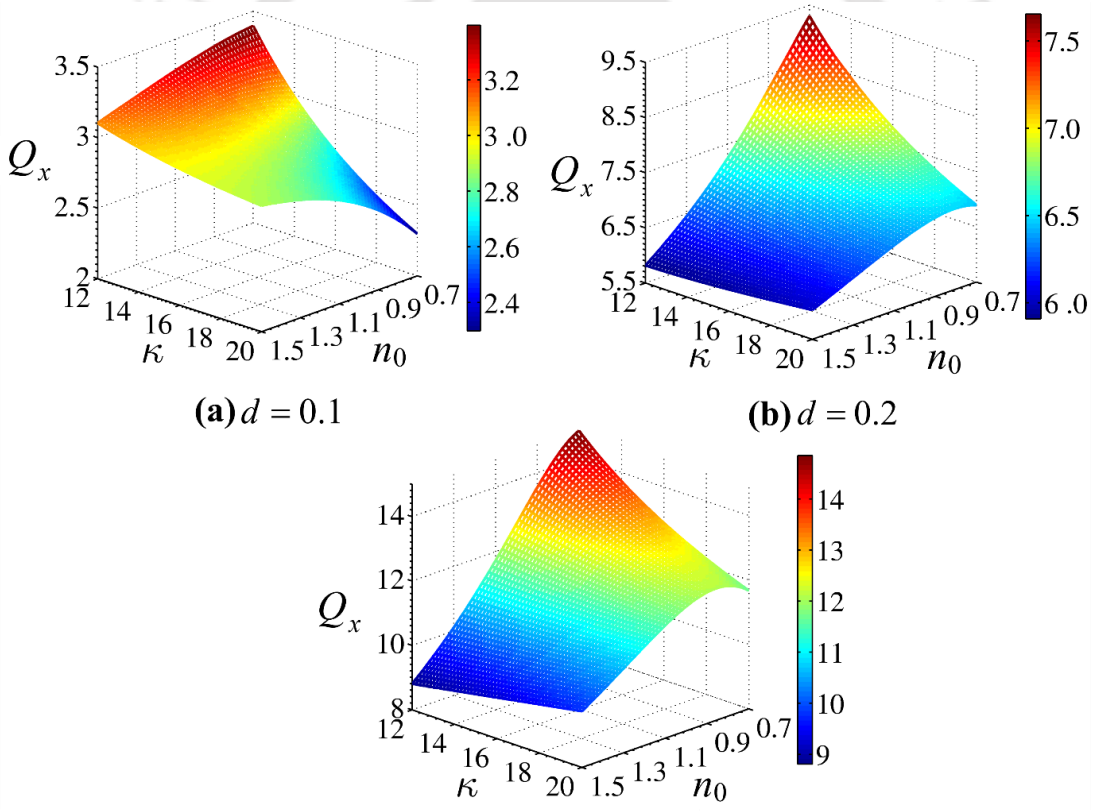

Figure 2.7: Surface plots in (a)-(c) depict the axial flow rate Q_x obtained on the $\kappa - n_0$ plane for different values of PEL thickness d (= 0.1, 0.2 and 0.3). To obtain these plots, the DH parameter of EL κ is varied from 12 to 20, whereas the power-law index n_0 is varied from 0.7 to 1.5. The other parameters considered for the present analysis are: $\kappa_p = 10$, $\alpha = 2.5$, $\Gamma = 0.5$.

Figure 2.7(a)-(c) represents the surface plots of the volumetric flow rate on the

$\kappa - n_0$ plane for three values of PEL thickness d (= 0.1, 0.2 and 0.3) respectively. It is worth mentioning here that an increment in the PEL thickness d from 0.1 to 0.3 enhances the charge concentration and hence, the potential (see Fig. 2.4(a)) in both the PEL as well as EL. Since an increment in the charge density leads to an augmentation in the electroosmotic body force in both PEL and EL, the higher flow velocity in the soft narrow-fluidic channels is observed for higher PEL thickness $(d = 0.3)$ as confirmed in Fig. 2.5(b). Accordingly, an enhancement in the flow rate through the channel with an increment in PEL thickness from $d = 0.1$ to 0.3, as observed in Figs. 2.7(a)-(c), signifies the effect of the magnitude of electrical forcing, which increases with an increment in the PEL thickness, on the underlying transport while all other parameters remain unaltered. In fact, with an increment in d, the cumulative effect of the electrical body force originating from the EDL being formed upon ionic interaction between polyelectrolyte and electrolyte, enhances the flow velocity for both the shear-thinning and shear-thickening fluids, leading to an enhancement in flow rate through the channel as apparent from Figs. 2.7(a)-(c). In Fig. 2.7(a), it is observed that, for lower values of κ (= 12), the flow rate in the channel is higher for shear-thinning fluid ($n_0 < 1$) than that of shear-thickening fluid ($n_0 > 1$), whereas for higher values of κ (= 20), the opposite scenario is observed. This observation can be attributed to the conglomeration of the two phenomena; one is a variation of the electrical forcing with κ, and the second one is the softness induced modification of the rheology of the non-Newtonian fluid. Since the viscous resistance applied to shear-thinning fluid ($n_0 < 1$) is less as compared to the shear-thickening fluid ($n_0 > 1$), the higher magnitude of electrical body force for a lower value of κ (= 12) enhances the transport of shear-thinning fluid ($n_0 < 1$) in the channel (as compared to the shear-thickening ($n_0 > 1$) fluid), leading to the higher flow rate of shear-thinning fluid ($n_0 < 1$) as observed in Fig. 2.7(a). However, for higher values of κ (= 20) in case of $d = 0.1$, the smaller magnitude of electrical body force implies a case of the rigid narrow-fluidic channel as elaborated before in the context of Fig. 2.5(b). For thinner PEL ($d = 0.1$) and for higher values of κ (= 20), the shear-thickening fluid ($n_0 > 1$) shows higher velocity than that of the shear-thinning fluid ($n_0 < 1$) due to higher transverse momentum exchange phenomena, approximately mimicking a rigid narrow-fluidic channel case for $d = 0.1$ (see Fig. 2.5(b)). However, in Figs. 2.7(b) and 2.7(c), we do not observe such phenomena due to a higher effect of the softness, induced by the increasing values of d = 0.2-0.3.

Having a closer look at Figs. 2.7(b)-(c), which depict the flow rate variation for d = 0.2 and 0.3 respectively, one may find that the flow rate for the shear-thinning fluid becomes higher in comparison to the shear-thickening fluid. To make a comment on this observation, it may be mentioned here that, with an increment in the PEL thickness d (= 0.2 and 0.3), the electroosmotic body force increases due to a relatively higher magnitude of the electrostatic potential and the thicker Debye length of the EDLs for d = 0.2 and 0.3. To be precise, because of the higher electrical body force, the rate of momentum transport by the shear-thinning fluid makes the flow velocity of these kinds of fluids to be either comparable (for d = 0.2) or even higher (for d = 0.3) than that of the shear-thickening fluid. Thus, the higher flow velocity gained by the shear-thinning fluid leads to a higher flow rate in the channel for d = 0.2 and 0.3, as evident in Figs. 2.7b)-(c).

2.2.5.2 Variation in Drag Parameter

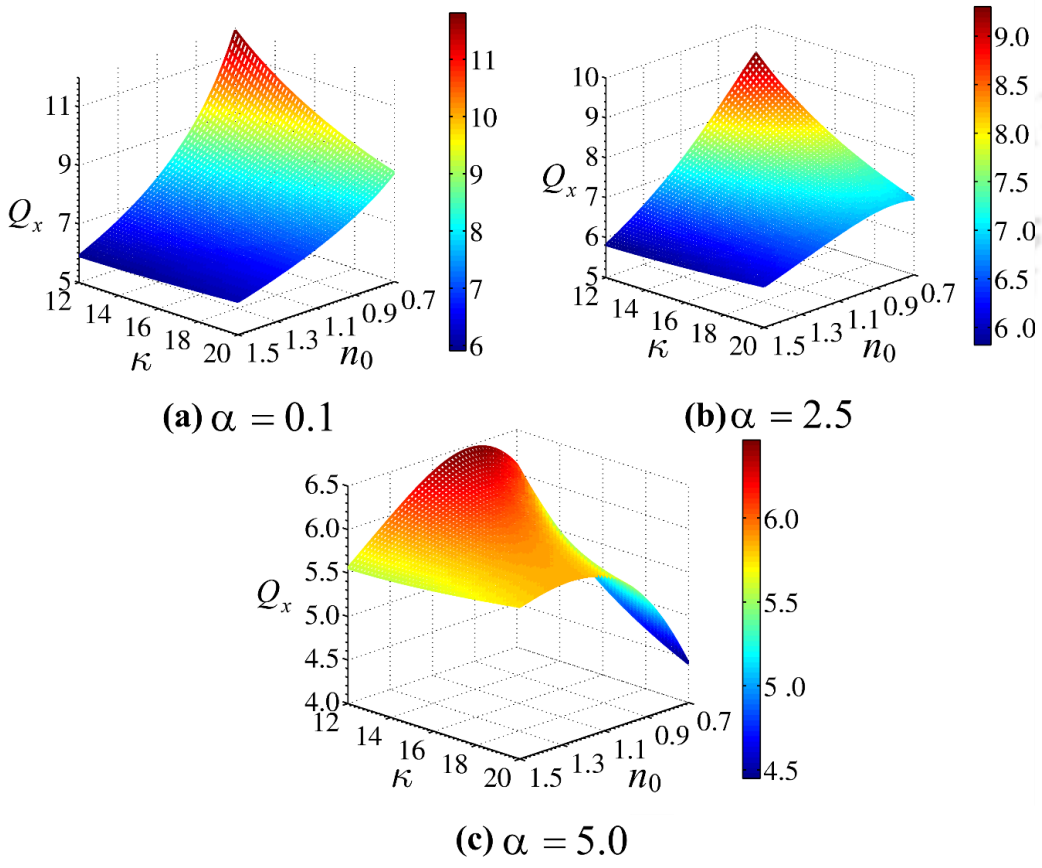

Figure 2.8: Surface plots in (a)-(c) depict the axial flow rate Q_x obtained on the $\kappa - n_0$ plane for different values of the drag parameter of PEL α (= 0.1, 2.5 and 5). To obtain these plots, the DH parameter of EL κ is varied from 12 to 20, whereas the power-law index n_0 is varied from 0.7 to 1.5. The other parameters considered for the present analysis are: $\kappa_p = 10$, $d = 0.2$, $\Gamma = 0.5$.

In Figs. 2.8(a)-(c), we delineate the effect of drag parameter α on the variation of

volumetric flow rate in the channel. Note that we have considered three different values of α (= 0.1, 2.5 and 5) for Figs. 2.8(a)-(c) respectively, while other parameters considered for plotting the figures are: $\kappa_p = 10$, $\Gamma = 0.5$, $d = 0.2$. The variation of the drag in the PEL is essentially a manifestation of either the change in the porosity or the permeability of the porous structure inside the PEL matrix for which the dimensional drag parameter μ_c is written as η / k_{PEL} (D. A. Nield & Bejan, 2006), where η is the viscosity of the fluid and k_{PEL} is the permeability of the porous structure due to polymer density in the PEL. Therefore, with an increment in the polymer or grafting density, the permeability of PEL decreases, which leads to a reduction in the fluid velocity in the PEL. In fact, a reduction in the flow velocity in PEL, accounting the exchange of transverse momentum phenomenon, further leads to a reduction of velocity in the EL domain as well. As a consequence of this reduction in flow velocity in both the layers (refer to Fig. 2.5(a)), we observe a reduction in the flow rate with an increment in the drag parameter from α = 0.1 to 5 as delineated in the Figs. 2.8(a)-(c). It is observed from Fig. 2.8(a) that the flow rate for a small value of drag parameter $\alpha = 0.1$ increases with lowering the DH parameter of EL κ from 20 to 12, while a change in the power-law index from 1.5 to 0.7 leads to an increment in flow rate as well. However, a closer look at Figs. 2.8(a)-(c) reveals that an increment in the drag parameter from $\alpha = 0.1$ to 5 reduces the flow rate in the channel for shear-thinning fluid ($n_0 < 1$) appreciably, whereas the variation of the flow rate of the shear-thickening fluid ($n_0 > 1$) with a change in α in the range considered for plotting the present analysis is not significant. For the flow through a soft channel, the shear-thinning fluid is more susceptible to the change in the drag parameter (either increase or decrease) than the shear-thickening fluid, attributed primarily to the relatively lesser apparent viscosity inherent with the class of shear-thinning fluid ($n_0 < 1$).

2.2.6 Softness Induced Enhancement in Net Throughput

We here discuss the flow rate enhancement in the soft narrow-fluidic channel as compared to the rigid narrow-fluidic channel. In doing so, we show in Figs. 2.9(a)-(b), the variation of the flow rate ratio Q_{SC}/Q_{RC}, defined as the ratio of flow rate in the soft narrow-fluidic channel Q_{SC} to the flow rate in the rigid narrow-fluidic channel Q_{RC}, with a change in the power-law index from 0.7 to 1.5, obtained for different values of d and α, respectively. It may be mentioned in this context here that for plotting the variation of flow

rate in a rigid narrow-fluidic channel Q_{RC} in Figs. 2.9(a)-(b), we have considered the thickness of the PEL d to be 0.01, essentially to mimic the underlying transport through a rigid narrow-fluidic channel.

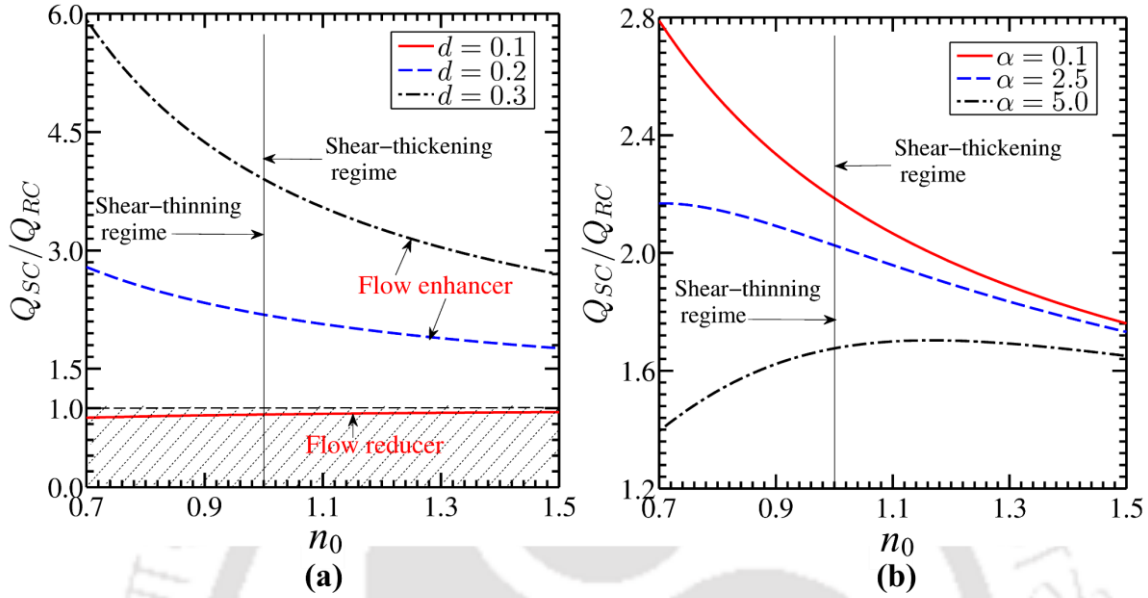

Figure 2.9: Plots show the variation of the flow rate ratio Q_{SC}/Q_{RC} with a power-law index n_0 which varies from 0.7 to 1.5. Q_{SC} and Q_{RC} are the volumetric flow rates in the soft and rigid narrow-fluidic channel, respectively. Plots depict in (a) the variation of Q_{SC}/Q_{RC} for different values of PEL thickness d (= 0.1, 0.2 and 0.3) and $\alpha = 0.1$; and in (b), for different values of drag parameter α (= 0.1, 2.5 and 5) and $d = 0.2$. The other parameters considered are: $\kappa = 12$, $\kappa_p = 10$ and $\Gamma = 0.5$.

It is observed from Figs. 2.9(a)-(b) that the ratio Q_{SC}/Q_{RC} is always higher than unity for all the values of d and α considered, except for the case of $d = 0.1$ in Fig. 2.9(a). As such, this observation holds true for the range of n_0 undertaken in the plotting the present figures. Grafting of PEL on the walls of the soft narrow-fluidic channel makes the induced potential ψ to be higher than that of the rigid narrow-fluidic channel, leading to a comparatively stronger electroosmotic body force being applied on the fluid mass in the EDL. In such cases, the soft narrow-fluidic channel can be called as the flow enhancer, except for the case of $d = 0.1$. It should be noted here that the magnitude of electrical forcing in such cases $d \leq 0.1$ is very less as the PEL thickness is very small as compared to the other cases shown in Figs. 2.9(a) and 2.9(b). Furthermore, for $d \leq 0.1$, the friction drag provided by the PEL to the fluid leads to a reduction in flow velocity for all classes of fluids (albeit reduction is higher for shear-thinning fluid) in Fig. 2.7. Thus, lesser electroosmotic force together with the frictional drag reduces the flow velocity, leading to

a reduction in net throughput as compared to the rigid channel as seen in Fig. 2.9(a). Hence, except $d = 0.1$, we observe an enhancement in net throughput for all the values of d and α considered in this analysis, calling itself a flow enhancer region.

In Fig. 2.9(a), we observe a decreasing trend of Q_{SC}/Q_{RC} with a change in the power-law index from 0.7 to 1.5, for $d = 0.2$ and $d = 0.3$, attributed primarily to the effect of the change in the fluid rheology from shear-thinning ($n_0 < 1$) to the shear-thickening behaviour of the fluid ($n_0 > 1$) on the underlying dynamics. Since the viscous resistance for the shear-thinning fluid is lesser than that of shear-thickening fluid, the flow rate obtained for shear-thinning fluid is higher than that shear-thickening fluid, as witnessed in Figs. 2.7(a)-(c). In fact, the observations reflected in Figs. 2.7(a)-(c) get further verified in Fig. 2.9(a), where we find a relatively higher flow rate enhancement of shear-thinning fluid than that of the shear-thickening fluid. Such region of the enhancement in the flow rate for $d \geq 0.1$ can be characterized as the flow enhancer. However, the region of $d \leq 0.1$ can be called as the flow reducer since the flow of the non-Newtonian fluid (for all values of n_0 = 0.7 – 1.5) is less than that of rigid narrow-fluidic channel case ($Q_{SC} < Q_{RC}$). Apart from this, in Fig. 2.9(a), we observe that Q_{SC}/Q_{RC} increases with an increment in the PEL thickness from 0.1 to 0.3. This is mainly attributed to an increment in the EDL thickness and induced potential (see Fig. 2.4(a)) with an increment in the PEL thickness from 0.1 to 0.3. An increment in d (from 0.1 to 0.3) increases the fluid velocity (see Fig. 2.5(b)) and culminates in an enhancement in the flow rate in the soft narrow-fluidic channel as observed in Fig. 2.9(a).

Next, in Fig. 2.9(b), we observe an increasing nature in the flow rate enhancement with a decrement in the drag parameter α from 5 to 0.1 even for the all the values of n_0 considered, mainly attributed to the reduction in the friction drag offered by the PEL to the fluid with a decrement in α. Since a decrement in α weakens the friction drag applied by the PEL on the fluid, the fluid velocity, as well as the flow rate in the channel, enhances with a decrement in α as observed in Fig. 2.9(b). However, in Fig. 2.9(b), we observe two different trends of the variation of Q_{SC}/Q_{RC} with a change in the power-law index n_0 from 0.7 to 1.5 for $\alpha = 5$. The flow rate ratio Q_{SC}/Q_{RC} initially increases with an increment in n_0 from 0.7 to 1, which is then followed by a decreasing trend as n_0 increases further from

1.0 to 1.5. We here make an effort to figure out the reason behind this observation as follows: it may be mentioned here that the higher friction drag on the flow field originating from the higher value of α (= 5) leads to a relatively higher reduction in flow velocity for shear-thinning fluids ($n_0 < 1$) since the apparent viscosity is lesser for this class of fluids. As such, the relative reduction in flow velocity and hence the flow rate becomes relatively lesser for the underlying transport of shear-thinning fluids through a soft channel, attributed to the stronger electrical forces stemming from the ionic interaction between electrolyte and polyelectrolyte. Notably, a relatively lesser reduction in flow rate through soft narrow-fluidic channel Q_{SC} than the rigid channel Q_{RC} leads to an increasing trend of Q_{SC}/Q_{RC} in the shear-thinning regime ($n_0 < 1$) as witnessed in Fig. 2.9(b). On the other hand, we observe a decreasing trend of Q_{SC}/Q_{RC} in the shear-thickening regime with increasing value of n_0 , i.e., with increasing non-Newtonian behaviour of the fluid, to be precise, with the increasing value of apparent viscosity of the fluid. The decrement in the flow velocity and its effect on the flow rate through the soft narrow-fluidic channel is relatively higher than the rigid narrow-fluidic channel, leading to a decreasing trend of Q_{SC}/Q_{RC} in the shear-thickening regime that too observed in Fig. 2.9(b). We attribute this observation to the effect of rheology-modulated enhancement in viscous drag on the flow dynamics. We would like to convey the following message in the context of the variation of flow rate ratio (Q_{SC}/Q_{RC}) vs n_0, obtained for a relatively higher value drag parameter α (= 5) as follows: in the shear-thinning regime ($n_0 < 1$), the electroosmotic body force originating from the EDL phenomenon due to a relatively stronger ionic interaction between polyelectrolyte and electrolyte takes a dominating role on the underlying transport, while the rheology-modulated viscous resistance governs the flow dynamics in the shear-thickening regime.

2.3 Summary

In the present chapter (Chapter 2), we have studied the electrohydrodynamics of the non-Newtonian fluids in a soft narrow-fluidic channel with the consideration of the electric double layer effect originating from the ionic interactions between polyelectrolyte and electrolyte. We have considered the Ostwald de'Waele power-law model for describing the non-Newtonian fluid rheology in this analysis. The main findings of this analysis are outlined as follows:

- The results unveiled that, the variation in the key parameters of this analysis, affect the electroosmotic body force, which upon interacting with the viscous force as modulated by the fluid rheology, alters the velocity distribution and flow rate variation in the channel non-intuitively. These parameters mainly include the DH parameter of EL, and the drag parameter and the thickness of PEL.
- We have investigated through this analysis that, a higher PEL thickness, lesser Darcy drag and adequately low DH parameter of EL leads to a high flow rate in the channel for shear-thinning fluids. Whereas on the other hand, the flow rate of shear-thickening fluids reduces for lower PEL thickness, higher Darcy drag and higher DH parameter of EL.
- In the present study, we have also shown a relative enhancement in the net throughput through the soft narrow-fluidic channel as compared to that of the rigid narrow-fluidic channel for different parameters PEL. Here, the analysis reveals two notable and distinct regimes. It is shown that a decrement in PEL thickness and increment in drag parameter leads to a reduction over the relative increment in the net throughput through the channel. These observations are suggestive of having PEL with low grafting density and higher charge concentration of PEL essentially for the enhancement of net throughput in the channel.
- A continual decrement in the relative enhancement of the net throughput or volumetric flow rate through the soft narrow-fluidic channel with increasing n_0 (i.e., with increasing non-Newtonian behaviour of fluid) for all d and α signifies the pronounced effect of the viscous resistance to the flow field, attributed primarily to the increment in apparent viscosity with n_0.

CHAPTER 3

Efficient Electroosmotic Mixing in a Narrow-Fluidic Channel: The Role of a Patterned-Soft Layer

Most of the μTAS used in different bio-microfluidic applications include a dedicated segment wherein an efficient mixing of such fluids, also counted as the *uncharged species*, with the targeted chemicals or medicines is primarily focused. In particular, such small scale platforms are in demand of a reduction in the mixing length, an increment in the retention time of candidate species (such as a bio-sample co-injected with a particular medicine), and the resultant enhanced mixing phenomenon (Hessel et al., 2005; N.-T. Nguyen & Wu, 2005). However, from an overview of several trials conducted by many researchers, in order to achieve the aforesaid deliverables in an accelerated manner, it appears that the possible distinctive functionalities rendered by the patterned-soft layer are yet to be taken into account. Considering this, we study in this chapter the mixing of uncharged species in a narrow-fluidic channel having the walls grafted with the patterned-soft layers. We consider two types of patterns: one is symmetric about the centerline, while the other is asymmetric. We also show in this study that the different patterning of the soft layer patches as well as the different physical parameters governing the physico-chemical characteristics of the soft layer considered in this analysis, tune the formation of Lamb vortices in the fluidic pathway and effectively enhance the mixing characteristics. Also, the present chapter critically discusses the onset of recirculation zones and a variation in the mixing length.

3.1 Mathematical Modelling

3.1.1 Problem Description

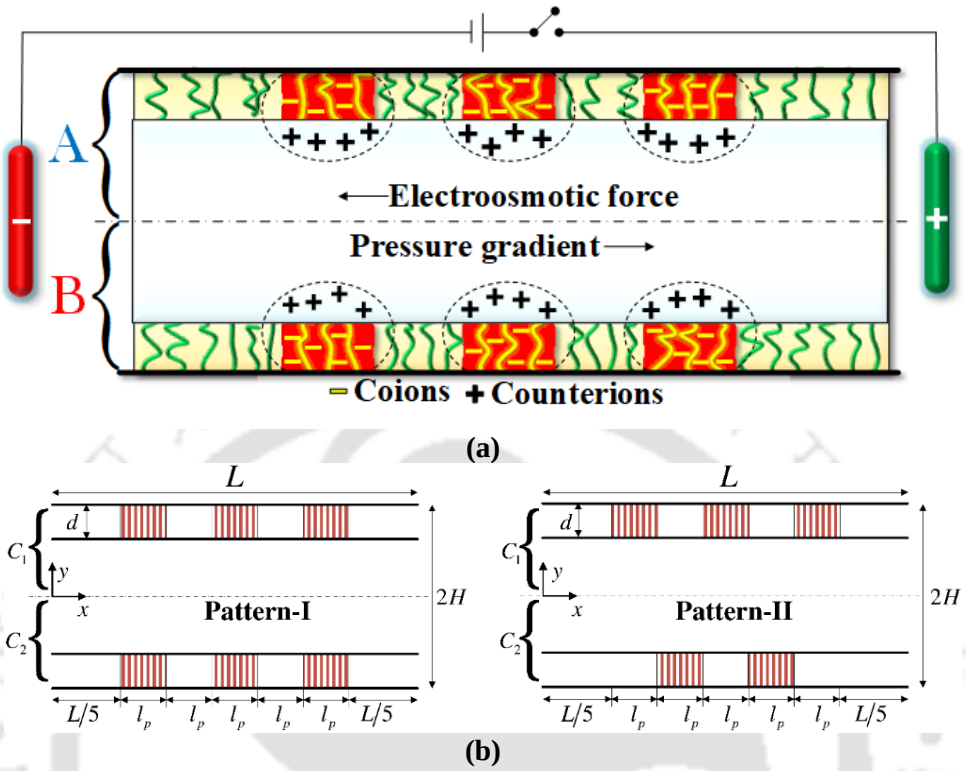

Figure 3.1: (a) Schematic of the patterned-soft narrow-fluidic channel: The red (dark grey in black-white) patch indicates the negatively charged polyelectrolyte layer whereas the remaining yellow (light grey in black-white) patch represents the uncharged polymer layer. (b) Types of patterns: Different types of grafting patterns (pattern-I and pattern-II) are shown in (b). The hatched section with the vertical lines represents the PEL patch, while the remaining section corresponds to the PL patch. L and $2H$ are the length and height of the channel, respectively. The aspect ratio, i.e., the ratio of length to height is considered as 5:1. The fraction $2L/5$ is sufficient to avoid the entry and exit effects of the channel. $l_p\,(=3L/25)$ is the patch length, and d is the thickness of both the PEL as well as the PL. However, for ease in the discussion, d is referred to as the thickness of PEL only. Note that all the quantities mentioned in the schematic diagram are dimensional.

The main purpose of using the patterned-soft layer, instead of a homogenous one, is the generation of local vortices in the focused channel passage. Deposited soft layer patches on the walls of the channel, in the presence of an electrolyte, intermittently form the electric double layers and set a local distribution of the electrostatic potential in their close vicinity. These local or intermittent EDLs formed near the PEL patches, further upon interaction with the external electric field initiates a local electroosmotic flow in the patched section. In this study, we have intentionally placed the electrodes of external electric source in such a way that this local EOF formed at the patched section opposes the pressure-driven flow and leads to the formation of local vortices therein. These vortices further assist in

achieving the characteristics of mixing, which are high in demand. The typical mechanism of vortex formation using the soft layer patches, as discussed before, is depicted in Fig. 3.1.

We show in Fig. 3.1(a) the schematic of the patterned-soft narrow-fluidic channel. The red patch indicates the negatively charged PEL, while the yellow patch represents the uncharged PL. These patches are grafted following two different patterns: pattern-I (symmetric) and pattern-II (asymmetric) (refer to Fig. 3.1(b)). In Fig. 3.1(a), the height and length of the channel are $2H$ and L respectively, while the width is considered to be much larger than the other two dimensions. Therefore, the analysis is practically two-dimensional. Note that the patch length $l_p = 3L/25$ is selected by considering the latest developments in the fabrication techniques such as micro-contact printing and block copolymerization techniques (S. Das et al., 2015; Husemann et al., 1999; Oded et al., 2016). Also, as observed in the later sections of *flow dynamics and the underlying analysis of mixing performance* (Sections 3.2-3.3), the patch length $l_p = 3L/25$ is sufficient to offer an effective enhancement in the mixing characteristics.

In Fig. 3.1, we also show two streams A and B. Stream-A has a negligible concentration of neutral species or particles, whereas stream-B is considered to have a higher concentration. This assumption is entirely justifiable from the perspective of the mixing applications. For example, one fluid stream having a higher concentration of biological or chemical species such as DNA or protein samples is transported through the channel to mix with another stream of a reagent, which has a deficiency of these samples. Therefore, the aim is to predict the concentration of neutral species in the mixing device. Accordingly, for the present study, in Fig. 3.1, the concentration of neutral species in stream-A (upper layer) and B (lower layer) is indicated by $c_1 = 0$ and $c_2 = C_{in}$ at the inlet.

3.1.2 Electrostatics

3.1.2.1 Induced Electrostatic Potential Distribution: Poisson-Boltzmann Equation

The present analysis deals with a slit narrow-fluidic channel with walls having grafted-soft layer patches, those intermittently generate the electrostatic potential in both the x and y direction in their own vicinity. Note that the polymeric layer patches, grafted between that of the consecutive two PEL's, do not induce any electric field as they do not bear any charges or ionic groups as PEL does. Therefore, the distribution of the electrostatic

potential ψ inside the polymeric patches follows the potential distribution set by the electrolyte. The direction in which the potential remains invariant in the present study is the z direction, i.e., $\partial\psi/\partial z = 0$. Considering these aspects, we have used the generalized form of the PB equations [Eqs. (2.9a)-(2.9b)] derived in Chapter 2: Section 2.1.1 and have modified for the present study into the expression given as (in a dimensionless form):

Electrolyte layer and polymeric patch

$$\frac{\partial^2\bar{\psi}}{\partial\bar{x}^2}+\frac{\partial^2\bar{\psi}}{\partial\bar{y}^2}=\bar{\kappa}^2\sinh\left(\bar{\psi}\right) \tag{3.1a}$$

Polyelectrolyte patch

$$\frac{\partial^2\bar{\psi}}{\partial\bar{x}^2}+\frac{\partial^2\bar{\psi}}{\partial\bar{y}^2}=\bar{\kappa}^2\sinh\left(\bar{\psi}\right)-\bar{\kappa}_p^2 \tag{3.1b}$$

3.1.2.2 Applied Electric Field

In the present study, the external electric field is applied to induce the electroosmotic flow in the opposite direction to the pressure-driven flow at the patched sections. This localized EOF leads to the formation of vortices. The distribution of applied electrostatic potential $\bar{\phi}_A$ can be obtained by the Laplace equation (R. J. Hunter, 1981), which is given in the dimensionless form as:

$$\frac{\partial^2\bar{\phi}_A}{\partial\bar{x}^2}+\frac{\partial^2\bar{\phi}_A}{\partial\bar{y}^2}=0 \tag{3.2}$$

Note that the direction of the applied electric field is conceivable from Fig. 3.1(a). The boundary conditions for solving the distribution of induced electrostatic potential $\bar{\psi}$ and applied electrostatic potential $\bar{\phi}_A$ [Eqs. (3.1)-(3.2)] are discussed in Section 3.1.5.2.

3.1.3 Hydrodynamics Coupled with PEL Electrostatics

In the present study, the flow is assumed to be steady, fully-developed, incompressible, and laminar. The body force acting in the electrolyte layer is only the electroosmotic force, while in the PEL and PL patch, an additional force, i.e., Darcy's frictional drag, also acts on the flow (Chanda et al., 2014). Accordingly, we frame two different sets of equations, one for the electrolyte layer [Eq. (3.3)], and one for PEL and PL patch [Eqs. (3.4)] modified with the additional drag force term. Note that we do not have to necessarily consider different electroosmotic body forces for these different regions (EL,

PEL, and PL) as the induced electric potential ψ and the applied electric potential ϕ_A is obtained over the entire domain before considering in Eqs. (3.3)-(3.4).

The two sets of equations are:

Electrolyte layer (first set)

x-momentum equation

$$\rho\left(u\frac{\partial u}{\partial x}+v\frac{\partial u}{\partial y}\right)=-\frac{\partial G}{\partial x}+\eta\left(\frac{\partial^2 u}{\partial x^2}+\frac{\partial^2 u}{\partial y^2}\right)+F_{E,x} \tag{3.3a}$$

y-momentum equation

$$\rho\left(u\frac{\partial v}{\partial x}+v\frac{\partial v}{\partial y}\right)=-\frac{\partial G}{\partial y}+\eta\left(\frac{\partial^2 v}{\partial x^2}+\frac{\partial^2 v}{\partial y^2}\right)+F_{E,y} \tag{3.3b}$$

Polyelectrolyte and polymeric patch (second set)

x-momentum equation

$$\rho\left(u\frac{\partial u}{\partial x}+v\frac{\partial u}{\partial y}\right)=-\frac{\partial G}{\partial x}+\eta\left(\frac{\partial^2 u}{\partial x^2}+\frac{\partial^2 u}{\partial y^2}\right)+F_{E,x}-\mu_c u \tag{3.4a}$$

y-momentum equation

$$\rho\left(u\frac{\partial v}{\partial x}+v\frac{\partial v}{\partial y}\right)=-\frac{\partial G}{\partial y}+\eta\left(\frac{\partial^2 v}{\partial x^2}+\frac{\partial^2 v}{\partial y^2}\right)+F_{E,y}-\mu_c v \tag{3.4b}$$

Continuity equation

$$\frac{\partial u}{\partial x}+\frac{\partial v}{\partial y}=0 \tag{3.5}$$

In these equations [Eqs. (3.3)-(3.5)], F_{E,x_i} is the electroosmotic body force where $x_{i=1,2}$ = (x, y) (Chanda et al., 2014; Donald A. Nield & Bejan, 2006). The electroosmotic body force F_{E,x_i} is given by:

$$F_{E,x_i}=\rho_e\left(-\frac{\partial \phi_A}{\partial x_i}\right) \tag{3.6}$$

where ρ_e is the charge density of electrolyte (J H Masliyah & Bhattacharjee, 2006; R. J. Hunter, 1981). We write Eqs. (3.3)-(3.5) in their dimensionless forms as:

Electrolyte layer

x-momentum equation

$$\mathrm{Re}\left(\bar{u}\frac{\partial \bar{u}}{\partial \bar{x}}+\bar{v}\frac{\partial \bar{u}}{\partial \bar{y}}\right)=-\frac{\partial \bar{G}}{\partial \bar{x}}+\frac{\partial^2 \bar{u}}{\partial \bar{x}^2}+\frac{\partial^2 \bar{u}}{\partial \bar{y}^2}+\bar{\kappa}^2\sinh\left(\bar{\psi}\right)\left(-\frac{\partial \bar{\phi}_A}{\partial \bar{x}}\right) \tag{3.7a}$$

y-momentum equation

$$\mathrm{Re}\left(\bar{u}\frac{\partial \bar{v}}{\partial \bar{x}}+\bar{v}\frac{\partial \bar{v}}{\partial \bar{y}}\right)=-\frac{\partial \bar{G}}{\partial \bar{y}}+\frac{\partial^2 \bar{v}}{\partial \bar{x}^2}+\frac{\partial^2 \bar{v}}{\partial \bar{y}^2}+\bar{\kappa}^2\sinh\left(\bar{\psi}\right)\left(-\frac{\partial \bar{\phi}_A}{\partial \bar{y}}\right) \tag{3.7b}$$

Polyelectrolyte and polymeric patch

x-momentum equation

$$\mathrm{Re}\left(\bar{u}\frac{\partial \bar{u}}{\partial \bar{x}}+\bar{v}\frac{\partial \bar{u}}{\partial \bar{y}}\right)=-\frac{\partial \bar{G}}{\partial \bar{x}}+\frac{\partial^2 \bar{u}}{\partial \bar{x}^2}+\frac{\partial^2 \bar{u}}{\partial \bar{y}^2}+\bar{\kappa}^2\sinh\left(\bar{\psi}\right)\left(-\frac{\partial \bar{\phi}_A}{\partial \bar{x}}\right)-\alpha^2\bar{u} \tag{3.8a}$$

y-momentum equation

$$\mathrm{Re}\left(\bar{u}\frac{\partial \bar{v}}{\partial \bar{x}}+\bar{v}\frac{\partial \bar{v}}{\partial \bar{y}}\right)=-\frac{\partial \bar{G}}{\partial \bar{y}}+\frac{\partial^2 \bar{v}}{\partial \bar{x}^2}+\frac{\partial^2 \bar{v}}{\partial \bar{y}^2}+\bar{\kappa}^2\sinh\left(\bar{\psi}\right)\left(-\frac{\partial \bar{\phi}_A}{\partial \bar{y}}\right)-\alpha^2\bar{v} \tag{3.8b}$$

Continuity equation

$$\frac{\partial \bar{u}}{\partial \bar{x}}+\frac{\partial \bar{v}}{\partial \bar{y}}=0 \tag{3.9}$$

In these equations, Reynolds number $\mathrm{Re}=\left(\rho u_{HS}\left(2H\right)\right)/\eta$, $\left(\bar{u},\bar{v}\right)=\left(u,v\right)/u_{HS}$, $\bar{G}=\left(G\left(2H\right)\right)/\left(\eta u_{HS}\right)$ and $\alpha^2=\left(\mu_c\left(2H\right)^2\right)/\eta$. Note that the reference length scale in the present study is $2H$. Once the velocity distribution is obtained in the entire domain, we calculate the distribution of the species concentration using the species transport equation, as discussed next.

3.1.4 Species Transport

For steady flows, the convection-diffusion equation for species transport is written as (Bird et al., 2006; H.-F. Huang & Lai, 2006):

$$u\frac{\partial c}{\partial x}+v\frac{\partial c}{\partial y}=D_S\left(\frac{\partial^2 c}{\partial x^2}+\frac{\partial^2 c}{\partial y^2}\right) \tag{3.10}$$

In Eq. (3.10), c is the concentration and D_S is the diffusion coefficient of species. As

discussed before in Section 3.1.1, we assume that stream-B has a higher concentration of particular species, i.e., $c = C_{in}$ at the inlet, and it is transported through the channel to mix with stream-A which has a deficiency of species, i.e., $c = 0$. Moreover, we assume that these species are uncharged and hence do not participate in the electrostatic interactions (Banerjee et al., 2019). We also assume that the diffusivity of both the species is almost the same. The dimensionless form of Eq. (3.10) reads as:

$$\mathrm{Re.Sc}\left(\bar{u}\frac{\partial \bar{c}}{\partial \bar{x}} + \bar{v}\frac{\partial \bar{c}}{\partial \bar{y}}\right) = \frac{\partial^2 \bar{c}}{\partial \bar{x}^2} + \frac{\partial^2 \bar{c}}{\partial \bar{y}^2} \tag{3.11}$$

In dimensionless form, the concentration of neutral species in streams A/B becomes $\bar{c} = 0/1$ respectively. In Eq. (3.11), $\bar{c} = c/C_{in}$ and Schmidt number $\mathrm{Sc} = \eta/(\rho D_s)$ (Bird et al., 2006). On solving Eq. (3.11), we further calculate the mixing efficiency defined as follows (Hadigol et al., 2011).

$$\xi_m(\bar{x}) = \left(1 - \frac{\int_{-0.5}^{0.5} \left|\bar{c}(\bar{x},\bar{y}) - \bar{c}_\infty\right| dy}{\int_{-0.5}^{0.5} \left|\bar{c}_0(\bar{y}) - \bar{c}_\infty\right| dy}\right) \times 100\% \tag{3.12}$$

$\bar{c}_0$ represents the concentration at the unmixed state, whereas $\bar{c}_\infty$ represents the mixed state. From here onwards, we do not use the overbar symbols to represent the dimensionless quantities for the sake of ease in the presentation.

3.1.5 Solution Methodology: Stream-Function/Vorticity Approach, Computational Domain, and Boundary Conditions

In the present study, to solve the governing equations viz., the PB equation [Eqs. (3.1a)-(3.1b)], Laplace equation for the applied electric field [Eq. (3.2)], Momentum and continuity equation [Eqs. (3.7)-(3.9)] and species transport equation [Eq. (3.11)], we use our in-house code consistent with the finite difference method. Important to mention, we invoke the stream-function/vorticity approach for the solution of momentum equations, as discussed in the next sub-section.

3.1.5.1 Stream-Function/Vorticity Approach

In the stream-function/vorticity approach, the momentum and continuity equations [Eqs. (3.7)-(3.9)] are converted into the stream function equation and vorticity equation.

The procedure is comprehensively discussed in the refereed literature (Patankar, 1980). The key point in appealing to this method is to avoid the tedious calculation of the pressure gradient and satisfy the continuity in the computational domain (Hsu, 1981). We write the dimensionless form of the stream-function/vorticity equation for the present analysis as:

$$u = \frac{\partial \psi_s}{\partial y} \text{ and } v = -\frac{\partial \psi_s}{\partial x} \tag{3.13}$$

$$\omega_v = \frac{\partial v}{\partial x} - \frac{\partial u}{\partial y} = -\left(\frac{\partial^2 \psi_s}{\partial x^2} + \frac{\partial^2 \psi_s}{\partial y^2} \right) \tag{3.14}$$

Electrolyte layer

$$\begin{aligned} \mathrm{Re}\left(u\frac{\partial \omega_v}{\partial x} + v\frac{\partial \omega_v}{\partial y} \right) = \frac{\partial^2 \omega_v}{\partial x^2} + \frac{\partial^2 \omega_v}{\partial y^2} + \frac{\partial}{\partial x}\left[\kappa^2 \sinh(\psi)\left(-\frac{\partial \phi_A}{\partial y} \right) \right] \\ - \frac{\partial}{\partial y}\left[\kappa^2 \sinh(\psi)\left(-\frac{\partial \phi_A}{\partial x} \right) \right] \end{aligned} \tag{3.15a}$$

Polyelectrolyte and polymeric patch

$$\begin{aligned} \mathrm{Re}\left(u\frac{\partial \omega_v}{\partial x} + v\frac{\partial \omega_v}{\partial y} \right) = \frac{\partial^2 \omega_v}{\partial x^2} + \frac{\partial^2 \omega_v}{\partial y^2} + \frac{\partial}{\partial x}\left[\kappa^2 \sinh(\psi)\left(-\frac{\partial \phi_A}{\partial y} \right) \right] \\ - \frac{\partial}{\partial y}\left[\kappa^2 \sinh(\psi)\left(-\frac{\partial \phi_A}{\partial x} \right) \right] - \alpha^2 \omega_v \end{aligned} \tag{3.15b}$$

In Eqs. (3.13)-(3.15), ψ_s and ω_v are the dimensionless stream function and vorticity, respectively. Using this set of equations [Eqs. (3.13)-(3.15)], we obtain the velocity distribution in the channel. The computational domain and the boundary conditions used to solve the governing equations are discussed in the next sub-section.

3.1.5.2 Computational Domain and Boundary Conditions

In Fig. 3.2, we schematically show the computational domain, including the transport equations of the present study. Figure 3.2(a) describes equations used for the electrostatics while the stream-function/vorticity equation [Eqs. (3.13)-(3.15)] is depicted in Fig. 3.2(b). Note that the Laplace equation for the applied electric field [Eq. (3.2)] and species transport equation [Eq. (3.11)], do not require interface boundary condition as they are homogenous in the entire computational domain. The interfaces I_1 and I_2 (represented by a thick straight line) in Figs. 3.2(a) and 3.2(b) correspond to only the PB equation [Eqs. (3.1a)-(3.1b)] and stream-function/vorticity equation [Eqs. (3.13)-(3.15)], respectively. The dashed lines in Figs. 3.2(a) and 3.2(b) represent the virtually absent interface while solving the corresponding equations. They do not exist while solving the PB equation and stream-function/vorticity equation, respectively. The regions separated by these virtual interfaces

have continuity in variables of the respective equations, i.e., PB equation [Eqs. (3.1a)-(3.1b)] in Fig. 3.2(a) and the stream-function/vorticity model [Eqs. (3.13)-(3.15)] in Fig. 3.2(b). Now using this terminology, we define the boundary conditions as follows.

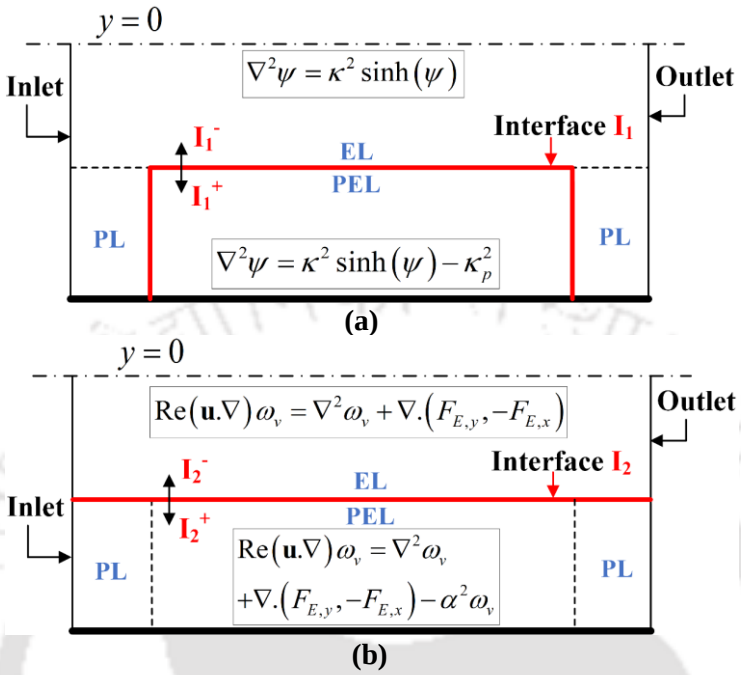

Figure 3.2: Schematics show the computational domain for (a) PB equation and (b) stream-function/vorticity equation. The interfaces- I1 and I2 (represented by a thick straight line) in schematics (a) and (b) correspond to the interface boundary conditions applied for solving the PB equations [Eq. (3.1)] and the stream-function/vorticity model [Eqs. (3.13)-(3.15)], respectively. In schematic (a), '$I1^{-}$' indicates the combined EL and PL region, while '$I1^{+}$' represents the PEL region only. Similarly, in a schematic (b), '$I2^{-}$' indicates the EL region only while '$I2^{+}$' represents the combined PEL and PL region. Note: (i) The interfaces represented by the dashed lines in both (a) and (b) do not play any role as the regions separated by them have continuity in variables of respective equations, i.e., PB equation [Eqs. (3.1)] and stream-function/vorticity model [Eqs. (3.13)-(3.15)]. (ii) For ease in the presentation, we have shown only one PEL patch.

Induced electrostatic potential distribution. To solve the induced electrostatic potential, we use no-flux condition at the inlet and outlet $\partial\psi/\partial x = 0$, and at the upper and lower walls of the channel $\partial\psi/\partial y = 0$. The first boundary condition stems from the fact that the polyelectrolyte layer does not establish any axial charge distribution in x-direction at the inlet and outlet. The second boundary condition is the zero flux condition at $y = \pm 0.5$ as the walls are assumed to be uncharged in this analysis (Chanda et al., 2014; A. Sadeghi, 2018b). At the interface- I_1 (refer to Fig. 3.2(a)), we use the continuity in the electrostatic potential $\left(\psi|_{I_1^-} = \psi|_{I_1^+}\right)$ and the gradient of the electrostatic potential $\left(\partial\psi/\partial\hat{n}|_{I_1^-} = \partial\psi/\partial\hat{n}|_{I_1^+}\right)$. Note that $\hat{n}$ represents the normal at the interface-I_1, i.e., in x

direction, $\hat{n} = x$, whereas in y direction $\hat{n} = y$.

Applied electrostatic potential distribution. For applied electrostatic potential distribution, we consider a no-flux condition at the upper and lower walls, i.e., $\left(\partial\phi_A/\partial y\right)\big|_{y=\pm 0.5} = 0$, whereas, at the inlet and outlet, we specify the applied electrostatic potential $\phi_A\big|_{x=0} = 0$ and $\phi_A\big|_{x=L} = L$. Note that, here, L is the dimensionless length, non-dimensionalized by $2H$.

Velocity distribution and stream-function/vorticity equation. To solve the flow dynamics, we specify velocity boundary condition at the inlet of the channel, i.e., $u = U_{in}$; $v = 0$; $\partial\psi_s/\partial y = U_{in}$; $\omega_v = -\partial^2\psi_s/\partial x^2$. At the outlet of the channel, we consider a fully-developed condition as $\partial u/\partial x = 0$; $\partial v/\partial x = 0$; $\partial^2\psi_s/\partial x^2 = 0$; $\partial\omega_v/\partial x = 0$. At upper and lower walls of the channel, a no-slip condition is considered, i.e., $u = 0$; $v = 0$; $\psi_s = U_{in}$; $\omega_v = -\partial^2\psi_s/\partial y^2$ and at the interface- I_2 (refer to Fig. 3.2(b)), we consider the continuity in the velocity field: $(u,v)\big|_{I_2^-} = (u,v)\big|_{I_2^+}$; $\psi_s\big|_{I_2^-} = \psi_s\big|_{I_2^+}$; $\omega_v\big|_{I_2^-} = \omega_v\big|_{I_2^+}$ as well as the gradient of the velocity at the interface-I_2: $\partial(u,v)/\partial\hat{n}\big|_{I_2^-} = \partial(u,v)/\partial\hat{n}\big|_{I_2^+}$; $\partial\psi_s/\partial\hat{n}\big|_{I_2^-} = \partial\psi_s/\partial\hat{n}\big|_{I_2^+}$; $\partial\omega_v/\partial\hat{n}\big|_{I_2^-} = \partial\omega_v/\partial\hat{n}\big|_{I_2^+}$.

Species transport. While solving the species transport, we consider the Dirichlet boundary condition at the inlet of the channel, i.e., $c_{x=0} = 0$ for $0 \le y \le 0.5$; and $c_{x=0} = 1$ for $-0.5 \le y \le 0$. At the outlet of the channel, we consider the first gradient of concentration to be equal to zero, i.e., $\partial c/\partial x\big|_{x=L} = 0$, whereas, at the upper and lower wall of the channel, a no-flux boundary condition $\partial c/\partial y\big|_{y=\pm 0.5} = 0$ is considered.

3.2 Flow Dynamics

3.2.1 Significance of the Physical and Geometrical Parameters of the System

In the present study, the inlet velocity U_{in} is an important parameter from the perspective of setting vortical flow (defined next) in the channel. The strength of the vortices depends on the magnitude of inlet velocity U_{in} and the magnitude of local EOF at the PEL patch. For a given strength of the applied electric potential ϕ_A and induced electric

potential ψ, a relatively higher U_{in} might dominate the strength of local EOF being developed in the opposite direction to the primary flow and hence, suppress the vortex formation as well as their strength at the PEL patches. *Therefore, for adequate vortical flow, the* u_{HS} *at the patched sections should be higher than* U_{in}. *On the contrary, the reasonably higher* U_{in} *is necessary for quick transportation of samples, ensuring rapid analysis in LOC platform.* Accounting these two aspects in tandem, we consider the range of U_{in} as 0.05 to 0.15. Note that this range of U_{in} is consistent with the microset-up and has been considered in the literature as well (Mondal, DasGupta, et al., 2014; X.-P. Wang et al., 2008). Next, to find the range of Reynolds number (Re) and Schmidt number (Sc), we consider the properties of universal solvent 'water' which are mentioned in the preceding chapter (Chapter 2). The diffusivities of the neutral species in streams A and B are of the order of 10^{-12} m^2/s (Bird et al., 2006), while the order of Smoluchowski velocity can be estimated as 10^{-5} m/s (J H Masliyah & Bhattacharjee, 2006; R. J. Hunter, 1981). For this set of parameters, the Reynolds number ranges from 10^{-2} to 10^{-4}, while the Schmidt number varies from 10^4 to 10^6.

Note that the significance of the remaining parameters, which are most pertinent with the PEL modulated electrohydrodynamics, is already discussed in the previous Chapter 2: Section 2.2.2. However, in interest to achieve the designated aim of the present study, the values or range of these parameters can be defined as DH parameter of EL $\kappa \in$ [5, 20], DH parameter of PEL κ_p = 10, PEL thickness $d \in$ [0.05, 0.2]

3.2.2 Model Benchmarking and Grid Dependence Study

Comparison of the present method with the COMSOL Multiphysics software. In Fig. 3.3(a), we compare our results with those obtained from the finite element method (FEM) based solver COMSOL Multiphysics™. While modelling the problem in COMSOL framework, we have used the same set of transport equations and boundary conditions as detailed in Section 3.1.5. The chosen mesh counts (22582) in COMSOL solver ensure greater accuracy of the results. In Fig. 3.3(a), the results of the present modelling framework show both qualitative and quantitative agreement with the results of COMSOL solver.

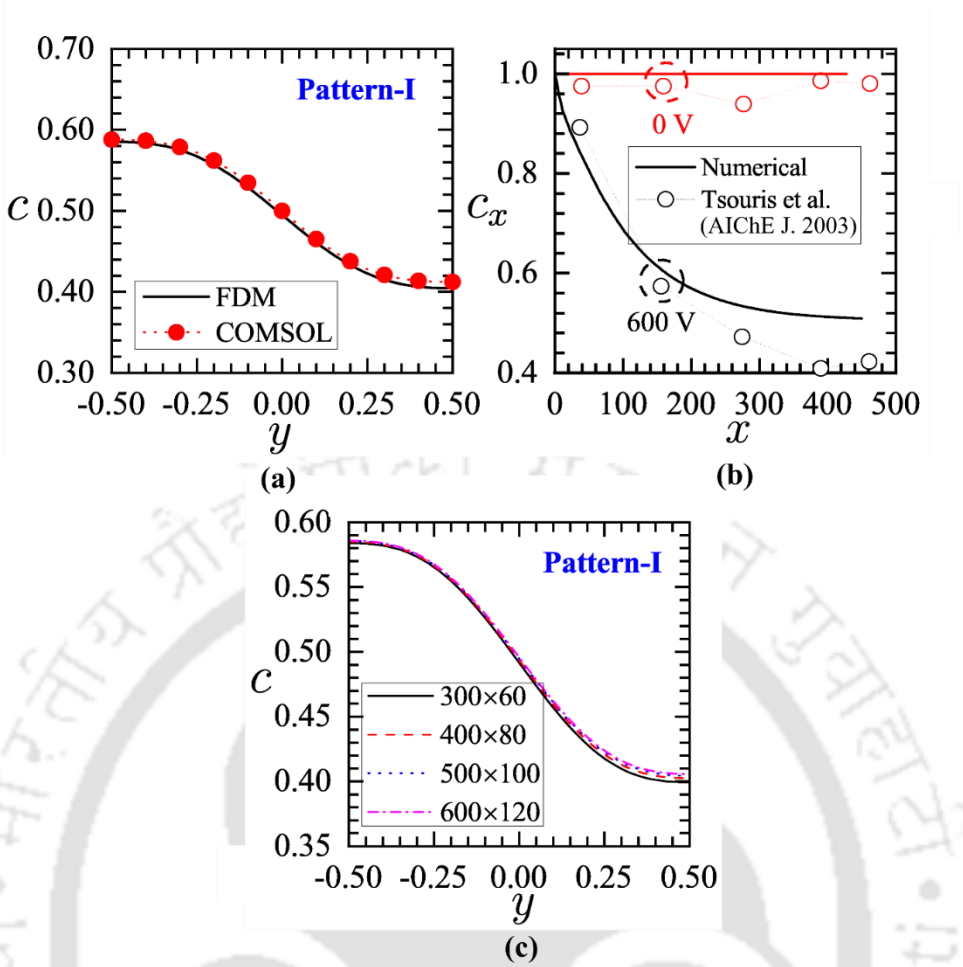

Figure 3.3: (a) Validation with FEM: Plots in (a) show the comparison between the concentration profiles obtained from the FDM and FEM (COMSOL) methods. The profiles are obtained at the outlet of the channel, i.e., at $x = 5$. The other parameters are: $U_{in} = 0.1$, $\mathrm{Re} = 10^{-3}$, $\mathrm{Sc} = 5\times10^{5}$, $\kappa = 15$, $d = 0.1$, $\alpha = 10$ and $\kappa_p = 10$. (b) Experimental validation: Plots in Fig. (b) show the validation of the present study with the experimental results of Tsouris et al. (2003) (Tsouris et al., 2003). The results are obtained for 0 V and 600 V. (c) Grid dependence study: Plots in Fig. (c) show the concentration c versus y coordinate, obtained for different grid points used viz. 300x60, 400x80, 500x100 and 600x120. The other parameters are: $U_{in} = 0.1$, $\mathrm{Re} = 10^{-3}$, $\mathrm{Sc} = 5\times10^{5}$, $\kappa = 15$, $d = 0.1$, $\alpha = 10$ and $\kappa_p = 10$.

Experimental validation. We compare in Fig. 3.3(b) the axial variation of species concentration obtained from the present mathematical model with the experimental results of Tsouris et al. 2003 (Tsouris et al., 2003). In the reported study (Tsouris et al., 2003), authors have investigated the mixing of pure butanol and butanol with a suspension of dye-Rhodamine-b in a '**T**' shaped rigid microchannel under the influence of combined pressure-driven and electroosmotic effects. Following the reported values, we consider that the mean flow speed is 24.5 mm/s. In order to mimic a rigid channel as considered in the reported study (Tsouris et al., 2003), the thickness of PEL and PL is taken as zero in our model.

Albeit, our results match well with the reported experimental results of Tsouris et al. 2003 (Tsouris et al., 2003), a slight deviation is seen in the variation. We attribute this deviation to the effect of disturbed flow at the '**T**' junction, which has been detailed by the authors in their reported analysis as well (Tsouris et al., 2003).

Grid dependence study. The plots depicted in Fig. 3.3(c) show the variation of concentration profile obtained for the different number of grid points $N_x \times N_y$ = 300x60, 400x80, 500x100 and 600x120. Note that N_x and N_y are the number of grid points in the x and y directions, respectively. From Fig. 3.3(c), it can be concluded that the difference between the profiles becomes negligibly small, with a change in the number of grid points, from 500x100 to 600x120. Accordingly, we have considered the number of grid points for the present computations as 500x100.

3.2.3 Electrostatic Potential Distribution

The contour plots in Figs. 3.4(a)-(d) depict the distribution of induced electrostatic potential ψ. We observe in Figs. 3.4(a)-(d) that the magnitude of ψ takes a higher value at the patched sections, while in the remaining domain, demarcated as the electroneutral region, it decays to zero. This observation points towards the presence of PEL patches at the walls. The local EDL formed at each PEL patch contributes to establishing a heterogeneous distribution of ψ, as witnessed in Figs. 3.4(a)-(d).

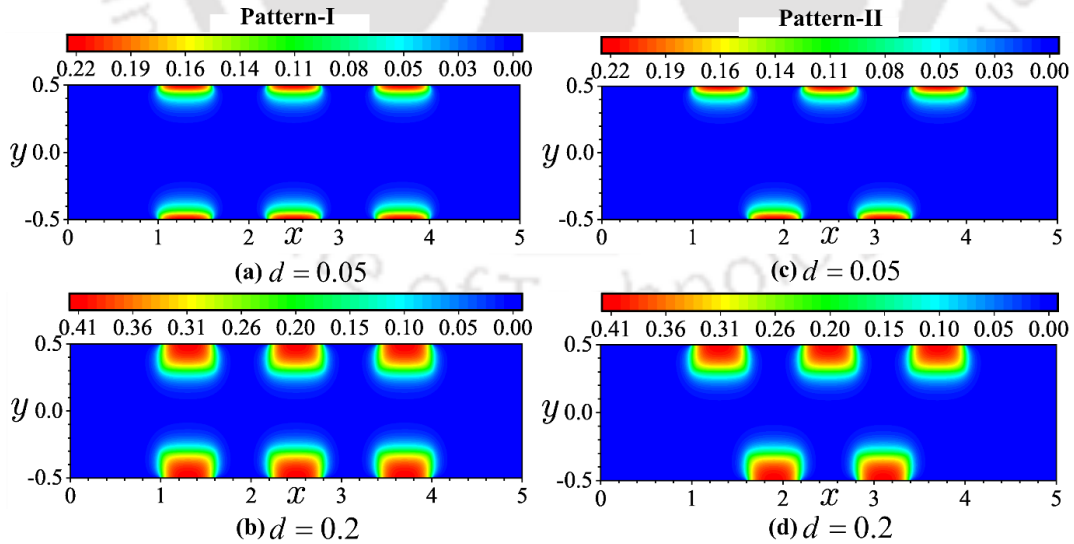

Figure 3.4: Contour plots in (a)-(d) show the distribution of induced electrostatic potential ψ for both the patterns, pattern-I [(a) and (b)] and pattern-II [(c) and (d)]. The plots are obtained for: (a) and (c) $d = 0.05$ and; (b) and (d) $d = 0.2$. The other parameters are: $\kappa = 15$ and $\kappa_p = 10$.

It is also observed in Figs. 3.4(a)-(d) that, in addition to the enhancement in the Debye length, an increment in the PEL thickness d also results in an enhancement in ψ in the patched section. In the soft narrow-fluidic channel, the increasing PEL thickness d promotes the electrostatic interactions among the polyelectrolyte and electrolyte ions. The higher electrostatic interactions lead to a higher magnitude of ψ and an increase in the Debye length, as observed in Figs. 3.4(a)-(d).

3.2.4 Velocity Distribution

3.2.4.1 Formation of Recirculation Zones: Momentum Exchange Phenomenon

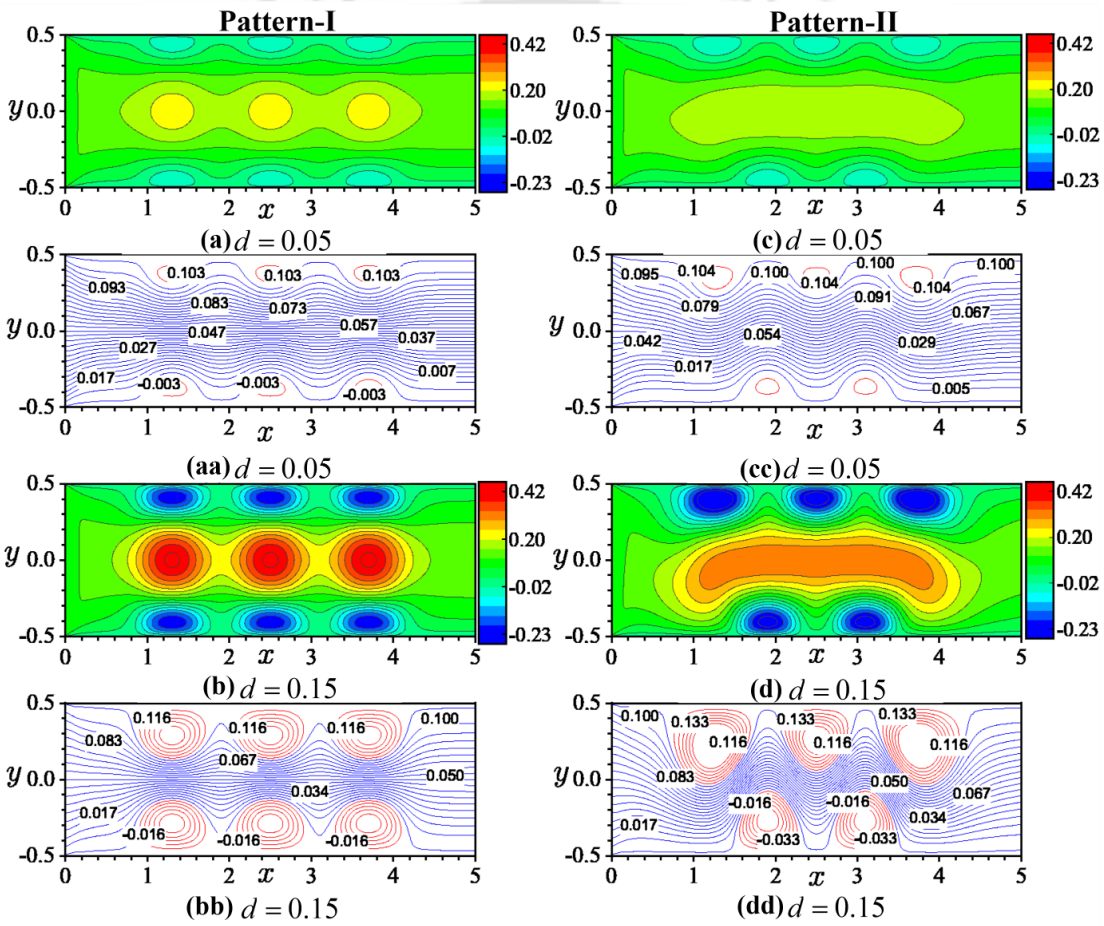

Figure 3.5: (a)-(d) Velocity contours: Contour plots show the velocity distribution for both the patterns, pattern-I and pattern-II, obtained for different values of PEL thickness d (= 0.05 and 0.15). The other parameters considered for this analysis are: $U_{in} = 0.1$, $\mathrm{Re} = 10^{-3}$, $\mathrm{Sc} = 5\times10^{5}$, $\kappa = 15$, $\alpha = 10$ and $\kappa_p = 10$. (aa)-(dd) Stream function contours: Contours of stream function for both the patterns, pattern-I and pattern-II, obtained for different values of PEL thickness d (= 0.05 and 0.15). The other parameters are: $U_{in} = 0.1$, $\mathrm{Re} = 10^{-3}$, $\mathrm{Sc} = 5\times10^{5}$, $\kappa = 15$, $\alpha = 10$ and $\kappa_p = 10$.

We plot in Figs. 3.5(a)-(d) and Figs. 3.5(aa)-(dd) the contour of u-velocity and

stream function, respectively, for pattern-I and pattern-II configurations. The depicted variations are obtained for different values of PEL thickness d = 0.05 and 0.15.

In Figs. 3.5(a)-(d), we observe that the u-velocity is positive in the electroneutral region, while it is negative in the patched section. We attribute this observation to the electroosmotic effect that stems due to the local EDL phenomenon. In the present study, PEL patches establish an EDL in the PEL matrix and give rise to an electroosmotic force. This electroosmotic body force, together with the Darcy drag acts as a resistive force to the primary flow. The onset of EOF at the patched section is supported by a negative flow velocity therein (Figs. 3.5(a)-(d)), while the flow velocity becomes positive in the remaining domain. On account of this phenomenon, the main flow experiences a loss in the axial momentum and establishes a recirculation zone near the PEL patch (Figs. 3.5(aa)-(dd)). Such channel flow with a rolling-up structure of the vortices is termed as the *vortical flow* (Bag & Bhattacharyya, 2018), as defined before. It is worth to add, this mechanized vortical flow formed at the PEL patch enforces the fluid towards the electroneutral region and forms a tortuous flow pattern (cf. Figs. 3.5(a)-(d)).

3.2.4.2 Flow Structures: Comparison Between Pattern-I and Pattern-II

As seen in Figs. 3.5(a)-(d), the magnitude of flow velocity, including its maximum and minimum value, is different for pattern-I and pattern-II. In pattern-I, on account of the symmetricity of the grafted patches, the main flow experiences resistance in a symmetric manner, and hence, the vortices formed at the patched section are identical to each other as witnessed in Figs. 3.5(aa) and 3.5(bb). Whereas, for pattern-II, the resistance offered to the mainstream flow by PEL patches is asymmetric, and hence, the structure of vortices is not identical (cf. Figs. 3.5(cc)-(dd)). As a consequence, in pattern-I, the formed vortices at any wall experience a *face-to-face* resistance to the vortices being formed at the other wall (cf. streamlines in Figs. 3.5(aa) and 3.5(bb)). Thus, the vortices get compressed to the wall in case of pattern-I (Figs. 3.5(aa) and 3.5(bb)). Therefore, the size and strength of the vortices for all values of d are found to be smaller for pattern-I than pattern-II (Figs. 3.5(aa)-(dd)). Important to mention, such interaction of neighbouring vortices is comparatively lesser in pattern-II as compared to pattern-I. Notably, the size of the asymmetric vortices for pattern-II is extended up to the center of the channel, whereas for pattern-I, they are confined to the channel walls. This asymmetric structure of vortices formed at the PEL patch for pattern-II not only opposes the mainstream flow therein but also provides resistance to the

main flow in the middle section of the channel, as seen in Figs. 3.5(a)-(d). On the other hand, for pattern-I, the symmetric structure of vortices restricts this resistance to the main stream flow in the patched section only. As a result, the upstream fluid velocity at the patched section is higher for pattern-II, while downstream fluid velocity at the electroneutral region is higher for pattern-I, as confirmed in Figs. 3.5(a)-(d).

In addition to these insights, we observe in Figs. 3.5(a)-(d) that with an increment in the PEL thickness d, the downstream fluid velocity (mainly due to inlet flow velocity) in the electroneutral region, as well as upstream fluid velocity (solely due to electroosmotic effect) in the PEL patches, get enhanced. In the soft narrow-fluidic channel, the PEL thickness is a leading factor for the modulation of the underlying electrohydrodynamics. As discussed before in Section 3.2.3, an increase in the size of the polyelectrolyte layer primarily leads to the enhancement in the magnitude of electrostatic potential ψ in the EDL. As a result, the electroosmotic body force acting in the PEL patch increases for a given strength of the applied electric field $\left|-\nabla\phi_A\right|$. The higher electroosmotic body force results in the enhanced upstream flow velocity as evident in Figs. 3.5(a)-(d). This enhancement in upstream velocity with increasing d further accelerates the momentum exchange phenomenon and leads to an increment in the strength as well as the size of the vortices at the patched section (see Figs. 3.5(aa)-(dd)). Notably, this enhancement in the vortex size further causes an effective squeezing of the *stream-tube* in the middle section of the channel. This effect leads to a higher downstream fluid velocity in the electroneutral region, as one can find in Figs. 3.5(a)-(d). *Thus, the unique feature of the present flow configuration promotes mixing efficiency without compromising the net flow velocity in the fluidic pathway.*

It is important to mention here that the vortex profile, as shown in Figs. 3.5(aa)-(dd) largely conforms to the Lamb vortex profile. In addition, pattern-II shows a non-trivial dynamics of Lamb vortices which is absent in pattern-I as the *face-to-face* approaching kinetics in pattern-I limits the formation of the non-trivial structure of Lamb vortices in the channel. To be precise, the asymmetric nature of Lamb vortex formation causes the vertical and lateral shift of vortex centroids in the channel for pattern-II.

3.2.4.3 Vortex Shifting Phenomenon: Effect of the PEL Thickness d

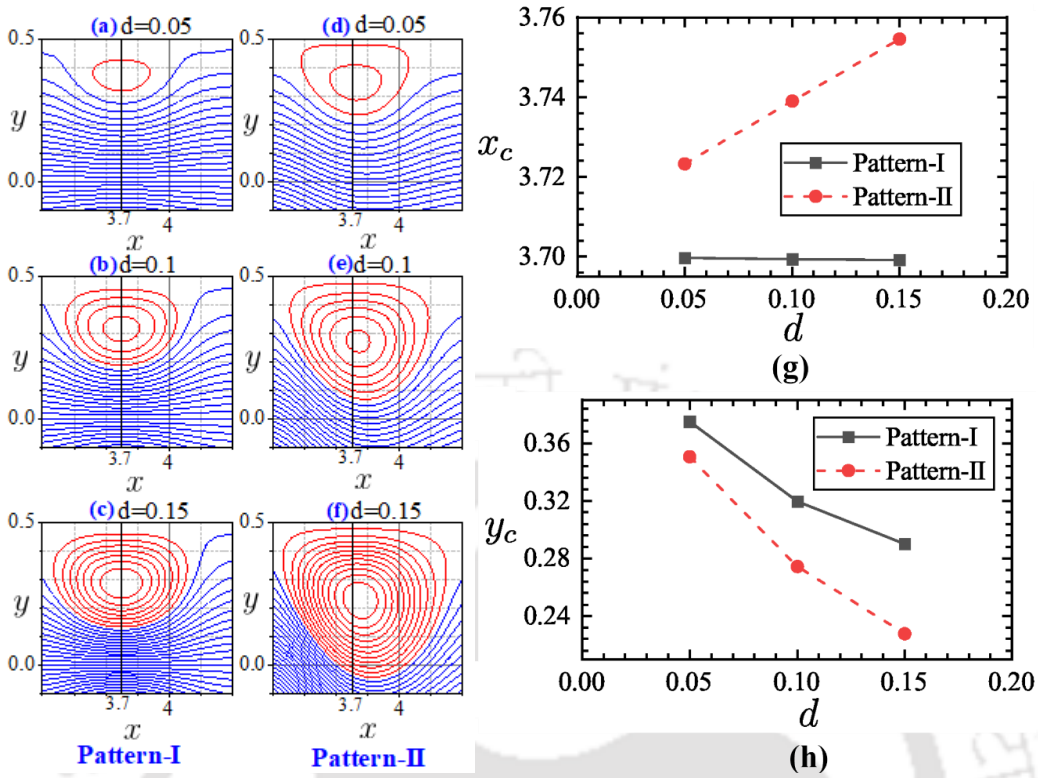

Figure 3.6: (a)-(f) Qualitative analysis of vortex shifting (Panel-A): Contour plots in (a)-(c) and (d)-(f) show the zoomed-in view of recirculation zones for pattern-I and pattern-II, respectively. The plots are obtained at the upper wall for PEL patch grafted at x = 3.7, for different values of PEL thickness d(= 0.05, 0.1, and 0.15). The other parameters are $\kappa = 15$, $\kappa_p = 10$, $\alpha = 10$, Sc = 5×10^5, Re=10^{-3} and $U_{in} = 0.1$. (g)-(h) Quantitative analysis of vortex shifting (Panel-B): The line plots in (g) and (h) show the variation in the x location and y location of the vortex centroid, respectively. The plots are obtained for both the patterns: pattern-I and pattern-II, with the variation in the PEL thickness d.

In Figs. 3.6(a)-(h), we quantify the vortex dynamics as realizable through the loci of their centroids. We observe in Figs. 3.6(a)-(h) that, for the higher value of PEL thickness d = 0.15, the vertical shift in the centroid of the vortex is high for pattern-II. Here, the PEL thickness is a contributing factor for the strength and the size of the recirculation zones being formed. Accountingly, the size and height of the vortices are expected to increase with an increment in PEL thickness d. (Height of the vortex refers to the distance of its centroid from the nearest wall). However, for the case of pattern-I, the vortices shed on the lower wall approach to those of the upper wall in a *face-to-face* mode as they are symmetric about the channel centerline. Notably, this *face-to-face* approaching kinetics of vortices limits the shifting of the centroid (both lateral and vertical) with a variation in PEL thickness d as seen in Figs. 3.5(aa)-(dd), Figs. 3.6(a)-(c) and Fig. 3.6(h). Whereas in pattern-II configuration, the asymmetric formation of vortices prohibits them from

approaching via the *face-to-face* mode.

As such, this unobstructed dynamics of the vortices for pattern-II configuration allow them to expand towards the central region of the channel (see Figs. 3.6(d)-(f)). Therefore, for pattern-II configuration, we observe a significant vertical shift in the centroid of the vortices with an increment in PEL thickness d, as witnessed in Figs. 3.6(d)-(f). Further, this asymmetric flow structure in pattern-II configuration creates the distorted streamlines in the flow field, presented in Figs. 3.5(cc)-(dd). Consequently, for pattern-II, the diverted flow field around any vortex disturbs the formation of the vortex at the next consecutive position, causing a lateral stretching in particular (cf. Fig. 3.6(g)). Moreover, with an increment in PEL thickness d, this lateral displacement intensifies (see Fig. 3.6(g)), primarily attributed to the enhancement of electroosmotic flow strength.

3.2.4.4 Lamb Vortex Profile: A Critical Review of the Velocity Distribution

In continuation of our discussion elaborated in the preceding section, we now discuss the effect of different governing parameters on the vortical flow. We show in Figs. 3.7(a)-(b) the velocity profiles at an axial location $x = 3.7$ for different values of drag parameter α (= 1, 10, and 100) and DH parameter of electrolyte κ (=5, 10, and 20), respectively. Note that the comparison between patterns I and II is already discussed in previous sections.

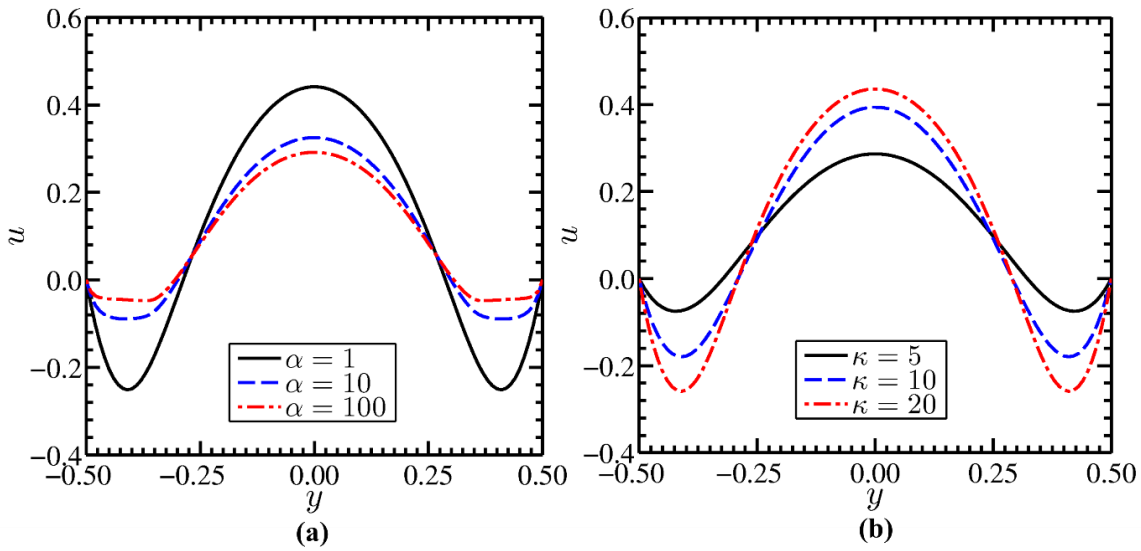

Figure 3.7: Plots show the velocity distribution for different values of (a) drag parameter α (= 1, 50 and 100) and (b) DH parameter of EL κ (= 5, 10 and 20) in pattern-I. The other parameters are (a) d = 0.15, κ = 15, κ_p = 10, Sc = 5×10^5, Re=10^{-3}, U_{in} = 0.1; (b) d = 0.15, α = 10, κ_p = 10, Sc = 5×10^5, Re=10^{-3}, U_{in} = 0.1. The profiles are obtained at the PEL patch located at x = 3.7.

We observe in Fig. 3.7(a) that, with an increment in α, the magnitude of fluid velocity in both upstream and downstream directions reduce. The grafted polyelectrolyte and polymeric macromolecules apply Darcy's frictional drag to the underlying transport. The magnitude of this drag is proportional to the grafting density of the PEL or PL (Chen & Das, 2016, 2017). Thus, an increment in the drag parameter fundamentally signifies an augmentation in the grafting density of polyelectrolyte and polymeric chains grafted on the walls of the channel. The effect of the frictional resistance for higher α extends to the entire domain of the channel. Thus, the overall effect of higher α results in a reduction in fluid velocity (upstream and downstream), as seen in Fig. 3.7(a).

In the present study, the strength of the local EOF increases with a reduction in κ. This increase in localized EOF is expected to increase the strength of the recirculation zones. Important to mention here that the higher recirculation strength compresses the fluid layers at the middle section of the channel (as discussed before), and leads to an augmentation in higher downstream flow velocity therein. Notably, the observations obtained from Fig. 3.7(b) contradicts our anticipation of having higher flow velocity in both the upstream and downstream directions with a reduction in κ. Notably, a decrease of κ from 20 to 5 has two significant effects to discuss in the purview of the present scenario. First, the magnitude of induced electrostatic potential increases. Second, a decrease in κ results in the overlapping EDLs being formed at the opposite walls. This overlapping phenomenon gives rise to even a non-zero value of the induced electrostatic potential at the center of the channel. As a consequence of this effect, the electroosmotic force acts as an opposing force in the entire domain for $\kappa = 5$. It is because of this overlapping phenomenon, the fluid velocity becomes very small for $\kappa = 5$ in both directions, as seen in Fig. 3.7(b). For the cases of higher κ, the *near-wall effect*[10] influences the main stream flow in the patched sections only and generate the recirculation zones.

3.3 Analysis of Mixing Performance

Having discussed the flow dynamics in detail, we now make an effort to understand the mixing performance in the channel. In Figs. 3.8(a)-(c), we show the concentration profiles for different values of (a) drag parameter α (= 1, 10 and 100), (b) DH parameter of EL κ (= 5, 10 and 20), and (c) PEL thickness d (= 0.05, 0.1 and 0.15). In Fig. 3.8(d),

[10] The '*near-wall effect*' refers to the confined effect of electrohydrodynamics near the walls of the channel.

we compare the concentration profiles of pattern-I and pattern-II. The insets of Figs. 3.8(a)-(d) show the contours of concentration for different pertinent parameters and patterns. The other parameters considered for the plotting are mentioned in the caption. It is worth mentioning here that the profiles in Figs. 3.8(a)-(c) are obtained at the outlet of the channel, while those in Fig. 3.8(d) are obtained for the patch located at $x = 3.7$. The depicted profiles describe the effectiveness of pattern-II configuration over pattern-I in the context of mixing efficiency. Note that in line with our proposition outlined above, the depicted variations in Fig. 3.8(d) underlines that the chances of achieving efficient mixing at the earliest section of the channel are higher for pattern-II configuration. In Figs. 3.8(a)-(d), the distorted contours signify the presence of the PEL patch at the wall. It is to be noted that, in the absence of PEL patches, the contours would have followed the direction of the pressure-driven flow only. However, the highly distorted contours in Figs. 3.8(a)-(c) is suggestive of the presence of PEL patch (for pattern-I at x = 1.3, 2.5, and 3.7). Note that the asymmetric distortion in Fig. 3.8(d) is due to the asymmetric nature of pattern-II.

3.3.1 Influence of Governing Parameters

Influence of the drag parameter **(α).** It is observed from Fig. 3.8(a) and in the inset therein that, the value of c for $\alpha = 1$ is nearly equal to 0.5, whereas, for α = 50 and 100, it deviates from the fully mixed state ($c \neq 0.5$). The contours of the concentration shown in the inset of respective figures witness the depicted variations. Albeit intuitive, we do mention here that, for approaching the perfectly mixed conditions, i.e., $c = 0.5$, the present system demands relatively larger recirculation zones to increases the retention time of the participating species. Notably, in case of higher values of α (= 50, 100), the relatively higher frictional drag reduces the upstream flow strength, and hence the size and strength of the Lamb vortex decreases. With increasing α, the strength of both the downstream pressure-driven flow and upstream local electroosmotic flow gets reduced, attributed to the higher flow resistance due to the higher drag force. It is because of this higher drag for higher α (= 50, 100), the strength of the momentum exchange phenomenon gets reduced and results in a reduction in the vortex strength. Whereas for $\alpha = 1$, the confined frictional drag at the PEL patch makes the scenario favourable for the formation of adequate vortices as confirmed through the Lamb vortex velocity profile in Fig. 3.7(a). In Fig. 3.7(a), the upstream and downstream velocity is higher for $\alpha = 1$. Eventually, the reduction in the drag parameter α from 100 to 1 increases the retention time and the mixing performance, as

observed in Fig. 3.8(a) and in the contours shown in the inset therein.

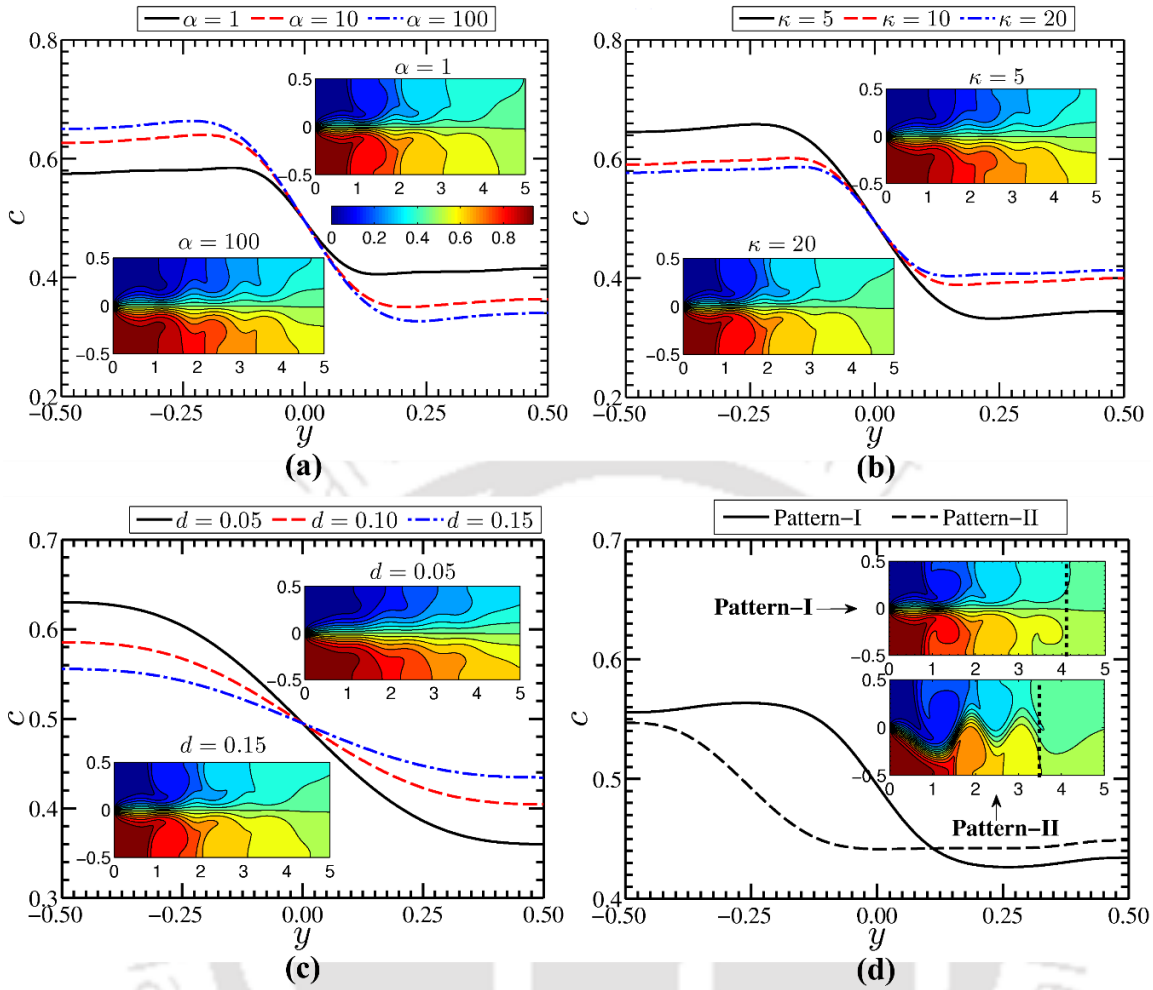

Figure 3.8: (a)-(c) Influence of governing parameters: Concentration profiles for pattern-I, obtained for different values of (a) drag parameter α (= 1, 10 and 100), (b) DH parameter of EL κ (= 5, 10 and 20) and PEL thickness d (= 0.05, 0.1 and 0.15). The profiles are obtained at the outlet, i.e., x = 5. (d) Influence of pattern architecture: Concentration profiles for pattern-I and pattern-II, obtained for d = 0.2 at x = 3.7. The other parameters considered for this analysis are: (a) $\kappa = 15$, $\kappa_p = 10$, $d = 0.15$, $Sc = 5\times10^5$, $Re=10^{-3}$, $U_{in} = 0.1$; (b) $\kappa_p = 10$, $d = 0.15$, $\alpha = 10$, $Sc = 5\times10^5$, $Re=10^{-3}$, $U_{in} = 0.1$; (c) $\kappa = 15$, $\kappa_p = 10$, $\alpha = 10$, $Sc = 5\times10^5$, $Re=10^{-3}$, $U_{in} = 0.1$; (d) $\kappa = 15$, $\kappa_p = 10$, $d = 0.2$, $\alpha = 10$, $Sc = 5\times10^5$, $Re=10^{-3}$, $U_{in} = 0.1$. The insets show the contours of concentration for different values of respective parameters and patterns. The vertical dotted lines in the insets of (d) indicate the vertical sections at a distance in the x direction from the inlet of the channel where the mixing occurs significantly ($\xi_m \geq 90\%$).

Influence of the DH parameter of EL **(κ).** Next, we observe in Fig. 3.8(b) and in the corresponding insets that with an increasing value of κ, the concentration at $x = 5$ becomes closer to 0.5. In the soft narrow-fluidic channel, a reduction in κ not only leads to a case of overlapping EDLs in the channel but also increases the magnitude of electrostatic potential ψ significantly. In fact, for the lower value of κ (= 5), we obtain a non-zero

electrostatic potential (overlapping EDLs) at the center of the channel. As a result, the electroosmotic force opposes the mainstream flow nearly in the entire domain of the channel, thus reducing the difference between the upstream and downstream flow. Whereas, for higher κ (= 20), it (electroosmotic velocity) opposes the downstream flow at the PEL patches only, generating a higher strength of the Lamb vortices (c.f inset of Fig. 3.8(b)) at the patched section. Consequently, higher retention time is obtained for $\kappa = 20$, and this higher retention time actively increases the mixing performance, as seen in Fig. 3.8(b) and insets of Fig. 3.8(b).

Influence of PEL thickness **(*d*).** It is observed in Fig. 3.8(c) and in the corresponding insets that, for the higher value of PEL thickness d (= 0.3), the concentration at the outlet nearly attains a value $c = 0.5$, whereas, for d = 0.1 and 0.2, it deviates from the fully mixed state (i.e. $c \neq 0.5$). In the soft narrow-fluidic channel, with an increment in PEL thickness, the local EOF at the patch increases and consequently gives rise to an increased momentum exchange between upstream and downstream flow, resulting in increased strength of recirculation zones at the patched sections. This phenomenon is realized by the increased size of the vortices and, consequently, by the shifting of the centroids with an increment of d in Figs. 3.5(aa)-(dd) and Figs. 3.6(a)-(h), respectively. As a result, the PEL thickness controlled flow dynamics increases the retention time of neutral species in streams A/B and leads to an enhancement in the mixing performance as realized by the contour profiles delineated in the insets of Fig. 3.8(d).

3.3.2 Influence of Pattern Architecture

In Fig. 3.8(d), we show the concentration profile for pattern-I and pattern-II. The insets show the concentration contours for the respective patterns. As observed in Fig. 3.8(d) and the inset therein, the value of c is close to 0.5 at $x = 3.7$ for pattern-II, while it deviates from 0.5 for pattern-I. Note that the plots are obtained at the patch located at $x = 3.7$. The *mixing length* is the axial location in the x- direction from the inlet of the channel, where the constituent streams significantly mix, i.e., the local mixing efficiency $\xi_m(x)$ reaches to 90%. In regard to that, we observe in the inset of Fig. 3.8(d) that for pattern-II, the mixing length is smaller than that of pattern-I. In Fig. 3.8(d), an expected mixing for pattern-I can be achieved at $x \sim 4.1$, whereas for pattern-II, it is achievable at $x \sim 3.5$ (refer to the vertical dotted lines shown in the insets of Fig. 3.8(d)). We attribute this difference in the mixing performance to the strength of the vortical zones obtained in

the channel. Notably, as observed in Figs. 3.5 and 3.6, the strength of the vortices is higher for pattern-II as compared to pattern-I. As a consequence, the retention time availed for the desired mixing of candidate species is sufficiently high for pattern-II. Therefore, a better mixing performance is obtained for pattern-II as compared to pattern-I, as witnessed in Fig. 3.8(d) and in the insets therein. This comparison is also graphically depicted in Fig. 3.9(b) wherein the variation in the mixing efficiency is shown along the x-direction for both the patterns I and II.

3.4 Practical Aspect of Novel Soft Micromixer

3.4.1 The Onset of Recirculation Zones

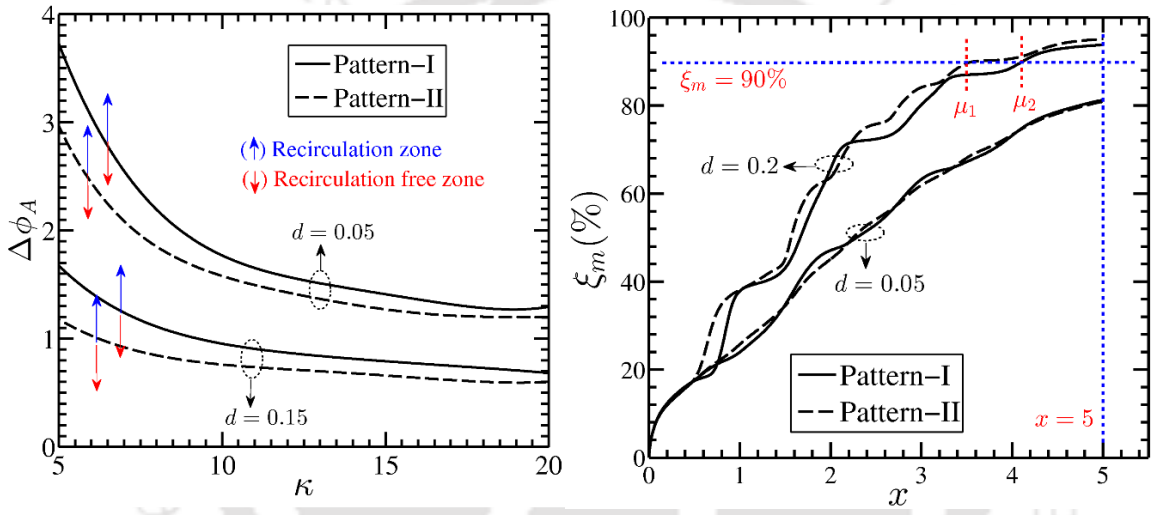

(a) **(b)**

Figure 3.9: (a) Onset of recirculation zones: Plots show the variation of horizontal applied electrostatic potential ($\Delta\phi_A$) with the DH parameter of EL (κ) for different values of PEL thickness d (= 0.05 and 0.15). A comparison between both the patterns, I and II are made. The other parameters are $\alpha = 10$, $\kappa_p = 10$, $Sc = 5\times10^5$, $Re=10^{-3}$ and $U_{in} = 0.1$. (b) Variation of mixing lengths: Plots show the variation in local efficiency with x for different d (= 0.05 and 0.2) and patterns, I and II. The horizontal dotted line shows $\xi_m = 90\%$, while the vertical dotted line show $x = 5$. The vertical dotted segments μ_1 and μ_2 on $\xi_m = 90\%$ line demarcates the mixing length of pattern-I and pattern-II for $d = 0.2$. The other parameters used for this analysis are $\kappa = 15$, $\kappa_p = 10$, $Re=10^{-3}$, $\alpha = 10$, $U_{in} = 0.1$. Note that the mixing length is the axial location from the inlet of the channel at which the local efficiency reaches 90%.

In the practical applications, for a fixed design of the soft micro-patterned mixer, the applied electric potential ϕ_A is the simplest tuning parameter to vary the strength and change the structure of the vortical flow. Taking a note on this aspect, we find here the strength of $\Delta\phi_A$ corresponding to the onset of the recirculation zone; and show in Fig. 3.9(a) the variation in $\Delta\phi_A$ versus the DH parameter of electrolyte κ. We consider PEL

thickness d (= 0.05 and 0.15) for Fig. 3.9(a), while both patterns are compared to see the underlying effect. At a particular value of $\Delta\phi_A$, the shear stress at the wall, particularly at the PEL patch, changes its sign due to the flow reversal phenomenon. It can be observed in Fig. 3.9(a) that with an increase in the value of κ (for fixed d) and d (for fixed κ), the magnitude of $\Delta\phi_A$ decreases. In present study, an increment in κ (for fixed d) and d (for fixed κ) favors the formation of vortical flow due to higher *near-wall effect* (refer to Fig. 3.7(b)) and an enhancement in the local EOF at the PEL patch (refer to Fig. 3.5), respectively.

Thus, an increase in the value of κ as well as d lowers the magnitude of $\Delta\phi_A$ as witnessed in Fig. 3.9(a). In addition to that, because of the asymmetric grafting in pattern-II, the *face-to-face* resistance offered by the vortices to each other is less for pattern-II. This feature enhances the onset of vertical flow in the pathway. Therefore, for pattern-II, the magnitude of $\Delta\phi_A$ is always less than that of pattern-I in Fig. 3.9(a). Moreover, on account of higher near-wall effect and lower Debye length for a higher value of κ (~20), we observe in Fig. 3.9(a) a negligible difference between the values of $\Delta\phi_A$ for pattern-I and II at $\kappa = 20$.

3.4.2 Variation in the Mixing Length

In the mixing phenomenon, the mixing length is also an important parameter from the perspective of the design of microassays. In the present study, the mixing length $x\big|_{(\xi_m=90\%)}$ is the axial location from the inlet of the channel at which the local mixing efficiency reaches 90% (Krishnaveni et al., 2017). In Fig. 3.9(b), we show the axial variation of local mixing efficiency for both the patterns obtained for d = 0.05 and 0.2. It is observed in Fig. 3.9(b) that the mixing length for higher PEL thickness $d = 0.2$ is lower than that of lower PEL thickness d = 0.05. We attribute this observation to the higher recirculation zones obtained due to higher EOF for $d = 0.2$. On account of the larger recirculation zone for $d = 0.2$, the concentration of the candidate neutral species can be retained (refer to Fig. 3.8(c)) at the earliest sections of the channel. This aspect is suggestive of the earliest efficient mixing. Notably, on account of higher PEL thickness $d = 0.2$, the mixing length of pattern-II is smaller than that of pattern-I, whereas for $d = 0.05$, they are almost the same. In the present study, higher PEL thickness renders adequate vortical flow in the channel [refer to Figs. 3.5 and 3.6]. Also, on account of asymmetric nature, the

vortical flow strength is comparatively higher for pattern-II than that of pattern-I. Therefore, as observed in Fig. 3.9(b) and in the inset of Fig. 3.8(d), the spatial efficiency is higher for pattern-II in the entire channel. This aspect is realized by the smaller mixing length for pattern-II configuration for a higher value of PEL thickness, i.e., $\mu_1 < \mu_2$. For thinner PELs $d = 0.05$, the strength of vortices is minimum; thus, the difference between the efficiencies and mixing lengths of pattern-I and pattern-II is insignificant. This aspect is reflected in Fig. 3.9(b) as well.

In the context of this discussion, it can be also stated here that the critical value of PEL thickness d at which the pattern-II starts to show a considerably minimum mixing length than that of the pattern-I is ~0.15. Therefore, in order to obtain comparatively a better mixing performance using pattern-II, the value of the PEL thickness should be higher than ~0.15. Nevertheless, an increment in the PEL thickness, carried out in order to enhance the mixing performance, even in case of pattern-I, should be restricted after certain limit. The reason behind setting such limit to an increment in the PEL thickness can be discussed as follows: in the present study, the PEL patches grafted on the walls of the channel establish a local electroosmotic flow that resists the mainstream pressure-driven flow. As a result, for a considerably higher thickness of the PEL, say up to the limit of approaching towards the case of inter-penetration of the PELs from the opposite walls of the channel, the electroosmotic flow (and the frictional drag force) may resist the pressure-driven flow in the entire channel cross-section and adversely influence the mixing. Therefore, an increment in the PEL thickness should be limited after certain limit. However, the estimation of such limit is beyond the scope of the present study as the stream-function/vorticity approach incorporated in the study may show erroneous results for a no-flow condition.

3.4.3 Effect of Spacing Between the PEL Patches

In the present study, the spacing between the PEL patches can also be a significant parameter that would induce variations in the mixing dynamics. The spacing between the PEL patches can be tuned by the modifications in the grafting techniques. However, while studying the effect of such parameter, the configurations of the pattern-I and pattern-II can be arranged in number of possible combinations. Therefore, for simplicity in the discussion, we have selected three different configurations which are given in the following (next page) Table 3.1.

Table 3.1: Three different configurations for each pattern, pattern-I and pattern-II, with corresponding variations in the dimensions are tabulated. Here, subscript 'u' stands for the upper wall, whereas subscript 'l' stands for the lower wall. All the fractions listed in the table are corresponding to the total length of the channel.

Pattern-I

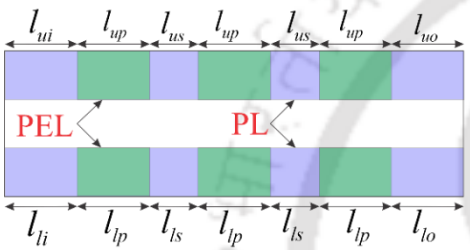

Configuration type	Upper wall				Lower wall			
	l_{ui}	l_{us}	l_{up}	l_{uo}	l_{li}	l_{ls}	l_{lp}	l_{lo}
A	5/25	3/25	3/25	5/25	5/25	3/25	3/25	5/25
B	6/25	2/25	3/25	6/25	6/25	2/25	3/25	6/25
C	13/50	1/25	3/25	13/50	13/50	1/25	3/25	13/50

Pattern-II

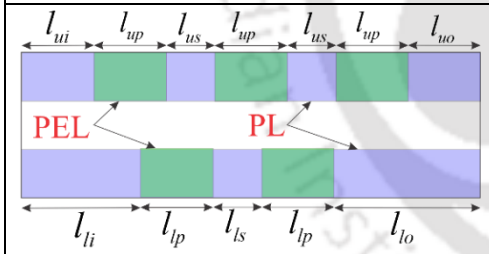

Configuration type	Upper wall				Lower wall			
	l_{ui}	l_{us}	l_{up}	l_{uo}	l_{li}	l_{ls}	l_{lp}	l_{lo}
A	5/25	3/25	3/25	5/25	8/25	3/25	3/25	8/25
B	6/25	2/25	3/25	6/25	17/50	2/25	3/25	17/50
C	13/50	1/25	3/25	13/50	9/25	1/25	3/25	9/25

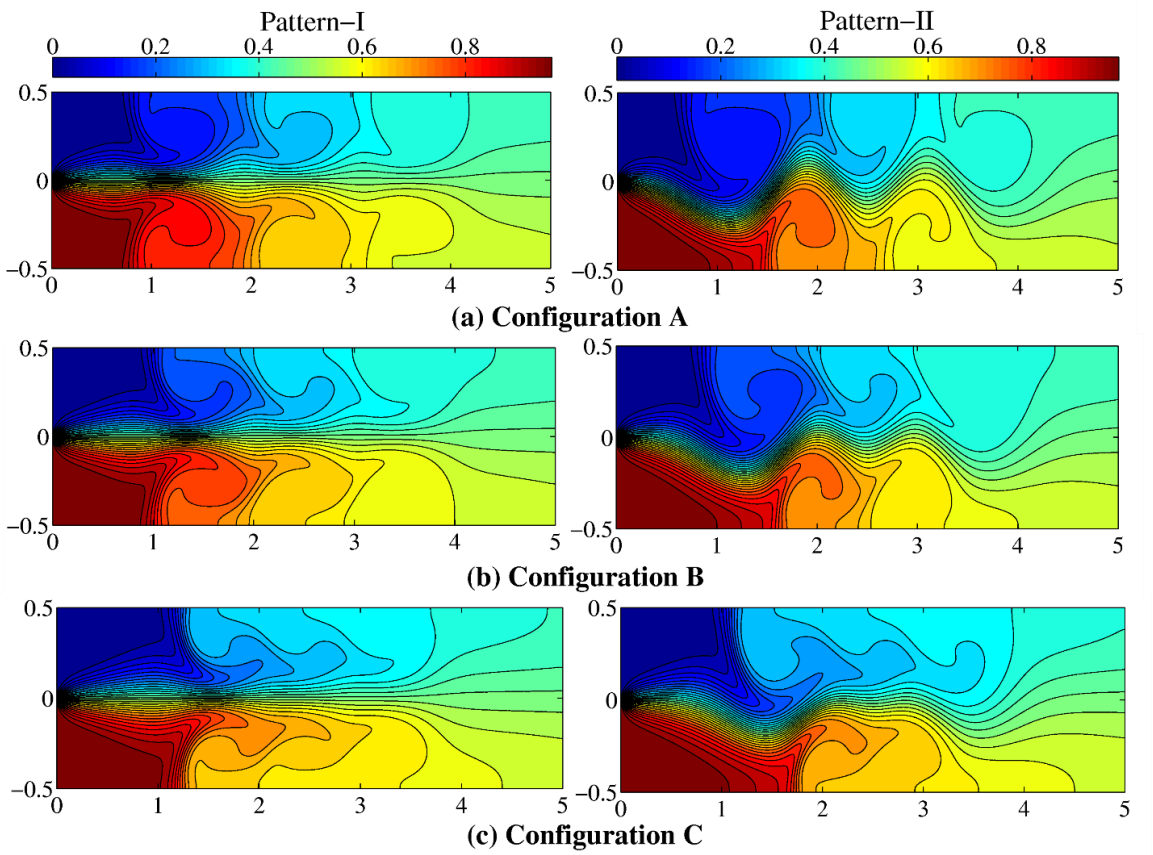

Figure 3.10: Contour plots depicting the concentration distribution in three different configurations viz, A, B and C, for both the patterns, pattern-I and II. The other parameters used for this analysis are: $\kappa = 15$, $\kappa_p = 10$, $d = 0.15$, $Sc = 5\times10^5$, $Re=10^{-3}$, $U_{in} = 0.1$, $\alpha = 10$.

To study the effect of spacing between the PEL patches, we have kept the patch length constant i.e., $3L/25$, whereas the other dimensions such as the spacing between the PEL patches $l_{(u/l)s}$, and the entry and exit lengths $l_{(u/l)i}$ and $l_{(u/l)o}$ are varied. The variation in these dimensions is tabulated in Table 3.1. The mixing dynamics obtained for these different configurations of both pattern-I and II are depicted in Fig. 3.10. It can be observed from Fig. 3.10(a)-(c) that a reduction in the spacing $l_{(u/l)s}$ from $3L/25$ to $L/25$ (i.e., from configuration A to C) for both patterns, pattern-I and II, causes a segregation of the vortices near the central region of the channel and hence demotes the effectiveness of the patterned structure grafted on the walls. In other words, the reduction in the spacing between the PEL patches minimizes the recirculation zone area in case of both the patterns (see Fig. 3.10(a)-(c)). As a result, the mixing performance with a reduction in the spacing between the PEL patches degrades as shown in Fig. 3.10(a)-(c).

3.5 Summary

In this study, we have proposed a novel approach to obtain efficient mixing in a narrow fluidic channel having the walls grafted with the patterned-soft layer. We outline some of the significant insights as follows:

1. The strength of the Lamb vortices and the mixing efficiency depend on the physical and geometrical parameters of the PEL patch. The variation in these parameters causes a change in either the electrostatic potential or a frictional drag at the PEL patch. From the present study, we have observed that for higher PEL thickness d (= 0.15), the higher value of the DH parameter of electrolyte κ (= 20), and for the lesser drag parameter of PEL α (= 1), the mixing efficiency is higher. For these parameters, the strengthened *near-wall effect* confines the resistance provided by the local EOF to the patched section only. This confined resistance stimulates the momentum exchange rate and leads to an enhancement in mixing.
2. It is observed that pattern-II configuration is more efficient from the perspective of micromixing, attributed primarily to the asymmetric formation of vortices. The asymmetric grafting of the PEL patch in pattern-II causes an additional loss in the axial momentum and generates a transverse momentum of similar strength. In fact, for pattern-II, the interaction between the neighbouring vortices is pronounced as compared to the pattern-I a
3. nd provides more retention time to the neutral species being mixed. This effect is more prominent for higher PEL thickness.
4. From this analysis, it also appears that the spacing between the PEL patches plays a significant role in altering the mixing performance and it is comparatively higher for maximum spacing considered in the present study.
5. We have also predicted the salient parameters, i.e., the mixing length and the strength of the applied electric potential at which the recirculation zones start. From the comparison between patterns I and II, pattern-II shows the smaller mixing length as well as required small magnitude of the critical electric field to generate the vortices.

CHAPTER 4

Tutorial Review of Mixing in a Rotating Soft Narrow-Fluidic Channel under the Electric Double Layer Effect: A Variational Calculus Approach

The soft layer modulated electroosmotic flow can render its enormous flow controllability towards ensuring augmented mixing in a narrow-fluidic channel mounted on a rotating disk. As highlighted in the first chapter, a flow in the rotating narrow-fluidic channels usually encounter several challenges viz., the adverse effect of Coriolis force at higher rotational speeds, and lack of bio-lubrication effect. At higher rotational speed, the Coriolis force arrests the momentum of the fluid being transported in the axial direction of the channel and leads to the almost rigid-body type motion (Kaushik et al., 2019; Raviv et al., 2003; Stewartson, 1957). This phenomenon may even affect the mixing characteristics. The grafting of soft polyelectrolyte layer in a rotating narrow-fluidic channel increases the net throughput even in the presence of the strong Coriolis force and improves a rapid and efficient mixing performance as well. In this chapter, we study the effect of the grafted soft layer on the electrohydrodynamics and its consequences on the underlying mixing in a rotating rectangular narrow-fluidic channel. Our analysis primarily focuses on the low Rossby number flow and develops a theoretical framework consistent with the variational calculus method for solving the underlying electrohydrodynamics in a rotating narrow-fluidic channel having built-in soft layers. By establishing the accuracy of the present theoretical approach, we first discuss the flow dynamics thoroughly and then move towards the mixing performance of the proposed micromixing assay from both qualitative assessment and quantitative estimation. On solving the Eulerian velocity fields, we further use the Lagrangian approach to understand the mixing in the present rotating-fluidic system. In the Lagrangian approach, the Poincaré map offers qualitative information about the mixing performance, while the entropy of the mixing offers a quantitative estimate of the mixing.

4.1 Electrohydrodynamics in a Rotating Soft Narrow-Fluidic Channel

4.1.1 Description of Rotating Soft Narrow-Fluidic Channel

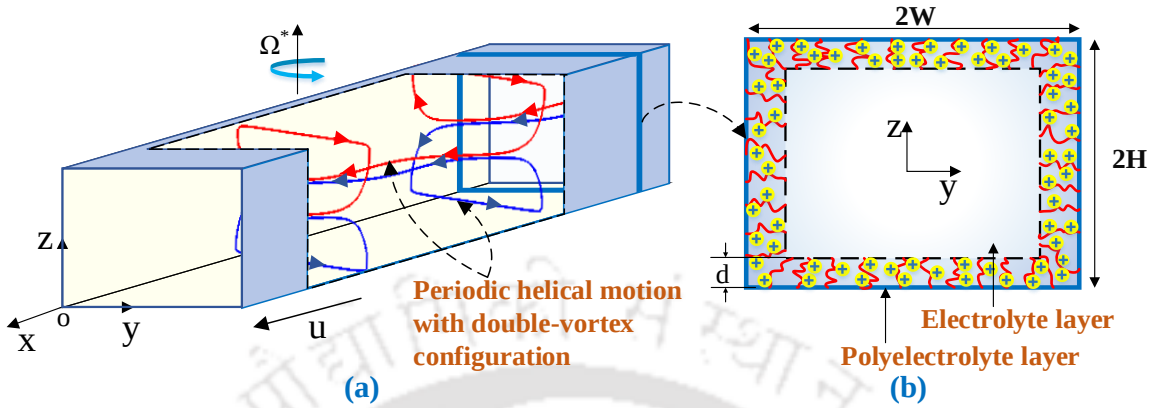

Figure 4.1: (a) Rotating soft narrow-fluidic channel: Schematic in (a) shows the soft narrow-fluidic channel rotating about z axis with a rotational speed Ω^*. The axial flow takes place in the positive x direction while the transverse and vertical flows occur in y and z directions, respectively. The periodic-helical motion adopted by the fluid particles is shown in the cut-section of (a). (b) Channel cross-section: Cross-section of the channel shown in (b) with two separate layers of electrolyte and polyelectrolyte in y – z plane. The height and width of the channel are '2H' and '2W' respectively, whereas the thickness of PEL is 'd'.

Figure 4.1 shows the schematic of the soft narrow-fluidic channel, rotating about z axis at a steady rotational speed $\mathbf{\Omega} = (0,0,\Omega^*)$. The walls of the channel are grafted with the soft PEL of a thickness d (see Fig. 4.1(b)). As shown in Fig. 4.1, the electroosmotic flow stems from the electrostatic interaction between the polyelectrolyte layer modulated EDL and the externally applied electric field $\mathbf{E} = (E_x,0,0)$. It assists the pressure-driven flow in the duct, which has a rectangular cross-section of height '$2H$' and width '$2W$', as shown in Fig. 4.1(a). The pressure-driven flow is maintained by the axial gradient of the gyrostatic pressure $\mathbf{p}_g$, which is the net effect of applied axial pressure gradient and the centrifugal acceleration (Kaushik *et al.* 2017b, 2017a). The axial flow developed from these primary actuation parameters is translationally symmetric along the duct, while the secondary flow with the vortical flow structure is symmetric about the transverse centerline of the channel (Hart 1971; Johnston *et al.* 1972; Lezius & Johnston 1976).

In the rotating frame of reference, the vortical flow takes place due to the Coriolis force. If the channel is observed from the inlet, the Coriolis force sweeps the fluid towards the right wall of the channel, from where it turns back to the horizontal walls, and then to the left wall. This typical flow trajectory gives rise to a double vortex configuration for

higher rotational speed (Kheshgi & Scriven 1985; Speziale 1982), causing periodic-helical motion of the fluid particles as shown in Fig. 4.1(a). The channel is considered to be sufficiently long, such that the flow structure at the intermediate cross-section (y - z plane - a region of our interest in this study) remains almost unaffected by the entry and exit effects of the channel. The flow in the channel is assumed to be free from convective inertia for a very small Reynolds number $\mathrm{Re}\,(\ll 1)$, typically considered in the microfluidic analysis (Ng & Qi 2015). Note that due to low $\mathrm{Re}(\ll 1)$, the underlying transport phenomenon falls in the regime of low Rossby number flow ($\mathrm{Ro} < 1$) as well. We may mention here that the Rossby number is the ratio of inertia force to the Coriolis force (Ng & Qi 2015). This order analysis is suggestive of the dominating effect of the Coriolis force on the underlying transport of the problem under present consideration.

4.1.2 PEL Electrostatics

In the present problem, we have considered that the electrostatic potential is invariant in the x direction. Therefore, it is the function of y and z coordinates only. Considering these aspects, we use the generalized form of the PB equation derived in Chapter 2: Section 2.1.1, and modify according to the present flow configuration as:

Electrolyte layer

$$\frac{\partial^2 \bar{\psi}}{\partial \bar{y}^2} + \frac{\partial^2 \bar{\psi}}{\partial \bar{z}^2} = \bar{\kappa}^2 \bar{\psi} \tag{4.1a}$$

Polyelectrolyte layer

$$\frac{\partial^2 \bar{\psi}}{\partial \bar{y}^2} + \frac{\partial^2 \bar{\psi}}{\partial \bar{z}^2} = \bar{\kappa}^2 \bar{\psi} - \bar{\kappa}_p^2 \tag{4.1b}$$

4.1.3 Rotational Hydrodynamics Coupled with PEL Modulated Electrostatics

In the present study, the primary flow $u(y,z)$ is driven by the combined influences of the pressure gradient and the electroosmotic force. In contrast, the secondary flow, depicted by $v(y,z)$ and $w(y,z)$ velocity components, is developed by the Coriolis force. The pressure gradient in x-direction corresponds to the gyrostatic pressure acting on the fluid, whereas the mass conservation constraint together with the Coriolis force $(\boldsymbol{\Omega}\times\mathbf{u})$ gives rise to the pressure gradients in the y and z directions (Ng & Qi 2015). If the effect of gravity is ignored, the governing equations for both the electrolyte layer and polyelectrolyte layer in the rotating frame of reference can be written as (Ng & Qi 2015):

Momentum conservation equation

Electrolyte layer

$$\rho\left(\frac{\partial \mathbf{u}}{\partial t}+\left(\mathbf{u}.\nabla\right)\mathbf{u}+2\left(\mathbf{\Omega}\times\mathbf{u}\right)\right)=-\nabla\mathbf{p}_g+\nabla.\left(\eta\mathbf{D}\right)+\rho_e\mathbf{E} \tag{4.2a}$$

Polyelectrolyte layer

$$\rho\left(\frac{\partial \mathbf{u}}{\partial t}+\left(\mathbf{u}.\nabla\right)\mathbf{u}+2\left(\mathbf{\Omega}\times\mathbf{u}\right)\right)=-\nabla\mathbf{p}_g+\nabla.\left(\eta\mathbf{D}\right)+\rho_e\mathbf{E}-\mu_c\mathbf{u} \tag{4.2b}$$

Continuity equation

$$\nabla.\mathbf{u}=0 \tag{4.3}$$

Note that, for ease in the presentation, we have considered the quantities pertaining to the rotational frame such as velocity field $\mathbf{u}$, same as that of the translational frame.

We further non-dimensionalize governing Eqs. (4.2)-(4.3), using the following reference and dimensionless parameters: $u_{ref}=u_{HS}=\left(-\varepsilon_e\zeta E_0\right)/\eta$, $l_{ref}=H$, $p_{g,ref}=\left(\eta u_{HS}\right)/H$, $t_{ref}=H/u_{HS}$, $\mathrm{Re}=\left(\rho u_{HS}H\right)/\eta$, $\mathrm{Re}_\omega=\left(2\mathbf{\Omega}\rho H^2\right)/\eta$ and $\alpha^2=\left(\mu_c H^2\right)/\eta$ (Kaushik *et al.* 2017a, 2017b; Kaushik & Chakraborty 2017; Ng & Qi 2015). Using these parameters, the dimensionless transport equations can be written as:

Momentum conservation equation

Electrolyte layer

$$\mathrm{Re}\left[\frac{\partial \bar{\mathbf{u}}}{\partial \bar{t}}+\left(\bar{\mathbf{u}}.\bar{\nabla}\right)\bar{\mathbf{u}}\right]+\left(\mathrm{Re}_\omega\times\bar{\mathbf{u}}\right)=-\bar{\nabla}\bar{\mathbf{p}}_g+\bar{\nabla}^2\bar{\mathbf{u}}+\bar{\kappa}^2\bar{\psi} \tag{4.4a}$$

Polyelectrolyte layer

$$\mathrm{Re}\left[\frac{\partial \bar{\mathbf{u}}}{\partial \bar{t}}+\left(\bar{\mathbf{u}}.\bar{\nabla}\right)\bar{\mathbf{u}}\right]+\left(\mathrm{Re}_\omega\times\bar{\mathbf{u}}\right)=-\bar{\nabla}\bar{\mathbf{p}}_g+\bar{\nabla}^2\bar{\mathbf{u}}+\bar{\kappa}^2\bar{\psi}-\alpha^2\bar{\mathbf{u}} \tag{4.4b}$$

Continuity equation

$$\nabla.\bar{\mathbf{u}}=0 \tag{4.5}$$

It is worth to mention here that the inverse of rotational Reynolds number Re_ω signifies the definition of Ekman number, which is nothing but the ratio of viscous force to the Coriolis force. Particularly for this study, the range of Ekman number is moderate as both the Coriolis force and viscous force are significant in this analysis. Also, in the present study, considering low $\mathrm{Re}(\ll 1)$, we have neglected the influence of inertia on the

underlying analysis. Owing to these approximations, and for the steady flow, Eqs. (4.4a) and (4.4b) can be rewritten as (Ng & Qi 2015):

Electrolyte layer

$$\mathrm{Re}_\omega \times \bar{\mathbf{u}} = -\bar{\nabla}\bar{\mathbf{p}}_g + \bar{\nabla}^2\bar{\mathbf{u}} + \bar{\kappa}^2\bar{\psi} \tag{4.6a}$$

Polyelectrolyte layer

$$\mathrm{Re}_\omega \times \bar{\mathbf{u}} = -\bar{\nabla}\bar{\mathbf{p}}_g + \bar{\nabla}^2\bar{\mathbf{u}} + \bar{\kappa}^2\bar{\psi} - \alpha^2\bar{\mathbf{u}} \tag{4.6b}$$

Finally, the system of governing equations for the present study can be written as:

Momentum conservation equation

Electrolyte layer

x momentum

$$-\mathrm{Re}_\omega\,\bar{v} = -\frac{\partial \bar{p}_g}{\partial \bar{x}} + \frac{\partial^2 \bar{u}}{\partial \bar{y}^2} + \frac{\partial^2 \bar{u}}{\partial \bar{z}^2} + \bar{\kappa}^2\bar{\psi} \tag{4.7a}$$

y momentum

$$\mathrm{Re}_\omega\,\bar{u} = -\frac{\partial \bar{p}_g}{\partial \bar{y}} + \frac{\partial^2 \bar{v}}{\partial \bar{y}^2} + \frac{\partial^2 \bar{v}}{\partial \bar{z}^2} \tag{4.7b}$$

z momentum

$$0 = -\frac{\partial \bar{p}_g}{\partial \bar{z}} + \frac{\partial^2 \bar{w}}{\partial \bar{y}^2} + \frac{\partial^2 \bar{w}}{\partial \bar{z}^2} \tag{4.7c}$$

Polyelectrolyte layer

x momentum

$$-\mathrm{Re}_\omega\,\bar{v} = -\frac{\partial \bar{p}_g}{\partial \bar{x}} + \frac{\partial^2 \bar{u}}{\partial \bar{y}^2} + \frac{\partial^2 \bar{u}}{\partial \bar{z}^2} + \bar{\kappa}^2\bar{\psi} - \alpha^2\bar{u} \tag{4.8a}$$

y momentum

$$\mathrm{Re}_\omega\,\bar{u} = -\frac{\partial \bar{p}_g}{\partial \bar{y}} + \frac{\partial^2 \bar{v}}{\partial \bar{y}^2} + \frac{\partial^2 \bar{v}}{\partial \bar{z}^2} - \alpha^2\bar{v} \tag{4.8b}$$

z momentum

$$0 = -\frac{\partial \bar{p}_g}{\partial \bar{z}} + \frac{\partial^2 \bar{w}}{\partial \bar{y}^2} + \frac{\partial^2 \bar{w}}{\partial \bar{z}^2} - \alpha^2\bar{w} \tag{4.8c}$$

Continuity equation

$$\frac{\partial \bar{v}}{\partial \bar{y}} + \frac{\partial \bar{w}}{\partial \bar{z}} = 0 \tag{4.9}$$

For brevity in the presentation, henceforth, we drop the overbars from the dimensionless variables and use a symbol Γ for $-\partial \overline{p}_g / \partial \overline{x}$.

4.2 Variational Calculus

4.2.1 Euler-Lagrange Form of Governing Equations and Boundary Conditions

We use the Ritz technique to solve the transport equations of the present flow configuration [Eqs. (4.1), (4.7)-(4.9)]. In this method, we first compose the total functional using the Euler-Lagrange forms of these equations. For this task, we multiply these equations with their corresponding test functions, integrate over the control volume, and then add them together to get the total functional of the system (Reddy & Rasmussen 1982; Rektorys 1977). The minimization of this functional with respect to the Ritz coefficients (introduced in subsection 4.2.3) gives the approximate solution to the problem. The derivation of the functional over the total domain (cross-section of the channel), instead of solving differential equations [Eqs. (4.1), (4.7)-(4.9)] for every sub-domain if any in the flow configuration sets uniformity in the solution over the entire cross-section of the channel (Sadeghi 2018; Sadeghi *et al.* 2020). This advantageous feature prevails even with the consideration of the polyelectrolyte layer, which forms a separate sub-domain, in the underlying analysis [Eqs. (4.1b) and (4.8)] (Sadeghi 2018; Sadeghi *et al.* 2019, 2020). In such a case, a single functional is derived for the entire cross-section, and the Darcy drag $\alpha^2 \mathbf{u}$ and the term κ_p^2 is made zero for the electrolyte layer [see Eqs. (4.1b) and (4.8)]. The final set of governing equations, which are needed to be solved over the complete channel cross-section, can be written as follows:

Poisson-Boltzmann equation

$$\frac{\partial^2 \psi}{\partial y^2} + \frac{\partial^2 \psi}{\partial z^2} = \kappa^2 \psi - \kappa_p^2 \tag{4.10}$$

Momentum conservation equation

x momentum

$$-\mathrm{Re}_\omega v = \frac{\partial^2 u}{\partial y^2} + \frac{\partial^2 u}{\partial z^2} + \Gamma + \kappa^2 \psi - \alpha^2 u \tag{4.11a}$$

y momentum

$$\mathrm{Re}_\omega u = -\frac{\partial p_g}{\partial y} + \frac{\partial^2 v}{\partial y^2} + \frac{\partial^2 v}{\partial z^2} - \alpha^2 v \tag{4.11b}$$

z momentum

$$0 = -\frac{\partial p_g}{\partial z} + \frac{\partial^2 w}{\partial y^2} + \frac{\partial^2 w}{\partial z^2} - \alpha^2 w \tag{4.11c}$$

Continuity equation

$$\frac{\partial v}{\partial y} + \frac{\partial w}{\partial z} = 0 \tag{4.12}$$

We write the boundary conditions that accompany the set of governing equations mentioned above [Eqs. (4.10)-(4.12)] as:

For the potential distribution

$$\left.\frac{\partial \psi}{\partial (y,z)}\right|_{y,z=\pm 1} = 0 \tag{4.13a}$$

$$\left.\frac{\partial \psi}{\partial (y,z)}\right|_{y,z=0} = 0 \tag{4.13b}$$

The boundary conditions in Eqs. (4.13a)-(4.13b) depict the no-flux boundary condition at the walls and the center (i.e., at y and z-axis), respectively.

For the velocity distribution

$$(u,v,w)\big|_{y,z=\pm 1} = 0 \tag{4.14a}$$

$$\left.\frac{\partial (u,v)}{\partial (y,z)}\right|_{y,z=0} = 0 \tag{4.14b}$$

$$w\big|_{y,z=0} = 0 \tag{4.14c}$$

The first boundary condition [Eq. (4.14a)] depicts the no-slip boundary condition at the walls of the channel for all velocity components u, v and w. The second boundary condition [Eq. (4.14b)] is considered for the symmetric nature of the profiles of both u and v velocity components at y and z-axis. The last boundary condition [Eq. (4.14c)] stands for the anti-symmetric nature of w velocity at y and z-axis.

4.2.2 Formulation of Functional

Let $\delta\psi$, δu, δv, δw and δp_g be the variations in ψ, u, v, w and p_g variables, where $\delta\psi, \delta u, \delta v, \delta w, \delta p_g \in H_0^2(\Omega_b)$ and Ω_b is the domain with boundary $\partial\Omega_b$. In the process of selection of these variations, it is necessary to take into account the inter-dependency of these variations ($\delta\psi$, δu, δv, δw and δp_g) on each other as the present

problem deals with the two-way coupled system of equations [Eqs. (4.10)-(4.12)]. In the rotational flow dynamics, an increment in v, w and p_g (secondary flow) leads to a reduction in the variable u (axial flow) due to Coriolis force and the induced pressure gradients in y and z directions. Whereas the potential distribution remains unaffected as it does not depend on the flow velocities due to insignificant ionic Peclet number (Bandopadhyay et al., 2016; Zaccone et al., 2009). Therefore, accounting all these aspects, we impose following sign conventions on the aforementioned variations as,

$$\delta\psi = +\text{ve},\ \delta u = +\text{ve},\ \delta v = -\text{ve},\ \delta w = -\text{ve},\ \delta p_g = -\text{ve}$$

To formulate the functional, we use the definition of the first variation for any function $F(y,z,\phi,\phi_y,\phi_z)=0$, where $\phi_y = \partial\phi/\partial y$ and $\phi_z = \partial\phi/\partial z$,

$$\delta I(\phi) = \int_{\Omega_b}\left[\frac{\partial F}{\partial \phi} - \frac{\partial}{\partial x}\left(\frac{\partial F}{\partial \phi_y}\right) - \frac{\partial}{\partial y}\left(\frac{\partial F}{\partial \phi_z}\right)\right]\delta\phi\, dydz \tag{4.15}$$

where $\delta I(\phi)$ is the first variation of functional $I(\phi)$ and $\delta\phi$ is the variation of $\phi(y,z)$. Applying the above definition [Eq. (4.15)] to the Eqs. (4.10)-(4.12), we get,

$$\delta I(\psi) = \int_{\Omega_b}\left[\frac{\partial^2\psi}{\partial y^2} + \frac{\partial^2\psi}{\partial z^2} - \kappa^2\psi + \kappa_p^2\right]\delta\psi\, dydz \tag{4.16a}$$

$$\delta I(u) = \int_{\Omega_b}\left[\frac{\partial^2 u}{\partial y^2} + \frac{\partial^2 u}{\partial z^2} + \kappa^2\psi - \alpha^2 u + \Gamma + \text{Re}_\omega v\right]\delta u\, dydz \tag{4.16b}$$

$$\delta I(v) = \int_{\Omega_b}\left[\frac{\partial^2 v}{\partial y^2} + \frac{\partial^2 v}{\partial z^2} - \frac{\partial p_g}{\partial y} - \alpha^2 v - \text{Re}_\omega u\right](-\delta v)\, dydz \tag{4.16c}$$

$$\delta I(w) = \int_{\Omega_b}\left[\frac{\partial^2 w}{\partial y^2} + \frac{\partial^2 w}{\partial z^2} - \frac{\partial p_g}{\partial z} - \alpha^2 w\right](-\delta w)\, dydz \tag{4.16d}$$

$$\delta I(p_g) = \int_{\Omega_b}\left[\frac{\partial v}{\partial y} + \frac{\partial w}{\partial z}\right](-\delta p_g)\, dydz \tag{4.16e}$$

In these Eqs. (4.16a)-(4.16e), the integrand of each integral represents the energy or work associated with the corresponding variable. The integrand of first integral [Eq. (4.16a)] represents the electric energy in the domain Ω_b, whereas the integrands of Eqs. (4.16b)-(4.16d) represent the kinetic energy associated with the velocities u, v and w (Reddy 1986; Reddy & Rasmussen 1982). In Eq. (4.16e), the integrand represents the flow work

done by the pressure to conserve the mass of the system (Reddy 1986; Reddy & Rasmussen 1982).

Now, we perform the integrations in Eqs. (4.16a)-(4.16e) and add them together to get the functional $\prod$ as,

$$\Pi = \int_{\Omega_b} \left[\left(\frac{\partial \psi}{\partial y}\right)^2 + \left(\frac{\partial \psi}{\partial z}\right)^2 + \left(\frac{\partial u}{\partial y}\right)^2 + \left(\frac{\partial u}{\partial z}\right)^2 - \left(\frac{\partial v}{\partial y}\right)^2 - \left(\frac{\partial v}{\partial z}\right)^2 - \left(\frac{\partial w}{\partial y}\right)^2 - \left(\frac{\partial w}{\partial z}\right)^2 \right.$$
$$\left. -\left(2\kappa^2\psi - 2\Gamma\right)u - 2\,\mathrm{Re}_\omega\, uv + \alpha^2\left(u^2 - v^2 - w^2\right) + 2p_g\left(\frac{\partial v}{\partial y} + \frac{\partial w}{\partial z}\right) + \kappa^2\psi^2 - 2\kappa_p^2\psi \right] dydz \tag{4.17}$$

4.2.3 Extremization of Functional: Ritz Method

Now, we obtain the solution to the problem using the Ritz method in which the variables u, v, w, p_g and ψ are approximated by the corresponding basis functions. Note that the selection of suitable basis functions is integral as well as an essential part of this method. We stick to the following basics for selecting these functions in the present endeavour, i.e., the basis functions should satisfy the boundary conditions given in Eqs. (4.13)-(4.14) as well as the symmetric or asymmetric nature of the variables (Ng & Qi 2015). In this study, the u and v velocity components, as well as the potential ψ has symmetric nature about y and z-axis. In contrast, the velocity w has an anti-symmetric nature about y and z-axis. Also, the basis function chosen for pressure should maintain orthogonality with functions that have already been selected for v and w velocity components. Accounting all these aspects, we consider the following test functions for the functional $\prod$ as:

$$\psi(y,z) = \sum_{i=1}^{M} \psi_{bi}\psi_{fi} = \sum_{i=1}^{M} \psi_{bi} \cos\left(l_{\psi i}\pi y\right)\cos\left(m_{\psi i}\pi z\right) \tag{4.18a}$$

$$u(y,z) = \sum_{i=1}^{M} u_{bi}u_{fi} = \sum_{i=1}^{M} u_{bi} \cos\left[\left(2l_{ui}+1\right)\pi\frac{y}{2}\right]\cos\left[\left(2m_{ui}+1\right)\pi\frac{z}{2}\right] \tag{4.18b}$$

$$v(y,z) = \sum_{i=1}^{M} v_{bi}v_{fi} = \sum_{i=1}^{M} v_{bi} \cos\left[\left(2l_{vi}+1\right)\pi\frac{y}{2}\right]\cos\left[\left(2m_{vi}+1\right)\pi\frac{z}{2}\right] \tag{4.18c}$$

$$w(y,z) = \sum_{i=1}^{M} w_{bi}w_{fi} = \sum_{i=1}^{M} w_{bi} \sin\left[\left(l_{wi}+1\right)\pi y\right]\sin\left[\left(m_{wi}+1\right)\pi z\right] \tag{4.18d}$$

$$p_g(y,z)=\sum_{i=1}^{M}p_{bi}p_{fi}=\sum_{i=1}^{M}p_{bi}\left(\begin{array}{l}\left(\sin\left[\left(l_{pi}+1\right)\pi y\right]\cos\left[\left(2m_{pi}+1\right)\pi\frac{z}{2}\right]\right)\\+p_c\left(\sin\left[\left(2l_{pi}+1\right)\pi\frac{y}{2}\right]\cos\left[\left(2m_{pi}+1\right)\pi\frac{z}{4}\right]\right)\end{array}\right) \tag{4.18e}$$

In Eqs. (4.18a)-(4.18e), the coefficients ψ_{bi}, u_{bi}, v_{bi}, w_{bi} and p_{bi} are the Ritz coefficients with respect to which functional given in Eq. (4.17) needs to be minimized. For minimization, we set,

$$\frac{\partial\Pi}{\partial\psi_{bi}}=0 \text{ where } \forall\psi_{bi}\in[1,M] \tag{4.19a}$$

$$\frac{\partial\Pi}{\partial u_{bi}}=0 \text{ where } \forall u_{bi}\in[1,M] \tag{4.19b}$$

$$\frac{\partial\Pi}{\partial v_{bi}}=0 \text{ where } \forall v_{bi}\in[1,M] \tag{4.19c}$$

$$\frac{\partial\Pi}{\partial w_{bi}}=0 \text{ where } \forall w_{bi}\in[1,M] \tag{4.19d}$$

$$\frac{\partial\Pi}{\partial p_{bi}}=0 \text{ where } \forall p_{bi}\in[1,M] \tag{4.19e}$$

where $l_{\psi i},l_{ui},l_{vi},l_{wi},l_{pi}\in[0,m]$ and $m_{\psi i},m_{ui},m_{vi},m_{wi},m_{pi}\in[0,m]$; hence, $M=(m+1)\times(m+1)$. After minimizing the functional given in Eq. (4.17), we get,

$$\sum_{j=1}^{M}\psi_{bj}\int_{\Omega_b}\left[\frac{\partial\psi_{fj}}{\partial y}\frac{\partial\psi_{fi}}{\partial y}+\frac{\partial\psi_{fj}}{\partial z}\frac{\partial\psi_{fi}}{\partial z}+\kappa^2\psi_{fj}\psi_{fi}\right]dydz=\int_{\Omega_b}\kappa_p^2\psi_{fi}dydz \tag{4.20a}$$

$$\begin{aligned}\sum_{j=1}^{M}u_{bi}\int_{\Omega_b}\left[\frac{\partial u_{fj}}{\partial y}\frac{\partial u_{fi}}{\partial y}+\frac{\partial u_{fj}}{\partial z}\frac{\partial u_{fi}}{\partial z}+\alpha^2u_{fj}u_{fi}\right]dydz&=\int_{\Omega_b}\left[\kappa^2\left(\sum_{k=1}^{M}\psi_{bk}\psi_{fk}\right)+\Gamma\right]u_{fi}dydz\\&+\int_{\Omega_b}\left[\mathrm{Re}_\omega\left(\sum_{k=1}^{M}v_{bk}v_{fk}\right)\right]u_{fi}dydz\end{aligned} \tag{4.20b}$$

$$\begin{aligned}\sum_{j=1}^{M}v_{bj}\int_{\Omega_b}\left[\frac{\partial v_{fj}}{\partial y}\frac{\partial v_{fi}}{\partial y}+\frac{\partial v_{fj}}{\partial z}\frac{\partial v_{fi}}{\partial z}+\alpha^2v_{fj}v_{fi}\right]dydz&=\int_{\Omega_b}\left[-\left(\sum_{k=1}^{M}p_{bk}\frac{\partial p_{fk}}{\partial y}\right)\right]v_{fi}dydz\\&-\int_{\Omega_b}\left[\mathrm{Re}_\omega\left(\sum_{k=1}^{M}u_{bk}u_{fk}\right)\right]v_{fi}dydz\end{aligned} \tag{4.20c}$$

$$\sum_{j=1}^{M}w_{bj}\int_{\Omega_b}\left[\frac{\partial w_{fj}}{\partial y}\frac{\partial w_{fi}}{\partial y}+\frac{\partial w_{fj}}{\partial z}\frac{\partial w_{fi}}{\partial z}+\alpha^2w_{fj}w_{fi}\right]dydz=\int_{\Omega_b}-\left(\sum_{k=1}^{M}p_{bk}\frac{\partial p_{fk}}{\partial z}\right)w_{fi}dydz \tag{4.20d}$$

$$\int_{\Omega_b}p_{fi}\left[\left(\sum_{j=1}^{M}v_{bj}\frac{\partial v_{fj}}{\partial y}\right)+\left(\sum_{j=1}^{M}w_{bj}\frac{\partial w_{fj}}{\partial z}\right)\right]dydz=0 \tag{4.20e}$$

In Eq. (4.20e), the basis function of pressure p_{fi} has an additional term p_2 $\left(=\sin\left[\left(2l_{pi}+1\right)\pi y/2\right]\cos\left[\left(2m_{pi}+1\right)\pi z/4\right]\right)$ with a coefficient p_c, which assists in maintaining the mass conservation in the domain. Otherwise, the boundary conditions imposed by function p_1 $\left(=\sin\left[\left(l_{pi}+1\right)\pi y\right]\cos\left[\left(2m_{pi}+1\right)\pi z/2\right]\right)$ lead to divergence in the continuity.

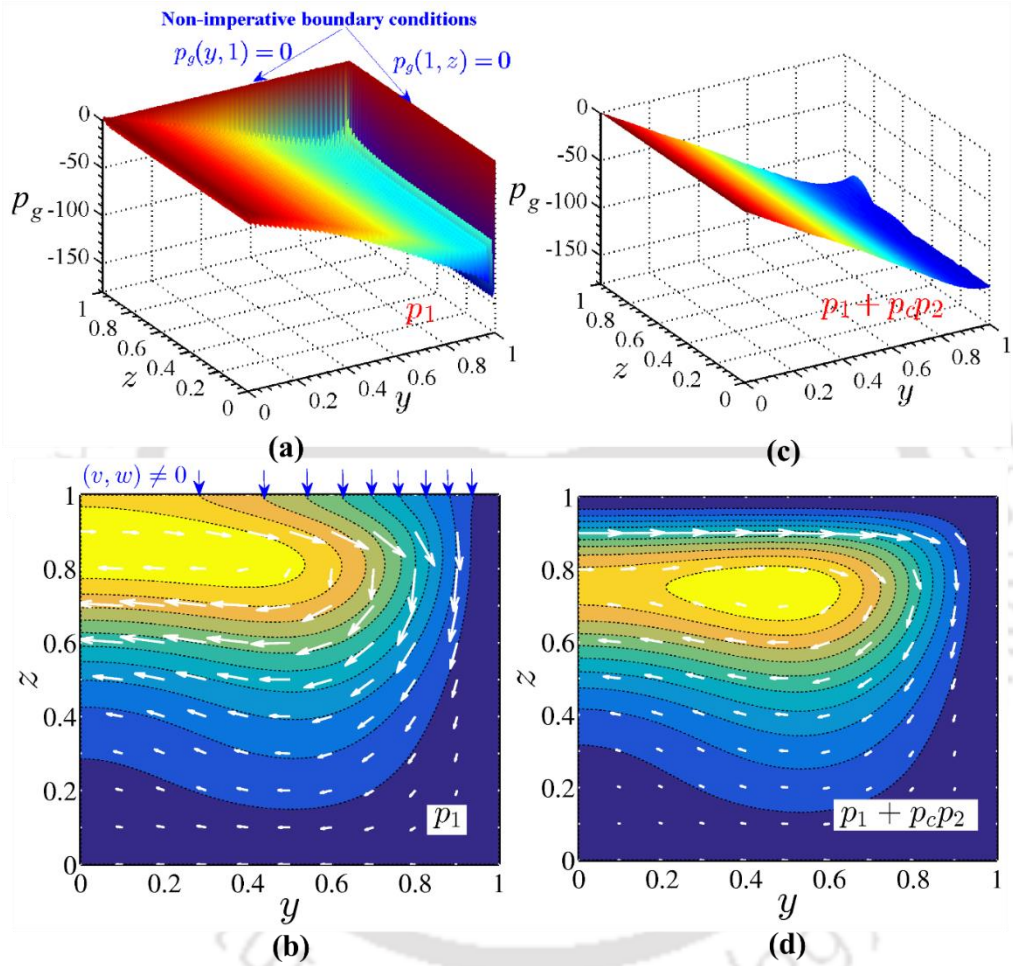

Figure 4.2: Surface plots of pressure distribution ((a) and (c)) and contour plots of secondary flow ((b) and (d)) for basis functions p_1 and $p_1 + p_c p_2$. The first column ((a) and (b)) depicts the case of basis function p_1 and second column ((c) and (d)) depicts the case of $p_1 + p_c p_2$. The contour plots of stream function ((b) and (d)) give the inference of the divergence in the mass conservation in the channel. The parameters considered to obtain these plots are: $\kappa_p = 10$, $d = 0.3$, $\alpha = 5$, $\Gamma = 0.5$, $Re_\omega = 100$, $\kappa = 12$ and $l_i \times m_i = 100 \times 100$.

The effect of these functions viz., p_1 and $p_1 + p_c p_2$ on the pressure distribution and the corresponding secondary flow development is shown in Fig. 4.2. The contour plots of the secondary flow in Figs. 4.2(b) and 4.2(d) help to analyze the divergence in the mass conservation $\nabla.\mathbf{u} = 0$. In case of divergence, the walls of the channel do not imitate the

streamlines. Thus, the streamlines of the secondary flow pass through the walls, signifying the transaction of fluid mass across the walls of the channel. In the present study, this phenomenon takes place for the basis function p_1 as evident in Fig. 4.2(b). The non-imperative boundary conditions at the walls $p_g(y,1) = p_g(1,z) = 0$ imposed by the basis function p_1 (see Fig. 4.2(a)) lead to divergence in $\nabla.\mathbf{u} = 0$ as shown in Fig. 4.2(b). In contrast, the additional term $p_c p_2$ in the basis function $p_1 + p_c p_2$ leads to the conservation of mass in the channel, as depicted by the parallel or non-crossing streamlines at the walls of the channel in Fig. 4.2(d). The modified pressure distribution, according to the basis function, $p_1 + p_c p_2$ is shown in Fig. 4.2(c). Note that the value of p_c is based on the order of the continuity equation $O(\nabla.\mathbf{u})$. For a given set of other physical parameters, the value of p_c is obtained as ~2.4 using the trial-and-error method.

The distribution of electrostatic potential ψ, velocity field $\mathbf{u}$, and pressure p_g in $y-z$ plane is obtained by solving Eq. (4.20) with the test functions given in Eq. (4.18). For a concise presentation, we do not outline the intermediate steps here. Instead, the detailed solution procedure to solve Eq. (4.20) is given in the Appendix-A.

4.3 Signifiance of Physical and Geometrical Parameters

In rotational microflows, the thickness of the Ekman layer varies between $O(10^1 - 10^2)\,\mu$m for the rotational speed of centrifuge up to 1000 rpm (Optima L-90K, Beckman Coulter, Inc.). The length scale of narrow-fluidic channels typically varies within the range $O(10^0 - 10^2)\,\mu$m (Duffy et al., 1999). Accordingly, the range of dimensionless rotational speed $\mathrm{Re}_\omega \left[= \left(2\boldsymbol{\Omega}\rho H^2\right)/\eta\right]$ can be estimated as $O(10^0 - 10^2)$ (Duffy et al., 1999). Note that tp estimate this range, we have considered the universal solvent 'water' as the working fluid (properties are mentioned in Chapter 2: Section 2.2.2). Besides, these rotation-dependent parameters, the parameters which govern the PEL modulated electrohydrodynamics, including the dimensionless pressure gradient, are also important in the present study. Note that the physical significance of these parameters is already elaborated in Chapter 2: Section 2.2.2. However, for the sake of brevity in the presentation, we state the values/range of these parameters pertinent to the present study as follows: DH parameter of EL $\kappa \in [12, 50]$, DH parameter of PEL $\kappa_p = 10$, PEL thickness $d \in [0.05,$

0.3], the dimensionless pressure gradient in x direction $\Gamma = 0.5$, and drag parameter of PEL $\alpha \in [1, 20]$.

4.4 Model Benchmarking

Before going to discuss the results at hand, we make an effort to benchmark our theoretical model in this section. In doing so, we take advantage of full-scale numerical simulations as elaborated next. Besides, we also discuss the consistency of the velocity profiles of the present problem from different perspectives, as reported in the literature.

4.4.1 Comparison with Finite Element Method Results

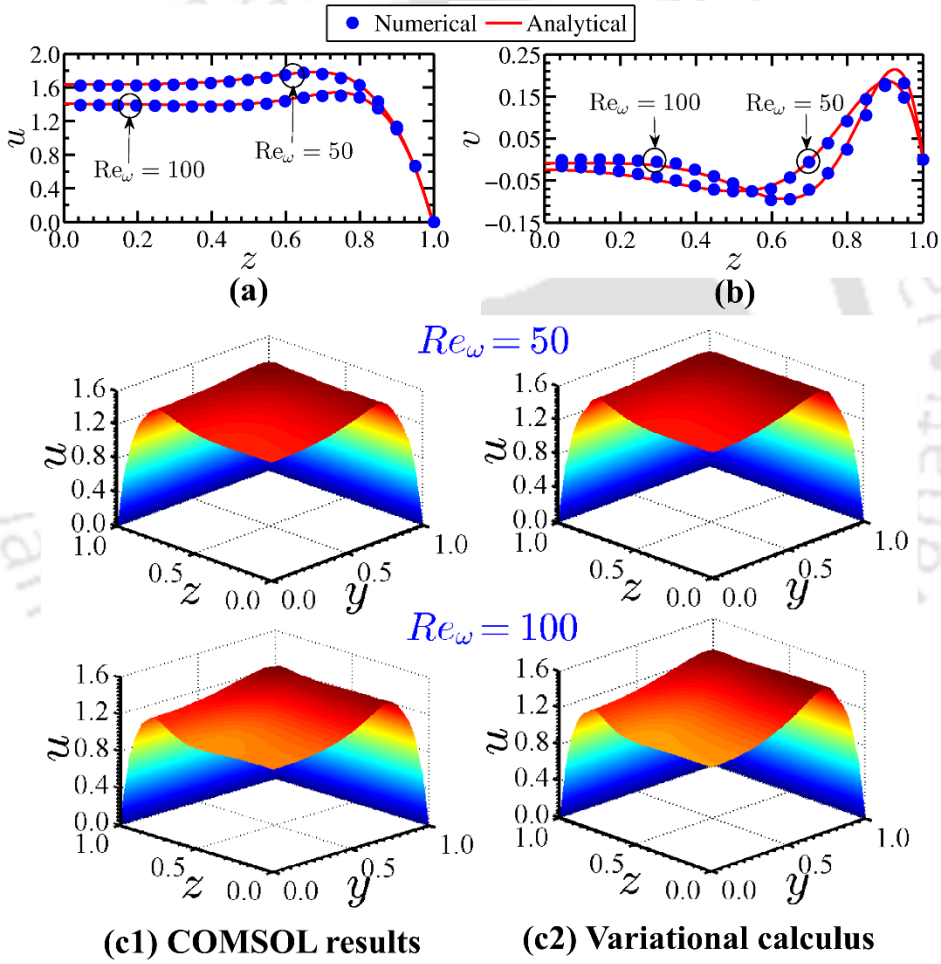

Figure 4.3: Validation plots of the variational calculus method for different rotational speeds $\mathrm{Re}_\omega = 50$ and $\mathrm{Re}_\omega = 100$. Validation through line plots: Comparison through the line plots (in (a) and (b)) of u and v velocity profile obtained at y = 0. Validation through surface plots: Comparison through the surface plots (in (c)) of u-velocity profile. The other parameters considered for this analysis are: $\kappa_p = 10$, d = 0.2, $\alpha = 5$, $\Gamma = 0.5$ and $\kappa = 12$.

In Figs. 4.3(a)-(c), we compare the results obtained from the variational calculus method with those obtained from the finite element method based COMSOL Multiphysics™ solver under identical condition, as mentioned in the caption. The plots in

Figs. 4.3(a) and 4.3(b) show 1D profiles of u-velocity and v-velocity obtained at $y = 0$, respectively, whereas the surface plots in Fig. 4.3(c) map the 3D velocity profiles, obtained for rotational speeds $\mathrm{Re}_\omega = 50$ and $\mathrm{Re}_\omega = 100$. Note that in variational calculus method, the number of basis functions selected to compute the velocity distribution corresponds to the number of indices. For the present analysis, we consider the number of functions in each direction, y and z, respectively as $l_i = 100$ and $m_i = 100$ for each variable u, v, w, p_g and ψ.

It may be mentioned here that for the validation plots depicted in Figs. 4.3(a)-(c), we use the creeping flow model for hydrodynamics and the Poisson equation for potential distribution in COMSOL solver. To obtain the fully developed flow, we use a considerably long channel of 3D rectangular geometry with length to height (or width) ratio $O\left(10^2\right)$ in the COMSOL framework.

It can be observed in Figs. 4.3(a)-(c) that the velocity profiles obtained from our theoretical model accurately mimic the results of the COMSOL solver. Quite notably, it is evident from Figs. 4.3(a) and 4.3(b) that the peak value of the axial velocity occurs at a distance approximately equal to $2\,\mathrm{Re}_\omega^{-1/2}$ (Kheshgi & Scriven, 1985; Speziale, 1982) from the horizontal wall of the channel. This observation is consistent with the theory of the linear Ekman layer, elaborated in Hart 1971 (Hart, 1971).

4.4.2 Consistency of the Flow Dynamics from Different Perspectives

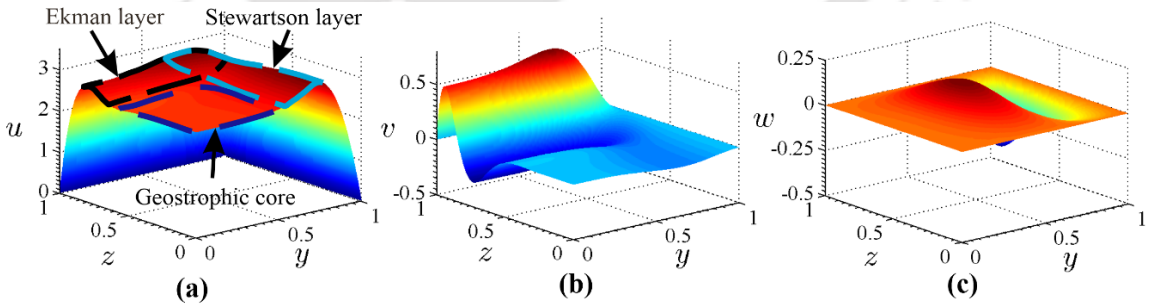

Figure 4.4: Velocity profiles of u, v and w velocity, obtained for $\kappa_p = 10$, $d = 0.3$, $\alpha = 5$, $\Gamma = 0.5$, $\mathrm{Re}_\omega = 150$ and $\kappa = 12$.

In the present set up, the flow is driven by the combined influences of the gyrostatic pressure gradient and the electroosmotic force. In the asymptotic limit of geostrophic plug flow (Ro~0), as depicted in Fig. 4.4(a), a plug-like axial velocity profile appears with a geostrophic core at the center, Ekman layer at the upper wall (i.e., at $z = +1$) and Stewartson

layer at the left wall of the channel (i.e., at $y = +1$). As seen in Fig. 4.4(a), the magnitude of axial velocity u increases from zero to its peak within both the Ekman layer and the Stewartson layer, while it assumes a nearly constant trend in the geostrophic core. To be precise, this typical flow behaviour is in complete agreement with the well-established Taylor-Proudman theorem, i.e., $\partial_z(u,v) = 0$ and $(u,v).(\partial_x p_g, \partial_y p_g) = 0$ (Pedlosky, 1987). Analogous to this theorem and upon satisfying the constraint of mass conservation principle $\nabla.\mathbf{u} = 0$, we obtain the profiles of v and w velocities as depicted in Figs. 4.4(b) and 4.4(c), respectively. Note that the flat depression in the velocities u and v at the inviscid interior emanates owing to the definite balance between the Coriolis force and the pressure gradient for $\mathrm{Re}_\omega >> O(10^0)$ (Kheshgi & Scriven, 1985; Speziale, 1982).

Notable insights, as observed from Figs. 4.3 and 4.4, are in support of the effectiveness of the variational calculus method in predicting the flow dynamics in grafted PEL modulated rotational fluidics. Having established the accuracy of the present theoretical model, we now proceed for the systematic discussion of the underlying transport features, as depicted in the forthcoming sections.

4.5 Effect of PEL on Rotational Electrohydrodynamics

It may be mentioned here that, in rotational microfluidics, the Coriolis force adversely affects the deliverance of the prime objective of the micro total analysis systems, i.e., augmented mixing without compromising the net throughput (Ng & Qi, 2015). Although assisted by the electroosmotic effect, yet the rotational induced forces bring in a restriction on the underlying mixing performance as well as on the net throughput beyond certain rotational speeds. Therefore, ensuring these objectives with equal priority demands a severe challenge in the design of state-of-the-art LOC based microfluidic devices. To this end, the grafted PEL at the walls of the narrow-fluidic channel has shown tremendous potential, attributed primarily to their inherent physico-chemical characteristics to control the underlying transport. Considering this feature of PEL, we discuss, in this section, the flow dynamics in a rotating narrow-fluidic channel, as influenced by the grafted PEL at the walls. Note that for the subsequent discussion, we consider a higher rotational speed, as manifested by a relatively larger $\mathrm{Re}_\omega (\gg 1)$.

4.5.1 Primary Flow

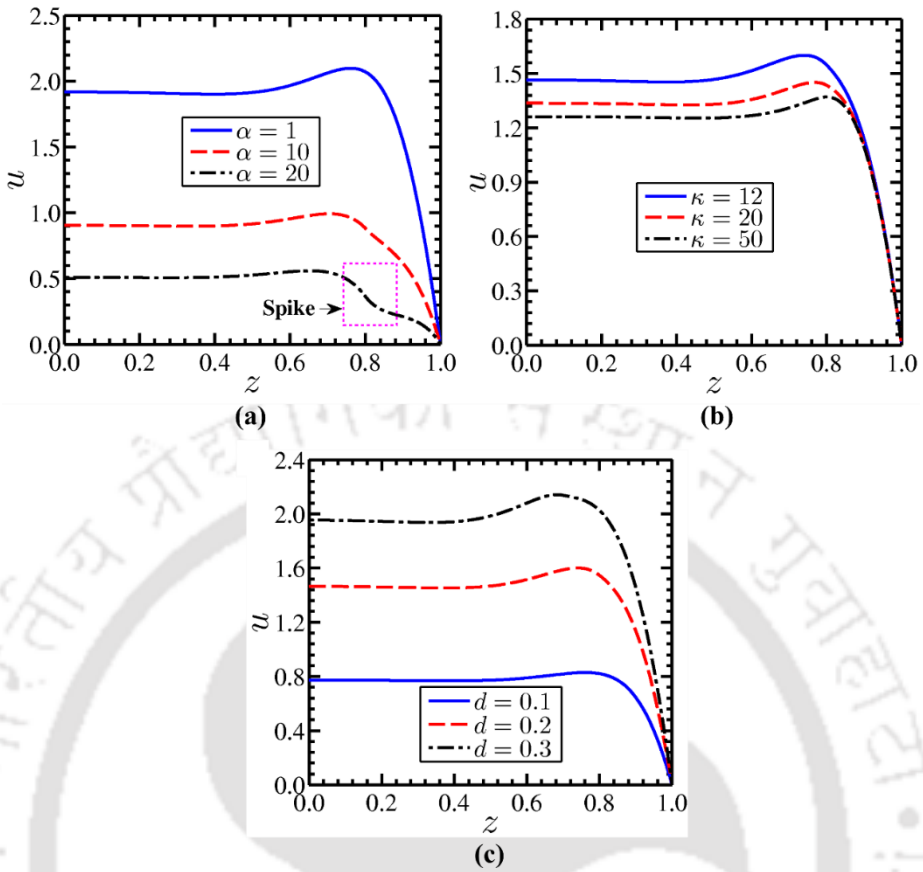

Figure 4.5: Plots of axial velocity for the variation of drag parameter α (= 1, 10 and 20), DH parameter of EL κ (= 12, 20 and 50) and PEL thickness d (= 0.1, 0.2 and 0.3). The other parameters considered for this analysis are: (a) $\kappa_p = 10$, d = 0.2, κ = 12, Γ = 0.5, $Re_\omega = 100$; (b) $\kappa_p = 10$, d = 0.2, α = 5, Γ = 0.5, $Re_\omega = 100$; and (c) $\kappa_p = 10$, α = 5, Γ = 0.5, $Re_\omega = 100$ and κ = 12.

In Figs. 4.5(a)-(c), the plots show the influence of the physico-chemical parameters of the PEL on the primary flow dynamics. For these plots, we have considered three different values of (a) drag parameter α (= 1, 10 and 20), (b) DH parameter of EL κ (= 12, 20 and 50), and (c) PEL thickness d (= 0.1, 0.2 and 0.3). The plots in Figs. 4.6(a) and 4.6(b) show the variation in the potential distribution with a change in κ and d respectively. In Fig. 4.6(c), the plots depict the variation of electroosmotic force F_e with κ. Note that the depicted variations in Fig. 4.6 are useful to correlate the distribution of axial flow velocity shown in Fig. 4.5. Also, the inferences of Fig. 4.6 will be referred to explain the results, as discussed in the forthcoming sections.

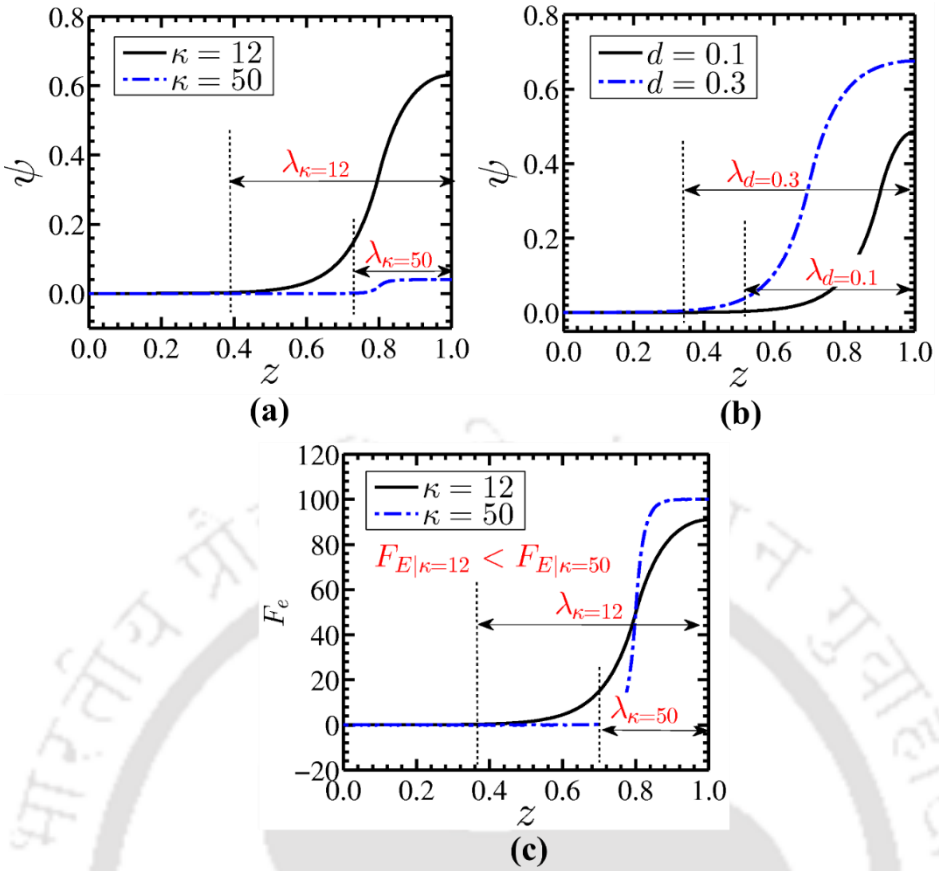

Figure 4.6: (a)-(b) Potential distribution: Plots show the distribution of the induced electrostatic potential ψ for different values of DH parameter of EL κ (= 12 and 50) and PEL thickness d (= 0.1 and 0.3), respectively. (c) Variation of electroosmotic force with DH parameter of EL: Plots show the variation of electroosmotic force (F_E) for different values of DH parameter of EL κ (= 12 and 50). The other parameters considered are: (a) and (c) $d = 0.2$, $\kappa_p = 10$; (b) $\kappa = 12$, $\kappa_p = 10$.

We observe in Fig. 4.5 that the primary flow and the intensity of depression in the geostrophic core are comparatively higher for lower values of α (= 1) and κ (= 12), and higher value of d (= 0.3); although the rotational speed is remaining unaltered. This variation in the intensity of depression in the geostrophic core is attributed to the effect of Coriolis force $\mathrm{Re}_\omega \times \mathbf{u}$, which not only varies with the rotational speed Re_ω but also depends on the magnitude of flow velocity $|\mathbf{u}|$ (Kheshgi & Scriven, 1985; Ng & Qi, 2015; Speziale, 1982). In the present study, the magnitude of flow velocity largely depends on the electroosmotic effect and Darcy's frictional drag in PEL, thus is governed by the magnitude of pertinent parameters viz., α, κ, and d. Note that α = 1 signifies relatively lower drag force in the PEL region, whereas, for κ =12 (Fig. 4.6(a)) and d = 0.3 (Fig. 4.6(b)), the electroosmotic effect becomes stronger. As shown in Figs. 4.6(a)-(c), for κ =12 and d = 0.3, the stronger ionic interactions between polyelectrolyte and electrolyte ions

leads to an increasing magnitude of electrostatic potential ψ, which, in turn, enhances the electroosmotic effect. It is also observed in Figs. 4.6(a)-(c) that the thickness of EDL obtained for κ=12 and d = 0.3 is higher than their respective counterparts, signifying a thicker influencing regime of the electroosmotic effect in the channel for the said values. A relatively higher magnitude of potential together with its influence up to a larger distance for d = 0.3, as seen in Fig. 4.6(b), is suggestive of achieving higher EDL thickness for the said value. Therefore, the magnitude of primary flow velocity is expected to be higher for lower α, lower κ, and higher d, as witnessed in Figs. 4.5(a)-(c). Quite notably, with an increasing magnitude in the flow velocity for $\kappa = 12$, $d = 0.3$ and $\alpha = 1$, the magnitude of the Coriolis force $\mathrm{Re}_{\omega} \times \mathbf{u}$ increases since it linearly scales with the flow velocity. Thus, the higher Coriolis force for $\kappa = 12$, $d = 0.3$ and $\alpha = 1$ results in a noticeable depression in the geostrophic core as seen in Figs. 4.5(a)-(c).

However, as observed in Fig. 4.5(b), the difference between the magnitude of fluid velocities obtained for two consecutive values of κ within its considered range $12 < \kappa < 50$ becomes minute. This observation is attributed to the close competition between the thicker influencing regime of smaller electroosmotic effect for the lower value of $\kappa = 12$ and the thinner influencing regime of higher electroosmotic force for the higher value of $\kappa = 50$. To support this argument, we have shown in Fig. 4.6(c) the variation of the electroosmotic force with a change in the DH parameter of EL. In Fig. 4.6(c), we can observe that despite having a higher magnitude of ψ (as observed in Fig. 4.6(a)), the magnitude of the electroosmotic force is smaller for $\kappa = 12$. On the contrary, for $\kappa = 50$ (see Fig. 4.6(c)), the electroosmotic force becomes higher, albeit the magnitude of ψ is seen to smaller (see Fig. 4.6(a)). In this variation, as per the definition of the electroosmotic force $\kappa^2\psi$, the higher counterion density of the electrolyte for $\kappa = 50$ gives rise to the higher magnitude of the electroosmotic force. However, due to thinner EDL for $\kappa = 50$ as shown in Fig. 4.6(a), the influence of electroosmotic force being acted in the domain is comparatively smaller than that for $\kappa = 12$ (see Fig. 4.6(c)). In other words, the thicker influencing regime of the electroosmotic effect corresponding to the thicker EDLs for $\kappa = 12$ plays a dominant role here. On account of this, a minute variation in the electroosmotic force is obtained in Fig. 4.6(c) for a change in κ from 12 to 50. Consequently, as observed in Fig. 4.5(b), the difference in the magnitude of u velocity profile becomes small when κ varies from 12 to 50. Precisely, it is because of this reason; the peak of u velocity for both the values of κ

(12 and 50), as observed in Fig. 4.5(b), occurs approximately at the same z-location. Notably, this observation signifies a small change in the Ekman layer thickness with a change in κ.

Also, we observe in Fig. 4.5(a) that the velocity profile obtained for α = 20 exhibits a small spike in the region close to the channel wall, albeit the appearance of such a spike is absent for the other cases under consideration. The presence of this spike in the velocity profile is attributed to the relatively larger Darcy drag force in the PEL region, realized for α = 20. For other values of α (= 1 and 10), the electroosmotic force dominates the flow dynamics as the drag force is comparatively lower. The higher electroosmotic force wipes out the appearance of a small spike from the respective velocity profiles, as seen in Fig. 4.5(a). The influence of these parameters is also significant for the development of secondary flows in the present flow configuration. Note that the formation of secondary flow vortices is of paramount significance towards meeting the demand for essential fluidic functionalities of the current endeavour, i.e., the rapid and enhanced mixing of the species being transported through the channel. Paying attention to this aspect, we make an effort to critically review the development of secondary flows in greater detail in the forthcoming section.

4.5.2 Secondary Flow

4.5.2.1 Development of Secondary Flows: Consistency with the Experimental Observations

The vortex structure pertaining to secondary flow obtained in the present study is exactly similar to the double vortex configuration reported in the literature (Ng & Qi, 2015). For the clear visualization of the double vortex, we show in Fig. 4.7(a), the contour plot of stream function obtained for $\kappa_p = 10$, $d = 0.05$, $\alpha = 1$, $\Gamma = 0.5$, $\mathrm{Re}_\omega = 100$ and $\kappa = 50$. As depicted in Fig. 4.7(a), the secondary flow assumes a double vortex configuration with a clockwise vortex in the upper half ($z > 0$), and a counter-clockwise vortex in the lower half ($z < 0$) of the channel. It is worth to mention here that the geometrical features of these vortices are reminiscent of the structure of the geostrophic vortices as reported in the literature (Ng & Qi, 2015; Pedlosky, 1987). Also, the double vortex configuration, as observed in Fig. 4.7(a), becomes similar with those captured in experimental investigations as well as numerical analysis (Kaushik, Mondal, et al., 2017; Kheshgi & Scriven, 1985; Jacob H. Masliyah, 1980; Ng & Qi, 2015; Speziale, 1982), albeit different from the

perspective of quantitative comparison.

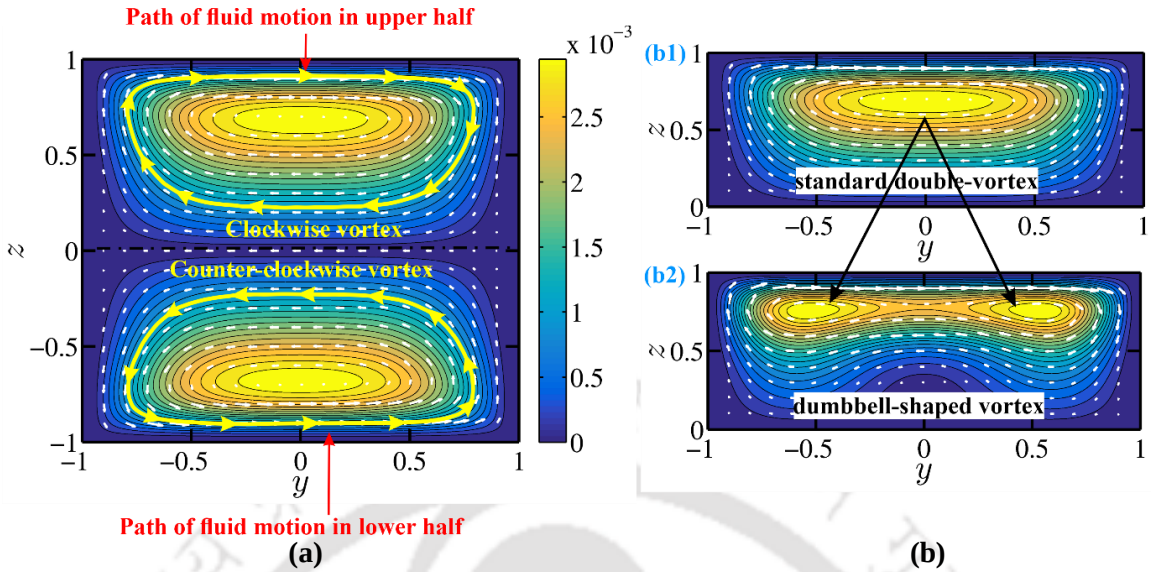

Figure 4.7: (a) Contour plot showing the double vortex configuration, with a clockwise vortex in the upper half of the cross-section and counter-clockwise vortex in the lower half. The analysis is performed for $\kappa_p = 10$, $d = 0.05$, $\alpha = 1$, $\Gamma = 0.5$, $Re_\omega = 100$ and $\kappa = 50$. Note that for depicting the symmetric nature of the vortices in each half of the channel, we plot the absolute stream function in (a). (b) Contour plots in (b1) standard double vortex and in (b2) dumbbell-shaped vortex demonstrating the shift in the centroid of the vortex. The standard double vortex in (b1) is obtained for $\kappa_p = 10$, $d = 0.05$, $\alpha = 20$, $\Gamma = 0.5$, $Re_\omega = 100$ and $\kappa = 50$ whereas the dumbbell-shaped vortex in (b2) is obtained for $\kappa_p = 10$, $d = 0.3$, $\alpha = 1$, $\Gamma = 0.5$, $Re_\omega = 100$ and $\kappa = 12$. Note that the values of the parameters considered for obtaining the standard double vortex in (b1) are similar to that of (a).

Pertinent to this analysis of the secondary flow vortices, we make an attempt here to discuss the formation of different vortex configurations under the influence of PEL modulated electrostatics. In the rotational fluidics, the non-trivial geometrical features of the secondary flow such as the double vortex configuration come into the picture because of the Coriolis force. The fluid under the influence of Coriolis force moves towards the vertical walls of the channel, from where it turns to the horizontal walls and then to the oppositely placed vertical walls of the channel (refer to the path of fluid motion shown in Fig. 4.7(a)). The path of such fluid motion in the entire cross-section gives rise to the formation of double vortex configuration. Such a vortex structure includes the clockwise vortex in the upper half and the counter-clockwise vortex in the lower half, as shown in Fig. 4.7(a).

Formation of standard double vortex configuration. For a comparatively smaller strength of the Coriolis force, the motion of the fluid as discussed above (in the context of Fig. 4.7(a)) remains undisturbed. In effect, the weak secondary flow corresponding to the

smaller strength of the Coriolis force makes a parallel arrangement of the streamlines at the middle-section (geostrophic core) and the horizontal walls (Ekman layer) of the channel (see Figs. 4.7(a)-(b1)). Such vortex geometry is commonly observed in the paradigm of rotational microfluidics and defined as *the standard double vortex* since its shape resembles what has been observed in the literature for both low Rossby number flows as well as low rotational Reynolds number flows (for weak Coriolis force) (Kheshgi & Scriven, 1985; Nandakumar et al., 1991; Ng & Qi, 2015). Note that such a small magnitude of Coriolis force $\mathrm{Re}_{\omega} \times \mathbf{u}$ is attributable to the weak strength of the primary flow (as discussed previously). As a result, we observe in Fig. 4.7(b1) that the higher PEL drag ($\alpha = 20$) or higher DH parameter of EL ($\kappa = 50$) or thin PEL ($d = 0.05$), leads to the development of a standard double vortex. Quite notably, combined effects of the weak primary flow strength (refer to Figs. 4.5(a)-(c) for primary flow) and the weak Coriolis force result in the standard double vortex structure, as discussed above.

Formation of the dumbbell-shaped vortex. For the stronger Coriolis force, the magnitude of secondary flow increases through the Ekman layer (Ng & Qi, 2015). It may be mentioned here that the stronger Coriolis force arises due to the higher magnitude of the primary flow strength. However, in contrast to the confinement of the secondary flow only in the Ekman layer, the primary flow is present over the entire cross-section of the channel. This feature is visualized in Figs. 4.5(a)-(c) wherein the primary flow seems to be present in the entire cross-section. Whereas the secondary flow, as shown in the contour plots (obtained for comparatively higher Coriolis force) of Figs. 4.8 and 4.9, is found to be present near the horizontal walls of the channel only. This observation is suggestive of the fact that the secondary flow due to its weak magnitude in the geostrophic core is getting compressed by the primary flow therein. As a result of this phenomenon together with the symmetric nature of the primary flow about the center of the channel, the secondary flow gets compressed in all directions from the geostrophic core. The overall effect of this underlying phenomenon gives rise to the shifting of fluid mass towards the corners and results in the formation of the separate centroids in each quadrant of the channel cross-section (refer to Fig. 4.7(b2)). Note that the shifting of fluid mass also causes the compression of streamlines near the horizontal walls of the channel (refer to Fig. 4.7(b2)). Under such conditions, the shape of the vortex formed in each half of the cross-section (upper and lower) is reminiscent of the dumbbell shape, thus termed as the *dumbbell-shaped vortex* (Ng & Qi, 2015). As per the definition of the Coriolis force, to obtain such a dumbbell-shaped vortex, the rotational

system needs comparatively higher magnitude of fluid velocity. As established in the literature, such requirement of the higher velocity field in the rigid rotating narrow-fluidic channel gets supplemented by the strong electroosmotic flow (Ng & Qi, 2015). It is worth mentioning here that the strength of the electroosmotic flow can be further enhanced by the use of grafted polyelectrolyte layer on the walls of the channel. The thicker electric double layer formed at the walls of the soft narrow-fluidic channels provides stronger electroosmotic flow and assist in the building of the Ekman layer. On account of this advantageous feature of the soft narrow-fluidic channel, we observe the dumbbell-shaped vortex in Fig. 4.7(b2) resulting from the higher primary flow (refer to Figs. 4.5(a)-(c)) obtained for the lower PEL drag ($\alpha = 1$), lower DH parameter of EL ($\kappa = 12$) and higher PEL thickness $(d = 0.3)$.

4.5.2.2 Secondary Flow Structure: Influence of the Physico-Chemical Parameters

Next, we show, in Figs. 4.8(a)-(d) and Figs. 4.9(a)-(c), the contour plots of secondary flow, obtained for different parameters pertinent to this analysis. Note that in Figs. 4.8(a)-(d), the effect of drag parameter α (= 1 and 20) and DH parameter of EL κ (= 12 and 50) on the secondary flow vortices are portrayed, while Figs. 4.9(a)-(c) describes the secondary flow structure for different PEL thickness d (= 0.05, 0.1 and 0.3). In Figs. 4.8(a)-(d) and Figs. 4.9(a)-(c), we find the dumbbell-shaped vortices, except for a higher drag parameter $\alpha = 20$ and lower PEL thickness $d \leq 0.1$. The vortex in each half (upper and lower half) of the channel cross-section divides itself to form a pair of vortices, each resembling the shape of the dumbbell lobe. Note that the formation of these compressed stream tubes, which are the consequences of the combined effect of the higher electroosmotic force and the Coriolis force on the underlying transport, signifies the higher Ekman pumping in the channel. Thus, it may be mentioned here that the presence of these dumbbell-shaped vortices in the secondary flow structure is an indication of the presence of higher electroosmotic force as well as the resulting Coriolis force (since the strength of the Coriolis force being $\mathrm{Re}_{\omega} \times \mathbf{u}$ indirectly depends on the electroosmotic force) in the present flow configuration. Therefore, the higher the strength of these forces, the higher will be the strength of dumbbell-shaped vortices appearing in the secondary flow structure.

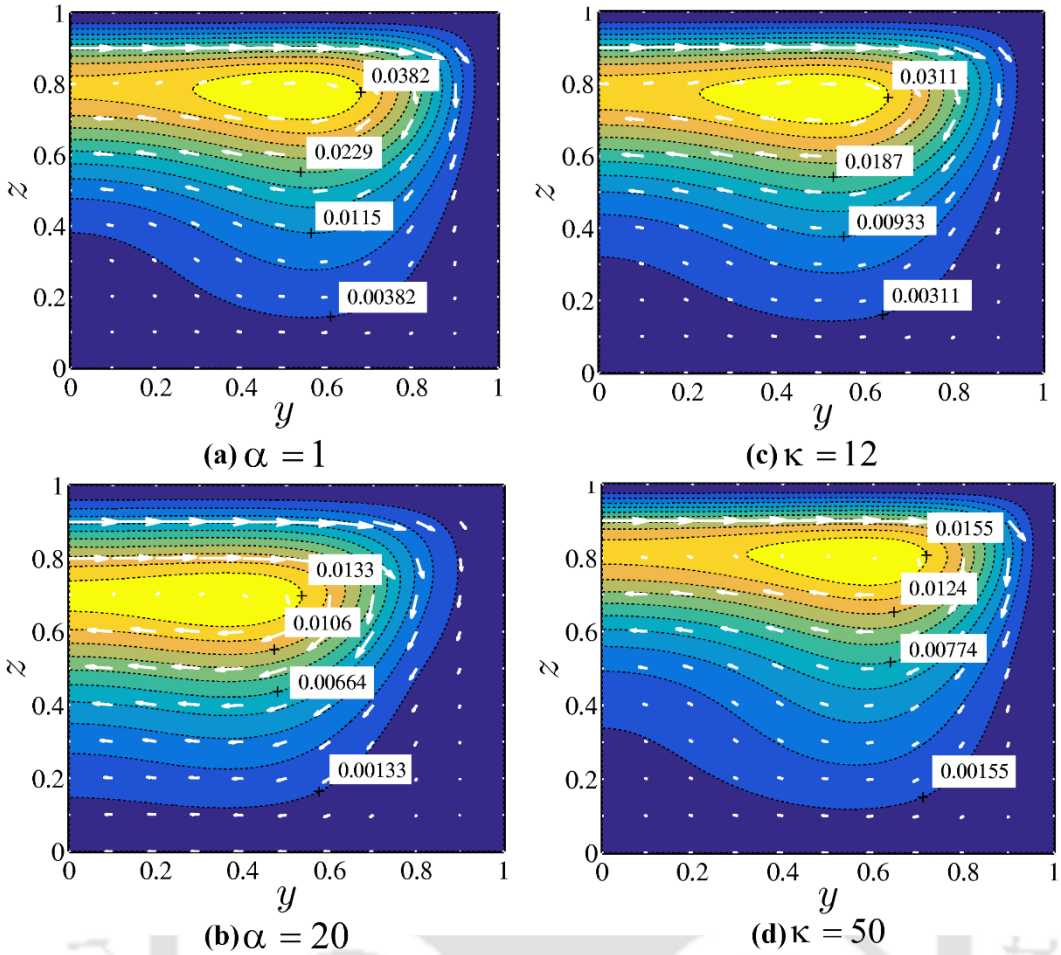

Figure 4.8: Contour plots show the secondary flow distribution in the channel for different values of (a)-(b) drag parameter α (= 1 and 20) and (c)-(d) DH parameter of EL κ (= 12 and 50). The other parameters considered for this analysis are: (a)-(b) $\kappa_p = 10$, $d = 0.2$, $\Gamma = 0.5$, $Re_\omega = 100$, $\kappa = 12$; (c)-(d) $\kappa_p = 10$, $d = 0.2$, $\alpha = 5$, $\Gamma = 0.5$, $Re_\omega = 100$.

Influence of the drag parameter. In Figs. 4.8(a)-(b), we observe the dumbbell-shaped vortices for $\alpha = 1$ and standard double vortex configuration for $\alpha = 20$. In case of a higher drag parameter α (= 20), Darcy's frictional drag offered by the PEL dominates over the electroosmotic force and reduces the fluid velocity. Notably for $\alpha = 20$, we observe a small spike in the axial velocity profile in Fig. 4.5(a). Thus, following the definition of the Coriolis force ($Re_\omega \times \mathbf{u}$), it can be argued here that the strength of the Coriolis force will be reduced for $\alpha = 20$. Precisely, this reduction in the strength of the Coriolis force reduces the Ekman pumping power, as manifested by the diffused streamline pattern near the horizontal walls, and results in the formation of the standard double vortex configuration in Fig. 4.8(b). On the contrary, for $\alpha = 1$, a relatively smaller magnitude of the frictional drag force as compared to that of $\alpha = 20$ strengthens the PEL modulated electroosmotic flow near the walls. This results in the higher secondary flow velocities in the channel and

a stronger Ekman pumping near the horizontal walls. Consequently, we observe the dumbbell-shaped vortices for $\alpha = 1$ in Fig. 4.8(a).

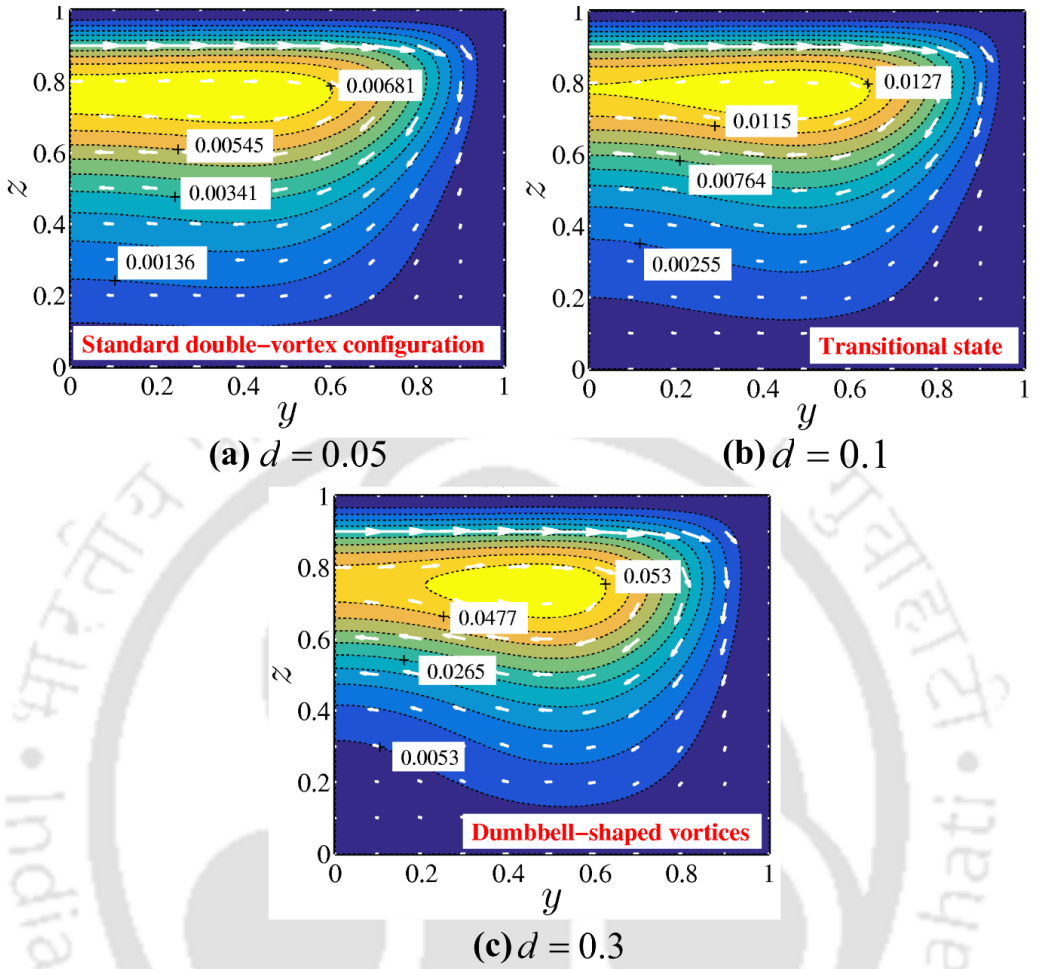

Figure 4.9: Contour plots show the secondary flow distribution in the channel for different values of PEL thickness d (= 0.05, 0.1 and 0.3). The other parameters considered for this analysis are: $\kappa_p = 10$, $\alpha = 5$, $\Gamma = 0.5$, $Re_\omega = 100$ and $\kappa = 12$.

Influence of the DH parameter of EL. In Figs. 4.8(c)-(d), we observe an insignificant change in the shape of vortex when the value of κ changes from 12 to 50. However, the value of stream function is observed to be high for $\kappa = 12$ than that of $\kappa = 50$, signifying the strength of higher secondary flow for $\kappa = 12$. This observation is attributed to the close competition between a thicker influencing regime of lower electroosmotic force for $\kappa = 12$ and a thinner influencing regime of higher electroosmotic force for $\kappa = 50$ (refer to Fig. 4.6(c) and section 6.1 for a detailed discussion). This complex variation in the electroosmotic force and its effective influencing regime near the walls (in Fig. 4.6(c)) with a change in κ gives rise to a minimal change in the primary flow, as observed in Fig. 4.5(b). It is because of this reason the difference in the velocity profiles as well as its consequences to establish a difference in the thickness of the Ekman layer for the chosen

values of κ becomes very small, as witnessed in Fig. 4.5(b). Notably, this minute variation in the Ekman layer thickness with κ, as observed in Fig. 4.5(b), is further reflected by a small change in the vortex structure in Figs. 4.8(c)-(d). It may be mentioned here that the influence of the Coriolis force on the underlying transport gives rise to this correlative effect between the primary flow (in Fig. 4.5(b)) and the secondary flow (in Figs. 4.8(c)-(d)). Note that the relatively thicker influencing regime of the electroosmotic force for $\kappa = 12$ assists in the formation of the dumbbell-shaped vortices with comparatively higher magnitude, as seen in Fig. 4.8(c).

Influence of PEL thickness. Next, in Figs. 4.9(a)-(c), we show the structure of the secondary flow vortices developed in the flow field for three different values of $d = 0.05$, 0.1 and 0.3, respectively. We observe in Fig. 4.9(c) the existence of dumbbell-shaped vortices for higher PEL thickness $d = 0.3$, having higher strength of the Ekman pumping as well. On the other hand, for $d = 0.1$, the vortex structure is in the transition state between the standard double vortex configuration and the dumbbell-shaped vortex, with a relatively lower strength of the Ekman pumping. Note that the special case of $d = 0.05$, which is almost closer to the case of a rigid channel, shows a perfect standard double vortex configuration in Fig. 4.9(a). We attribute these observations to the variation of the electroosmotic force under the modulation of PEL thickness. The higher the PEL thickness, higher will be the electrostatic potential, as shown in Fig. 4.6(b), and this higher potential boosts up both the electroosmotic force (directly) as well as the Coriolis force (indirectly following the magnitude of flow velocity). Consequently, the higher magnitude of the Coriolis force arising from the relatively higher PEL thickness $d = 0.3$ gives rise to higher Ekman pumping and hence results in the formation of the dumbbell-shaped vortices as apparent from Fig. 4.9(c). In contrast, the transitional feature of the secondary flow vortex for smaller PEL thickness ($d = 0.1$), as seen in Fig. 4.9(b), is due to the reduction in the strength of both the electroosmotic and Coriolis forces for the pertinent case.

Quite notably, the transitional state of vortex structure obtained for $d = 0.1$ is showing a similar qualitative configuration with the vortices developed in the rotational flows through a rigid, narrow channel. To substantiate this inference further in the context of the present analysis, we show in Fig. 4.9(a) the vortex structure for PEL thickness $d = 0.05$. As can be seen in Fig. 4.9(a), we can get a perfect standard double vortex pattern for $d = 0.05$, which is similar to the reported vortex structure formed in a rigid rotating narrow channel (Ng & Qi, 2015). Note that for such a small PEL thickness $d = 0.05$, the

influence of PEL on the flow dynamics can be considered to be negligible, thus the underlying transport feature signifying the flow scenario of a rigid, narrow channel with a common pressure-driven configuration.

The secondary flow vortices being developed in the flow field of the present configuration are essential for the mixing phenomenon in the rotating channel. It is worth to mention here that the augmented secondary flow strength for the cases of $\kappa = 12$ (Fig. 4.8(c)) and $d = 0.3$ (Fig. 4.9(c)) alongside the formation of standard double vortex configuration observed for $\alpha = 20$ in Fig. 4.8(b), plays an essential role in the mixing dynamics when the rotational speed of the channel is considerably high. From the ongoing discussion, it can be inferred that the flow dynamics in a rotating narrow-fluidic channel with a built-in polyelectrolyte layer exhibits the modulation of complex secondary flow vortices, as evident from Figs. 4.8 and 4.9. The attributable feature behind this observation is the grafted polyelectrolyte layer modulated enriched interfacial electrostatics and its effect on the alteration in the magnitude of the rotation induced forcing. To be precise, as a result of this analysis presented till now, we believe that the imposition of soft polyelectrolyte layers offers an avenue in tuning the structure as well as the strength of recirculation zones (equivalently, the secondary flow vortices) being formed in the flow field. In view of this unique feature of the soft polyelectrolyte layer on the electrohydrodynamics in the rotating narrow-fluidic channel, we next make an effort to look at its extended effect on the underlying mixing dynamics critically.

4.6 Effect of PEL Modulated Electrohydrodynamics on the Mixing: Analysis, Results, and Discussion

In line with the prime objective of the present endeavour, we have investigated in this section the mixing dynamics in the soft narrow-fluidic channel embedded in the rotating platform. We look at the underlying mixing from the perspective of both qualitative and quantitative assessments. To perform the qualitative analysis, we focus on the Poincaré maps at different axial locations of the channel. On the other hand, to quantify the mixing strength, we analyze the variation in the mixing index obtained by using the concept of entropy of mixing. Both these methods are based on the Lagrangian approach, in which the passive tracer particles of multispecies are traced in the 3D computational domain with the help of Eulerian velocity fields. We now systematically discuss the procedure and results obtained from these methods as follows.

4.6.1 Poincaré Maps

To obtain the qualitative information of the mixing dynamics, we focus on the Poincaré maps obtained at different axial locations of the channel. The traces of the passive tracer particles in 3D computational domain produce the Poincaré maps. These traces can be calculated by using the following Lagrangian equations, which rely on the Eulerian velocity fields (u, v, w) obtained from the previous calculations.

$$u = \frac{\partial x}{\partial t} \tag{4.21a}$$

$$v = \frac{\partial y}{\partial t} \tag{4.21b}$$

$$w = \frac{\partial z}{\partial t} \tag{4.21c}$$

It can be seen that Eqs. (4.21a) -(4.21c) are integrable with respect to time. In contrast, the Poincaré maps show the y and z locations of the particles in the cross-section of the channel at the desired axial (along x-coordinate for this analysis) location. This implies that the secondary flow velocities should be integrated with respect to the axial coordinate x. In doing so, we have divided Eqs. (4.21b) and (4.21c) by Eq. (4.21a).

$$\frac{\partial y}{\partial x} = \frac{v}{u} \tag{4.22a}$$

$$\frac{\partial z}{\partial x} = \frac{w}{u} \tag{4.22b}$$

The magnitudes of the velocities u, v and w at the updated locations (y and z) are obtained by using the function-griddedInterpolant(cubic) in Matlab 2019a. Unless mentioned specifically, the step size in the axial direction, i.e., Δx is taken as 10^{-3}, and the total length of the channel, to be consistent with our previous assumption made in Section 4.4.1, is considered as 10^3. In Fig. 4.10(a), the sample trajectories of a few tracer particles of two different types [particles $P_{a,1}$ and $P_{a,2}$ in Figs. 4.10(a) and 4.10(b)] are shown in the 3D computational domain.

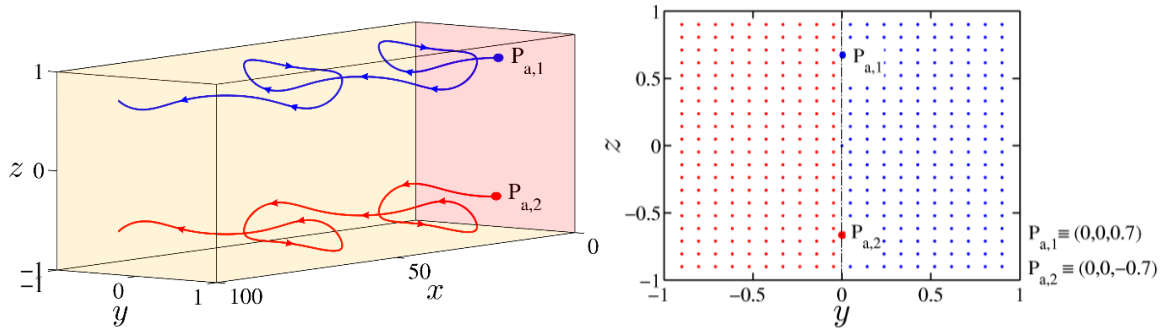

(a) **(b)**

Figure 4.10: (a) Sample trajectories of tracer particles in the 3D computational domain: Trajectories of a few tracer particles (Pa,1 and Pa,2) in a 3D computational domain are shown in (a) for $\kappa_p = 10$, $d = 0.3$, $\Gamma = 0.5$, $Re_\omega = 150$, $\kappa = 12$ and $\alpha = 5$. Pa,1 and Pa,2 are initially located at (0,0,0.7) and (0,0,-0.7) respectively. (b) Poincaré map at inlet: Specified initial positions of 20×20 tracer particles in the $y - z$ cross-section shown in (b). The colours of the particles: red and blue, distinguish the species considered for the calculation.

In Fig. 4.10(a), we observe that the tracer particles ($P_{a,1}$ and $P_{a,2}$), trapped in the dumbbell-shaped vortices (depicted in Figs. 4.8 and 4.9), follow a *periodic-helical* motion, primarily attributed to the periodic motion of the fluid particles therein. Also, the trajectory of a blue particle $P_{a,1}(\equiv(0,0,0.7))$ released from the upper half of the channel exactly forms a mirror image of the trajectory of red particle $P_{a,2}(\equiv(0,0,-0.7))$ released from the lower half. Note that the pathlines of particles $P_{a,1}$ and $P_{a,2}$ depicted in Fig. 4.10(a) show similar morphology with the corresponding streamline contours shown in Figs. 4.8 and 4.9. By depicting the traces of particles $P_{a,1}$ and $P_{a,2}$ in Fig. 4.10(a), we intend to convey that in the present flow configuration, the stream of the particles (represented by blue particle $P_{a,1}$) released from the upper half of the channel (about the line $z = 0$ and parallel to y-axis) will mix insignificantly with the particles (represented by red particle $P_{a,2}$) being released in the lower half. In regard to this aspect, we have considered here that the particles of the different species are injected through the left half and right half (two symmetry halves about the line $y = 0$ and parallel to z-axis) of the channel, as shown in Fig. 4.10(b). The colours of the particles, red for the right half and blue for the left half (if observed from the inlet), distinguish the species considered for the calculation.

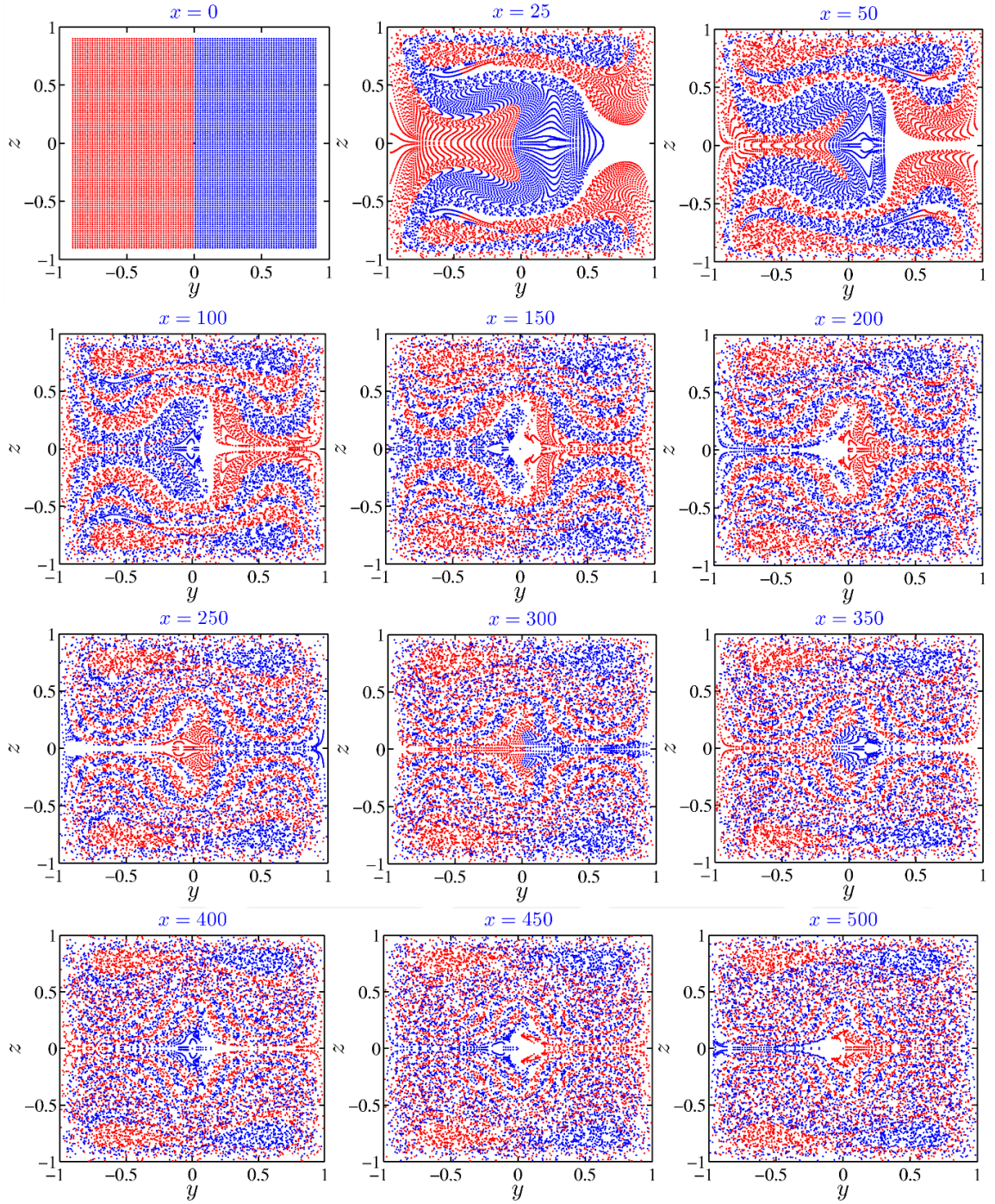

Figure 4.11: Axial evolution of the Poincaré maps: Plots show the axial evolution of the Poincaré maps, obtained for $\kappa_p = 10$, $d = 0.3$, $\Gamma = 0.5$, $Re_\omega = 150$, $\kappa = 12$ and $\alpha = 5$. These parameters are similar to that of considered for figure 4. The plots are obtained at: x = 0, 25, 50, 100, 150, 200, 250, 300, 350, 400, 450 and 500. The number of particles considered is 100x100.

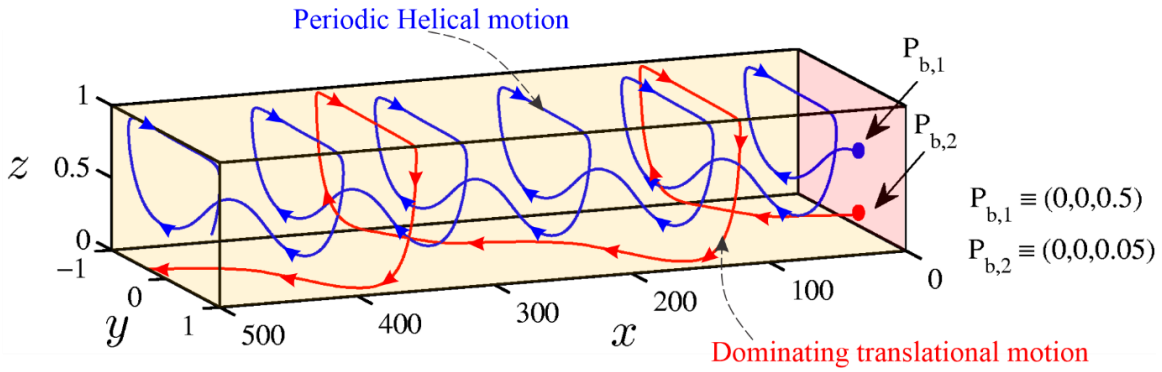

Figure 4.12: Trajectories depicting the variation in the periodicity obtained in the motion of two different particles (Pb,1 and Pb,2) initially located at (0,0,0.5) and (0,0,0.05), respectively. Note that the plots are depicted in the upper half section of the channel. The other parameters considered for this analysis are: $\kappa_p = 10$, $d = 0.3$, $\Gamma = 0.5$, $Re_\omega = 150$, $\kappa = 12$ and $\alpha = 5$.

Having outlined the solution procedure at the beginning of this section, we now discuss the axial evolution of the Poincaré maps depicted in Fig. 4.11 for $\kappa_p = 10$, $d = 0.2$, $\Gamma = 0.5$, $Re_\omega = 150$, $\kappa = 12$, and $\alpha = 5$. We observe in Fig. 4.11 that, beyond the location $x = 350$, the change in the Poincaré maps is insignificant except at the geostrophic core of the channel. This observation is suggestive of the efficient mixing of species, albeit qualitative, beyond $x = 350$ and except the core region. As shown in Fig. 4.12, the attributable factor behind this observed discrepancy at the core region is the delay in attaining the periodic behaviour of the fluid particles therein (precisely, the periodic motion is getting delayed). The location of the blue particle $P_{b,1}(\equiv(0,0,0.5))$ and the red particle $P_{b,2}$ $(\equiv 0,0,0.05)$ shown in Fig. 4.12, represents the particles being released from the non-geostrophic and geostrophic region of the channel, respectively. Each belongs to different species (red/blue). In the non-geostrophic region, the periodicity in the motion is quickly obtained almost after $x = 50$, visualized from the trajectory of particles in the dumbbell-shape for $x > 50$ (see Figs. 4.11 and 4.12(blue particle $P_{b,1}$)). However, the trajectories of the particles at the core region (red particle $P_{b,2}$ in Fig. 4.12) attain well-defined periodicity at a sufficiently larger distance from the inlet ($x = 500$), as observed in Figs. 4.11 and Fig. 4.12(see for red particle $P_{b,2}$). The periodicity of this motion depends on the strength of secondary flow developed in the flow field. However, due to the very small magnitude of v and w velocities at the geostrophic core (as shown by the surface plots in Figs. 4.4(b) and 4.4(c)), the strength of secondary flow and its effect in developing the periodic fluid motion becomes minuscule in the interior. Consequently, the primary flow (u -velocity) imposes the dominating translational motion instead of a periodic motion to the fluid particles at the geostrophic core, as observed in Fig. 4.12. This flow feature results in

qualitatively poor mixing at the geostrophic core as compared to that at the non-geostrophic region. This observation also implies that for the given set of governing parameters, the particles mostly passing through the core region encounter a relatively larger mixing length. For example, to achieve approximately complete mixing, the particles (red particle $P_{b,2}$) being released from the core region are expected to travel a considerable distance in the channel. This aspect is visualized from the depicted variations in both the Figs. 4.11 and 4.12: in Fig. 4.11, the stream of particular species at the core region remains poorly mixed even up to axial distance $x = 500$; and in Fig. 4.12, the time taken by red particle $P_{b,2}$ to complete the particular number of circulations (say, two in this case) is higher than that of a blue particle $P_{b,1}$.

4.6.1.1 Influence of Physico-Chemical Parameters of PEL on Mixing

Next, in Fig. 4.13, we show the influence of the physico-chemical parameters of the grafted PEL on the mixing performance using the Poincaré maps. The other parameters considered to obtain the current plots (mentioned in the caption of Fig. 4.13) are the same as that considered for depicting the secondary flow in Figs. 4.8 and 4.9. Note that in Fig. 4.13, we have intentionally shown the Poincaré maps at a section corresponding to the axial location $x = 500$, where the candidate streams of the species are partially mixed for all the cases considered. At a considerably distant axial location, precisely, at the location closer to the outlet of the channel, a change in the magnitude of pertinent parameter does not bring a noticeable difference in the Poincaré maps. This observation justifies a complete mixing at that location.

In Fig. 4.13, we observe that the mixing quality obtained for $\alpha = 20$, $\kappa = 12$ and $d = 0.3$ at an axial location $x = 500$ are qualitatively higher than that of their respective counterpart. Also, as seen in Fig. 4.13, for the other values of the chosen parameters, the particles of different species are yet to be significantly mixed until the location $x = 500$ is reached. This observation underlines the competitive strength of the dumbbell-shaped vortices vis-à-vis the effect of standard double vortex configuration on the underlying mixing phenomenon. For $\alpha = 20$, the size of the recirculation zone (standard double vortex configuration) is larger, as seen in Fig. 4.8(b), whereas the strength of the dumbbell-shaped vortices for $\kappa = 12$ and $d = 0.3$, as seen in Figs. 4.8(c) and 4.9(c) respectively, becomes higher. This higher strength and size of the vortices obtained for the cases mentioned above further lead to an enhancement in the characteristics of the chaotic region, thus resulting in

enhanced mixing performance. This observation also infers that the mixing length, i.e., the distance from the inlet of the channel where the streams significantly mix, is comparatively smaller for the cases of $\alpha = 20$, $\kappa = 12$ and $d = 0.3$.

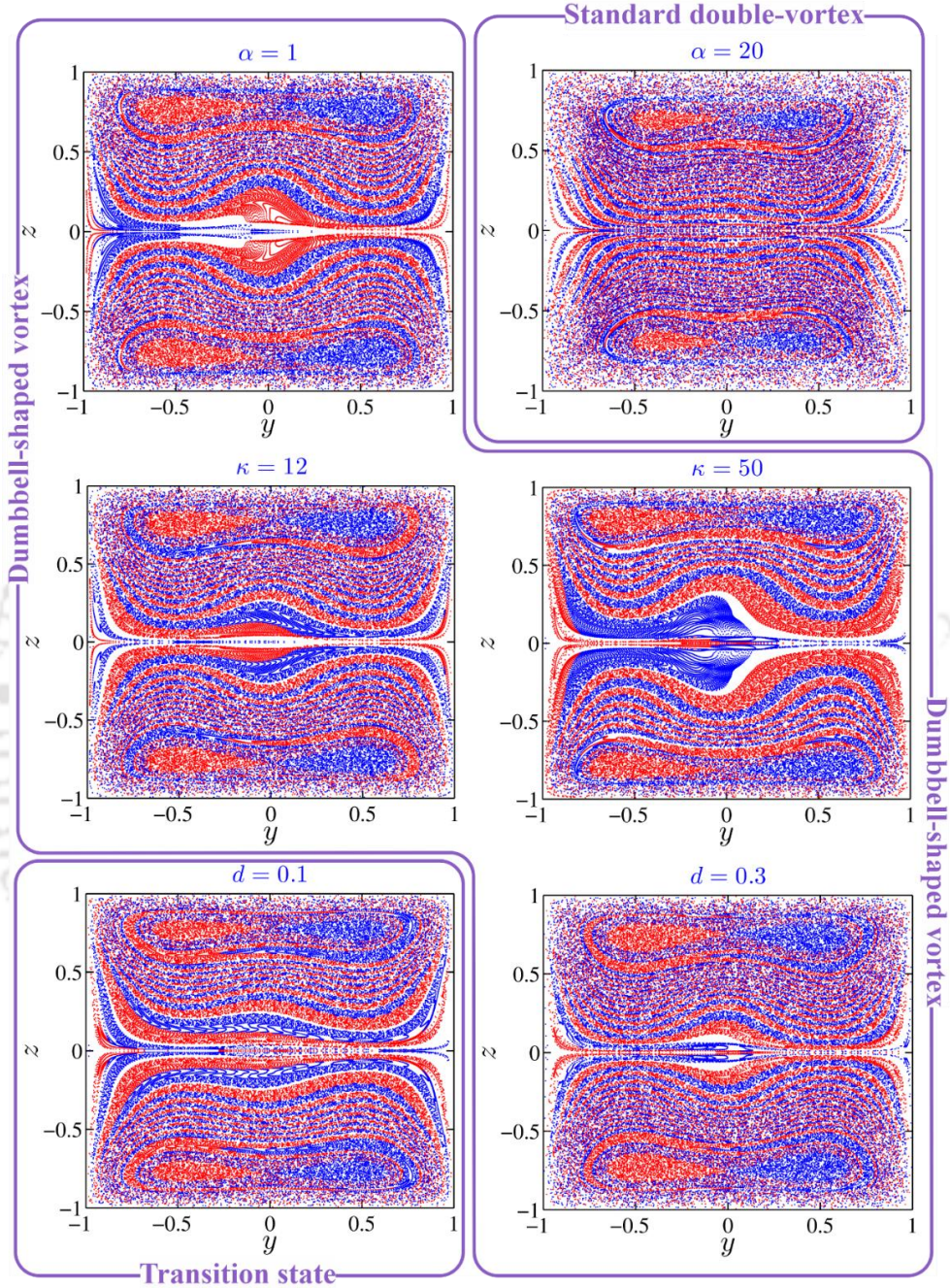

Figure 4.13: Qualitative assessment for the influence of governing parameters on mixing dynamics: Poincaré sections obtained at x = 500 to show the influence of governing parameters on the underlying mixing dynamics. The parameters considered are: drag parameter α (= 1, 20); DH parameter of EL κ (= 12, 50); and PEL thickness d (= 0.1, 0.3). The other parameters considered for the calculation are: for variation in α - $\kappa_p = 10$,Γ = 0.5, $Re_\omega = 100$, d = 0.2, κ = 12; for variation in κ - $\kappa_p = 10$, α = 5, Γ = 0.5, $Re_\omega = 100$, d = 0.2; and for variation in d - $\kappa_p = 10$, α = 5, Γ = 0.5, $Re_\omega = 100$, κ = 12. The number of particles considered is 250 x 250.

In the context of this discussion, it is important to mention here that in Fig. 4.13, we observe a minute difference between the Poincaré maps of $d = 0.1$ and $d = 0.3$. Note that for $d = 0.1$, the present fluidic setup approaches toward resembling a rigid, narrow channel and, therefore, gives rise to the formation of secondary flow vortex, which is in a transition state between the standard double vortex configuration and dumbbell-shaped vortex (discussed before in Section 4.5.2.2). Notably, the area of the recirculation zone for this transition state at $d = 0.1$ is higher than that of the dumbbell-shaped vortices obtained for $d = 0.3$ (refer to Figs. 4.9(b)-(c)). In contrast, the strength of the vortices for $d = 0.3$ is higher than that of $d = 0.1$ as seen in Figs. 4.9(b)-(c). On account of this competition between the strength and the size of the vortices, we obtain almost an equal mixing performance for both the values of d (= 0.1, 0.3), as witnessed in Fig. 4.13. Also, it can be added here that the mixing performance obtained in a rigid channel can be higher than that of the channel having thicker PELs grafted on its wall. The vortex structure obtained for the case of minimal PEL thickness (say $d = 0.05$) has a very higher recirculation area (refer to Fig. 4.9(a)) as compared to that of the higher PEL thickness (cf. Fig. 4.9(c)). However, a smaller PEL thickness ($d = 0.05$) has some adverse consequences on the underlying mixing, as discussed from the quantitative perspective in the next Section 4.6.2. Also, in Section 4.6.2, we will highlight the effect of a higher frictional drag, mainly stemming from the grafted PEL, on the mixing performance since it has similar adverse consequences.

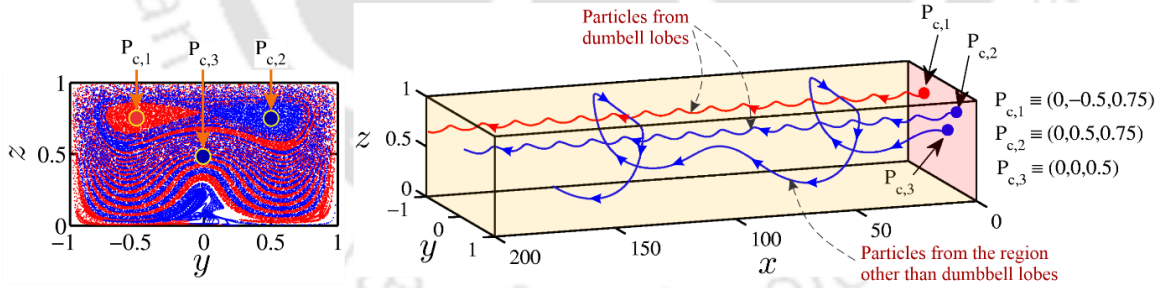

(a) **(b)**

Figure 4.14: (a) Locations of the particles at x = 500: Pc,1(≡(0,-0.5,0.75)) and Pc,2(≡(0,0.5,0.75)) are located in the dumbbell lobes whereas Pc,3(≡(0,0,0.5)) is located in the remaining region of the dumbbell-shaped vortices. (b) Trajectories depicting the isolated motion of the particles Pc,1(≡(0,-0.5,0.75)) and Pc,2(≡(0,0.5,0.75)), from the particle Pc,3(≡(0,0,0.5)). The other parameters considered for this analysis are: $\kappa_p = 10$, $d = 0.3$, $\Gamma = 0.5$, $Re_\omega = 150$, $\kappa = 12$ and $\alpha = 5$. Note that for this analysis, we have considered the intermediate segment of the channel.

Also, we observe in Fig. 4.13 that the lobes of the dumbbell-shaped vortices trap the particles of both the species. This phenomenon adversely affects the mixing performance following the event discussed as follows. The particles from these lobes do

not enter into the chaotic regime; instead, keep on moving following the undisturbed trajectories. Such trajectories are shown in Figs. 4.14(a)-(b). In Figs. 4.14(a)-(b), the plots demarcate the isolated motion of the particles $P_{c,1}(\equiv(0,-0.5,0.75))$ and $P_{c,2}(\equiv(0,0.5,0.75))$ located inside the dumbbell lobes, from a particle $P_{c,3}(\equiv(0,0,0.5))$ moving through the remaining region of the dumbbell-shaped vortex. It can be seen in Fig. 4.14 that the particles $P_{c,1}$ and $P_{c,2}$ from the dumbbell lobes never interact with a particle $P_{c,3}$ from the remaining dumbbell-shaped region. Throughout the length of the channel, the number density of particular species residing inside the dumbbell lobes (represented by particles $P_{c,1}$ and $P_{c,2}$) remains unaltered. As a result, the entropy of such discrete sections (lobes) remains constant, attributed primarily to non-intrusion of other species' particles into the lobes. This is a disadvantage of the rotational micromixers, even in the presence of the PEL modulated electrostatics. However, for $d = 0.1$ and $\alpha = 20$, the density of trapped particles inside the lobes is negligible due to the standard double vortex configuration (refer to Fig. 4.13).

The insights gained from Fig. 4.13 will be of help for the design of the proposed rotating microfluidic devices, ensuring efficient mixing. To this end, the parameters modulating the PEL electrostatics (κ, d), and the underlying hydrodynamics (α) seem to have huge consequences on the underlying mixing within the limit of asymptotic geostrophic plug flow. Having discussed the qualitative analysis of the mixing, we now focus on the quantification of the mixing dynamics in the following section.

4.6.2 Entropy of Mixing and Mixing Index

To quantify the mixing dynamics following the Lagrangian approach, we analyze the variation in the mixing index, obtained by using the concept of entropy of mixing. In this method, the computational domain represented by the Poincaré sections in Fig. 4.13 is equally divided into a finite number of discrete cells. A task integrated with this approach is to estimate the probability of finding the particles of each species indexed to each cell. The entropy of mixing in that cell is the logarithmic function of this probability, and it is the total entropy of the considered Poincaré section if averaged over the entire map. The total entropy of mixing for each Poincaré section is given by,

$$S = -\sum_{i=1}^{N_C}\left[\chi_i \sum_{j=1}^{N_S}\left(n_{i,j}\log\left(n_{i,j}\right)\right)\right] \tag{4.23}$$

In Eq. (4.23), N_C is the number of flow cells, N_S is the number of species, i, j are the

indices for cells, species, respectively, and $n_{i,j}$ is the fraction of species j in the i^{th} cell. Note that χ_i is the weighting function for each cell. It is zero if only the single type of species is present in the cell i, and it is unity if all kinds of species are present in the i^{th} cell. Further, we normalize this local entropy on the scale of [0, 1] using the maximum entropy of that Poincaré section. The maximum entropy of the specific Poincaré section is given by,

$$S_{\max} = -N_C \log\left(\frac{1}{N_S}\right) \tag{4.24}$$

The normalized entropy (or mixing index I_m) is given by,

$$I_m = \frac{S}{S_{\max}} \tag{4.25}$$

The mixing index I_m varies between '0' and '1', signifying '0' as the poor mixing quality and '1' as the complete mixing quality. Note that the value of the mixing index varies with the number of flow cells. The lower number of flow cells artificially increases the value of mixing index and vicé versa. Therefore, similar to the grid dependency test typically considered in the paradigm of computational fluid dynamics, the optimum number of flow cells can be finalized after performing the cell dependency test. However, the estimation of the mixing index using a higher number of cells increases the computational time for each Poincaré section. In view of that, we finalize 20×20 flow cells per Poincaré section to estimate the mixing index after performing the cell dependency test.

The axial variation of the mixing index under the influence of different governing parameters is shown in Fig. 4.15. In Fig. 4.15, we consider different values of (a) drag parameter of PEL α (= 1, 10, 20), (b) DH parameter of EL κ (= 12, 20, 50) and (c) PEL thickness d (= 0.05, 0.1, 0.2 and 0.3). We observe from Fig. 4.15 that for all the parameters considered, the mixing index increases in the axial direction. This observation signifies the enhancement in the mixing performance with an increment in the distance from the inlet. The appearance of small oscillations in the plots of Fig. 4.15 is attributed to the discrepancy in the probability of finding particular species in a fixed cell at x^{th} and $(x+1)^{th}$ Poincaré sections. The continuous motion of the particles in the 3D computational domain tunes this probability and, at times, adjusts the magnitude of the weighting function $\beta_i(0/1)$ of a

particular i^{th} cell between each consecutive iteration in the x direction. As a consequence, we observe the appearance of oscillation in the mixing index variation along the axial direction of the channel in Fig. 4.15. Noteworthily, a continuous increment in the mixing index along the length of the channel indicates the efficient performance of the proposed microfluidic mixer. The influence of different other parameters on the mixing index is discussed in detail as follows.

In Figs. 4.15(a)-(b), we observe that the magnitude of the mixing index I_m obtained for higher drag parameter α (= 20) and lower DH parameter of EL κ (= 12), respectively, is higher than that of their respective counterparts. These observations are attributed to the higher area of standard double vortex configuration for $\alpha = 20$ observed in Fig. 4.8(b), as well as the higher strength of the dumbbell-shaped vortices for $\kappa = 12$ observed in Fig. 4.8(c).

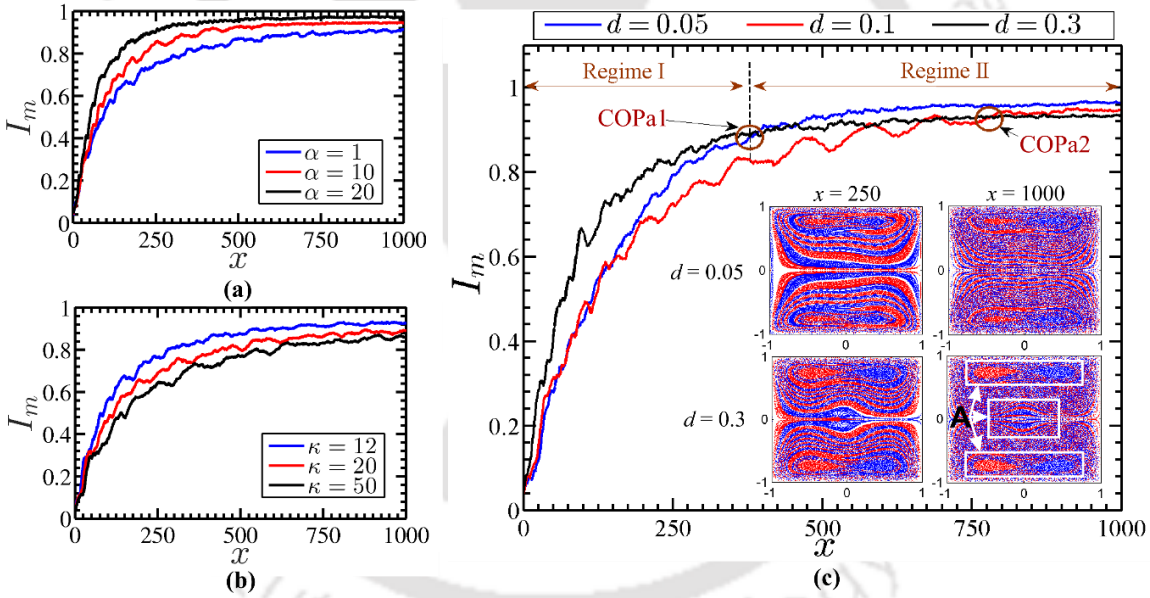

Figure 4.15: Quantitative assessment for the influence of governing parameters on mixing dynamics: Plots showing the variation of mixing index I_m in axial direction for different values of (a) drag parameter of PEL α (= 1, 10 and 20), (b) DH parameter of EL κ (= 12, 20 and 50), and (c) PEL thickness d (= 0.05, 0.1, and 0.3). The other parameters considered for analysis are: (a) $\kappa_p = 10$, $\Gamma = 0.5$, $Re_\omega = 100$, d = 0.2, κ = 12; (b) $\kappa_p = 10$, α = 5, $\Gamma = 0.5$, $Re_\omega = 100$, d = 0.2; and (c) $\kappa_p = 10$, α = 5, $\Gamma = 0.5$, $Re_\omega = 100$, κ = 12. The insets in (c) show the Poincaré maps for both values of PEL thickness d(= 0.05, 0.3) at two different axial locations x = 250 and 1000.

The plots in Fig. 4.15(c) show the variation of the mixing index I_m with PEL thickness d (= 0.05, 0.1, and 0.3). The insets in Fig. 4.15(c) show the Poincaré maps for both the values of PEL thickness $d\,(=0.05, 0.3)$ obtained at different axial locations x =

250 and 1000. A soft narrow-fluidic channel with $d = 0.05$ mimics a rigid narrow channel. In Fig. 4.15(c), we observe that, after a certain x location labelled as the Cross Over Point (COP) – COPa1 with regime I and II in Fig. 4.15(c), the mixing index for minimal PEL thickness $d = 0.05$ becomes higher than that of higher PEL thickness $d = 0.3$. Notably, this observation is in agreement with our prediction of mixing, as discussed in Section 4.6.1. In the comparison of d =0.1 and 0.3, such point of inflexion, named as COPa2, appears at a comparatively larger distance from the inlet of the channel. It is the fact that the competition between the relatively larger area of the recirculation zone obtained for the smaller PEL thickness ($d = 0.05$ in Fig. 4.9(a) and $d = 0.1$ in Fig. 4.9(b)), and the higher strength of the dumbbell-shaped vortices for higher PEL thickness ($d = 0.3$ for Fig. 4.9(c)) plays a key role here. To discuss this aspect, we take the help of insets depicted in Fig. 4.15(c). As shown in the insets of Fig. 4.15(c), for $d = 0.05$, the size of the recirculation zone is higher than that of $d = 0.3$. This observation is applicable for both the axial locations $x = 250$ (in regime I) and $x = 1000$ (in regime II). Despite that, as observed in Fig. 4.15(c), the higher strength of the dumbbell-shaped vortices obtained for $d = 0.3$ dominating over the initial channel length, as shown by regime I. On the other hand, in the remaining length of the channel, identified by regime II, the higher area of the standard double vortex obtained for $d = 0.05$ still prevails. Consequently, the value of I_m is higher for $d = 0.3$ in regime I and $d = 0.05$ in regime II. Note that the mixing comparison obtained for $d = 0.1$ and $d = 0.3$ can be explained from a similar perspective, as discussed above. For this case, a closer look at the point of inflexion COPa2 is necessary.

Moreover, in consistence with the observations of Figs. 4.12 and 4.14, we observe a similar phenomenon in the insets of Fig. 4.15(c) as follows: the large isolated volume of species trapped in the dumbbell lobes and the geostrophic core of the channel for the case of $d = 0.3$ causes a reduction in the mixing index. This isolated region of species ('A') is shown in Fig. 4.15(c) for $d = 0.3$ and $x = 1000$. Notably, the region where the species reside as isolated or nearly isolated ('A') is minimal in case of $d = 0.05$ (refer to inset corresponding to $d = 0.05$ and $x = 1000$ in Fig. 4.15(c)), causing an increase in the mixing index in regime II of Fig. 4.15(c). It is also worth mentioning here that the observation obtained in Fig. 4.15(c) is not consistent with the drag parameter variation. Over the total length of the channel, the strength of the vortices for the drag parameter $\alpha = 20$ (see Fig. 4.8(b)) is comparatively high to show a very high mixing performance as compared to the case $\alpha = 1$ (Fig. 4.8(a)).

In line with our observation and subsequent discussion in Section 4.6.1, here in Fig. 4.15 it is observed that for the fixed Re_{Ω} (= 100), the mixing length obtained for higher α (= 20), lower κ (= 12) and higher d (= 0.3), is comparatively smaller as compared to that of their respective counterparts. This observation constitutes the proof of the enhancement in the mixing efficiency under the influence of PEL modulated electrohydrodynamics in the rotating microfluidic platform. In this context, we would like to discuss an important point as follows: although the mixing efficiency obtained at the outlet, as depicted in Fig. 4.15, is relatively higher for higher drag parameter $\alpha = 20$ and very small PEL thickness $d = 0.05$ (a representing case of the insignificant effect of PEL, i.e., almost a rigid narrow channel), the net throughput, which is proportional to the axial velocity, becomes lesser for $\alpha = 20$ and $d = 0.05$, as shown in Figs. 4.16(a) and 4.16(c), respectively.

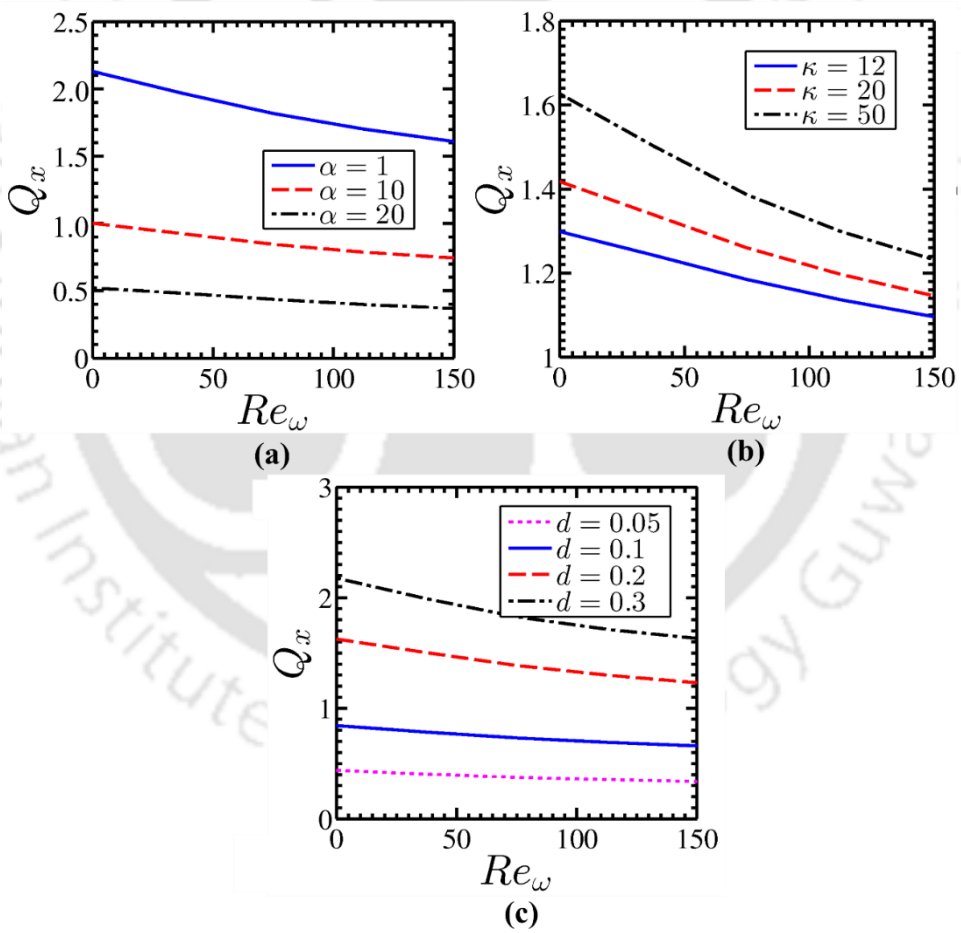

Figure 4.16: Plots showing the variation of axial flow rate Q_x with a rotational speed of the channel Re_{ω} for different values of (a) drag parameter of PEL α (= 1, 10 and 20), (b) DH parameter of EL κ (= 12, 20 and 50), and (c) PEL thickness d (= 0.05, 0.1, 0.2, 0.3). The other parameters considered to plots these results are: (a) $\kappa_p = 10$, $\Gamma = 0.5$, $\mathrm{Re}_{\omega} = 100$, $d = 0.2$, $\kappa = 12$; (b) $\kappa_p = 10$, $\alpha = 5$, $\Gamma = 0.5$, $\mathrm{Re}_{\omega} = 100$, $d = 0.2$; and (c) $\kappa_p = 10$, $\alpha = 5$, $\Gamma = 0.5$, $\mathrm{Re}_{\omega} = 100$, $\kappa = 12$.

Figure 4.16 depicts the variation of the axial flow rate Q_x with the rotational speed of the channel Re_ω for different parameters mentioned in the caption. From the ongoing discussion, we would like to iterate here that achieving a higher mixing efficiency through the imposition of the grafted polyelectrolyte layer demands a compromisation in the net throughput for a relatively higher drag parameter $\alpha = 20$ and very small PEL thickness $d = 0.05$. As a result, for these relevant cases, the present soft narrow fluidic configuration will again imitate the similar characteristics of the rigid narrow channel, thus rendering an unacceptable outcome. However, for lower κ (= 12), the higher electroosmotic effect offers higher mixing performance as well as enhances the net axial throughput in the channel (see Fig. 4.16(b)). Thus, taking a note on this aspect, the judicial selection of the physico-chemical structure of PEL seems to be imperative for the optimum mixing performance without negotiating the throughput in the proposed mixer substantially.

4.7 Summary

We have theoretically investigated in this study the flow dynamics and its consequences to the underlying chaotic mixing phenomenon in a soft rotating narrow-fluidic channel. The important findings obtained from the present analysis are elaborated as follows:

- For a fixed rotational speed of the channel Re_ω, the Coriolis force, which also leads to the inviscid geostrophic core formation, becomes the sole function of the flow velocity. As a consequence, by increasing the magnitude of primary flow through strong electroosmotic pumping and a weak frictional drag, we achieve a considerable intensity of the geostrophic depression in the interior of the channel. The strong electroosmotic pumping in the present study is achievable for small DH parameters of EL κ (= 12) and higher PEL thickness d (= 0.3), whereas to realize the effect of a weak frictional drag on the underlying flow dynamics, we consider a small drag parameter of PEL α (= 1). An increase in the intensity of the geostrophic depression in the core further results in a thin regime of the Ekman layer for the aforementioned cases [smaller κ (= 12), smaller α (= 1), and higher d (=0.3)]. Such formation of thin Ekman layer for these cases (smaller κ, smaller α, and higher d) further helps to achieve efficient mixing in the channel, even for the higher rotational speed of the channel. However, owing to the close competition between the strength of the corresponding electroosmotic force and its influencing regime, the change in the Ekman layer thickness is observed to be

insignificant for the variation in κ.

- Pertaining to the secondary flow analysis, we have observed three specific vortex configurations: a standard double vortex configuration for $\alpha = 20$ and $d = 0.05$; dumbbell-shaped vortices for $\kappa \sim$ (12-50), $d = 0.3$ and $\alpha = 1$; and transitional state between the first two vortex configurations for $d = 0.1$. Of these, the dumbbell-shaped vortices formed due to higher strength of Ekman pumping observed for strong electroosmotic effect in case of $\kappa = 12$, bring in more chaotic nature to the secondary flow, which in turn, establish an excellent mixing performance. Whereas, in contrast, by increasing the recirculation zone of the standard double vortex configuration, the higher frictional drag for $\alpha = 20$ provides a good quality of mixing. Notably, the large recirculation zone of standard double vortex configuration, which also appears in case of very small PEL thickness $d = 0.05$, plays an essential role to reduce the mixing length substantially. This is the key observation of this study. However, a notable compromise in the axial flow rate Q_x obtained for higher drag parameter $\alpha = 20$ and very small PEL thickness $d = 0.05$ is suggestive of the restricted use of these cases ($\alpha = 20$ and $d = 0.05$) for the mixing enhancement. This inference underlines that the narrow-fluidic channel with built-in polymeric layers (supposedly provides higher drag in the PEL) or rigid narrow-fluidic channel (equivalence in very small PEL thickness) imbedded in CD platforms contradicts the prime objectives of achieving the maximum axial throughput and mixing performance simultaneously with equal priority. However, as shown in this analysis, this is not the case with variation in the DH parameter of EL.
- The results of the present study also indicate that the tracer particles residing at the geostrophic core impede the process of mixing. The primary flow velocity at the geostrophic core, which substantially dominates its effect by imparting translational motion to this stream of particles, is the key cause for this retardation of the mixing process. More interestingly, it is also observed that the particles trapped inside the lobes of dumbbell-shaped vortices never interact with the particles of species co-injected at the inlet. For both the cases mentioned above, the information entropy at the geostrophic core and the lobes of the dumbbell-shaped vortices remain almost unaltered and minimum over the total length of the channel, thus augmenting the mixing length unreasonably. This aspect remains a challenge for further studies in this research paradigm.

CHAPTER 5

Rheology-modulated High Electrochemomechanical Energy Conversion in Soft Narrow-Fluidic Channel

In the previous chapters, we have highlighted the significance of a soft layer modulated electrohydrodynamics in three different applications viz., transport of biofluids, mixing in microfluidic assays and a rotating narrow-fluidic channel. However, a vast majority of the existing literature which deals with the implementation of the soft layer in various applications also points towards the significance of a soft layer in electrochemomechanical energy conversion phenomenon (Chanda et al., 2014; Chen et al., 2018; Chen & Das, 2015a). Despite that, the shear-thinning and elastic nature of the viscoelastic fluid which was found to increase the magnitude of the streaming potential (Bandopadhyay & Chakraborty, 2012) and hence, the energy conversion efficiency has never been considered in tandem with a grafted polyelectrolyte layer. In such cases, it is anticipated that the shear-thinning and elastic behaviour of the viscoelastic fluid and the soft layer modulated rich electrochemistry cumulatively promote the strengthening of the streaming current and consequently, improve the energy conversion. Recognizing this aspect of both the viscoelastic fluid and the soft layer, in this study, we investigate the influence of a viscoelastic fluid on the streaming potential generation in a soft narrow-fluidic channel. To represent the rheology of viscoelastic fluid accurately, we employ a simplified Phan-Thien-Tanner model. The potential distribution and based on that the underlying energy conversion phenomenon is analyzed in the limit of Debye-Hückel approximation and one without Debye-Hückel approximation. We also investigate in this study the effect of slip at the solid (wall)-liquid interface, and the conductance of Stern layer and that of the walls of the channel on the underlying energy conversion efficiency.

5.1 Problem Description

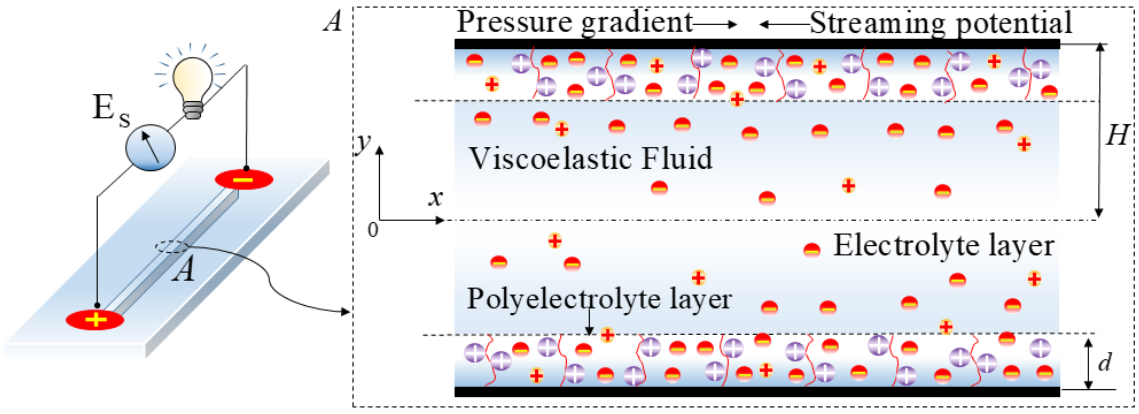

Figure 5.1: Schematic diagram depicts the pressure-driven transport of viscoelastic fluid through the soft narrow-fluidic channel. The channel is symmetric about $y = 0$ and has height $2H$. The brush-like structure near the walls represents the PEL of thickness d.

The schematic in Fig. 5.1 shows the rectangular channel in which the viscoelastic fluid is made to flow under the influence of externally applied pressure gradient. The length (directed along the axial direction) and width (in the third direction) of the channel are considered to be infinitely large so that the flow in the channel can be assumed to be unidirectional. However, the potential at the walls, i.e., at $y = \pm H$ is assumed to be in the range, which satisfies both the possibilities, i.e., in the limit of Debye-Hückel approximation for $|\psi_{wall}| \leq 25\,\text{mV}$ as well as beyond the Debye-Hückel approximation for $|\psi_{wall}| \geq 25\,\text{mV}$ (Chen & Das, 2015a). Accordingly, for a systematic discussion, we have first described our analysis pertinent to the regime of '*with Debye-Hückel approximation*' in section 5.2 and then proceeded to the analysis obtained in the limit of '*without Debye-Hückel approximation*' in section 5.3.

5.2 Analysis with Debye-Hückel Approximation

The discussion in this section is restricted to the Debye-Hückel approximation.

5.2.1 Mathematical Formulation

5.2.1.1 Electrostatics

For the present flow configuration, pertinent to the unidirectionality of the flow, we have assumed here that the induced electrostatic potential inside the soft narrow-fluidic channel is invariant in the x direction and it is a function of y coordinate only. Also, in the present study, considering the symmetry about the channel centerline, we solve the

governing equations for the lower half of the channel. Accordingly, we simplify the dimensionless Poisson-Boltzmann equations [Eqs. (2.9a)-(2.9b)] derived in Chapter 2: Section 2.1.1 to the following forms as:

Electrolyte layer

$$\frac{d^2\bar{\psi}_e}{d\bar{y}^2} = \bar{\kappa}^2\bar{\psi}_e \tag{5.1a}$$

Polyelectrolyte layer

$$\frac{d^2\bar{\psi}_p}{d\bar{y}^2} = \bar{\kappa}^2\bar{\psi}_p - \bar{\kappa}_p^2 \tag{5.1b}$$

Note that the significance of the parameters and the variables involved in these Eqs. (5.1a)-(5.1b) is already elaborated in the previous chapters.

$$\left.\begin{array}{ll} \text{No- flux condition at the walls} & \left.\dfrac{\partial\bar{\psi}_p}{\partial\bar{y}}\right|_{\bar{y}=-1} = 0 \\ \text{Continuity in } \bar{\psi} \text{ at the PEL/ EL interface} & \left.\bar{\psi}_e\right|_{\bar{y}=-1+\bar{d}} = \left.\bar{\psi}_p\right|_{\bar{y}=-1+\bar{d}} \\ \text{Continuity in } \partial\bar{\psi}/\partial\bar{y} \text{ at the PEL/ EL interface} & \left.\dfrac{\partial\bar{\psi}_e}{\partial\bar{y}}\right|_{\bar{y}=-1+\bar{d}} = \left.\dfrac{\partial\bar{\psi}_p}{\partial\bar{y}}\right|_{\bar{y}=-1+\bar{d}} \\ \text{Symmetry condition at the center} & \left.\dfrac{\partial\bar{\psi}_e}{\partial\bar{y}}\right|_{\bar{y}=0} = 0 \end{array}\right\} \tag{5.2}$$

To solve Eqs. (5.1a)-(5.1b), we use the exact boundary conditions which are employed in Chapter 2: Section 2.1.3. Therefore, the description of all the boundary conditions for the present problem remains almost the same as reported in Chapter 2: Section 2.1.3. These boundary conditions, according to the present problem, can be simplified to the expressions as given in Eq. (5.2) (Chanda et al., 2014). Using these boundary conditions mentioned in Eq. (5.2), we obtain the closed-form solution of Eqs. (5.1a)-(5.1b) as:

Electrolyte layer

$$\bar{\psi}_e = \left(\frac{1}{\bar{\kappa}_r^2}\right)\frac{\sinh\left(\bar{\kappa}\bar{d}\right)}{\sinh\left(\bar{\kappa}\right)}\cosh\left(\bar{\kappa}\bar{y}\right) \tag{5.3a}$$

Polyelectrolyte layer

$$\bar{\psi}_p = \left(\frac{1}{\bar{\kappa}_r^2}\right)\left[1 - \frac{\sinh\left(\bar{\kappa} - \bar{\kappa}\bar{d}\right)}{\sinh\left(\bar{\kappa}\right)}\cosh\left(\bar{\kappa} + \bar{\kappa}\bar{y}\right)\right] \tag{5.3b}$$

where $\kappa_r = \kappa/\kappa_p$.

5.2.1.2 Electrohydrodynamics

For an accurate description of the elastic nature of the viscoelastic fluid, we use the Phan-Thien-Tanner model in this study (Ferrás et al., 2016). Albeit the consideration of PTT model brings complexity in the mathematical analysis, it is deduced from the network theory instead of using any empirical relation. The model merits several advantageous features such as it precisely depicts the elastic and shear-thinning nature, memory effect, recoil effect, and normal stress effect of the viscoelastic fluid (Ferrás et al., 2016). It accurately predicts the shear-thinning behaviour at higher relaxation time and can interpret the rheology of various viscoelastic fluids too. On account of these features, several researchers have employed the sPTT model for analyzing the flow behaviour of viscoelastic fluid in microchannels (A. M. Afonso et al., 2013; A. M. M. Afonso et al., 2009; Ferrás et al., 2016). Some of the viscoelastic fluids which can be well-described using the sPTT model are as follows: different combinations of Polyisobutylene (PIB) and tetradecane, the liquid state of HDPE, soft biological tissues, sodium hyaluronate in human and veterinary ophthalmology, PET resins and so on (F. P. T. Baaijens et al., 1994; H. P. W. Baaijens et al., 1995; Schoonen et al., 1998). All the above aspects suggest that the sPTT model is deemed a sufficient model to reveal the primary effect of viscoelasticity for the ongoing investigation. It is important to add here that to incorporate this model in the analysis; it is essential to have information about the elongation parameter ε and the relaxation time λ of the viscoelastic fluid in hand. The constitutive equation for the sPTT model can be given as (Thien & Tanner, 1977).

$$f\left(\mathrm{tr}\,\boldsymbol{\tau}\right)\boldsymbol{\tau}+\lambda\left[\frac{\partial\boldsymbol{\tau}}{\partial t}+\mathbf{u}.\nabla\boldsymbol{\tau}-\left[\left(\nabla\mathbf{u}\right)^{T}.\boldsymbol{\tau}+\boldsymbol{\tau}.\nabla\mathbf{u}\right]\right]=2\eta\mathbf{D} \tag{5.4}$$

The function $f\left(\mathrm{tr}\,\boldsymbol{\tau}\right)$ observed in Eq. (5.4) for the linear sPTT model is given by (Ferrás et al., 2016):

$$f\left(\tau_{xx}\right)=1+\frac{\varepsilon\lambda\tau_{xx}}{\eta} \tag{5.5}$$

In Eq. (5.5), τ_{xx} is the normal stress in x direction. On further simplification of Eq. (5.4) for unidirectional flow, we arrive at the following equations:

$$f\left(\tau_{kk}\right)\tau_{xx}=2\lambda\frac{du}{dy}\tau_{xy} \tag{5.6a}$$

$$f\left(\tau_{kk}\right)\tau_{yy}=0 \tag{5.6b}$$

$$f\left(\tau_{kk}\right)\tau_{xy} = \eta\frac{du}{dy} + \lambda\frac{du}{dy}\tau_{yy} \tag{5.6c}$$

Note that the term τ_{xy} is used to represent the shear stress as $\tau_{xy,p}$ in PEL and $\tau_{xy,e}$ in EL, if not written specifically. From Eq. (5.6b), $\tau_{yy} = 0$ as $f(\tau_{kk}) = 0$ gives a trivial solution to the problem (Ferrás et al., 2016). Therefore, Eqs. (5.6a) and (5.6c) can be modified:

$$\tau_{xx} = 2\frac{\lambda}{\eta}\tau_{xy}^2 \tag{5.7a}$$

$$f\left(\tau_{xx}\right)\tau_{xy} = \eta\frac{du}{dy} \tag{5.7b}$$

Using Eqs. (5.5) and (5.7), we obtain the final differential form of the constitutive equation as:

$$\eta\frac{du}{dy} = \tau_{xy} + 2\varepsilon\tau_{xy}^3\frac{\lambda^2}{\eta^2} \tag{5.8}$$

The expression for the shear stress τ_{xy} appearing in Eq. (5.8) can be derived from the Cauchy momentum equation, which is described in dimensional form as (Ferrás et al., 2016).

Electrolyte layer

$$0 = -\frac{dG}{dx} + \frac{d\tau_{xy,e}}{dy} + \rho_e E_S \tag{5.9a}$$

Polyelectrolyte layer

$$0 = -\frac{dG}{dx} + \frac{d\tau_{xy,p}}{dy} + \rho_e E_S - \mu_c u_p \tag{5.9b}$$

In Eqs. (5.9a) and (5.9b), E_S is the streaming potential. The other variables appearing Eqs. (5.9a) and (5.9b) are well-defined in the previous studies. We write the dimensionless form of Eqs. (5.8)-(5.9) as:

Constitutive equation for linear sPTT model

$$\frac{d\bar{u}}{d\bar{y}} = \bar{\tau}_{xy} + 2\varepsilon Wi_k^2\bar{\tau}_{xy}^3 \tag{5.10}$$

Momentum equations

Using Eqs. (5.9a)-(5.9b) and the potential distribution given in Eqs. (5.3a)-(5.3b), we simplify the momentum equation as (in a dimensionless form):

Electrolyte layer

$$\frac{d\bar{\tau}_{xy,e}}{d\bar{y}} = -\bar{\Gamma} - \left(\frac{1}{\bar{\kappa}_r^2}\right)\frac{\sinh\left(\bar{\kappa}\bar{d}\right)}{\sinh\left(\bar{\kappa}\right)}\bar{\kappa}^2\bar{E}_S\cosh\left(\bar{\kappa}\bar{y}\right) \tag{5.11a}$$

Polyelectrolyte layer

$$\frac{d\bar{\tau}_{xy,p}}{d\bar{y}} = -\bar{\Gamma} + \bar{\alpha}^2\bar{u}_p - \bar{\kappa}^2\bar{E}_S\left(\frac{1}{\bar{\kappa}_r^2}\right)\left[1 - \frac{\sinh\left(\bar{\kappa} - \bar{\kappa}\bar{d}\right)}{\sinh\left(\bar{\kappa}\right)}\cosh\left(\bar{\kappa} + \bar{\kappa}\bar{y}\right)\right] \tag{5.11b}$$

To obtain these dimensionless forms, we have used the following dimensionless quantities as: $\bar{\tau}_{xy} = \tau_{xy}/\left((\eta u_{SH})/H\right)$, $\bar{E}_S = E_S/E_0$, $Wi_k = (\lambda u_{SH})/H$ (Weissenberg number) (Ferrás et al., 2016). For the present problem, the expression of the $\bar{\Gamma}$ and $\bar{\alpha}$ are: $\bar{\Gamma} = (-dG/dx)/((\eta u_{SH})/H^2)$ and $\bar{\alpha} = \sqrt{(\mu_C H^2)/\eta}$. To solve the constitutive equation [Eq. (5.10)] and the momentum equation [Eqs. (5.11a)-(5.11b)], we use the following boundary conditions (Ferrás et al., 2016).

$$\left.\begin{array}{ll} \text{No-slip boundary condition at the walls} & \bar{u}_p\big|_{\bar{y}=-1} = 0 \\ \text{Dirichlet condition at PEL/ EL interface} & \bar{u}_p\big|_{\bar{y}=-1+\bar{d}} = \bar{u}_e\big|_{\bar{y}=-1+\bar{d}} \\ \text{Continuity in shear stress at PEL/ EL interface} & \bar{\tau}_{xy,p}\big|_{\bar{y}=-1+\bar{d}} = \bar{\tau}_{xy,e}\big|_{\bar{y}=-1+\bar{d}} \\ \text{Symmetry condition at the center of the channel} & \bar{\tau}_{xy,e}\big|_{\bar{y}=0} = 0 \end{array}\right\} \tag{5.12}$$

Note that the description of all boundary conditions mentioned in Eq. (5.12) is already reported in the context of boundary conditions of hydrodynamics in Chapter 2: Section 2.1.3. Using these boundary conditions [Eq. (5.12)], we numerically solve the governing equations of the electrohydrodynamics [Eqs. (5.10)-(5.11)], as discussed in detail in Section 5.2.2.

5.2.1.3 Streaming Potential

To estimate the streaming potential in the channel, we set total ionic current equal to zero (i.e., total ionic current = streaming current (i_S) + conduction current (i_C) = 0) (Chanda et al., 2014; Davidson & Xuan, 2008a; Goswami & Chakraborty, 2010).

$$i = 2e_0 z_e \int_{-H}^{0}\left(u_+ n_{e,+} - u_- n_{e,-}\right)dy = 0 \tag{5.13}$$

In Eq. (5.13), $u_\pm = u + (z_{e,\pm}e_0E_S/f_\pm)$ is the ionic velocity. Since we consider the symmetric electrolyte, i.e., $z_e = +z_{e,+} = -z_{e,-}$, the ionic friction coefficients $(\pm f)$ can also be tuned as

$f = +f_+ = -f_-$ (Chanda et al., 2014). These considerations reduce Eq. (5.13) to the following form as (Davidson & Xuan, 2008a; Goswami & Chakraborty, 2010):

$$i = 2e_0 z_e \int_{-H}^{0} u\left(n_{e,+} - n_{e,-}\right) dy + \frac{2z_e^2 e_0^2 E_S}{f} \int_{-H}^{0} \left(n_{e,+} + n_{e,-}\right) dy = i_S + i_C = 0 \qquad (5.14)$$

Upon simplification and using the potential distribution given in Eqs. (5.3a)-(5.3b), we obtain the final dimensionless form of the streaming potential with the consideration of Debye-Hückel approximation as:

$$\bar{E}_S = -\frac{1}{\bar{R}}\left(\frac{1}{\bar{\kappa}_r^2}\right)\left\{\int_{-1}^{-1+\bar{d}} \bar{u}_p \left[1 - \frac{\sinh\left(\bar{\kappa} - \bar{\kappa}\bar{d}\right)}{\sinh\left(\bar{\kappa}\right)}\cosh\left(\bar{\kappa} + \bar{\kappa}\bar{y}\right)\right] d\bar{y} + \int_{-1+\bar{d}}^{0} \bar{u}_e \frac{\sinh\left(\bar{\kappa}\bar{d}\right)}{\sinh\left(\bar{\kappa}\right)}\cosh\left(\bar{\kappa}\bar{y}\right) d\bar{y}\right\} \qquad (5.15)$$

In Eq. (5.15), $\bar{R} = \left(z_e^2 e_0^2 \eta\right) \Big/ f \varepsilon_e k_B T$ is a dimensionless parameter and following the existing studies, its value is selected as '1' throughout the present problem (Chanda et al., 2014). Important to note, while calculating the streaming potential using zero ionic current expression, we assume that the polyelectrolyte ions do not take part in the convection, as they remain immobile in the entire process (Chanda et al., 2014).

5.2.1.4 Electroviscous Effect

The streaming potential is physically characterized as the only source of induction of upstream migration of the counterions in the EDLs. It may be mentioned here that this effect resists the influence of pressure gradient applied across the channel and leads to a reduction in the resultant downstream volumetric flow. This reduction in the volumetric flow due to the upstream conduction of the ions is theoretically manifested as the enhancement in the effective viscosity of the fluid being transported. This phenomenon is termed as the electroviscous effect in the paradigm of electrohydrodynamics**.** The electroviscous effect is calculated as the ratio of flow rate only due to the pressure gradient $\bar{Q}_{\bar{\Gamma}}$ to the flow rate due to the combined influences of both the applied pressure gradient and streaming potential generated $\bar{Q}_{\bar{\Gamma}+\bar{E}_S}$ across the channel (Chanda et al., 2014; Chen & Das, 2015a; Patwary et al., 2016).

$$\frac{\eta_{eff}}{\eta} = \frac{\bar{Q}_{\bar{\Gamma}}}{\bar{Q}_{\bar{\Gamma}+\bar{E}_S}} \qquad (5.16)$$

5.2.1.5 Electrochemomechanical Energy Conversion Efficiency

The electrochemomechanical efficiency ξ_C in the purview of electrically actuated transport is defined as the ratio of the electric work output in terms of streaming potential generation in the channel to the imposed mechanical energy in terms of the applied pressure gradient across the channel. Mathematically, the dimensionless form of efficiency can be written as (Chanda et al., 2014; Chen et al., 2018; H Daiguji et al., 2004):

$$\xi_C = \frac{\frac{\bar{i}_S}{2}.\frac{\bar{E}_S}{2}}{\bar{\Gamma}\bar{Q}_{in}} \tag{5.17}$$

In Eq. (5.17), $\bar{\Gamma}\bar{Q}_{in}$ is the input power, and it is calculated using the pressure-driven flow rate only, i.e., $\bar{Q}_{in} = \bar{Q}_{\bar{\Gamma}}$ (Patwary et al., 2016). The numerator of Eq. (5.17) corresponds to the maximum output power. While deriving Eq. (5.17), we have taken into account that the 'figure of merit' Z_m for the present study is much lesser than 0.6. The figure of merit describes the energy conversion capacity of the particular system (Gross & Osterle, 1968). The highest value of Z_m obtained in the present study, as apparent from the results of forthcoming sections, is less than 0.2. This limit of Z_m allows us to use the expression of *efficiency corresponding to the maximum power output* (given in Eq. (5.17)) essentially for the *maximum efficiency*, albeit they are discrete quantities. It may be mentioned here that such range of $Z_m (0 < Z_m \leq 6\times10^{-1})$ is pertinent for all kinds of electrokinetic flows as reported by Xuan and Li (Xuan & Li, 2006).

From here onwards, we omit the overbars from the dimensionless quantities for ease in the presentation.

5.2.2 Solution Procedure

5.2.2.1 Computational Domain and Numerical Method

We use the finite difference method to solve the transport equations of electrohydrodynamics [Eqs. (5.10)-(5.11)] accompanied with the boundary conditions, as mentioned in Eq. (5.12). The computational domain for the present problem is shown in Fig. 5.2(a). Note that the flow considered in the study is fully developed in x direction. Therefore, we have divided the computational domain in the vertical y direction using the

set of N_y+1 grid lines with $(i=0)\triangleq(y=0)$ and $(i=N_y)\triangleq(y=-1)$. The location of the PEL/EL interface in Fig. 5.2(a) is defined by $(1-d)N_y$.

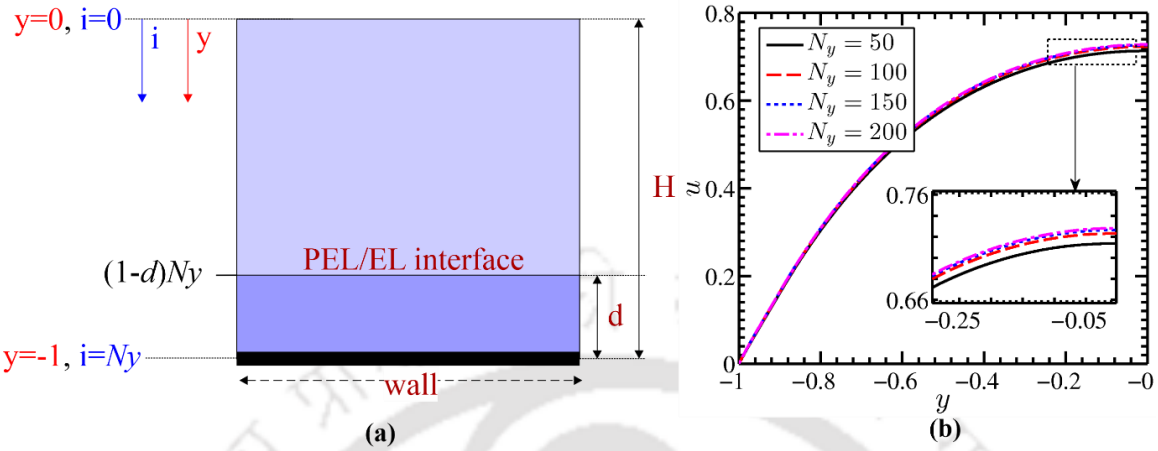

Figure 5.2: (a) Computational domain: Schematic in (a) shows the computational domain of the present study. (b) Grid dependence study: Plots in (b) show the velocity profiles obtained for different number of grid points N_y = 50, 100, 150 and 200. The inset in (b) shows the zoomed-in view of grid dependence test plots for a particular range of u and y scales. The other parameters used for this analysis are: $d = 0.1$, $\kappa_p = 10$, $\alpha = 3.0$, $\kappa = 20$, $\Gamma = 1.0$.

Analogous to this computational domain shown in Fig. 5.2(a), we now discretize the governing equations using appropriate discretization schemes discussed as follows:

Constitutive equation for sPTT model

$$u_i = u_{i+1} - \left[\tau_{xy,i} + 2\varepsilon Wi_k^2 \tau_{xy,i}^3\right]\Delta y : \forall i \in \left[0, N_y - 1\right] \tag{5.18}$$

Momentum equation

$$\tau_{xy,i} = \left[-\Gamma + \beta\alpha^2 u_i - \kappa^2 E_S \psi_i\right]\Delta y + \tau_{xy,(i-1)} : \forall i \in \left[1, N_y\right] \tag{5.19}$$

In Eq. (5.19), β is the flag parameter which is defined as:

$$\beta = \begin{cases} 0 & 0 \le i < (1-d)N_y \\ 1 & (1-d)N_y \le i \le N_y \end{cases}$$

It can be observed from Eqs. (5.18)-(5.19) that, the constitutive equation of the sPTT model [Eq. (5.18)] is discretized by using forward difference scheme, whereas the Cauchy momentum equation [Eq. (5.19)] is discretized by employing the backward difference scheme. Note that the discretization techniques for Eqs. (5.18)-(5.19) are based on the fact that the boundary conditions of velocity u and shear stress τ_{xy} are known only at $y=-1$ (i.e., $i=N_y$) and $y=0$ (i.e., $i=0$), respectively. Whereas at the opposite locations (i.e., at

$y = 0$ and $y = -1$), the value of u and τ_{xy} are, respectively, unknown. We solve Eqs. (5.18)-(5.19) using the Gauss-Seidel method in a coupled manner. In doing so, we also take into account that the shear stress τ_{xy} in Eq. (5.19) is a function of streaming potential E_S which can be solved using Eq. (5.15). The integration appearing in Eq. (5.15) is performed numerically using the trapezoidal rule. Note that the variables in Eqs. (5.18)-(5.19) viz., u_i, ψ_i and $\tau_{xy,i}$, have equivalent values in the respective domains of EL and PEL, i.e., $u_i = u_{e,i}$ in EL and $u_i = u_{p,i}$ in PEL; and so on for the others (ψ_i and $\tau_{xy,i}$). The convergence of the solution is obtained by setting the root mean squared error calculated over the entire computational domain to $O\left[10^{-10}\right]$.

5.2.2.2 Grid Dependence Study

The plots in Fig. 5.2(b) represent the grid dependence study, obtained for the different number of grid points N_y = 50, 100, 150 and 200. The inset in Fig. 5.2(b) shows the zoomed-in view of the grid dependence test plots for a particular range of u and y scale. For this assessment, we have considered the unique case of thinner EDL typically observed in this study for the higher value of the DH parameter of EL $\kappa = 20$ and smaller PEL thickness $d = 0.1$. The other parameters used for this test are mentioned in the caption of Fig. 5.2(b). It can be observed from Fig. 5.2(b) and inset therein that the change in the shape and magnitude of the velocity profile becomes negligible after the number of grid points $N_y = 100$. Therefore, in the forthcoming sections, we have considered $N_y = 100$ number of grid points to obtain the plots ensuring that the results presented are grid-independent.

5.2.3 Significance of Physical and Geometrical Parameters

In the present study, the magnitude of the applied pressure gradient is a crucial parameter from two different perspectives: First, its order should comply with the condition of the simplified PTT model, which is implemented to describe the rheology of viscoelastic fluid. The simplified PTT model considers a negligible non-affine slip of the polymeric macromolecules. Albeit, the effect of viscoelasticity is realized under the application of a high-pressure gradient, the strength of pressure gradient should be of the order of several kPa/m essentially to maintain the polyelectrolyte chains undeformed in the absence of non-affine slip parameter. Secondly, to maintain the flow through the channel against the

resistance to the frictional losses, a reasonably higher-pressure gradient is necessary, which is in sharp contrast to the former requirement. With concern to these facets, we have considered the value of non-dimensional pressure gradient $\Gamma = (-dG/dx)/((\eta u_{SH})/H^2)$ as 1 in the present study. For u_{HS} of the order of 10^{-4} m/s and height of the channel in the range $O\left(10^0 - 10^1\right)$ μm, the order of dimensional pressure gradient becomes $O(10^5)$ Pa/m for $\Gamma = 1$.[11] This estimated value of dimensional pressure gradient complies with the aforementioned pivotal facets.

To obtain the effect of viscoelasticity, we vary the viscoelastic parameter εWi_k^2 from 0.0 to 1.5 (Ferrás et al., 2016). This range can be estimated by following order of magnitude analysis: The viscosity of viscoelastic fluids varies in the range 10^{-1} to 10^{-3} Pa.sec (Joseph, 1990), while the extensibility parameter ε falls within the range 0.1 to 0.01. The relaxation time scale is chosen of the order of 10^{-3} sec (Kaushik, Abhimanyu, et al., 2017; Kaushik, Mondal, et al., 2017; Kunti et al., 2018; Mondal, DasGupta, Bandopadhyay, et al., 2015).

Note that the significance of the remaining parameters of this present chapter is discussed in detail in Chapter 2 since most of these parameters deal with the PEL modulated electrostatics and the frictional drag. Therefore, in the ongoing discussion, instead of discussing their significance in detail, we state the values/range of these parameters pertinent to the present study as follows: DH parameter of EL $\kappa \in [1, 20]$, PEL thickness $d \in [0.1, 0.3]$, DH parameter of PEL $\kappa_p = 10$, and drag parameter of PEL $\alpha \in [1, 3]$.

5.2.4 Model Validation

Before proceeding to the results, we validate the present theoretical model from different perspectives. In Fig. 5.3(a), we have compareed our results with the experimental results of Heyden et al. (van der Heyden et al., 2007) in which the authors have successfully developed a power generation mechanism in nanofluidic channels. Since the authors have considered a Newtonian fluid for conducting experiments in a rigid nanochannel, we use in our analysis $\alpha = 0$, $\varepsilon Wi_k^2 = 0$ and $d = 0$ for the required comparison. For this validation the value of dimensionless pressure gradient Γ and DH parameter of EL κ are calculated from the following reported dimensional quantities: charge of an electron $e_0 = 1.6 \times 10^{-19}$ C

[11] Note that the physical significance of these parameters is discussed in detail in Chapter 2: Section 2.2.2.

; absolute temperature $T = 298\,\mathrm{K}$; permittivity of the solution $\varepsilon_e = 6.95\times10^{-10}\,\mathrm{C^2N^{-1}m^{-2}}$; neutral charge density $n_\infty = 1000 N_A M$, where $N_A = 6.022\times10^{23}\,\mathrm{mol^{-1}}$ and M is a molar concentration; length of the channel $L = 4.5\times10^{-3}\,\mathrm{m}$; Boltzmann constant $k_B = 1.38064\times10^{-23}\,\mathrm{m^2kg\,s^{-2}\,K^{-1}}$ and ionic friction coefficient $f = 5\times10^{-12}\,\mathrm{kg/s}$ (Koneshan et al., 1998; J H Masliyah & Bhattacharjee, 2006). In Fig. 5.3(a), the results are compared for two separate values of KCL concentrations viz., 1 mM, and 0.1 mM.

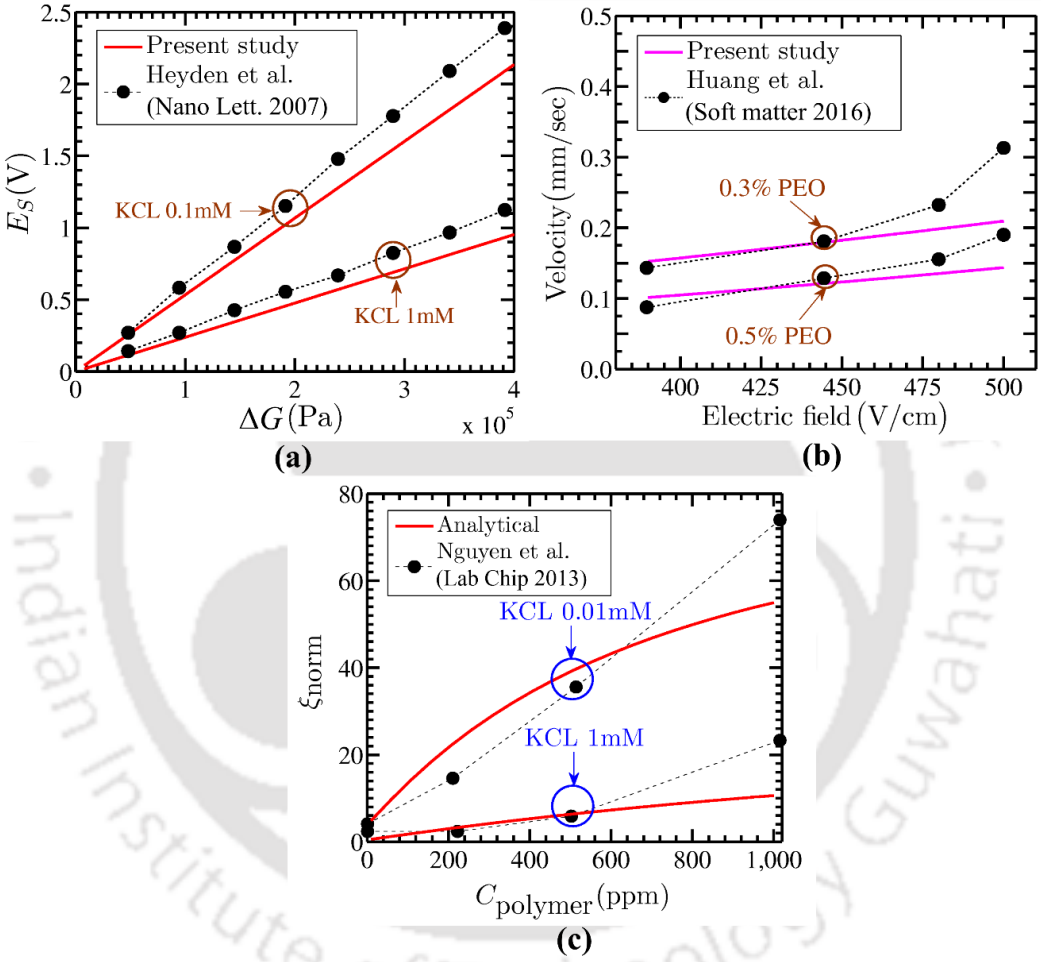

Figure 5.3: Plots show the validation of the present model with the reported experimental results. (a) Comparison of the streaming potential obtained from the current model with the results of Heyden et al. (van der Heyden et al., 2007). (b) Comparison of the flow velocity of viscoelastic fluid obtained from the present model with the experimental results of Huang et al. (Y. Huang et al., 2016). (c) Qualitative comparison of conversion efficiency variation with polymer concentration in ppm, obtained for two different values of electrolyte (KCL) concentrations 0.01mM and 1mM, same as considered in the referred study of Huang et al. (Y. Huang et al., 2016).

In Fig. 5.3(b), we compare the results obtained from the present model with the experimental results of Huang et al. (Y. Huang et al., 2016). In the reported study, the authors have performed an experimental analysis of electroosmotic transport of non-

Newtonian fluid through the rigid microchannel. Fluid considered for the experimentation is shear-thinning in nature and, hence can be approximately validated using the viscoelastic rheology. For validation, we have considered two cases of polyethylene oxide (PEO) concentration: 0.3% and 0.5% by weight. The concentration of sodium chloride (NaCl) considered for this analysis is 1 mM. The values of relaxation time for both the PEO concentrations 0.3% and 0.5% are: 0.003 sec and 0.005 sec respectively; whereas the values of viscosities are 0.005 Pa.s and 0.01 Pa.s respectively (Mukherjee et al., 2017). The extensibility parameter considered for both the cases is 0.01. To validate our model with these experimental results, we consider that the streaming potential generated in the channel is negligible, and the externally applied electric field solely actuates the flow. Ensuring a common basis for the comparison, the pressure gradient considered for obtaining the plots in Fig. 5.3(b) becomes negligibly small. Also, to mimic the rigid channel as considered by Huang et al. (Y. Huang et al., 2016), we consider the thickness of PEL to be zero.

In Fig. 5.3(c), we show the qualitative comparison of the results obtained from the present mathematical model with the experimental results of Nguyen et al. (T. Nguyen et al., 2013). In the referred study, the authors have investigated the change in the conversion efficiency for two different KCL solutions (of 0.01mM and 1mM) when the polymer-polyacrylic acid was added in each solution in stepwise increasing manner. While validating the experimental result, we have considered PEL thickness to be zero as the results reported by Nguyen et al. (T. Nguyen et al., 2013) are obtained for rigid microchannel. Apart from this, the other parameters required for the validation are similar to what have been considered in Nguyen et al. (T. Nguyen et al., 2013).

Having a look at Figs. 5.3(a)-(c), it is observed that the results obtained from the present study accurately match with the reported experimental results of pertinent paradigm (Y. Huang et al., 2016; T. Nguyen et al., 2013; van der Heyden et al., 2007) for the minimal values of pressure drop, electric field strength and polymer concentration, respectively. For the higher values of these parameters (pressure drop, electric field strength and polymer concentration), we observe a significant deviation of the present results from the respective experimental observations (see Figs. 5.3(a)-(c)). In order to achieve a quantitative validation of our analysis with the experimental results for the chosen set of parametric values, a full-scale numerical simulation may be necessary.

5.2.5 Results and Discussion

5.2.5.1 Influence of Viscoelasticity on Streaming Potential and Electroviscous Effect

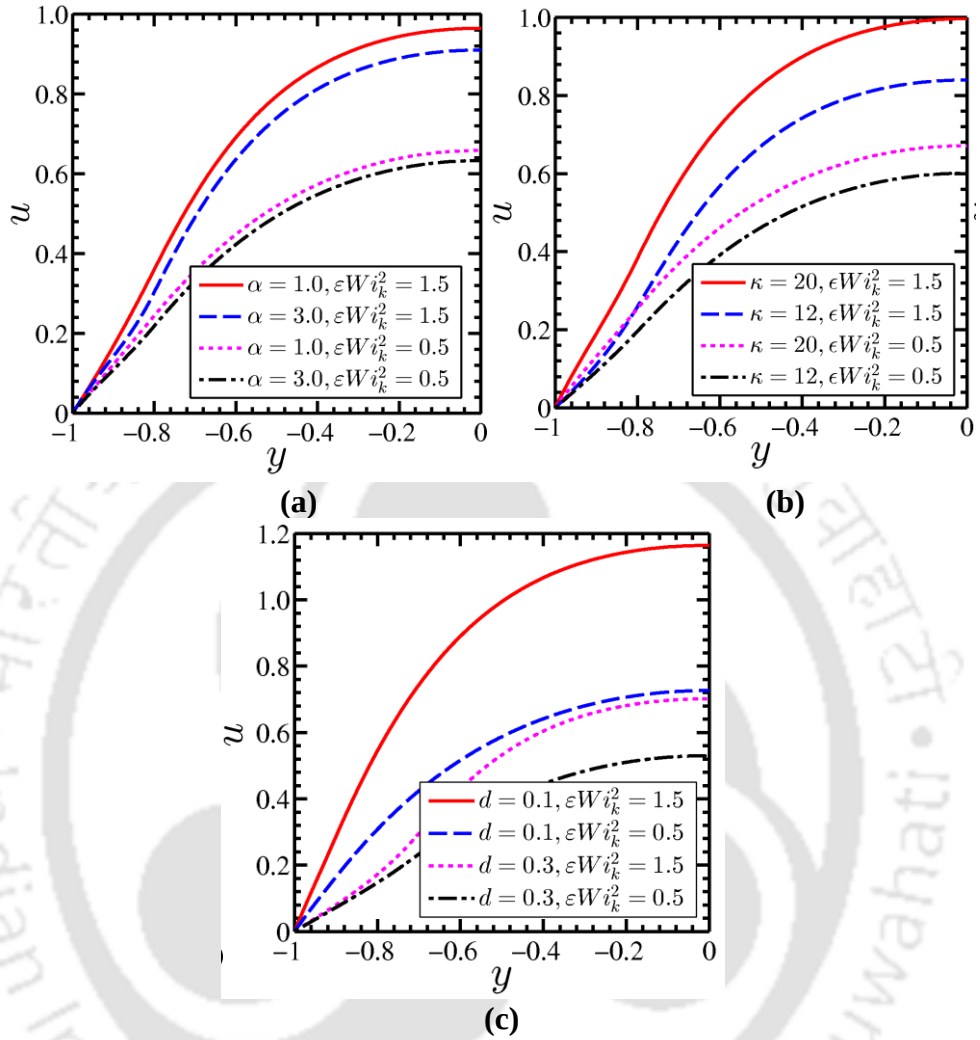

Figure 5.4: Plots show the velocity profiles for different values of (a) drag parameter α (= 1, 3), (b) DH parameter of EL κ(= 12, 20) and (c) PEL thickness d(= 0.1, 0.3), obtained for two values of viscoelastic parameter εWi_k^2(= 0.5,1.5). The other parameters used for the above plots are: (a) κ = 16, κ_p = 10, Γ = 1.0, d = 0.2; (b) d = 0.2, κ_p = 10, Γ = 1.0, α = 2.0; and (c) κ = 16, κ_p = 10, Γ = 1.0, α = 2.0.

The plots in Figs. 5.4(a)-(c) show the velocity profiles for drag parameter α (= 1, 3), DH parameter of EL κ (= 12, 20), and PEL thickness d (= 0.1, 0.3), respectively. The variations depicted in Figs. 5.4(a)-(c) are obtained for two different values of the viscoelastic parameter εWi_k^2 (= 0.5 and 1.5). It is observed in Fig. 5.4(a) that the magnitude of flow velocity reduces with an increment in α from 1 to 3 for all the values of the viscoelastic parameter. An increment in α from 1 to 3 indicates an increment in the frictional drag of PEL. Such increment in the flow resistance with an increment in α further reduces the flow velocity in the fluidic confinement. Therefore, Fig. 5.4(a), it is

observed that with an increment in the drag parameter α, the fluid velocity decreases. Notably, this reduction in the fluid velocity with an increase in α causes a reduction in the streaming of counterions in the channel. As a consequence, the magnitudes of E_S as well as η_{eff}/η decrease with an increment in the drag parameter α as confirmed in Figs. 5.5(a) and 5.5(d), respectively. In Figs. 5.5(a)-(f), we show the variation of streaming potential and electroviscous effect with three different parameters: drag parameter α, DH parameter of EL κ, and PEL thickness d; obtained for three different values of the viscoelastic parameter εWi_k^2 (= 0.5, 1.0 and 1.5).

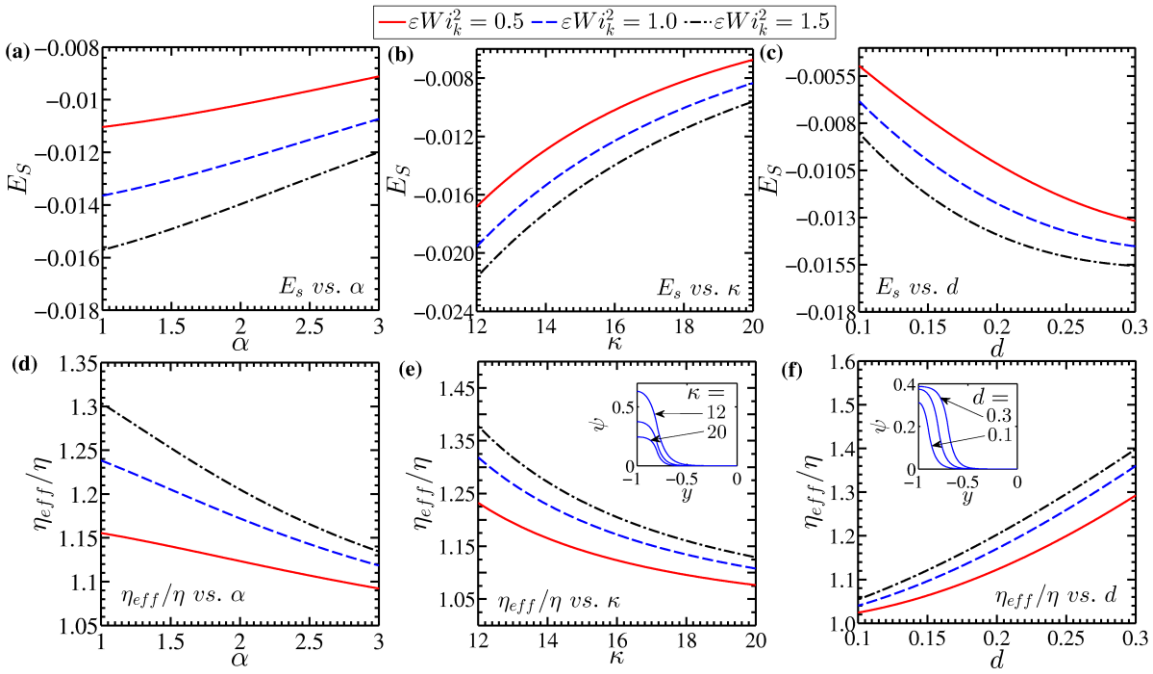

Figure 5.5: Plots in (a-c) and (d-f) show the variation of streaming potential (E_S) and electroviscous effect η_{eff}/η respectively, with drag parameter α, DH parameter of EL κ and PEL thickness d, respectively. The plots are obtained for three different values of viscoelastic parameter εWi_k^2(= 0.5, 1.0 and 1.5). The other parameters used for this analysis are: (a) and (d) $\kappa = 16$, $\kappa_p = 10$, $\Gamma = 1.0$, $d = 0.2$; (b) and (e) $d = 0.2$, $\kappa_p = 10$, $\Gamma = 1.0$, $\alpha = 2.0$; and (c) and (f) $\kappa = 16$, $\kappa_p = 10$, $\Gamma = 1.0$, $\alpha = 2.0$. The insets in (e) and (f) show the profiles of electrostatic potential for three different values of (e) DH parameter of EL κ(= 12, 16 and 20) and (f) PEL thickness d (= 0.1, 0.2 and 0.3).

In Figs. 5.4(b) and 5.4(c), we observe a reduction in the flow velocity with a decrement in κ and an increment in d, respectively. These observations hold for all the values of the viscoelastic parameter εWi_k^2 (= 0.5, 1.0, and 1.5) considered. To discuss these trends of the velocity profile, we need to look at what effect does the streaming potential and the electroviscous effect make on the velocity profiles through the observations of Figs.

5.5(b)-(c) and Figs. 5.5(e)-(f). In soft narrow-fluidic channels, with a reduction in κ or an increment in d, the electrostatic potential increases [cf. inset of Figs. 5.5(e) and 5.5(f)], which in effect leads to a rise in the magnitude of streaming potential as well as the electroviscous effect in the channel as seen in Figs. 5.5(b)-(c) and Figs. 5.5(e)-(f). This increased magnitude of E_S and η_{eff}/η further leads to an enhancement in the resistance to the flow of viscoelastic fluid in the soft narrow-fluidic channels. Therefore, we observe in Figs. 5.4(b) and 5.4(c) a substantial reduction in the flow velocity with a reduction in κ and an increment in d respectively.

The plots depicted in Figs. 5.4(a)-(c) also reveal that the magnitude of flow velocity increases with an increment in the viscoelastic parameter εWi_k^2. This is primarily attributed to the effect of enhancement of the shear-thinning nature of the viscoelastic fluid. For viscoelastic fluid, the extra normal stress τ_{xx} is the main contributing factor for its viscoelasticity since with an increment in the viscoelastic parameter εWi_k^2 or relaxation time λ, the magnitude of τ_{xx} significantly increases and affects the flow dynamics accordingly. As a result, the fluid upon experiencing a higher shear-thinning nature acquires higher flow velocity for a higher value of the viscoelastic parameter, as observed in Figs. 5.4(a)-(c). The extended effect of this increment in the flow velocity with an increment in the viscoelastic parameter is further realized in the variation of streaming potential and electroviscous effect as well. As the flow velocity in the channel increases with an increment in εWi_k^2, the streaming of the counterions becomes higher for a higher value of εWi_k^2. This enhancement in the counterion convection further leads to an increment in the streaming potential and the electroviscous effect with increment in εWi_k^2. Therefore, in Figs. 5.5(a)-(f), we observe that with an increment in the viscoelastic parameter, the magnitude of streaming potential, as well as the electroviscous effect increases. From the ongoing discussion, it may be inferred here that the required enhancement in the magnitude of streaming potential can be obtained only by proper tuning of the viscoelastic parameter of the fluid without disturbing flow parameters as well as the geometrical parameters of the fluidic pathways.

5.2.5.2 Effect of Viscoelasticity on Electrochemomechanical Efficiency

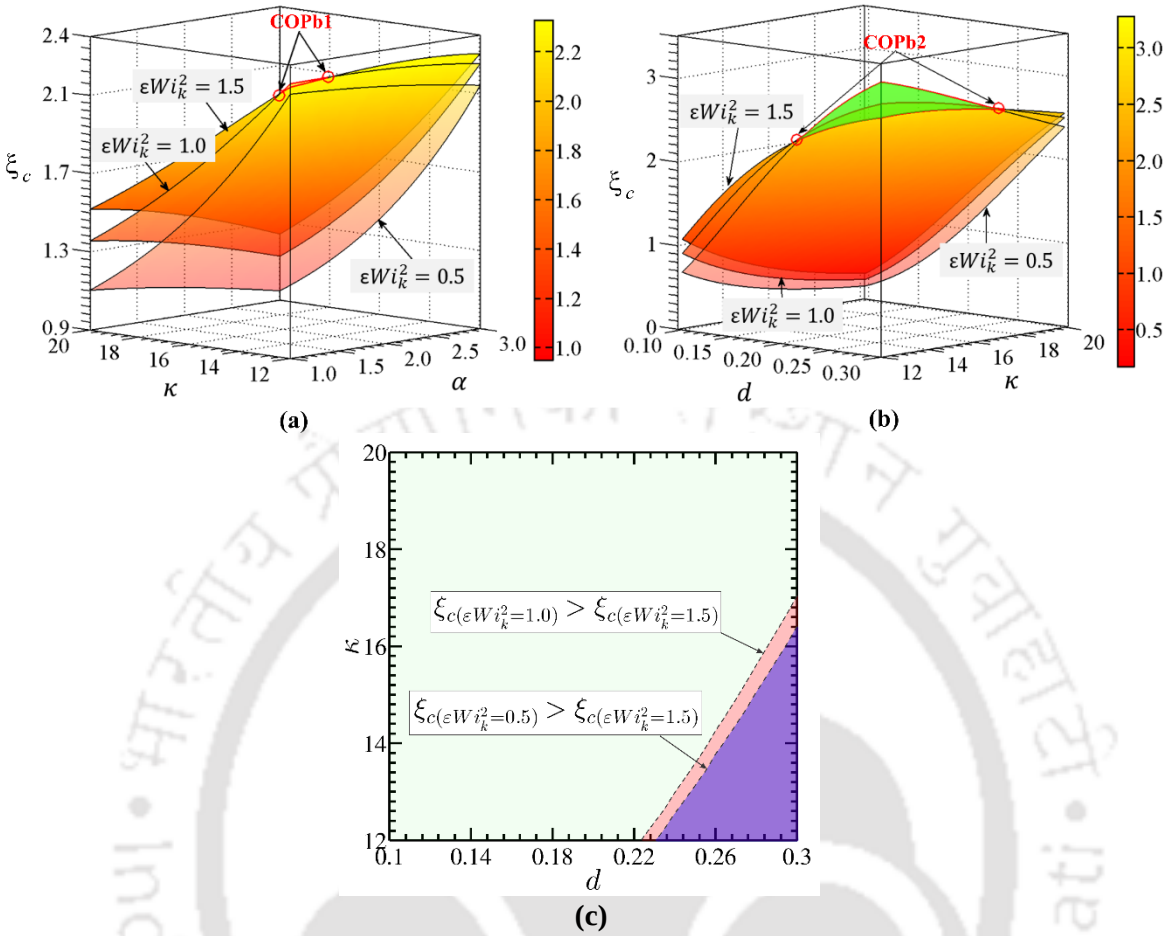

Figure 5.6: (a) Surface plots show the variation of conversion efficiency with the DH parameter of EL (κ) and drag parameter of PEL (α) for three different values of viscoelastic parameter εWi_k^2(= 0.5, 1.0 and 1.5). (b) Surface plots show the variation of conversion efficiency with the DH parameter of EL (κ) and PEL thickness (d) for three different values of viscoelastic parameter εWi_k^2(= 0.5, 1.0 and 1.5). The other parameters considered for the analysis are (a) $\Gamma = 1.0$, $d = 0.2$, $\kappa_p = 10$; and (b) $\Gamma = 1.0$, $\alpha = 2.0$, $\kappa_p = 10$. (c) Inversion lines demarcating the regimes (shown by dark colors) in which the higher viscoelastic parameter ($\varepsilon Wi_k^2 = 1.5$) offers the lower conversion efficiency as compared to the other values of the viscoelastic parameter i.e., $\varepsilon Wi_k^2 = 0.5$ and $\varepsilon Wi_k^2 = 1.0$. The other parameters selected for this analysis are same as that of (b).

Now, we discuss the variation of conversion efficiency with the variation of the drag parameter of PEL, DH parameter of EL, and thickness of PEL. The surface plots in Figs. 5.6(a)-(b) show the variation in conversion efficiency in κ-α plane and d-κ plane, respectively, for three different values of the viscoelastic parameter εWi_k^2 (= 0.5, 1.0, and 1.5). It is observed from Figs. 5.6(a)-(b) that, for all values of κ, α and d, the conversion efficiency is higher for higher values of εWi_k^2 (= 1.5), except for the window of parameters those lie within the cross over points– COPb1 (in Fig. 5.6(a)) and COPb2 (in Fig. 5.6(b))

(refer to shaded portions near the COPb1 and COPb2). An increment in the viscoelastic parameter εWi_k^2 from 0.5 to 1.5 indicates an increment in the viscoelasticity of fluid. This increment in εWi_k^2 leads to a rise in the magnitude of normal stress τ_{xx} and enhance the flow velocities in the channel (see Fig. 5.4). As a result, such an increase in the flow velocity further stimulates the phenomenon of streaming potential generation for higher values of εWi_k^2 (= 1.5) $\varepsilon Wi_k^2 \left(=1.5\right)$ as seen in Figs. 5.5(a)-(c). This observation is further reflected in Figs. 5.6(a)-(b), where we observe a higher conversion efficiency for higher values of εWi_k^2 (= 1.5) except in the region highlighted for COPb1 and COPb2, respectively.

The reason behind this inversion or occurrence of COPb1 and COPb2 (respectively in Figs. 5.6(a)-(b)) is explained as follows: for the present study, a reduction in α (from 3 to 1) or a reduction in κ (from 20 to 12) or an increment in εWi_k^2 (from 0.5 to 1.5) or an increment in d (from 0.1 to 0.3), gives rise to an enhancement in the magnitude of streaming potential in the channel (refer to Figs. 5.5(a)-(c)). The higher magnitude of the streaming potential, obtained for the above-mentioned parameters, leads to an increase in the adverse electroviscous effect as well (see Figs. 5.5(d)-(f)). This increment in the electroviscous effect further reduces the magnitude of the velocity and hence the streaming current, at a steady-state or until the current neutrality condition [Eq. (5.14)] is satisfied [c.f. Figs. 5.5(d)-(f)]. As an effect, even for a higher input power obtained by a higher input flow rate for $\alpha = 1$, εWi_k^2 = 1.5, and the higher electrostatic potential for the cases of $\kappa = 12$, $d = 0.3$, we obtain comparatively lesser conversion efficiency, albeit anticipated to be higher for the given cases, as witnessed in Figs. 5.6(a)-(b). Because of this, in the region highlighted for COPb1 (in Fig. 5.6(a)) and COPb2 (in Fig. 5.6(b)), the conversion efficiency obtained for the higher value of the viscoelastic parameter εWi_k^2 = 1.5 becomes lesser than that of the lower value εWi_k^2 = 0.5.

While analyzing these variations, it should be mentioned here that these results are obtained either at the steady-state or at the time when the current neutrality condition (total current equal to zero) is attained in the channel. This implies that in situations when streaming current and conduction current are not the same, the magnitude of flow velocity and the streaming potential will be relatively higher for the higher viscoelastic parameter. Whereas in a steady-state or at the current neutrality condition, the streaming current and

conduction current will be almost equal, and hence, the electroviscous effect will try to reduce the throughput in the channel. Therefore, for steady-state analysis as considered in this study, we observe a significant reduction in the magnitude of velocity for relatively lower values of κ (= 12) and α (= 1) as well as higher values of d (= 0.3) and $\varepsilon Wi_k^2 \left(=1.5\right)$. This reduced magnitude of velocity further leads to a decrease in the output power in the region highlighted for COPb1 and COPb2 respectively in Figs. 5.6(a)-(b), which, without the electroviscous effect, is estimated to be high.

The underlying electrohydrodynamics in the region highlighted for COPb1 (in Fig. 5.6(a)) and COPb2 (in Fig. 5.6(b)) reflects a reverse scenario, which one may not anticipate for the higher magnitude of the viscoelastic parameter. To establish the thermodynamic equilibrium during fluid transportation in the channel, the higher viscoelasticity of fluid brings down the streaming of the counterions so that the current neutrality condition is satisfied. As such, an enhancement of adverse electroviscous effect in the channel as modulated by the lower values of the drag parameter and DH parameter of EL, and higher PEL thickness attenuates the streaming current in the process. This phenomenon eventually leads to a decrement in the output power (equivalently decrement in the efficiency) for higher values of the viscoelastic parameter, as observed in Figs. 5.6(a)-(b). However, except for the region highlighted for COPb1 and COPb2, the efficiency becomes higher for the higher values of the viscoelastic parameter considered in this analysis, as witnessed in Figs. 5.6(a)-(b), respectively.

Note that such inversion in the variation of the conversion efficiency for different viscoelastic parameters occurs at different values of parameters related to the polyelectrolyte layer (such as κ and d). This inference can be clearly visualized from Fig. 5.6(c). In Fig. 5.6(c), the inversion lines demarcate the regimes (shown by dark colours) in which the conversion efficiency for higher value of the viscoelastic parameter $\left(\varepsilon Wi_k^2 =1.5\right)$ is lower than that of the lower value of the viscoelastic parameter $\left(\varepsilon Wi_k^2 =0.5,1.0\right)$. Note that the regimes in Fig. 5.6(c) are depicted for the variation shown in Fig. 5.6(b) as the inversions in the conversion efficiency obtained in Fig. 5.6(b) are vivid. In Fig. 5.6(c), we observe that the inversion in the conversion efficiency first takes place in case of $\varepsilon Wi_k^2 =1.0$ and then in case of $\varepsilon Wi_k^2 =0.5$. This variation in the occurrence of the inversion lines in case of εWi_k^2 = 0.5 and 1.0 is attributed to the difference in the shear-thinning nature

of the viscoelastic fluids. Due to higher viscoelasticity obtained for the case of $\varepsilon Wi_k^2 = 1.0$, the first inversion is observed for $\varepsilon Wi_k^2 = 1.0$ and then for the case of $\varepsilon Wi_k^2 = 0.5$, as the viscoelasticity is comparatively lower in this case $\left(\varepsilon Wi_k^2 = 0.5\right)$.

5.3 Analysis without Debye-Hückel Approximation

In this section, we discuss the influence of potential distribution obtained beyond the limit of the Debye-Hückel approximation, on the streaming potential generation phenomenon. The higher wall potential (greater than 25 mV) is obtained by setting the value of κ/κ_p ratio less than 1 (Chen & Das, 2015a). In the context of this approximation, it is important to mention here that in microfluidics, for small DH parameter ratio κ/κ_p or equivalently for larger EDL thickness, the EDLs from the opposite or nearest walls of the channel may overlap with each other. Consequently, the potential at the center of the channel becomes non-zero and attains higher magnitude as compared to that of the non-overlapping EDL case (Chen & Das, 2015a). This phenomenon of overlapping EDLs further leads to a significant deviation in the magnitudes of streaming potential and electroviscous effect, as reported in the literature (Chen & Das, 2015a). For the present case of analysis obtained beyond the DH approximation, the dimensionless modified transport equations take the following form.

Electrolyte layer

$$\frac{d^2\psi_e}{dy^2} = \kappa^2 \sinh\left(\psi_e\right) \tag{5.20a}$$

Polyelectrolyte layer

$$\frac{d^2\psi_p}{dy^2} = \kappa^2 \sinh\left(\psi_p\right) - \kappa_p^2 \tag{5.20b}$$

Accordingly, the momentum equation alongside the equation governing the variation of the streaming potential gets modified into the subsequent form as:

Momentum equations

Electrolyte layer

$$\frac{d\tau_{xy,e}}{dy} = -\Gamma - \kappa^2 E_S \sinh\left(\psi_e\right) \tag{5.21a}$$

Polyelectrolyte layer

$$\frac{d\tau_{xy,p}}{dy} = -\Gamma + \alpha^2 u_p - \kappa^2 E_S \sinh\left(\psi_p\right) \tag{5.21b}$$

Streaming potential

$$E_S = \frac{-\int_{-1}^{0} u \sinh(\psi)\, dy}{R\int_{-1}^{0} \cosh(\psi)\, dy} \tag{5.22}$$

Note that to solve the governing equations consistent with the analysis beyond the Debye-Hückel approximation, we have used the similar numerical method which is elaborated in Section 5.2.2. However, for the PB equation pertinent to this case [Eqs. (5.20a)-(5.20b)] (wall potential is higher than 25mV); we use the central difference scheme.

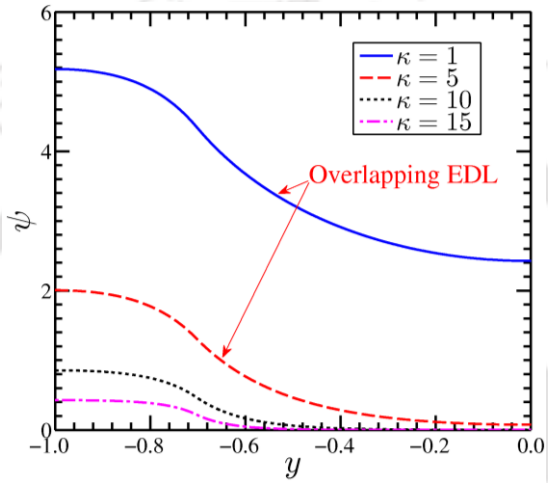

Figure 5.7: Plots show the potential distribution for four different values of the DH parameter of EL κ (= 1, 5, 10, and 15). The other parameters considered for this analysis are: $d = 0.3$, $\kappa_p = 10$.

In Fig. 5.7, the plots show the potential distribution obtained for four different values of the DH parameter of EL κ (= 1, 5, 10, and 15). Note that for $\kappa = 1$ and $\kappa = 5$ (equivalently for κ/κ_p = 0.1 and 0.5) the dimensionless wall potential becomes higher than 1 (i.e., the dimensional potential is greater than 25mV) as seen in Fig. 5.7. In addition to that, in Fig. 5.7, for $\kappa = 1$ and $\kappa = 5$, the potential distribution implies the presence of the overlapping EDLs as the value of the potential obtained at the center of the channel, i.e., at $y = 0$, is non-zero. Needless to mention, the presence of overlapping phenomena leads to higher potential distribution across the entire domain of the channel, as seen in Fig. 5.7. The existence of higher potential in the domain fetches a non-trivial variation in the streaming potential as the electroviscous effect is more pronounced for these cases ($\kappa = 1$ and $\kappa = 5$). The rationale behind such variation is explained before in Sections 5.2.5.1 and 5.2.5.2. Note that the occurrence of overlapping EDLs not only depends on the ratio κ/κ_p but also on the PEL thickness d. Next, we show the modulations obtained in the conversion efficiency with respect to different selective tunable parameters of the present system such

as drag parameter α, PEL thickness d, and viscoelastic parameter εWi_k^2.

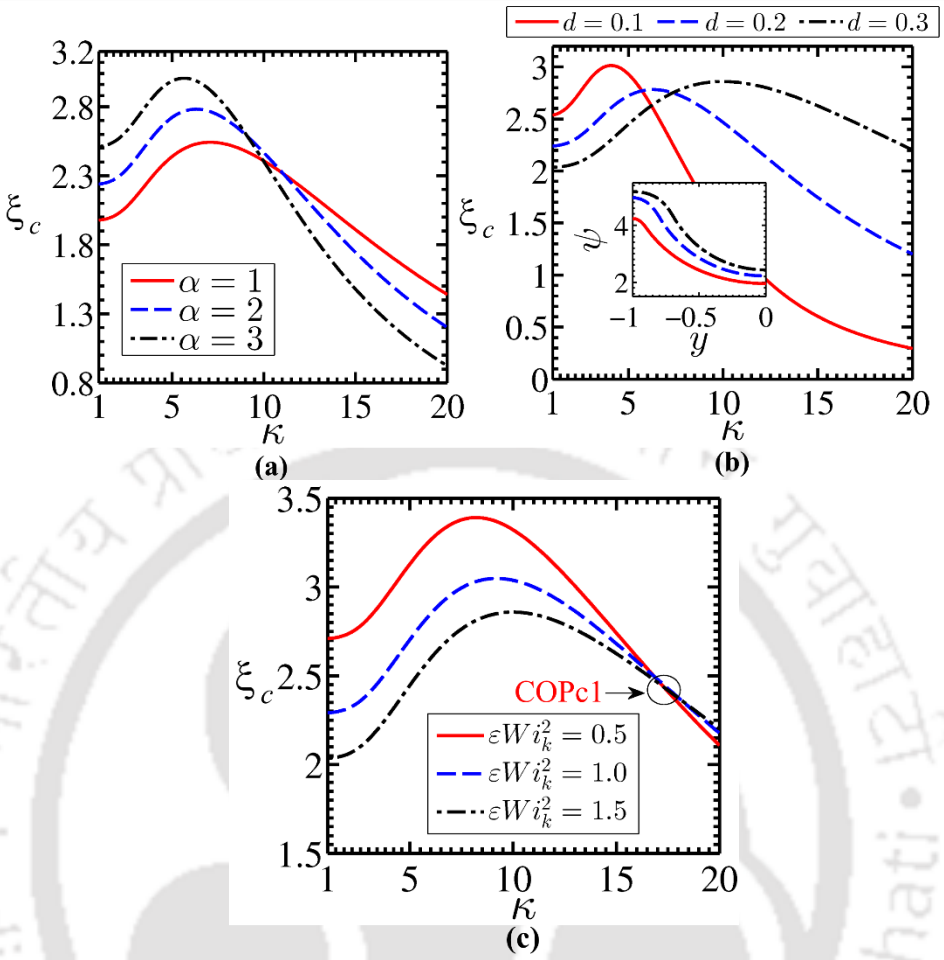

Figure 5.8: Plots show the variation in the conversion efficiency ξ_C versus DH parameter of EL κ for different values of (a) Drag coefficient α (= 1, 2 and 3); (b) PEL thickness d (= 0.1, 0.2 and 0.3) and (c) viscoelastic parameter εWi_k^2 (= 0.5, 1.0 and1.5). The other parameters used for the analysis are: (a) $\varepsilon Wi_k^2 = 1.5$, $\Gamma = 1.0$, $d = 0.2$, $\kappa_p = 10$; (b) $\Gamma = 1.0$, $\varepsilon Wi_k^2 = 1.5$, $\kappa_p = 10$, $\alpha = 2.0$; and (c) $d = 0.3$, $\Gamma = 1.0$, $\alpha = 2.0$, $\kappa_p = 10$.

Figures 5.8(a)-(c) show the variations of conversion efficiency with DH parameter of EL κ, obtained for different values of drag parameter α (= 1, 2 and 3), PEL thickness d (= 0.1, 0.2 and 0.3) and viscoelastic parameter εWi_k^2 (= 0.5, 1.0 and 1.5) respectively. The other parameters used for obtaining these plots are mentioned in the caption. From Figs. 5.8(a)-(c), it is observed that the conversion efficiency ξ_C initially increases with an increment in κ, attains a higher value, and then decreases as κ increases further. This particular variation in ξ_C versus κ is attributed to the variation in the electrostatic potential in the channel. In soft micro/nanochannel, an increment in the value of κ (from $\kappa = 1$) leads to a reduction in the magnitude of induced potential ψ (shown in Fig. 7), due to

which, the magnitude of streaming potential as well as the electroviscous effect reduces [refer to the trends of Figs. 5.5(b) and 5.5(e)]. As such, this decrease in the electroviscous effect stimulates the streaming current in the underlying transport process. Therefore, with an initial increment in κ after $\kappa = 1$, an increment in ξ_C is observed for all cases of Fig. 5.8. At a certain value of κ, the conversion efficiency ξ_C attains a maximum value. This peak value of ξ_C depends on the magnitude of selective parameters such as PEL thickness, drag parameter, and viscoelastic parameter [see Figs. 5.8(a)-(c)]. Beyond this maximum value, an increment in κ further leads to a reduction in the electrostatic potential, which, as a consequence, reduces the streaming potential and the conversion efficiency in the channel. As a result, the increasing-decreasing trend of conversion efficiency ξ_C with an increment in κ is observed in Figs. 5.8(a)-(c). Therefore, from the ongoing discussion and Figs. 5.8(a)-(c), it can also be inferred that with an increase in the electroviscous effect (in the present case for lower α, higher d and higher εWi_k^2), the peak efficiency shifts towards the higher value of κ as seen in Figs. 5.8(a)-(c).

In the analysis pertaining to the case of without Debye-Hückel approximation, the PEL thickness also modulates the overlapping phenomenon, as witnessed in Fig. 5.8(b) since the PEL thickness also determines the corresponding thickness of EDL in the channel. Larger the PEL thickness, more significant will be the thickness of EDL, and at times, the chances of having overlapping EDLs in the channel will be higher. Besides, the magnitude of the electrostatic potential at the center, i.e., $\psi_e\big|_{y=0}$ also increases with an increment in the PEL thickness d as can be seen from the inset of Fig. 5.8(b). As a result, the electroviscous effect increases with an increase in d from 0.1 to 0.3 and causes the shift in the peak value of efficiency towards the higher value of κ as verified in Fig. 5.8(b). On the similar background of the discussion, i.e., the electroviscous effect, the shift in the peak value of efficiency with a change in the drag parameter of PEL α and viscoelastic parameter εWi_k^2, as observed in Figs. 5.8(a) and 5.8(c), can be explained.

Note that the variation of the efficiency with the drag parameter α and viscoelastic parameter εWi_k^2 seen in Figs. 5.8(a) and 5.8(c) is analogous to the variations depicted in the surface plots of Figs. 5.6(a)-(b) (refer to Section 5.2.5.2). In Fig. 5.8(c), we observe the onset of COPc1 in the variation of conversion efficiency. Having a closer look at Fig. 5.8(c) vis-à-vis Fig. 5.6(b), one may find that this COPc1 [appearing in the variation in Fig. 5.8(c)]

is analogous to the same appearing in Fig. 5.6(b). This observation underlines that the onset of COPc1 in the variation of conversion efficiency is not merely due to overlapping EDL phenomenon. Rather, as discussed in Section 5.2.5.2, the onset of COPc1 is mainly due to the complex interplay between the viscoelastic nature of the electrolyte and the interfacial electrochemistry as modulated by the grafted PEL on the channel.

5.4 Influence of Slip at the Walls

Consideration of a slip at the walls of the channel in micro/nanoscale systems has shown significant potential towards the development in the streaming potential in recent years (Davidson & Xuan, 2008b; Garai & Chakraborty, 2010; Goswami et al., 2015; Goswami & Chakraborty, 2010; Ren & Stein, 2008). Despite being a passive modulator of the flow velocity, the slip length at the walls of the channel help enhancing the convection of ions, thus resulting in a higher streaming current through the channel (Garai & Chakraborty, 2010; Goswami & Chakraborty, 2010). For the present study, the slip length and the corresponding slip velocity at the walls are related by the following expression (Garai & Chakraborty, 2010; Goswami & Chakraborty, 2010):

$$u_p\Big|_{y=-1} = -ls\left.\frac{du_p}{dy}\right|_{y=-1} \tag{5.23}$$

An increase in the slip length ls at the wall, i.e., at $|y|=1$ enhances the slip velocity at the walls and hence, results in higher flow velocity in the entire channel through the viscous diffusion. Consequently, the streaming rate of the counterions becomes higher in the channel, further causing an effective increment in the streaming current. However, such increase in the streaming current with slip length, that too is expected to get strengthened by the flow of the viscoelastic fluid (the higher viscoelasticity of fluid promotes the streaming rate of the ions as discussed in the previous sections), may lead to a strong electroviscous effect in the channel. As discussed before, this stronger electroviscous effect leads to the attenuation in the energy conversion efficiency. This adverse influence of electroviscous effect with increasing the slip length becomes more prominent if the analysis is performed beyond the Debye-Hückel approximation, i.e., the wall potential exceeds the value 25 mV. Such variation in the streaming potential being generated with the slip length ls is depicted in Fig. 5.9.

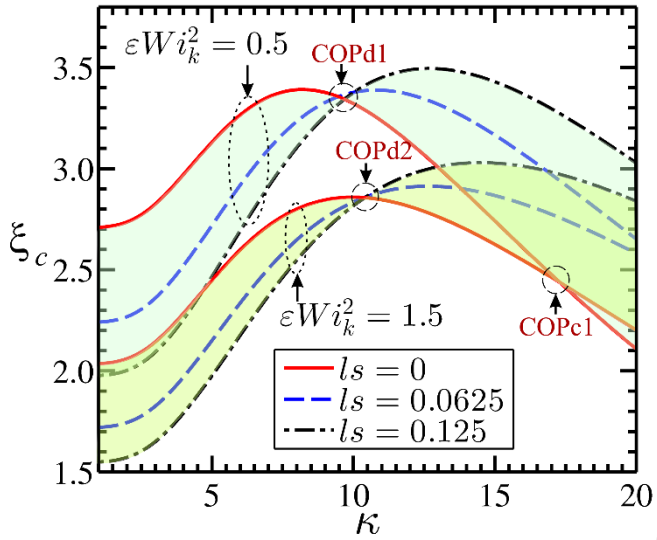

Figure 5.9: Influence of slip at the walls on the energy conversion: Plots show the variation of energy conversion efficiency ξ_C with DH parameter of EL κ for different values of slip length ls (= 0, 0.0625 and 0.125) and viscoelastic parameter εWi_k^2 (= 0.5 and 1.5). The other parameters considered for this analysis are: $d = 0.3$, $\Gamma = 1.0$, $\alpha = 2.0$, $\kappa_p = 10$. The shaded portions with different colours help to identify the set of plots obtained for the particular value of the viscoelastic parameter εWi_k^2.

The plots in Fig. 5.9 show the combined effect of the viscoelastic parameter εWi_k^2 and slip length ls on the variation of conversion efficiency ξ_C with the DH parameter of EL κ. Note that the chosen values of κ include the regimes pertaining to both the *with DH approximation* ($\kappa_r \geq 1$) and *without DH approximation* ($\kappa_r \leq 1$). The other parameters considered for the analysis are mentioned in the caption of Fig. 5.9. The values of slip lengths considered in the present analysis are consistent with those used in the literature (Goswami et al., 2015; Rivero & Cuevas, 2012). It is observed in Fig. 5.9 that for both the values of the viscoelastic parameter εWi_k^2 (= 0.5 and 1.5), the efficiency is higher for $ls = 0$ before the cross over points COPd1 and COPd2 respectively, whereas it is higher for $ls = 0.125$ beyond COPd1 and COPd2. Such variation of efficiency with slip length for the chosen values of κ and the occurrence of COPd1 and COPd2 in Fig. 5.9 is attributed to the adverse influence of the electroviscous effect. Before COPd1 and COPd2, the electroviscous effect is high due to the higher flow velocity for higher slip length ls (= 0.125) and higher electrostatic potential obtained in case of lower value of κ. As a result, for the lower value of κ, we observe lesser efficiency for higher slip lengths ls (= 0.125) before COPd1 and COPd2 in Fig. 5.9. Whereas, beyond COPd1 and COPd2, the electroviscous effect imposes minute resistance to the streaming current, thus we obtain higher efficiency for higher values of slip length $ls = 0.125$, as shown in Fig. 5.9.

However, as predicted previously, it is also observed in Fig. 5.9 that the efficiency in both the regimes ($\kappa_r \geq 1$ and $\kappa_r \leq 1$) is observed to be smaller for higher εWi_k^2 (= 1.5) than that of $\varepsilon Wi_k^2 = 0.5$, for all values of slip length, except $ls = 0$. For $ls = 0$, we observe a cross over point COPc1, which is previously observed in Fig. 5.8(c) as well. Therefore, for the case of $ls = 0$, the reader may refer to the discussion made in the context of Fig. 5.8(c). Whereas in case of non-zero slip lengths ls (= 0.0625 and 0.125), the flow velocity in the channel achieves considerably higher magnitude due to higher viscoelasticity for $\varepsilon Wi_k^2 = 1.5$, thus offering higher electroviscous effect and lower conversion efficiency for higher $\varepsilon Wi_k^2 (= 1.5)$ overall values of $\kappa \sim$ (1 to 20). It is also observed in Fig. 5.9 that, with an increase in the slip length ls, the peak efficiency shifts towards the higher value of κ. A plausible reason behind this phenomenon could be the electroviscous effect, which becomes considerably higher in case of higher slip length due to higher flow velocity observed pertinent to these cases. As a result, the present system needs a comparatively higher value of κ to minimize the influence of electroviscous effect in the channel for higher slip lengths, thus showing a shift in the peak value of efficiency with an increment in κ for higher slip lengths.

5.5 Effect of Wall and Stern Layer Conductance

The conductance of the Stern layer and that of the walls of the channel, through the conduction current or electroviscous effect, additionally imposes a resistance to the streaming current, thus diminishing the energy conversion efficiency. However, the viscoelastic fluid, which itself promotes the enhancement in the streaming rate of the counterions through the enhancement of the flow velocities, may strengthen the conversion efficiency even with the consideration of conductance of Stern layer and that of walls of the channel. Given that, we show in Figs. 5.10(a)-(b) the variation in the conversion efficiency with the DH parameter of EL for different values of Stern layer conductance and wall conductance, respectively. The Stern layer conductance in the present flow configuration can be accommodated by modifying the current neutrality condition as follows (Davidson & Xuan, 2008a; Goswami & Chakraborty, 2010):

$$i = 2e_0 z_e \int_{-H}^{0} u\left(n_{e,+} - n_{e,-}\right) dy + \frac{2z_e^2 e_0^2 E_S}{f} \int_{-H}^{0} \left(n_{e,+} + n_{e,-}\right) dy + 2\sigma_{stern} E_S = 0 \qquad (5.24)$$

Note that Eq. (5.24) is in the dimensional form. The last term $2\sigma_{stern} E_S$ in Eq. (5.24)

corresponds to the conductance of the Stern layer where σ_{stern} is the Stern layer conductance. On simplification, the modified expression of the streaming potential in the dimensionless form can be obtained as (overbars are neglected):

$$E_S = \frac{-\int_{-1}^{0} u \sinh(\psi)\, dy}{\left(R\int_{-1}^{0} \cosh(\psi)\, dy\right) + \mathrm{Du}} \tag{5.25}$$

In above Eq. (5.25), Dukhin number $\mathrm{Du}\left[=(\sigma_{stern}\eta)/(2\varepsilon_e k_B T n_\infty H)\right]$ is the ratio of the conductance of the Stern layer to the conductance, which causes the streaming current or the bulk conductance (Goswami & Chakraborty, 2010). Pertaining to its range typically considered in the literature, the value of the Dukhin number is found to be of the order of $O(10^0 - 10^2)$ (Goswami & Chakraborty, 2010). Note that Eq. (5.25) is derived for the analysis beyond Debye-Hückel approximation.

To consider the wall conductance in the present analysis, we simply modify the wall boundary condition for solving the potential distribution as (in dimensionless form and with overbar neglected) (Goswami & Chakraborty, 2010):

$$\left.\frac{d\psi_p}{dy}\right|_{y=-1} = \gamma_w \tag{5.26}$$

In Eq. (5.26), $\gamma_w = (\sigma_{wall} H)/(\varepsilon_e \psi_{ref})$ (Goswami & Chakraborty, 2010). Incorporating these equations Eqs. (5.25) and (5.26) in the set of transport equations governing the underlying electrohydrodynamics in the present configuration [Eqs. (5.10) and (5.21)], we have obtained the results as plotted in Figs. 5.10(a)-(b). Note that for simplistic presentation and more importantly, to highlight the influence of the rheology of viscoelastic fluid on the underlying streaming potential generation phenomenon, we distinctively show the effect of Stern layer conductance and wall conductance in Figs. 5.10(a)-(b), respectively. Otherwise, the coupling of all the effects (Stern layer conductance, wall conductance and viscoelasticity) together will bring the added complexity in the underlying analysis. This added complexity will not only make it difficult to interpret the results at hand but also will prohibit us from obtaining the flow physics of our interest, i.e., the efficacy of the viscoelastic fluid in the electrochemomechanical energy conversion essentially by isolating their individual effect.

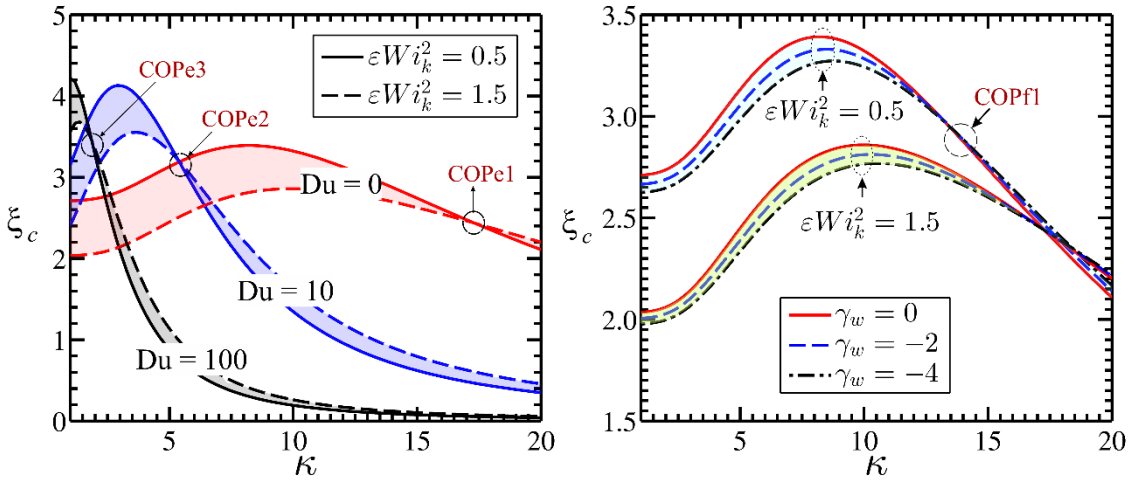

(a) **(b)**

Figure 5.10: (a) Influence of Stern layer conductance: Plots show the variation of energy conversion efficiency ξ_C with DH parameter of EL κ for different values of Dukhin number Du (= 0, 10 and 100) and viscoelastic parameter εWi_k^2 (= 0.5 and 1.5). (b) Influence of wall conductance: Plots show the variation of energy conversion efficiency ξ_C with DH parameter of EL κ for different values of γ_w(= 0, -2 and -4) and viscoelastic parameter εWi_k^2 (= 0.5 and 1.5). The other parameters considered for this analysis are: $d = 0.3$, $\Gamma = 1.0$, $\alpha = 2.0$, $\kappa_p = 10$. The shaded portions with different colours help to identify the set of plots obtained for the particular value of the parameter, Dukhin number in the case of (a) and viscoelastic parameter in the case of (b).

It is observed in Fig. 5.10(a) that the conversion efficiency ξ_C decreases with an increase in the Dukhin number, indicating the presence of strong electroviscous effect for higher conductance of Stern layer in case of higher Dukhin number Du (= 100). However, for the very small values of κ (~1), the efficiency for higher Du(=100) appears to be higher as compared to that of the lower value of Du(= 0). The physical reasoning behind this observation is as follows: The higher conductance of the Stern layer promotes the higher conduction current, signifying a higher magnitude of streaming potential as compared to that of lower Stern layer conductance. This phenomenon occurs at very high electrostatic potential obtained for a lower value of κ (= 1) (refer to Fig. 5.7 for the effect of κ on potential distribution). As a result, the efficiency achieved for the higher value of Du is comparatively higher than that of the lower value of Du, at a smaller value of κ. However, a reduction in the electrostatic potential with an increment in κ reduces the streaming potential but allows the higher conductance of Stern layer for higher Du(= 100) to generate higher electroviscous effect as compared to that of lower Du(= 0). It is because of this reason, we observe lower conversion efficiency for higher Du(= 100) at a higher value of κ (> 5) in Fig. 5.10(a).

In addition to that, in Fig. 5.10(a), it is also observed that despite having changes in

the efficiency due to the change in the Stern layer conductance, the trend of efficiency variation with viscoelastic parameter εWi_k^2 remains almost unaltered as apparent from the depicted plots in Fig. 5.10(a) for the particular value of Du (say, 100). Notably, these trends are similar to those as depicted in Fig. 5.6 and Fig. 5.8(c). As a consequence, we observe in Fig. 5.10(a) the occurrence of cross over points COPe1, COPe2 and COPe3 pertaining to the variation in εWi_k^2. Also, depending on the strength of electroviscous effect obtained differently for each Dukhin number, the location of COPe1, COPe2 and COPe3 varies on the scale of κ as observed in Fig. 5.10(a). However, because of the higher flow velocity in the channel for the viscoelastic fluid having higher viscoelasticity $\varepsilon Wi_k^2 = 1.5$, the streaming potential developed in the channel becomes higher. The higher streaming potential for $\varepsilon Wi_k^2 = 1.5$ increases the conversion efficiency as compared to that of lower $\varepsilon Wi_k^2 = 0.5$ for each Dukhin number beyond the respective cross over points (refer to Fig. 5.10(a)). Therefore, even in the presence of such adverse consequences of Stern layer conductance on energy conversion phenomenon, the viscoelastic fluid plays a significant role in enhancing the conversion efficiency as observed in Fig. 5.10(a).

Unlike the variation of the conversion efficiency (ξ_C) as seen in Fig. 5.10(a), we observe in Fig. 5.10(b) the non-intuitive variation of ξ_C with a change in the variation of the wall conductance as well. The physical reasoning behind the variation of ξ_C as outlined in the previous section can be still applied to explain the variations depicted in Fig. 5.10(b). Also, the occurrence of cross over point COPf1 can be explained from a similar perspective as discussed in the context of Fig. 5.10(a). However, pertaining to the discussion of the effect of wall conductance on the conversion efficiency, as depicted in Fig. 5.10(b), it may be mentioned here that an increase in the wall conductance modulated (γ_w) electrostatic potential gives rise to an enhancement in the streaming potential. Here, the wall conductance, unlike the case of Stern layer conductance, does not increase the conduction current directly. Therefore, the higher magnitude of the wall conductance γ_w (= -4), by increasing the magnitude of electrostatic potential, gives rise to a higher electroviscous effect. It is because of this higher electroviscous effect, we observe lesser conversion efficiency for higher γ_w (= -4) for the chosen values of the viscoelastic parameter as witnessed in Fig. 5.10(b). However, in sharp contrast to the variation of ξ_C with the Stern

layer conductance, we observe in Fig. 5.10(b) that the higher viscoelastic parameter does not increase the conversion efficiency significantly for higher wall conductance of the channel. Quite notably, this observation holds for the total predefined range of DH parameter of EL $\kappa \sim$ (1-20), as evident from Fig. 5.10(b).

5.6 Summary

In this problem, we have studied the rheology-modulated enhancement in the electrochemomechanical energy conversion in soft narrow-fluidic channels using the linear simplified PTT model for viscoelastic fluid. The important findings obtained from this analysis are listed as follows:

- An increment in the flow velocity obtained with an increase in εWi_k^2, on account of a relatively higher shear-thinning nature of the fluid, leads to an enhancement in the streaming potential as well as the conversion efficiency. We have shown that for the given flow conditions, the maximum efficiency achieved from the underlying transport of elastic non-Newtonian fluids (viscoelastic fluid) is much higher than that of the Newtonian fluid.
- Also, it is seen that for some cases like higher values of PEL thickness ($d > 0.2$), lower values of drag parameter ($\alpha < 2$), and DH parameter of EL ($\kappa < 16$), the higher electroviscous effect opposes the streaming current, leading to a reduction in the electrochemomechanical energy conversion efficiency in the channel. This variation with the parameters which are related to the PEL is attributed to the strong electrokinetics and the less frictional drag provided by it. Therefore, it can be argued here that although the viscoelastic fluid improves the streaming of the counterions from the diffuse layer; for the mentioned window of PEL parameters, the higher conduction current generated due to the strong electrokinetics and lower frictional drag of the PEL impedes such motion of counterions and thus, reduce the conversion efficiency.
- This effect gets furthermore pronounced when the potential distribution is obtained without Debye-Hückel approximation, i.e., the wall potential is higher than 25mV. This assumption leads to a higher magnitude of potential in the entire domain of the channel, implicating the phenomenon of overlapping EDL. Consequently, the pronounced electroviscous effect obtained in this case imposes a non-triviality in the electrochemomechanical energy conversion.
- Towards designing the efficient energy converter, in addition to the viscoelasticity of

the fluid and PEL modulated electrostatics, we have also explored the possible avenues to enhance the conversion efficiency by considering the conductance of Stern layer, the conductance of channel walls, and the hydrodynamic slippage at the solid (wall)-liquid interface. However, except for the variation of wall conductance, the other effects like the variation in the slip length at walls and the conductance of the Stern layers following enhancement in the viscoelasticity of the fluid bring about significantly higher conversion efficiency.

CHAPTER 6

Epilogue

Through the present dissertation, we have elaborated various analyses conducted for the selected problems, which are based on two important electrokinetic phenomena, namely the electroosmotic flow and the streaming potential generation. The mathematical modelling, solution procedure and the results of each problem have been discussed thoroughly in the previous chapters, Chapters 2-5. In this last chapter, we present our epilogue, in which we have summarized our findings and the inferences obtained from all the analyses conducted.

Transport of biofluids, mixing in narrow fluidic assays and rotating narrow-fluidic channel, and the energy conversion in the micro/nanofluidic batteries are the potential microfluidic applications, for which we have investigated that the grafted polyelectrolyte layer through the non-trivial electroosmotic effect and modulation of the flow resistance can render a paradigm shift in their design aspects. In the purview of this theme, the present dissertation describes the following four different problems with pertinent mathematical modelling, their solution procedures and the results obtained from each analysis.

- *Softness Induced Enhancement in a Net Throughput of Non-Linear Biofluids in Narrow-Fluidic Channels under the Electric Double Layer Phenomenon.*
- *Efficient Electroosmotic Mixing in a Soft Narrow-Fluidic Channel: The Role of a Patterned-soft Layer.*
- *Tutorial Review of Mixing in a Rotating Soft Narrow-Fluidic Channel under the Electric Double Layer Effect: A Variational Calculus Approach.*
- *Rheology-modulated High Electrochemomechanical Energy Conversion in Soft Narrow-Fluidic Channel.*

A brief summary of our findings and the inferences obtained from these analyses are presented as follows.

In **Chapter 2**, we have described the electrohydrodynamics of a non-Newtonian fluid in the soft narrow-fluidic channel under the influence of the EDL phenomenon. It was observed through this analysis that the complex interplay between the non-Newtonian

rheology and the interfacial electrochemistry in the presence of PEL on the walls leads to non-intuitive variations in the underlying flow dynamics in the channels. We have shown in this analysis, a relative enhancement in the net throughput through a soft narrow-fluidic channel for both the shear-thinning and shear-thickening fluids. This observation is attributed to the stronger electrical body forces stemming from the ionic interactions between the polyelectrolyte and electrolyte. The chapter also illustrates that higher apparent viscosity inherent to the class of shear-thickening fluid weakens the softness induced enhancement in the volumetric flow rate for the shear-thickening fluids since the viscous resistance offered to the field becomes higher for the transport of shear-thickening fluid.

In **Chapter 3**, we have proposed a novel and efficient mixing technique in a soft narrow-fluidic channel under the influence of electrical forcing. It was shown here that a grafted PEL added as a patch to the channel wall modulates the EDL which under the influence of an applied electric field leads to the formation of Lamb vortices at the patched sections and promotes the mixing therein. Through a quantitative description, we have revealed the effect of different patterns on the underlying mixing phenomenon in the convective mixing regime. We have also discussed the impact of key parameters on the mixing efficiency, the onset of the recirculation zone, and the variation in the mixing length in soft matter systems. The key parameters mainly include the thickness and the drag parameter of the grafted soft layer, and the thickness of the electric double layer. Finally, considering the practicability of the present problem, we have unveiled the values of several design parameters for which the mixing efficiency in the channel reaches the maximum.

We have studied, **in Chapter 4**, the effect of the grafted soft layer on the mixing dynamics in the rotating microfluidic channel. In this analysis, we have introduced for the first time a variational calculus approach to solve PEL modulated electrohydrodynamics in the rotating rectangular soft narrow-fluidic channel. For the qualitative estimation of the mixing dynamics, we have focused on the Poincaré map analysis, while the entropy of mixing approach was used for the mixing quantification. Results showed that the grafted polyelectrolyte layer in contact with the ionic solution leads to the development of an electric double layer, which upon interacting with the external electric field, strengthens the electroosmotic pumping in the fluidic channel. Such polyelectrolyte layer modulated strong electroosmotic pumping together with its intrinsic feature of offering a frictional drag to the underlying transport helps to modulate the primary as well as the secondary flows in the channel under the influence of rotational forces. Also, it was shown through

this analysis that alteration in the electroosmotic pumping and frictional drag force, tunable through the thickness of the grafted polyelectrolyte layer leads to the formation of the dumbbell-shaped vortex and results in an enhancement in the underlying mixing.

In **Chapter 5**, we have described the influence of viscoelastic fluid on the enhancement of the electrochemomechanical energy conversion efficiency in the polyelectrolyte layer grafted narrow-fluidic channels. We have obtained the velocity distribution using the simplified Phan-Thien-Tanner model and calculated the conversion efficiency in the purview of both with and without Debye-Hückel approximations. The analysis unveiled that an increase in the fluid velocity obtained with an increment in the shear-thinning nature of the viscoelastic fluid promotes the streaming of the counterions, which in turn enhances the conversion efficiency. Also, it was shown that the increased electroviscous effect due to higher rate of conduction current being developed results in a reduction in the predicted enhancement of the conversion efficiency. This phenomenon was observed for a window of parameters viz. higher PEL thickness, higher viscoelastic parameter, and lower DH parameter of the electrolyte. Also, we have reported that the relatively higher electrostatic potential stemming from the overlapping electric double layers and the higher wall potential (greater than 25 mV), leads to non-intuitive variation in the conversion efficiency following the pronounced influence of the electroviscous effect. While targeting an increment in the conversion efficiency by using the viscoelastic fluid and grafted polyelectrolyte layer, we have also examined the influence of slip at the walls of the channel and the spatial variation of electrical conductance in the Stern layer and that of walls of the channel. However, the rheology-modulated enhancement in the efficiency was found to be effective in case of the Stern layer conductance and interfacial slip at the walls of the channel.

From all the analyses presented through this dissertation, it comes to notice that the polyelectrolyte layer can singularly re-engineer the up-to-date LOC or μTAS platforms towards an objective of achieving effective and promising outcomes. The applications discussed in here can also lead to a separate assembly of altogether a new device which can be useful in in-vitro detection of diseases. Most oftenly, these devices can be assembled with the electroosmotic flow setup as the applied electric field is proved to be the efficient and handy tool to improvise the narrow-fluidic transport (N.-T. Nguyen et al., 2002). It is also believed that the insights obtained through these studies will facilitate the improvement in the functionalities of, in particular, the biological, clinical and pathological devices, and

artificial implants. However, for enhancing the functionalities of such devices with an incorporation of the soft PEL, the conducted analyses will necessitate consideration of a few more additional aspects which are described as follows.

Scope of future work. From a review of all the analyses conducted in the present thesis, it appears that the objectives defined for each problem can be further extended by using a few non-trivial approaches which have not been addressed yet. These approaches include the implementation of the end-charged polyelectrolyte brushes, the charge on the walls of the channel; and the consideration of pH-dependent charge density and the ion-partitioning effect. One of the important aspects that still remained unaddressed is the molecular-level interaction between the macromolecules of the polyelectrolytes and the polymers, and its consequences on the electroosmotic flow and the streaming potential generation. With concern to Chapter 5, wherein we have investigated the role of polyelectrolyte layer on the mixing dynamics through the rotating narrow-fluidic channel, the convective inertia on the flow dynamics can be considered to capture several other fundamental as well as interesting issues of the underlying mixing phenomenon. For a sufficiently high Reynolds number, the standard double vortex configuration or dumbbell-shaped vortices bifurcate into a non-trivial four vortex configuration, thus expected to affect the mixing performance. In such cases, the elevated roll-cell instability is another fundamental concern (Kheshgi & Scriven, 1985; Speziale, 1982) to be accounted for in the underlying analysis.

APPENDIX A: VARIATIONAL CALCULUS APPROACH (SOLUTION PROCEDURE)

The final set of equations [Eqs. (4.20a)-(4.20e)] derived in Section 4.2.3 (Extremization of Functional: Ritz Method), can be written in terms of matrix notations as:

Poisson Boltzmann equation	$\psi_{ij}\psi_{bi} = \psi_{ci}$	(A.1)
u velocity equation	$u_{ij}u_{bi} = u_{1i} + u_{2ik}v_{bk}$	(A.2)
v velocity equation	$v_{ij}v_{bi} = v_{1ik}p_{bk} + v_{2ik}u_{bk}$	(A.3)
w velocity equation	$w_{ij}w_{bi} = w_{1ik}p_{bk}$	(A.4)
Continuity equation	$w_{pij}w_{bi} + v_{pij}v_{bi} = 0$	(A.5)

Where **for Eq. (A.1),** we can write,

$$\psi_{ij} = \int_{\Omega_b}\left[\frac{\partial\psi_{fj}}{\partial y}\frac{\partial\psi_{fi}}{\partial y} + \frac{\partial\psi_{fj}}{\partial z}\frac{\partial\psi_{fi}}{\partial z} + \kappa^2\psi_{fj}\psi_{fi}\right]dydz$$

$$= \frac{\left[\pi^2\left(l_{\psi i}l_{\psi j} + m_{\psi i}m_{\psi j}\right) + \kappa^2\right]}{4}\delta_{l_{\psi i},l_{\psi j}}\delta_{m_{\psi i},m_{\psi j}}\left(1+\delta_{0,l_{\psi i}}\delta_{0,l_{\psi j}}\right)\left(1+\delta_{0,m_{\psi i}}\delta_{0,m_{\psi j}}\right)$$

$\psi_{ci} = \int_{\Omega_b}\kappa_p^2\psi_{fi}dydz = \kappa_p^2\left(a_1 + a_2 + a_3\right)$ where the expressions of a_1, a_2 and a_3 can be given as:

$$a_1 = \frac{\sin\left[l_{\psi i}\pi\left(1-d\right)\right]\sin\left[m_{\psi i}\pi\left(d-1\right)\right]}{\left(l_{\psi i}+\delta_{0,l_{\psi i}}\right)\left(m_{\psi i}+\delta_{0,m_{\psi i}}\right)\pi^2} + \frac{\left(1-d\right)\sin\left[m_{\psi i}\pi\left(d-1\right)\right]\delta_{0,l_{\psi i}}}{\left(m_{\psi i}+\delta_{0,m_{\psi i}}\right)\pi}$$

$$+\frac{\sin\left[l_{\psi i}\pi\left(1-d\right)\right]d\,\delta_{0,m_{\psi i}}}{\left(l_{\psi i}+\delta_{0,l_{\psi i}}\right)\pi} + \left(1-d\right)d\,\delta_{0,l_{\psi i}}\delta_{0,m_{\psi i}}$$

$$a_2 = \frac{\sin\left[m_{\psi i}\pi\left(1-d\right)\right]\sin\left[l_{\psi i}\pi\left(d-1\right)\right]}{\left(l_{\psi i}+\delta_{0,l_{\psi i}}\right)\left(m_{\psi i}+\delta_{0,m_{\psi i}}\right)\pi^2} + \frac{\left(1-d\right)\sin\left[l_{\psi i}\pi\left(d-1\right)\right]\delta_{0,m_{\psi i}}}{\left(l_{\psi i}+\delta_{0,l_{\psi i}}\right)\pi}$$

$$+\frac{\sin\left[m_{\psi i}\pi\left(1-d\right)\right]d\,\delta_{0,l_{\psi i}}}{\left(m_{\psi i}+\delta_{0,m_{\psi i}}\right)\pi} + \left(1-d\right)d\,\delta_{0,l_{\psi i}}\delta_{0,m_{\psi i}}$$

$$a_3 = \frac{\sin\left[l_{\psi i}\pi\left(d-1\right)\right]\sin\left[m_{\psi i}\pi\left(d-1\right)\right]}{\left(l_{\psi i}+\delta_{0,l_{\psi i}}\right)\left(m_{\psi i}+\delta_{0,m_{\psi i}}\right)\pi^2} + \frac{\sin\left[m_{\psi i}\pi\left(d-1\right)\right]d\delta_{0,l_{\psi i}}}{\left(m_{\psi i}+\delta_{0,m_{\psi i}}\right)\pi}$$
$$+\frac{\sin\left[l_{\psi i}\pi\left(d-1\right)\right]d\delta_{0,m_{\psi i}}}{\left(l_{\psi i}+\delta_{0,l_{\psi i}}\right)\pi} + d^2\delta_{0,l_{\psi i}}\delta_{0,m_{\psi i}}$$

For Eq. (A.2), we can write u_{ij} as

$$u_{ij} = \int_{\Omega_b}\left[\frac{\partial u_{fj}}{\partial y}\frac{\partial u_{fi}}{\partial y} + \frac{\partial u_{fj}}{\partial z}\frac{\partial u_{fi}}{\partial z} + \alpha^2 u_{fj}u_{fi}\right]dydz$$
$$= \frac{\pi^2}{16}\left[\left(2l_{ui}+1\right)\left(2l_{uj}+1\right)+\left(2m_{ui}+1\right)\left(2m_{uj}+1\right)\right]\delta_{l_{ui}l_{uj}}\delta_{m_{ui}m_{uj}} + \alpha^2\left(b_1b_2+b_3b_4+b_1b_3\right)$$

where the constants b_1, b_2 and b_3 can be written as:

$$b_1 = \left[\begin{array}{l}\frac{\left(1-\delta_{l_{ui}l_{uj}}\right)}{2\pi}\left(-\frac{\sin\left[\left(l_{ui}-l_{uj}\right)\pi\left(1-d\right)\right]}{l_{ui}-l_{uj}+\delta_{l_{ui}l_{uj}}}-\frac{\sin\left[\left(l_{ui}+l_{uj}+1\right)\pi\left(1-d\right)\right]}{l_{ui}+l_{uj}+1}\right)\\ -\delta_{l_{ui}l_{uj}}\left(\frac{\sin\left[\pi\left(2l_{ui}\left(d-1\right)+d\right)\right]-\left(2l_{ui}+1\right)\pi d}{2\pi\left(2l_{ui}+1\right)}\right)\end{array}\right]$$

$$b_2 = \left[\begin{array}{l}\frac{\left(1-\delta_{m_{ui}m_{uj}}\right)}{2\pi}\left(\frac{\sin\left[\left(m_{ui}-m_{uj}\right)\pi\left(1-d\right)\right]}{m_{ui}-m_{uj}+\delta_{m_{ui}m_{uj}}}+\frac{\sin\left[\left(m_{ui}+m_{uj}+1\right)\pi\left(1-d\right)\right]}{m_{ui}+m_{uj}+1}\right)\\ +\frac{\delta_{m_{ui}m_{uj}}}{2}\left(1-d+\frac{\sin\left[\left(2m_{ui}+1\right)\pi\left(1-d\right)\right]}{\left(2m_{ui}+1\right)\pi}\right)\end{array}\right]$$

$$b_3 = \left[\begin{array}{l}\frac{\left(1-\delta_{m_{ui}m_{uj}}\right)}{2\pi}\left(-\frac{\sin\left[\left(m_{ui}-m_{uj}\right)\pi\left(1-d\right)\right]}{m_{ui}-m_{uj}+\delta_{m_{ui}m_{uj}}}-\frac{\sin\left[\left(m_{ui}+m_{uj}+1\right)\pi\left(1-d\right)\right]}{m_{ui}+m_{uj}+1}\right)\\ -\delta_{m_{ui}m_{uj}}\left(\frac{\sin\left[\pi\left(2m_{ui}\left(d-1\right)+d\right)\right]-\left(2m_{ui}+1\right)\pi d}{2\pi\left(2m_{ui}+1\right)}\right)\end{array}\right]$$

$$b_4 = \left[\begin{array}{l} \dfrac{\left(1-\delta_{l_{ui}l_{uj}}\right)}{2\pi}\left(\dfrac{\sin\left[\left(l_{ui}-l_{uj}\right)\pi\left(1-d\right)\right]}{l_{ui}-l_{uj}+\delta_{l_{ui}l_{uj}}} + \dfrac{\sin\left[\left(l_{ui}+l_{uj}+1\right)\pi\left(1-d\right)\right]}{l_{ui}+l_{uj}+1} \right) \\ + \dfrac{\delta_{l_{ui}l_{uj}}}{2}\left(1-d+\dfrac{\sin\left[\left(2l_{ui}+1\right)\pi\left(1-d\right)\right]}{\left(2l_{ui}+1\right)\pi} \right) \end{array} \right]$$

Also, in Eq. (A.2), u_{1i} can be expressed as, $u_{1i} = u_{11ik}\psi_{bk} + u_{12i}$, where the terms u_{11ik}, ψ_{bk} and u_{12i} have the expressions:

$$u_{11ik} = \int_{\Omega_b} \kappa^2 \psi_{fk} u_{fi} dydz$$

$$= \kappa^2 \left[\frac{\cos\left[\left(l_{\psi k}+l_{ui}\right)\pi\right]}{\left(1+2\left(l_{\psi k}+l_{ui}\right)\right)\pi} + \frac{\cos\left[\left(l_{\psi k}-l_{ui}\right)\pi\right]}{\left(1+2\left(l_{ui}-l_{\psi k}\right)\right)\pi} \right] \times \left[\left[\frac{\cos\left[\left(m_{\psi k}+m_{ui}\right)\pi\right]}{\left(1+2\left(m_{\psi k}+m_{ui}\right)\right)\pi} + \frac{\cos\left[\left(m_{\psi k}-m_{ui}\right)\pi\right]}{\left(1+2\left(m_{ui}-m_{\psi k}\right)\right)\pi} \right] \right]$$

$$u_{12i} = \int_{\Omega_b} G u_{fi} dydz = \frac{4G\cos\left(l_{ui}\pi\right)\cos\left(m_{ui}\pi\right)}{\left(2l_{ui}+1\right)\left(2m_{ui}+1\right)\pi^2}$$

$$u_{2ik} = \int_{\Omega_b} \mathrm{Re}_\omega v_{fk} u_{fi} dydz = \frac{\mathrm{Re}_\omega}{4}\delta_{l_{ui}l_{vk}}\delta_{m_{ui}m_{vk}}$$

For Eq. (A.3), we can write the expression of v_{ij} as:

$$v_{ij} = \int_{\Omega_b} \left[\frac{\partial v_{fj}}{\partial y}\frac{\partial v_{fi}}{\partial y} + \frac{\partial v_{fj}}{\partial z}\frac{\partial v_{fi}}{\partial z} + \alpha^2 v_{fj} v_{fi} \right] dydz = u_{ij}$$

where

$$v_{1ik} = -\int_{\Omega_b} \frac{\partial p_{fk}}{\partial y} v_{fi} dydz = -\frac{l_{pk}\delta_{m_{vi}m_{pk}}}{2}\left[\frac{\cos\left[\left(l_{pk}-l_{vi}\right)\pi\right]}{2l_{vi}-2l_{pk}+1} + \frac{\cos\left[\left(l_{vi}+l_{pk}\right)\pi\right]}{2l_{vi}+2l_{pk}+1} \right] +$$

$$+ p_c \left\{ -\frac{\left(2l_{pk}+1\right)\delta_{l_{vi}l_{pk}}}{2}\left[\frac{\sin\left[\left(1+4m_{vi}-2m_{pk}\right)\dfrac{\pi}{4}\right]}{4m_{vi}-2m_{pk}+1} + \frac{\sin\left[\left(3+4m_{vi}+2m_{pk}\right)\dfrac{\pi}{4}\right]}{4m_{vi}+2m_{pk}+3} \right] \right\}$$

$$v_{2ik} = \int_{\Omega_b} -\mathrm{Re}_\omega u_{fk} v_{fi} dydz = -\frac{\mathrm{Re}_\omega}{4}\delta_{l_{vi}l_{uk}}\delta_{m_{vi}m_{uk}}$$

For Eq. (A.4), we can write w_{ij} as:

$$w_{ij} = \int_{\Omega_b} \left[\frac{\partial w_{fj}}{\partial y}\frac{\partial w_{fi}}{\partial y} + \frac{\partial w_{fj}}{\partial z}\frac{\partial w_{fi}}{\partial z} + \alpha^2 w_{fj} w_{fi} \right] dydz$$

$$= \frac{\pi^2 \delta_{l_{wi}l_{wj}} \delta_{m_{wi}m_{wj}}}{4}\left[l_{wi}l_{wj} + m_{wi}m_{wj} \right] + \alpha^2 \left(c_1 c_2 + c_3 c_4 + c_1 c_3 \right)$$

where the constants $c_1, c_{2,} c_3$ and c_4 can be expressed in the following forms as:

$$c_1 = \left(1-\delta_{l_{wi}l_{wj}}\right)\left(\frac{l_{wj}\cos\left[l_{wj}\pi\left(d-1\right)\right]\sin\left[l_{wi}\pi\left(d-1\right)\right] - l_{wi}\cos\left[l_{wi}\pi\left(d-1\right)\right]\sin\left[l_{wj}\pi\left(d-1\right)\right]}{\left(l_{wi}-l_{wj}+\delta_{l_{wi}l_{wj}}\right)\left(l_{wi}+l_{wj}+\delta_{l_{wi}l_{wj}}\right)\pi} \right)$$

$$-\delta_{l_{wi}l_{wj}}\left(1-\delta_{0,l_{wi}}\delta_{0,l_{wj}}\right)\left(\frac{\sin\left[2l_{wi}\pi\left(d-1\right)\right]-2l_{wi}\pi d}{4\pi\left(l_{wi}+\delta_{0,l_{wi}}\right)} \right)$$

$$c_2 = \left(1-\delta_{m_{wi}m_{wj}}\right)\left(\frac{m_{wj}\cos\left[m_{wj}\pi\left(d-1\right)\right]\sin\left[m_{wi}\pi\left(1-d\right)\right] + m_{wi}\cos\left[m_{wi}\pi\left(d-1\right)\right]\sin\left[m_{wj}\pi\left(d-1\right)\right]}{\left(m_{wi}-m_{wj}+\delta_{m_{wi}m_{wj}}\right)\left(m_{wi}+m_{wj}+\delta_{m_{wi}m_{wj}}\right)\pi} \right)$$

$$+\frac{\delta_{m_{wi}m_{wj}}\left(1-\delta_{0,m_{wi}}\delta_{0,m_{wj}}\right)}{4}\left(2-2d+\frac{\sin\left[2m_{wi}\pi\left(d-1\right)\right]}{\left(m_{wi}+\delta_{0,m_{wi}}\right)\pi} \right)$$

$$c_3 = \left(1-\delta_{m_{wi}m_{wj}}\right)\left(\frac{m_{wj}\cos\left[m_{wj}\pi\left(d-1\right)\right]\sin\left[m_{wi}\pi\left(d-1\right)\right] - m_{wi}\cos\left[m_{wi}\pi\left(d-1\right)\right]\sin\left[m_{wj}\pi\left(d-1\right)\right]}{\left(m_{wi}-m_{wj}+\delta_{m_{wi}m_{wj}}\right)\left(m_{wi}+m_{wj}+\delta_{m_{wi}m_{wj}}\right)\pi} \right)$$

$$-\delta_{m_{wi}m_{wj}}\left(1-\delta_{0,m_{wi}}\delta_{0,m_{wj}}\right)\left(\frac{\sin\left[2m_{wi}\pi\left(d-1\right)\right]-2m_{wi}\pi d}{4\pi\left(m_{wi}+\delta_{0,m_{wi}}\right)} \right)$$

$$c_4 = \left(1-\delta_{l_{wi}l_{wj}}\right)\left(\frac{l_{wj}\cos\left[l_{wj}\pi\left(d-1\right)\right]\sin\left[l_{wi}\pi\left(1-d\right)\right] + l_{wi}\cos\left[l_{wi}\pi\left(d-1\right)\right]\sin\left[l_{wj}\pi\left(d-1\right)\right]}{\left(l_{wi}-l_{wj}+\delta_{l_{wi}l_{wj}}\right)\left(l_{wi}+l_{wj}+\delta_{l_{wi}l_{wj}}\right)\pi} \right)$$

$$+\frac{\delta_{l_{wi}l_{wj}}\left(1-\delta_{0,l_{wi}}\delta_{0,l_{wj}}\right)}{4}\left(2-2d+\frac{\sin\left[2l_{wi}\pi\left(d-1\right)\right]}{\left(l_{wi}+\delta_{0,l_{wi}}\right)\pi} \right)$$

$$w_{1ik} = -\int_{\Omega_b} \frac{\partial p_{fk}}{\partial z} w_{fi} dydz = \frac{\delta_{l_{wi}l_{pk}} \left(2m_{pk}+1\right)}{4} \left[\frac{\cos\left[\left(m_{wi}-m_{pk}\right)\pi\right]}{2m_{wi}-2m_{pk}+1} + \frac{\cos\left[\left(m_{wi}+m_{pk}\right)\pi\right]}{2m_{wi}+2m_{pk}+1} \right]$$

$$+ p_c \left\{ \frac{\left(2m_{pk}+1\right)}{2\pi} \left[\frac{\cos\left[\left(l_{pk}-l_{wi}\right)\pi\right]}{2l_{wi}-2l_{pk}+1} + \frac{\cos\left[\left(1+l_{wi}+l_{pk}\right)\pi\right]}{2l_{wi}+2l_{pk}+3} \right] \times \right.$$

$$\left. \left[\frac{\sin\left[\left(3+4m_{wi}-2m_{pk}\right)\frac{\pi}{4}\right]}{-2m_{pk}+4m_{wi}+3} - \frac{\sin\left[\left(5+4m_{wi}+2m_{pk}\right)\frac{\pi}{4}\right]}{4m_{wi}+2m_{pk}+5} \right] \right\}$$

For Eq. (A.5), we can write wp_{ij} and vp_{ij} as:

$$wp_{ij} = \int_{\Omega_b} p_{fi} \frac{\partial w_{fj}}{\partial z} dydz = \frac{\left(m_{wj}+1\right)\delta_{l_{pi}l_{wj}}}{2} \left[\frac{\cos\left[\left(m_{wj}-m_{pi}\right)\pi\right]}{2m_{pi}-2m_{wj}+1} + \frac{\cos\left[\left(m_{pi}+m_{wj}\right)\pi\right]}{2m_{pi}+2m_{wj}+1} \right]$$

$$+ p_c \left\{ -\frac{2\left(m_{wj}+1\right)}{\pi} \left[\frac{\cos\left[\left(l_{pi}-l_{wj}\right)\pi\right]}{2l_{pi}-2l_{wj}-1} + \frac{\cos\left[\left(1+l_{pi}+l_{wj}\right)\pi\right]}{2l_{pi}+2l_{wj}+3} \right] \times \right.$$

$$\left. \left[\frac{\cos\left[\left(5-2m_{pi}+4m_{wj}\right)\frac{\pi}{4}\right]}{2m_{pi}-4m_{wj}-3} + \frac{\sin\left[\left(5+2m_{pi}+4m_{wj}\right)\frac{\pi}{4}\right]}{2m_{pi}+4m_{wj}+5} \right] \right\}$$

$$vp_{ij} = \int_{\Omega_b} p_{fi} \frac{\partial v_{fj}}{\partial y} dydz = \frac{\delta_{m_{pi}m_{vj}} \left(2l_{vj}+1\right)}{4} \left[\frac{\cos\left[\left(l_{pi}-l_{vj}\right)\pi\right]}{2l_{pi}-2l_{vj}-1} + \frac{\cos\left[\left(l_{pi}+l_{vj}\right)\pi\right]}{2l_{pi}+2l_{vj}+1} \right]$$

$$+ p_c \left\{ -\frac{\left(2l_{vj}+1\right)\delta_{l_{pi}l_{vj}}}{2} \left[\frac{\cos\left[\left(3-2m_{pi}+4m_{vj}\right)\frac{\pi}{4}\right]}{-4m_{vj}+2m_{pi}-1} + \frac{\sin\left[\left(3+2m_{pi}+4m_{vj}\right)\frac{\pi}{4}\right]}{4m_{vj}+2m_{pi}+3} \right] \right\}$$

REFERENCES

Abhimanyu, P., Kaushik, P., Mondal, P. K., & Chakraborty, S. (2016). Transiences in rotational electro-hydrodynamics microflows of a viscoelastic fluid under electrical double layer phenomena. *Journal of Non-Newtonian Fluid Mechanics*, *231*, 56–67.

Afonso, A. M., Alves, M. A., & Pinho, F. T. (2013). Analytical solution of two-fluid electro-osmotic flows of viscoelastic fluids. *Journal of Colloid and Interface Science*, *395*(1), 277–286.

Afonso, A. M., Alves, M. A., & Pinho, F. T. (2009). Analytical solution of mixed electro-osmotic/pressure driven flows of viscoelastic fluids in microchannels. *Journal of Non-Newtonian Fluid Mechanics*, *159*(1–3), 50–63.

Alipanah, M., & Ramiar, A. (2017). High efficiency micromixing technique using periodic induced charge electroosmotic flow: A numerical study. *Colloids and Surfaces A: Physicochemical and Engineering Aspects*, *524*(April), 53–65.

Alom Ruiz, S., & Chen, C. S. (2007). Microcontact printing: A tool to pattern. *Soft Matter*, *3*(2), 168–177.

Andrews, J., & Das, S. (2015). Effect of finite ion sizes in electric double layer mediated interaction force between two soft charged plates. *RSC Adv.*, *5*(58), 46873–46880.

Azimi, S., Nazari, M., & Daghighi, Y. (2017). Developing a fast and tunable micro-mixer using induced vortices around a conductive flexible link. *Physics of Fluids*, *29*(3), 032004.

Baaijens, F. P., Baaijens, H. P., Peters, G. W., & Meijer, H. E. (1994). An experimental and numerical investigation of a viscoelastic flow around a cylinder. *Journal of Rheology*, *38*(2), 351–376.

Baaijens, H. P., Peters, G. W., Baaijens, F. P., & Meijer, H. E. (1995). Viscoelastic flow past a confined cylinder of a polyisobutylene solution. *Journal of Rheology*, *39*(6), 1243–1277.

Bag, N., & Bhattacharyya, S. (2018). Electroosmotic flow of a non-Newtonian fluid in a microchannel with heterogeneous surface potential. *Journal of Non-Newtonian Fluid Mechanics*, *259*(May 2017), 48–60.

Bandopadhyay, A., & Chakraborty, S. (2011). Steric-effect induced alterations in streaming potential and energy transfer efficiency of non-newtonian fluids in narrow confinements. *Langmuir*, *27*(19), 12243–12252.

Bandopadhyay, A., & Chakraborty, S. (2012). Giant augmentations in electro-hydro-dynamic energy conversion efficiencies of nanofluidic devices using viscoelastic fluids. *Applied Physics Letters*, *101*(4), 043905.

Bandopadhyay, A., & Chakraborty, S. (2015). Consistent prediction of streaming potential in non-Newtonian fluids: the effect of solvent rheology and confinement on ionic conductivity. *Physical Chemistry Chemical Physics : PCCP*, *17*(11), 7282–7290.

Bandopadhyay, A., Goswami, P., & Chakraborty, S. (2014). Effect of streaming current on helical flows of power law fluids. *Physics of Fluids*, *26*(12), 122003.

Bandopadhyay, A., Tripathi, D., & Chakraborty, S. (2016). Electroosmosis-modulated

peristaltic transport in microfluidic channels. *Physics of Fluids*, *28*(5), 052002.

Banerjee, A., Nayak, A. K., & Weigand, B. (2019). Enhanced mixing and flow reversal in a modulated microchannel. *International Journal of Mechanical Sciences*, *155*, 430–439.

Basati, Y., Mohammadipour, O. R., & Niazmand, H. (2019). Numerical investigation and simultaneous optimization of geometry and zeta-potential in electroosmotic mixing flows. *International Journal of Heat and Mass Transfer*, *133*, 786–799.

Benson, L., Yeh, L.-H., Chou, T.-H., & Qian, S. (2013). Field effect regulation of Donnan potential and electrokinetic flow in a functionalized soft nanochannel. *Soft Matter*, *9*(41), 9767.

Berli, C. L. A. (2010a). Output pressure and efficiency of electrokinetic pumping of non-Newtonian fluids. *Microfluidics and Nanofluidics*, *8*(2), 197–207.

Berli, C. L. A. (2010b). Electrokinetic energy conversion in microchannels using polymer solutions. *Journal of Colloid and Interface Science*, *349*(1), 446–448.

Berli, C. L. A. (2013). The apparent hydrodynamic slip of polymer solutions and its implications in electrokinetics. *Electrophoresis*, *34*(5), 622–630.

Berli, C. L. A., & Olivares, M. L. (2008). Electrokinetic flow of non-Newtonian fluids in microchannels. *Journal of Colloid and Interface Science*, *320*(2), 582–589.

Bird, R. B., Stewart, W. E., & Lightfoot, E. N. (2006). *Transport Phenomena* (second). John Wiley & Sons, Inc.

Brilliantov, N. V., Budkov, Y. A., & Seidel, C. (2016). Generation of mechanical force by grafted polyelectrolytes in an electric field: application to polyelectrolyte-based nano-devices. *Philosophical Transactions of the Royal Society A: Mathematical, Physical and Engineering Sciences*, *374*(2080), 20160143.

Chabra, R. P., & Richardson, J. F. (2008). *Non-Newtonian Flow and Applied Rheology* (Butterworth-Hienemann (ed.); 2nd ed.). Elsevier Ltd.

Chanda, S., Sinha, S., & Das, S. (2014). Streaming potential and electroviscous effects in soft nanochannels: towards designing more efficient nanofluidic electrochemomechanical energy converters. *Soft Matter*, *10*(38), 7558–7568.

Chang, C.-C., & Wang, C.-Y. (2011). Rotating electro-osmotic flow over a plate or between two plates. *Physical Review E*, *84*(5), 056320.

Chen, G., & Das, S. (2015a). Streaming potential and electroviscous effects in soft nanochannels beyond Debye-Hückel linearization. *Journal of Colloid and Interface Science*, *445*, 357–363.

Chen, G., & Das, S. (2015b). Electroosmotic transport in polyelectrolyte-grafted nanochannels with pH-dependent charge density. *Journal of Applied Physics*, *117*(18), 185304.

Chen, G., & Das, S. (2016). Anomalous Shrinking–Swelling of Nanoconfined End-Charged Polyelectrolyte Brushes: Interplay of Confinement and Electrostatic Effects. *The Journal of Physical Chemistry B*, *120*(27), 6848–6857.

Chen, G., & Das, S. (2017). Massively Enhanced Electroosmotic Transport in

Nanochannels Grafted with End-Charged Polyelectrolyte Brushes. *The Journal of Physical Chemistry B*, *121*(14), 3130–3141.

Chen, G., Sachar, H. S., & Das, S. (2018). Efficient electrochemomechanical energy conversion in nanochannels grafted with end-charged polyelectrolyte brushes at medium and high salt concentration. *Soft Matter*, *14*(25), 5246–5255.

Chew, Y. T., Xia, H. M., & Shu, C. (2007). *Fluid Micromixing Technology and Its Applications for Biological and Chemical Processes* (pp. 16–20).

Daiguji, H, Yang, P., Szeri, A., & Majumdar, A. (2004). Electrochemomechanical energy conversion in nanofluidicchannels. *Nano Letters*, *4*(12), 2315-2322.

Daiguji, Hirofumi, Oka, Y., Adachi, T., & Shirono, K. (2006). Theoretical study on the efficiency of nanofluidic batteries. *Electrochemistry Communications*, *8*(11), 1796–1800.

Das, S., Banik, M., Chen, G., Sinha, S., & Mukherjee, R. (2015). Polyelectrolyte brushes: theory, modelling, synthesis and applications. *Soft Matter*, *11*(44), 8550–8583.

Das, S., & Chakraborty, S. (2010). Effect of Conductivity Variations within the Electric Double Layer on the Streaming Potential Estimation in Narrow Fluidic Confinements. *Langmuir*, *26*(13), 11589–11596.

Das, T., Das, S., & Chakraborty, S. (2009). Influences of streaming potential on cross stream migration of flexible polymer molecules in nanochannel flows. *The Journal of Chemical Physics*, *130*(24), 244904.

Davidson, C., & Xuan, X. (2008a). Effects of Stern layer conductance on electrokinetic energy conversion in nanofluidic channels. *Electrophoresis*, *29*(5), 1125–1130.

Davidson, C., & Xuan, X. (2008b). Electrokinetic energy conversion in slip nanochannels. *Journal of Power Sources*, *179*(1), 297–300.

de Kerchove, A. J., & Elimelech, M. (2005). Relevance of Electrokinetic Theory for "Soft" Particles to Bacterial Cells: Implications for Bacterial Adhesion. *Langmuir*, *21*(14), 6462–6472.

Demachi, H., Matsui, O., Abo, H., & Tatsu, H. (2000). Simulation model based on non-newtonian fluid mechanics applied to the evaluation of the embolic effect of emulsions of iodized oil and anticancer drug. *CardioVascular and Interventional Radiology*, *23*(4), 285–290.

Dhar, J., Ghosh, U., & Chakraborty, S. (2014). Alterations in streaming potential in presence of time periodic pressure-driven flow of a power law fluid in narrow confinements with nonelectrostatic ion-ion interactions. *Electrophoresis*, *35*(5), 662–669.

Donath, E., & Voigt, A. (1986). Streaming current and Steaming potential on structured surfaces. *J. Colloid Interface Sci.*, *109*(1), 122.

Ducrée, J., Haeberle, S., Brenner, T., Glatzel, T., & Zengerle, R. (2006). Patterning of flow and mixing in rotating radial microchannels. *Microfluidics and Nanofluidics*, *2*(2), 97–105.

Duffy, D. C., Gillis, H. L., Lin, J., Sheppard, N. F., & Kellogg, G. J. (1999).

Microfabricated Centrifugal Microfluidic Systems: Characterization and Multiple Enzymatic Assays. *Analytical Chemistry*, *71*(20), 4669–4678.

Ebrahimi, S., Hasanzadeh-Barforoushi, A., Nejat, A., & Kowsary, F. (2014). Numerical study of mixing and heat transfer in mixed electroosmotic/ pressure driven flow through T-shaped microchannels. *International Journal of Heat and Mass Transfer*, *75*, 565–580.

Fahraeus, R., & Lindqvist, T. (1930). The viscosity of the blood in narroe capillary tubes. *Journal of American Physiological Society*, *8*, 562–568.

Ferrás, L. L., Afonso, A. M., Alves, M. A., Nóbrega, J. M., Pinho, F. T. (2016). Electro-osmotic and pressure-driven flow of viscoelastic fluids in microchannels: Analytical and semi-analytical solutions. *Physics of Fluids*, *28*(9), 093102.

Freudenberg, U., Zimmermann, R., Schmidt, K., Behrens, S. H., & Werner, C. (2007). Charging and swelling of cellulose films. *Journal of Colloid and Interface Science*, *309*(2), 360–365.

Garai, A., & Chakraborty, S. (2010). Steric effect and slip-modulated energy transfer in narrow fluidic channels with finite aspect ratios. *Electrophoresis*, *31*(5), 843–849.

Gorthi, S. R., Gaikwad, H. S., Mondal, P. K., & Biswas, G. (2020). Surface Tension Driven Filling in a Soft Microchannel: Role of Streaming Potential. *Industrial & Engineering Chemistry Research*, *59*(9), 3839–3853.

Goswami, P., & Chakraborty, S. (2010). Energy Transfer through Streaming Effects in Time-Periodic Pressure-Driven Nanochannel Flows with Interfacial Slip. *Langmuir*, *26*(1), 581–590.

Goswami, P., Kumar Mondal, P., Dutta, S., & Chakraborty, S. (2015). Electroosmosis of Powell-Eyring fluids under interfacial slip. *Electrophoresis*, *36*(5), 703–711.

Gross, R. J., & Osterle, J. F. (1968). Membrane transport characteristics of ultrafine capillaries. *The Journal of Chemical Physics*, *49*(1), 333–339.

Hadigol, M., Nosrati, R., Nourbakhsh, A., & Raisee, M. (2011). Numerical study of electroosmotic micromixing of non-Newtonian fluids. *Journal of Non-Newtonian Fluid Mechanics*, *166*(17–18), 965–971.

Hart, J. E. (1971). Instability and secondary motion in a rotating channel flow. *Journal of Fluid Mechanics*, *45*(02), 341.

Hessel, V., Löwe, H., & Schönfeld, F. (2005). Micromixers—a review on passive and active mixing principles. *Chemical Engineering Science*, *60*(8–9), 2479–2501.

Hsieh, S.-S., & Yang, T.-K. (2008). Electroosmotic flow in rectangular microchannels with Joule heating effects. *Journal of Micromechanics and Microengineering*, *18*(2), 025025.

Hsu, C.-J. (1981). Numerical Heat Transfer and Fluid Flow. *Nuclear Science and Engineering*, *78*(2), 196–197.

Hu, S., Ren, X., Bachman, M., Sims, C. E., Li, G. P., & Allbritton, N. (2002). Surface Modification of Poly(dimethylsiloxane) Microfluidic Devices by Ultraviolet Polymer Grafting. *Analytical Chemistry*, *74*(16), 4117–4123.

Huang, H.-F., & Lai, C.-L. (2006). Enhancement of mass transport and separation of species by oscillatory electroosmotic flows. *Proceedings of the Royal Society A: Mathematical, Physical and Engineering Sciences*, *462*(2071), 2017–2038.

Huang, Y., Chen, J., Wong, T., & Liow, J.-L. (2016). Experimental and theoretical investigations of non-Newtonian electro-osmotic driven flow in rectangular microchannels. *Soft Matter*, *12*(29), 6206–6213.

Hughes, C., Yeh, L. H., & Qian, S. (2013). Field effect modulation of surface charge property and electroosmotic flow in a nanochannel: Stern layer effect. *Journal of Physical Chemistry C*, *117*(18), 9322–9331.

Husemann, M., Mecerreyes, D., Hawker, C. J., Hedrick, J. L., Shah, R., & Abbott, N. L. (1999). Surface-Initiated Polymerization for Amplification of Self-Assembled Monolayers Patterned by Microcontact Printing. *Angewandte Chemie International Edition*, *38*(5), 647–649.

J Mastropietro, D. (2013). Rheology in Pharmaceutical Formulations-A Perspective. *Journal of Developing Drugs*, *02*(02), 2–7.

Johnston, J. P., Halleent, R. M., & Lezius, D. K. (1972). Effects of spanwise rotation on the structure of two-dimensional fully developed turbulent channel flow. *Journal of Fluid Mechanics*, *56*(03), 533.

Joseph, D. D. (1990). *Fluid Dynamics of Viscoelastic Liquids* (Vol. 84). Springer New York.

Kaushik, P., Abhimanyu, P., Mondal, P. K., & Chakraborty, S. (2017). Confinement effects on the rotational microflows of a viscoelastic fluid under electrical double layer phenomenon. *Journal of Non-Newtonian Fluid Mechanics*, *244*(2), 123–137.

Kaushik, P., & Chakraborty, S. (2017). Startup electroosmotic flow of a viscoelastic fluid characterized by Oldroyd-B model in a rectangular microchannel with symmetric and asymmetric wall zeta potentials. *Journal of Non-Newtonian Fluid Mechanics*, *247*, 41–52.

Kaushik, P., Mondal, P. K., & Chakraborty, S. (2016). Flow dynamics of a viscoelastic fluid squeezed and extruded between two parallel plates. *Journal of Non-Newtonian Fluid Mechanics*, *227*, 56–64.

Kaushik, P., Mondal, P. K., & Chakraborty, S. (2017). Rotational electrohydrodynamics of a non-Newtonian fluid under electrical double-layer phenomenon: the role of lateral confinement. *Microfluidics and Nanofluidics*, *21*(7), 1–16.

Kaushik, P., Mondal, P. K., Kundu, P. K., & Wongwises, S. (2019). Rotating electroosmotic flow through a polyelectrolyte-grafted microchannel: An analytical solution. *Physics of Fluids*, *31*(2), 022009.

Kheshgi, H. S., & Scriven, L. E. (1985). Viscous flow through a rotating square channel. *Physics of Fluids*, *28*(10), 2968.

Koneshan, S., Lynden-Bell, R. M., & Rasaiah, J. C. (1998). Friction Coefficients of Ions in Aqueous Solution at 25 °C. *Journal of the American Chemical Society*, *120*(46), 12041–12050.

Koranlou, A., Ashrafizadeh, S. N., & Sadeghi, A. (2019). Enhanced electrokinetic energy

harvesting from soft nanochannels by the inclusion of ionic size. *Journal of Physics D: Applied Physics*, *52*(15), 155502.

Krishnaveni, T., Renganathan, T., Picardo, J. R., & Pushpavanam, S. (2017). Numerical study of enhanced mixing in pressure-driven flows in microchannels using a spatially periodic electric field. *Physical Review E*, *96*(3), 033117.

Kunti, G., Mondal, P. K., Bhattacharya, A., & Chakraborty, S. (2018). Electrothermally modulated contact line dynamics of a binary fluid in a patterned fluidic environment. *Physics of Fluids*, *30*(9), 092005.

Lezius, D. K., & Johnston, J. P. (1976). Roll-cell instabilities in rotating laminar and trubulent channel flows. *Journal of Fluid Mechanics*, *77*(1), 153–174.

Li, S. X., Jian, Y. J., Xie, Z. Y., Liu, Q. S., & Li, F. Q. (2015). Rotating electro-osmotic flow of third grade fluids between two microparallel plates. *Colloids and Surfaces A: Physicochemical and Engineering Aspects*, *470*, 240–247.

Liu, Y., & Jian, Y. (2019). The Effects of Finite Ionic Sizes and Wall Slip on Entropy Generation in Electroosmotic Flows in a Soft Nanochannel. *Journal of Heat Transfer*, *141*(10), 1–11.

Loucaides, N., Ramos, A., & Georghiou, G. E. (2012). Configurable AC electroosmotic pumping and mixing. *Microelectronic Engineering*, *90*, 47–50.

Makino, K., & Ohshima, H. (2011). Soft particle analysis of electrokinetics of biological cells and their model systems. *Science and Technology of Advanced Materials*, *12*(2), 023001.

Masliyah, J H, & Bhattacharjee, S. (2006). *Electrokinetic and Colloid Transport Phenomena*. Wiley.

Masliyah, Jacob H. (1980). On laminar flow in curved semicircular ducts. *Journal of Fluid Mechanics*, *99*(3), 469–479.

Matin, M. H., & Ohshima, H. (2016). Thermal transport characteristics of combined electroosmotic and pressure driven flow in soft nanofluidics. *Journal of Colloid and Interface Science*, *476*, 167–176.

Matin, Meisam Habibi, & Ohshima, H. (2015). Combined electroosmotically and pressure driven flow in soft nanofluidics. *Journal of Colloid and Interface Science*, *460*, 361–369.

Mondal, P. K., DasGupta, D., Bandopadhyay, A., & Chakraborty, S. (2014). Pulsating flow driven alteration in moving contact-line dynamics on surfaces with patterned wettability gradients. *Journal of Applied Physics*, *116*(8), 084302.

Mondal, P. K., DasGupta, D., Bandopadhyay, A., Ghosh, U., & Chakraborty, S. (2015). Contact line dynamics of electroosmotic flows of incompressible binary fluid system with density and viscosity contrasts. *Physics of Fluids*, *27*(3), 032109.

Mondal, P. K., DasGupta, D., & Chakraborty, S. (2015). Rheology-modulated contact line dynamics of an immiscible binary system under electrical double layer phenomena. *Soft Matter*, *11*(33), 6692–6702.

Mondal, P. K., Ghosh, U., Bandopadhyay, A., DasGupta, D., & Chakraborty, S. (2014).

Pulsating electric field modulated contact line dynamics of immiscible binary systems in narrow confinements under an electrical double layer phenomenon. *Soft Matter*, *10*(42), 8512–8523.

Mukherjee, S., Das, S. S., Dhar, J., Chakraborty, S., & DasGupta, S. (2017). Electroosmosis of Viscoelastic Fluids: Role of Wall Depletion Layer. *Langmuir*, *33*(43), 12046–12055.

Nandakumar, K., Raszillier, H., & Durst, F. (1991). Flow through rotating rectangular ducts. *Physics of Fluids A: Fluid Dynamics*, *3*(5), 770–781.

Nayak, A. K. (2014). Analysis of mixing for electroosmotic flow in micro/nano channels with heterogeneous surface potential. *International Journal of Heat and Mass Transfer*, *75*, 135–144.

Nayak, A. K., Banerjee, A., & Weigand, B. (2018). Mixing and charge transfer in a nanofluidic system due to a patterned surface. *Applied Mathematical Modelling*, *54*, 483–501.

Ng, C.-O., & Qi, C. (2015). Electro-osmotic flow in a rotating rectangular microchannel. *Proceedings of the Royal Society A: Mathematical, Physical and Engineering Sciences*, *471*(2179), 20150200.

Nguyen, N.-T., Huang, X., & Chuan, T. K. (2002). MEMS-Micropumps: A Review. *Journal of Fluids Engineering*, *124*(2), 384.

Nguyen, N.-T., & Wu, Z. (2005). Micromixers—a review. *Journal of Micromechanics and Microengineering*, *15*(2), R1–R16.

Nguyen, T., Xie, Y., De Vreede, L. J., Van Den Berg, A., & Eijkel, J. C. T. (2013). Highly enhanced energy conversion from the streaming current by polymer addition. *Lab on a Chip*, *13*(16), 3210–3216.

Nield, D. A., & Bejan, A. (2006). Convection in Porous Media Convection in Porous Media. In *Control* (Vol. 24). Springer New York.

Nield, Donald A., & Bejan, A. (2006). Convection in Porous Media Third Edition. In *Control* (Vol. 24). Springer New York.

Oded, M., Kelly, S. T., Gilles, M. K., Müller, A. H. E., & Shenhar, R. (2016). Periodic nanoscale patterning of polyelectrolytes over square centimeter areas using block copolymer templates. *Soft Matter*, *12*(20), 4595–4602.

Olivares, M. L., Vera-Candioti, L., & Berli, C. L. (2009). The EOF of polymer solutions. *Electrophoresis*, *30*(5), 921–928.

Pacheco, J. R. (2008). Mixing enhancement in electro-osmotic flows via modulation of electric fields. *Physics of Fluids*, *20*(9).

Patankar, S. V. (1980). *Numerical heat transfer and fluid flow*.

Patwary, J., Chen, G., & Das, S. (2016). Efficient electrochemomechanical energy conversion in nanochannels grafted with polyelectrolyte layers with pH-dependent charge density. *Microfluidics and Nanofluidics*, *20*(2), 37.

Pedlosky, J. (1987). *Geophysical Fluid Dynamics*. Springer New York.

Peng, R., & Li, D. (2016). Electroosmotic flow in single PDMS nanochannels. *Nanoscale*, *8*(24), 12237–12246.

Poddar, A., Maity, D., Bandopadhyay, A., & Chakraborty, S. (2016). Electrokinetics in polyelectrolyte grafted nanofluidic channels modulated by the ion partitioning effect. *Soft Matter*, *12*(27), 5968–5978.

Poortinga, A. T., Bos, R., Norde, W., & Busscher, H. J. (2002). Electric double layer interactions in bacterial adhesion to surfaces. *Surface Science Reports*, *47*(1), 1–32.

Prucker, O., Habicht, J., Park, I.-J., & Rühe, J. (1999). Photolithographic structuring of surface-attached polymer monolayers. *Materials Science and Engineering: C*, *8–9*, 291–297.

Qian, S., & Bau, H. H. (2002). A chaotic electroosmotic stirrer. *Analytical Chemistry*, *74*(15), 3616–3625.

R. J. Hunter. (1981). *Zeta Potential in Colloid Science: Principles and Applications*. Academic Press.

Raviv, U., Giasson, S., Kampf, N., Gohy, J.-F., Jérôme, R., & Klein, J. (2003). Lubrication by charged polymers. *Nature*, *425*(6954), 163–165.

Reddy, J. N. (1986). *Applied Functional Analysis and Variational Methods in Engineering*. Mc Graw-Hill.

Reddy, J. N., & Rasmussen, M. L. (1982). *Advanced Engineering Analysis*. Wiley.

Rektorys, K. (1977). *Variational Methods in Mathematics, Science and Engineering*. Springer Netherlands.

Ren, Y., & Stein, D. (2008). Slip-enhanced electrokinetic energy conversion in nanofluidic channels. *Nanotechnology*, *19*(19).

Reshadi, M., & Saidi, M. H. (2019). Tuning the dispersion of reactive solute by steady and oscillatory electroosmotic–Poiseuille flows in polyelectrolyte-grafted micro/nanotubes. *Journal of Fluid Mechanics*, *880*, 73–112.

Rivero, M., & Cuevas, S. (2012). Analysis of the slip condition in magnetohydrodynamic (MHD) micropumps. *Sensors and Actuators, B: Chemical*, *166–167*, 884–892.

Sadeghi, A. (2018a). Micromixing by two-phase hydrodynamic focusing: A 3D analytical modeling. *Chemical Engineering Science*, *176*, 180–191.

Sadeghi, A. (2018b). Theoretical modeling of electroosmotic flow in soft microchannels: A variational approach applied to the rectangular geometry. *Physics of Fluids*, *30*(3), 032004.

Sadeghi, A., Azari, M., & Hardt, S. (2019). Electroosmotic flow in soft microchannels at high grafting densities. *Physical Review Fluids*, *4*(6), 063701.

Sadeghi, M., Saidi, M. H., Moosavi, A., & Sadeghi, A. (2020). Unsteady solute dispersion by electrokinetic flow in a polyelectrolyte layer-grafted rectangular microchannel with wall absorption. *Journal of Fluid Mechanics*, *887*, A13.

Saville, D. A. (1977). Electrokinetic Effects with Small Particles. *Annual Review of Fluid Mechanics*, *9*(1), 321–337.

Schoonen, J. F., Swartjes, F. H., Peters, G. W., Baaijens, F. P., & Meijer, H. E. (1998). A 3D numerical/experimental study on a stagnation flow of a polyisobutylene solution. *Journal of Non-Newtonian Fluid Mechanics*, *79*(2–3), 529–561.

Speziale, C. G. (1982). Numerical study of viscous flow in rotating rectangular ducts. *Journal of Fluid Mechanics*, *122*(1), 251.

Stewartson, K. (1957). On almost rigid rotations. *Journal of Fluid Mechanics*, *3*(1), 17–26.

Stone, H. A., Stroock, A. D., & Ajdari, A. (2004). Engineering Flows in Small Devices. *Annual Review of Fluid Mechanics*, *36*(1), 381–411.

Thien, N. P., & Tanner, R. I. (1977). A new constitutive equation derived from network theory. *Journal of Non-Newtonian Fluid Mechanics*, *2*(4), 353–365.

Tsouris, C., Culbertson, C. T., DePaoli, D. W., Jacobson, S. C., de Almeida, V. F., & Ramsey, J. M. (2003). Electrohydrodynamic mixing in microchannels. *AIChE Journal*, *49*(8), 2181–2186.

van der Heyden, F. H. J., Bonthuis, D. J., Stein, D., Meyer, C., & Dekker, C. (2007). Power Generation by Pressure-Driven Transport of Ions in Nanofluidic Channels. *Nano Letters*, *7*(4), 1022–1025.

von Werne, T. A., Germack, D. S., Hagberg, E. C., Sheares, V. V., Hawker, C. J., & Carter, K. R. (2003). A Versatile Method for Tuning the Chemistry and Size of Nanoscopic Features by Living Free Radical Polymerization. *Journal of the American Chemical Society*, *125*(13), 3831–3838.

Wang, G.-J., Hsu, W.-H., Chang, Y.-Z., & Yang, H. (2004). Centrifugal and Electric Field Forces Dual-Pumping CD-Like Microfluidic Platform for Biomedical Separation. *Biomedical Microdevices*, *6*(1), 47–53.

Wang, H., Iovenitti, P., Harvey, E., & Masood, S. (2003). Numerical investigation of mixing in microchannels with patterned grooves. *Journal of Micromechanics and Microengineering*, *13*(6), 801–808.

Wang, X.-P., Qian, T., & Sheng, P. (2008). Moving contact line on chemically patterned surfaces. *Journal of Fluid Mechanics*, *605*, 59–78.

Xie, Z. Y., & Jian, Y. J. (2014). Rotating electroosmotic flow of power-law fluids at high zeta potentials. *Colloids and Surfaces A: Physicochemical and Engineering Aspects*, *461*(1), 231–239.

Xing, J., & Jian, Y. (2018). Steric effects on electroosmotic flow in soft nanochannels. *Meccanica*, *53*(1–2), 135–144.

Xuan, X., & Li, D. (2006). Thermodynamic analysis of electrokinetic energy conversion. *Journal of Power Sources*, *156*(2), 677–684.

Yang, J., Lu, F., Kostiuk, L. W., & Kwok, D. Y. (2003). Electrokinetic microchannel battery by means of electrokinetic and microfluidic phenomena. *Journal of Micromechanics and Microengineering*, *13*(6), 963–970.

Zaccone, A., Wu, H., Gentili, D., & Morbidelli, M. (2009). Theory of activated-rate processes under shear with application to shear-induced aggregation of colloids. *Physical Review E*, *80*(5), 1–8.

Zhao, B., Brittain, W. J., Zhou, W., & Cheng, S. Z. D. (2000). Nanopattern Formation from Tethered PS- b -PMMA Brushes upon Treatment with Selective Solvents. *Journal of the American Chemical Society*, *122*(10), 2407–2408.

Zhao, C., & Yang, C. (2011). An exact solution for electroosmosis of non-Newtonian fluids in microchannels. *Journal of Non-Newtonian Fluid Mechanics*, *166*(17–18), 1076–1079.

Zhao, C., Zholkovskij, E., Masliyah, J. H., & Yang, C. (2008). Analysis of electroosmotic flow of power-law fluids in a slit microchannel. *Journal of Colloid and Interface Science*, *326*(2), 503–510.

LIST OF PUBLICATIONS

Publications from the present thesis

1. **Gaikwad, H. S.**, Kumar, G., & Mondal, P. K. (2020). Efficient electroosmotic mixing in a narrow-fluidic channel: the role of a patterned soft layer. *Soft Matter*, 16(27), 6304–6316.
2. **Gaikwad, H. S.**, & Mondal, P. K. (2020a). Tutorial Review of Mixing in a Rotating Soft Microchannel under Electrical Double Layer Effect: A Variational Calculus Approach. http://arxiv.org/abs/2007.14901
3. **Gaikwad, H. S.**, & Mondal, P. K. (2020b). Rheology Modulated High Electrochemo- mechanical Energy Conversion in Soft Narrow-Fluidic Channel. *Journal of Non-Newtonian Fluid Mechanics*, 104381. https://doi.org/10.1016/j.jnnfm.2020.104381
4. **Gaikwad, H. S.**, Mondal, P. K., & Wongwises, S. (2018). Softness Induced Enhancement in Net Throughput of Non-Linear Bio-Fluids in Nanofluidic Channel under EDL Phenomenon. *Scientific Reports*, 8(1), 1–16.

Other publications

1. Agrawal, M. S., **Gaikwad, H. S.**, Mondal, P. K., & Biswas, G. (2019). Analysis and experiments on the spreading dynamics of a viscoelastic drop. *Applied Mathematical Modelling*, 75, 201–209.
2. **Gaikwad, H.**, Basu, D. N., & Mondal, P. K. (2016). Electroosmotic transport of immiscible binary system with a layer of non-conducting fluid under interfacial slip: The role applied pressure gradient. *Electrophoresis*, 37(14), 1998–2009.
3. **Gaikwad, H.**, & Mondal, P. K. (2016). Slip driven electroosmotic transport through porous media. *Electrophoresis*, 38(5), 596–606.
4. **Gaikwad, H. S.**, Baghel, P., Sarma, R., & Mondal, P. K. (2019). Transport of neutral solutes in a viscoelastic solvent through a porous microchannel. *Physics of Fluids*, 31(2), 022006.
5. **Gaikwad, H. S.**, Basu, D. N., & Mondal, P. K. (2017a). Non-linear drag induced irreversibility minimization in a viscous dissipative flow through a micro-porous channel. *Energy*, 119, 588–600.
6. **Gaikwad, H. S.**, Basu, D. N., & Mondal, P. K. (2017b). Slip driven micro-pumping of binary system with a layer of non-conducting fluid under electrical double layer phenomenon. *Colloids and Surfaces A: Physicochemical and Engineering Aspects*, 518, 166–172.
7. **Gaikwad, H. S.**, Mondal, P. K., Basu, D. N., Chimres, N., & Wongwises, S. (2018). Analysis of the Effects of Joule Heating and Viscous Dissipation on Combined Pressure-Driven and Electrokinetic Flows in a Two-Parallel Plate Channel with Unequal Constant Temperatures. *Proceedings of the Institution of Mechanical Engineers, Part E: Journal of Process Mechanical Engineering*, 233(4), 1–9.
8. **Gaikwad, H. S.**, Mondal, P. K., & Wongwises, S. (2017). Non-linear drag induced entropy generation analysis in a microporous channel: The effect of conjugate heat transfer. *International Journal of Heat and Mass Transfer*, 108, 2217–2228.
9. **Gaikwad, H. S.**, Roy, A., & Mondal, P. K. (2020). Autonomous filling of a viscoelastic fluid in a microfluidic channel: Effect of streaming potential. *Journal of Non-Newtonian Fluid Mechanics*, 282, 104317.
10. **Gaikwad, H. S.**, Roy, A., Mondal, P. K., Chimres, N., & Wongwises, S. (2019). Irreversibility analysis in a slip aided electroosmotic flow through an

asymmetrically heated microchannel: The effects of joule heating and the conjugate heat transfer. *Analytica Chimica Acta*, 1045, 85–97.

11. Gorthi, S. R., **Gaikwad, H. S.**, Mondal, P. K., & Biswas, G. (2020). Surface Tension Driven Filling in a Soft Microchannel: Role of Streaming Potential. *Industrial & Engineering Chemistry Research*, 59(9), 3839–3853.

12. Mondal, P. K., **Gaikwad, H.**, Kundu, P. K., & Wongwises, S. (2017). Effect of thermal asymmetries on the entropy generation analysis of a variable viscosity Couette–Poiseuille flow. *Proceedings of the Institution of Mechanical Engineers, Part E: Journal of Process Mechanical Engineering*, 231(5), 095440891668823.

13. Sarma, R., **Gaikwad, H.**, & Mondal, P. K. (2017). Effect of Conjugate Heat Transfer on Entropy Generation in Slip-Driven Microflow of Power Law Fluids. *Nanoscale and Microscale Thermophysical Engineering*, 21(1), 26–44.